

ISOTHERMAL DRYING OF PORE NETWORKS: INFLUENCE OF PORE STRUCTURE ON DRYING KINETICS

**(Isotherme Trocknung von Porennetzwerken:
Einfluss der Porenstruktur auf die Trocknungskinetik)**

Dissertation

zur Erlangung des akademischen Grades

**Doktoringenieur
(Dr.-Ing.)**

von **Anton Irawan, MEng**
geboren am 01.10.1975 in Silungkang, Indonesien

genehmigt durch die Fakultät für Verfahrens- und Systemtechnik
der Otto-von-Guericke-Universität Magdeburg

Promotionskommission: Jun.-Prof. Dr. rer. nat. habil. Ulrich Tallarek (Vorsitz)
Prof. Dr.-Ing. habil. Eckehard Specht (Gutachter)
Dr. Thomas Metzger (Gutachter, Betreuer)
Prof. Dr.-Ing. habil. Evangelos Tsotsas (Betreuer)
Dr. rer. nat. habil. Peter Streitenberger (Mitglied)
Dr. Marc Prat, DR (Mitglied)

eingereicht am 31. Mai 2006

Promotionskolloquium am 10. Juli 2006

*This work is dedicated with pride
to my parents...
...and with love to my wife and my son*

Acknowledgements

This thesis is submitted to the Faculty of Process and System Engineering in fulfillment of the requirements for the degree of Doctoringenieur (Dr.-Ing) at Otto-von-Guericke-University of Magdeburg. This project was carried out at the chair of Thermal Process Engineering, Institute of Process Engineering from March 2003 to May 2006.

First, I thank God for giving me the ability to finish this work.

I would like to thank **Prof. Dr.-Ing. habil. Evangelos Tsotsas** for giving me the opportunity to live and study in Magdeburg, Germany, also for support, advice and guidance to my project.

I would like to express my heartfelt thanks to **Dr. Thomas Metzger** for his effective guidance, clear instructions, constructive ideas and valuable discussions in my project, also for helping my family to live in Magdeburg.

I express many thanks to the DFG (Deutsche Forschungsgemeinschaft) for financial support via the graduate school GK 828

“Micro-Macro Interactions in Structured Media and Particle Systems”.

I also thank **Prof. Dr. Gerald Warnecke** (speaker of graduate school) and **Prof. Dr.-Ing. Albrecht Bertram** (ex-speaker) for supporting me in finishing my project.

I would also like to thank **Prof. Patrick Perre** (Nancy, France), **Dr. Marc Prat** (Toulouse, France), **Prof. Henk van As** (Wageningen, Netherlands) and **Dr. Pavel Capek** (Praha, Czech Republic) for nice and fruit discussion about pore networks in Magdeburg.

To other students in GK 828, especially to **Thai Vu Hong**, **Vikranth Kumar Surasani**, **Ga Sashikumar** and **Jitendra Kumar**, I say many thanks for good discussion about my project and for good environment to study and to learn about the culture of their countries. I also say many thanks to the staff and members of the chair of Thermal Process Engineering, especially to **Dr. Milan Stakic** and **Suherman** for fruitful discussions.

Finally, I would like to thank my parents and family (my wife and son) for their love, kindness, encouragement, and understanding. I dedicate this thesis, that I have worked very hard for, to you.

Abstract

Drying is quite an old method to remove liquid from inside of a porous material such as wood, food, paper, ceramics, building materials, textiles, granular products, pharmaceuticals and electronic devices. The kinetics of this liquid removal depends on the material properties of its solid phase as well as on pore structure. In order to optimize the drying process for good product quality and energy considerations, theoretical modelling of the involved transport phenomena is necessary. Essentially, there are two approaches of modelling, namely the continuum and the discrete approach.

The traditional approach treats the partially saturated porous medium as a fictitious continuum, and transport is described by effective parameters, which depend on saturation and pore structure. The macroscopic conservation equations for mass and enthalpy are obtained by volume averaging or homogenization, which both require a length scale separation of pore phenomena and macroscopic variation of relevant state variables such as moisture content. This requirement is not fulfilled in general, so that the second approach of discrete modelling is an alternative. In this method, the porous medium is represented by a pore network, and transport phenomena are directly investigated at the pore scale. Besides modelling of drying kinetics, such network models might also be used to calculate the effective parameters of the continuous model.

The aim of this project is to study the influence of pore structure on convective drying behaviour by pore network modelling under isothermal conditions. To this purpose, a literature pore network model has been extended to describe the influence of liquid viscosity and lateral vapour transfer in the gas-side boundary layer. This model was applied to two- and three-dimensional networks of different pore size distribution and pore space topology.

Four different two-dimensional network structures were investigated: the first has a monomodal pore size distribution; the remaining three all have a bimodal pore size distribution but differ in the correlated spatial arrangement of micro and macro pores. All results are given as drying curves and phase distributions during drying. It was found that, for favourable drying with a long first drying period, a bimodal pore size distribution is essential and both micro and macro pore phase must be continuous. For efficient evaporation from wet spots on the network surface, the micro pores must additionally have a good spatial distribution. The role of boundary layer thickness, and especially lateral vapour transfer in this boundary layer, was systematically investigated and assessed by comparison with literature models.

The importance of liquid viscosity in comparison with capillary forces was studied by variation of mean and standard deviation of monomodal pore size distributions. For broad distributions, capillary pumping is effective, whereas for narrow distributions, the network rather dries out with a receding front. It could also be shown that for bimodal distributions, liquid viscosity is less significant for overall drying behaviour.

Concerning the influence of random generation of pore radii in the 50x50 networks, drying of all network structures was investigated by the Monte Carlo method. Additionally, the merit of periodic boundary conditions to increase effective network size was studied.

A limited number of three-dimensional network drying simulations has also been carried out because they can more realistically describe certain transport phenomena in drying, like capillary pumping, than modelling in only two dimensions.

Zusammenfassung

Die Trocknung ist ein altes Verfahren, um Flüssigkeit aus porösen Materialien zu trennen, wie zum Beispiel Holz, Lebensmittel, Papier, Keramiken, Baustoffe, Textilien, granulare Medien, Pharmazeutika und elektronische Bauelemente. Die Kinetik dieser Trennung hängt ab von den Materialeigenschaften des Feststoffs sowie der Porenstruktur. Um den Trocknungsprozess hinsichtlich der Produktqualität und des Energieverbrauchs zu optimieren, ist die Modellierung der beteiligten Transportprozesse nötig. Im Wesentlichen gibt es hierzu zwei Ansätze, nämlich die Kontinuums- und die diskrete Modellierung.

Der traditionelle Ansatz behandelt das teilgesättigte poröse Medium als fiktives Kontinuum, und der Transport wird mittels effektiver Parameter beschrieben, welche von Sättigung und Porenstruktur abhängen. Die makroskopischen Erhaltungsgleichungen für Masse und Enthalpie werden durch Volumenmittelung oder Homogenisierung abgeleitet; beide Methoden basieren auf einer Unabhängigkeit der Größenskalen von Phänomenen in einzelnen Poren und der makroskopischen Variation relevanter Zustandsgrößen, wie der Feuchte. Diese Bedingung ist jedoch nicht allgemein erfüllt, so dass der zweite Ansatz der diskreten Modellierung eine Alternative darstellt. In dieser Methode wird das poröse Medium durch ein Netzwerk aus Poren repräsentiert, und Transportphänomene werden direkt auf der Porenebene beschrieben. Neben der Modellierung der Trocknungskinetik könnten Netzwerkmodelle auch dazu dienen, die effektiven Parameter des Kontinuumsmodells zu berechnen.

Das Ziel dieser Arbeit ist es, den Einfluss der Porenstruktur auf das Verhalten bei der Konvektionstrocknung mittels Porennetzwerkmodellierung unter isothermen Bedingungen zu untersuchen. Zu diesem Ziel wurde ein Netzwerkmodell aus der Literatur um den Einfluss der Reibungseffekte in der Flüssigkeit und die laterale Dampfdiffusion in der gasseitigen Grenzschicht erweitert. Dieses Modell wurde auf zwei- und dreidimensionale Netzwerke mit verschiedener Porengrößenverteilung und Topologie des Porenraumes angewendet.

Vier verschiedene zweidimensionale Netzwerkstrukturen wurden untersucht: die erste besitzt eine monomodale Porengrößenverteilung; die anderen drei haben alle eine bimodale Porengrößenverteilung, unterscheiden sich jedoch in der räumlich korrelierten Anordnung von Mikro- und Makroporen. Alle Ergebnisse werden als Trocknungskurven und räumliche Flüssigkeitsverteilungen während der Trocknung dargestellt. Es wurde festgestellt, dass für günstiges Trocknungsverhalten mit einem langen ersten Trocknungsabschnitt eine bimodale Porengrößenverteilung essentiell ist und dass sowohl die Mikroporenphase als auch die Makroporenphase kontinuierlich sein müssen. Für effektive Verdunstung von der teilbefeuchteten Netzwerkoberfläche, müssen die Mikroporen eine gute räumliche Verteilung aufweisen. Die Rolle der Grenzschichtdicke, und insbesondere des lateralen Dampftransports in der Grenzschicht, wurde systematisch untersucht und im Vergleich mit Literaturmodellen bewertet. Die Bedeutung der flüssigen Viskosität im Vergleich zu Kapillarkräften wurde untersucht, indem für monomodale Porengrößenverteilungen Mittelwert und Standardabweichung variiert wurden. Für breite Verteilungen ist die Kapillarströmung effektiv, während Netzwerke mit kleiner Verteilungsbreite eher mit einem wandernden Trocknungsspiegel austrocknen. Es konnte auch gezeigt werden, dass sich für bimodale Verteilungen Reibungseffekte kaum auf das globale Trocknungsverhalten auswirken.

Bezüglich des Einflusses der zufälligen Porenradiengenerierung in den 50x50 Netzwerken, wurde die Trocknung aller Netzwerkstrukturen mit der Monte-Carlo-Methode untersucht. Zudem wurden die Vorzüge periodischer Randbedingungen, um die Netzwerke effektiv zu vergrößern, betrachtet. Eine begrenzte Anzahl dreidimensionaler Netzwerksimulationen wurde ebenfalls durchgeführt, da diese einige Transportphänomene während der Trocknung, wie die Kapillarströmung, besser beschreiben können als zweidimensionale Modelle.

TABLE OF CONTENTS

Abstract	iv
Zusammenfassung	v
Table of Contents	vi
Nomenclature	viii
Introduction.....	1
1 Pore Network Modelling in Literature.....	4
1.1 Overview.....	4
1.2 Porous Media.....	4
1.3 Drying of Porous Media.....	9
1.4 Continuum Versus Discrete Approach	11
1.5 Isothermal Drying of Pore Networks.....	12
1.5.1 Pore Network Model by Nowicki et al.....	13
1.5.2 Pore Network Model by Prat et al.....	17
1.5.3 Pore Network Model by Yiotis et al.....	29
1.5.4 Pore Network Model by Segura et al.....	32
2 Description of Isothermal Pore Network Drying Model.....	35
2.1 Overview.....	35
2.2 Data Structures of Geometry.....	36
2.2.1 Data Structures of Geometry in 2D Square Network.....	38
2.2.2 Data Structures of Geometry in Boundary Layer.....	40
2.2.3 Periodic Boundary Conditions.....	41
2.2.4 Algorithm to Generate Data Structures.....	42
2.3 Drying Algorithm.....	43
2.3.1 Throat and Pore Saturation.....	43
2.3.2 Drying Kinetics.....	46
2.3.3 Time Step for Negligible Viscosity.....	52

2.3.4	Liquid Cluster Labelling.....	52
2.3.5	Viscous Effect in Liquid Phase.....	56
2.4	Updating Liquid Volume and Calculating Network Saturation.....	60
2.5	Summary.....	62
3	Pore Network Drying Simulations and Discussion.....	64
3.1	Overview.....	64
3.2	Network Geometry and Simulation Parameters.....	65
3.3	Drying of 2D Square Networks in Absence of Viscous Effects.....	68
3.3.1	Influence of Structure.....	69
3.3.2	Influence of Lateral Transfer in Boundary Layer.....	76
3.3.3	Influence of Wet Surface Fraction.....	79
3.3.4	Influence of Connectivity.....	82
3.4	Drying of 2D Square Networks with Liquid Viscosity.....	85
3.4.1	Position of Boundary Condition (Equilibrium Vapour Pressure).....	87
3.4.2	Influence of Periodic Boundary Condition.....	88
3.4.3	Influence of Structure.....	89
3.4.4	Influence of Liquid Viscosity.....	90
3.4.5	Influence of Pore Size Distributions.....	96
3.4.6	Influence of Network Depth.....	104
3.5	Drying of 3D Cubic Networks with Viscous Effect.....	105
3.6	Concluding Remarks	111
	Conclusion and Future Works.....	112
	References	114

Nomenclature

Latin symbols

A	exchange area	m^2
a	distance between two nodes	m
b	the space distribution coefficient	–
D	diffusivity	m^2s^{-1}
G	flow conductivity	$kg\ s^{-1}\ Pa^{-1}$
g	gravitational acceleration	$m\ s^{-2}$
K	absolute permeability	m^2
k	relative permeability	–
L	throat length	m
L'	vertical distance between two nodes in boundary layer	m
\tilde{M}	molar mass	$kg\ kmol^{-1}$
\dot{M}	mass flow rate	$kg\ s^{-1}$
\dot{m}	mass flux	$kg\ m^{-2}\ s^{-1}$
n	number of vertical nodes in boundary layer	–
p	pressure	Pa
\tilde{R}	ideal gas constant	$J\ kmol^{-1}\ K^{-1}$
r	throat radius	m
r_0	mean throat radius	m
S	saturation	–
T	absolute temperature	K
t	time	s
u	drying air velocity	$m\ s^{-1}$
V	volume	m^3
v	average liquid velocity	$m\ s^{-1}$
X	moisture content	kg water/kg solid
\tilde{y}	molar vapour fraction	-
\dot{N}	molar flow rate	$kmol\ s^{-1}$
z	depth of network	m
Z	coordination number	

Greek symbols

β	mass transfer coefficient	m s^{-1}
δ	vapour diffusion coefficient	$\text{m}^2 \text{s}^{-1}$
Δ	difference	–
ε	boundary layer thickness	m
η	dynamic viscosity	Pa s
λ	thermal conductivity	$\text{Wm}^{-1}\text{K}^{-1}$
ν	kinematic viscosity	$\text{m}^2 \text{s}^{-1}$
$\dot{\nu}$	dimensionless drying rate	–
ρ	density	kg m^{-3}
σ	surface tension	N m^{-1}
σ_0	standard deviation of pore size distribution	m
φ	wet surface fraction	–
Φ	reduction factor in drying rate	–
ψ	porosity	–

Subscripts and superscripts

a	air
bl	boundary layer
c	capillary
eff	effective
fw	free water
g	gas
i, j	pore indices
k	throat index
m	meniscus
p	cluster index
s	surface of network
tot	total network
v	vapour
w	water
∞	bulk of air
$*$	saturation / equilibrium

Dimensionless numbers

B	Bond number	$(\Delta\rho g L^2)/\sigma$
Ca	Capillary number	$(L_k \eta_w \dot{M}_v)/(\rho_w r_0^2 \sigma \sigma_0)$
Re	Reynolds number	$u L_{tot}/\nu$
Sc	Schmidt number	ν/δ
Sh	Sherwood number	$\beta L_{tot}/\delta$

Abbreviations

BT	breakthrough
CMT	cluster meniscus throats
CRP	constant rate period
DC	disconnected cluster
FRP	falling rate period
IP	invasion percolation
$IPDG$	invasion percolation in a destabilizing gradient
$IPSG$	invasion percolation in a stabilizing gradient
M	moving meniscus
MC	main cluster
MCD	main cluster disconnection
PSD	pore size distribution
S	stationary meniscus
SMT	single meniscus throat

INTRODUCTION

Background

Drying is quite an old method to remove liquid from a porous material such as wood, food, paper, ceramics, textile, building materials, granular media, electronic devices and pharmaceuticals. Some of the reasons to remove liquid from material by drying are to preserve these materials from decreasing of product quality (microbial growth in the food) or to transport the products easily from one place to another. The removal of liquid from inside of porous media depends on the material properties, such as properties of solid and fluid (gas and liquid) as well as on pore structure and on drying conditions. Although drying is a traditional method to remove liquid from a material, drying of porous media is still an interesting subject to study some transport phenomena from the large scale (dryer) to the pore scale (inside porous media). The transport mechanisms that can be studied in porous media are liquid diffusion in multi component systems, vapour diffusion due to different partial vapour pressure, capillary flow in liquid phase, flow in liquid films, menisci moving in the throats and evaporation at these menisci.

Water can flow and escape from inside porous media by several mechanisms. Liquid moves from the biggest meniscus pores to small surface pores by capillary pressure differences (capillary forces). Simultaneously, friction forces will limit this liquid flow. When capillary flow can supply liquid to the surface menisci at the maximum evaporation rate, the drying rate is still at high level as a period of constant drying rate (*CRP*). The constant drying rate continues until the capillary flow can not supply enough liquid for evaporation. At this condition, the drying rate is at low level as a period of falling rate (*FRP*) and the surface of the porous medium will dry out. Then, the vapour can move from menisci to the bulk of drying air by diffusion due to existing gradient of partial vapour pressure.

The transport mechanisms of drying of porous media have been investigated by many research groups using experiments or simulations since some decades. Due to difficulty to observe these phenomena by experiment at the pore scale, only modelling of drying can provide the link to the macroscopic drying behaviour which is accessible experimentally. Whitakers approach (1998 [42]) is a first method to describe comprehensively all relevant microscopic phenomena of drying of porous media utilizing coupled macroscopic equations for heat and mass transfer. A volume averaging technique is used to enable treating of the partially saturated porous medium as a continuum. In this continuous approach, several effective transport parameters are needed to solve mass, momentum and heat transfer such as absolute and relative permeability (K and k), effective diffusivity (D_{eff}) and effective thermal conductivity (λ_{eff}).

Laurindo and Prat (1998 [13], 1998 [14]) explained, however, that the continuum approach has a lack in the length scale separation (necessary for volume averaging or homogenization) because it can not be fulfilled for all structures of porous media. Due to development in statistical physics, computation and image analysis of porous media, the discrete approach by pore network modelling is a powerful tool to realistically describe and investigate transport phenomena of drying of porous media at the pore scale. These discrete methods simulate drying of porous media by observing the phenomena pore by pore.

Pore network modelling for drying was developed by Daian and Saliba (1991 [5]) in order to study moisture migration in the porous material. Nowicki et al. (1992 [20]) described drying

of porous media by a pore network model with biconically shaped throats. Prat (1993 [23]) introduced a modified invasion percolation model for drying of porous media where pores are only nodes and throats contain the liquid. Yiotis et al. (2001 [37]) defined in their modelling the function of throats and pores in different way than Prat. In Yiotis et al., the throat is only a connector between two pores and the pore contains all liquid (water). Segura and Toledo, (2005 [28], 2005 [29], 2005 [30]) studied a pore network model in drying of porous media that is based on Prat's model.

Most of these researchers used network models to study influence of physical effects on the drying behaviour without looking at the influence of porous structure. Only Segura and Toledo (2005 [28]) studied the influence of pore size distribution by changing standard deviation of throat radius, without significant results. Nobody studied, up to now, comprehensively the influence of pore structure.

Research Objectives

This project tried to investigate systematically and comprehensively the influence of the porous structure on the drying behaviour. In the terms 2D and 3D networks, the porous structure is determined by the size distribution of throat radii, number of connectivity, and topology of large and small pore phases for bimodal pore size distributions. Until now, all research groups in network modelling fail to reproduce the first drying period as a constant drying rate period at the beginning of the drying process. This project also tried to model the constant drying period by investigating transport in the boundary layer and by looking at different network structures.

Scope of Study

The network model in this project is based on the modified invasion percolation model for isothermal conditions by Prat (1993 [23]). The pores are assumed as nodes without liquid inside them, and the cylindrical throats contain all liquid (water). The throat radius was generated according to a normal random distribution. Two types of throat radius were used in order to create monomodal and bimodal pore size distributions and the network structure was chosen to have different topology. The different topologies of network structure were: all throats have small radii (monomodal), both small and large throats form a continuous phase from surface to bottom of the network (bimodal), regions of small throats are separated by a continuous phase of large throats (bimodal) and regions of large throats are separated by a continuous phase of small throats (bimodal). Additionally, networks of different connectivity were investigated. The network model was further developed by using a periodic boundary condition and by including the boundary layer and viscous effect in the liquid phase.

The drying of 2D and 3D networks was simulated for all network structures of different topology in order to investigate the influence of structure, pore size distribution and liquid viscosity on drying kinetics. The network model with different boundary layer thickness was compared to the Schlünder model. Monte Carlo simulations were performed in order to assess the influence of randomness on the drying behaviour. The results of network modelling were also compared with the drying of a bundle of capillaries by use of appropriate network geometry.

Outline of Dissertation

This dissertation contains three main chapters, which contain a literature review about pore network modelling in the drying of porous media, the model description of this project, and the presentation and discussion of the results, respectively. In chapter 1, a short description of porous media and of drying of porous media will be given. The important part of this chapter is a description of the network models and the results on drying for all research groups.

The network model in this project was based on Prat's work. The details of the network model in this project will be described in chapter 2. Chapter 2 consists of two big parts, which explain how to generate the data structures describing network geometry and how to build the drying algorithm. The data structures define the neighbouring relationship between pores and throats in network and boundary layer, and need some input parameters such as coordination number, size of network (in 2D and 3D) and air velocity above the network. In the part of the drying algorithm, saturation in the network, liquid cluster labelling and drying kinetics will be described. The drying algorithm has some rules to define the state of pores and throats, to calculate time step and to update state of throats and label the liquid throats. The model will be extended to the influence of liquid viscosity.

The results of this project will be shown in chapter 3. Four different networks will be simulated in this project in order to study different topology. The results are divided into three major parts which are 2D network simulations with negligible liquid viscosity, 2D network simulation with liquid viscosity and 3D network simulation with liquid viscosity. Some variations of pore size distribution are also simulated in order to derive its influence on the drying behaviour.

CHAPTER 1

PORE NETWORK MODELLING

IN LITERATURE

1.1 Overview

Literature work about pore network modelling in drying of porous media will be presented in this chapter in order to give some basis to this project. Firstly, porous media as drying material are explained. Transport phenomena of drying of porous media are discussed. In this part, the drying curve, as representative of drying kinetics, is shown. Before going into the details of pore network modelling (discrete approach), the alternative approach, namely continuous modelling of drying porous of media, will be explained and a comparison will be given. Finally, methods and results of some research groups on drying of porous media by pore network modelling will be described.

1.2 Porous Media

In everyday life, one encounters porous media with different pore structure. Porous media are materials which are made up of a pore space and a solid matrix. The pore space as void fraction of the porous medium consists of pores (nodes) and throats (bond) as connections between pores. The pores and throats are distributed randomly inside the porous medium and, as they have irregular shapes, the structure of porous medium is very complex (see Figure 1.1).

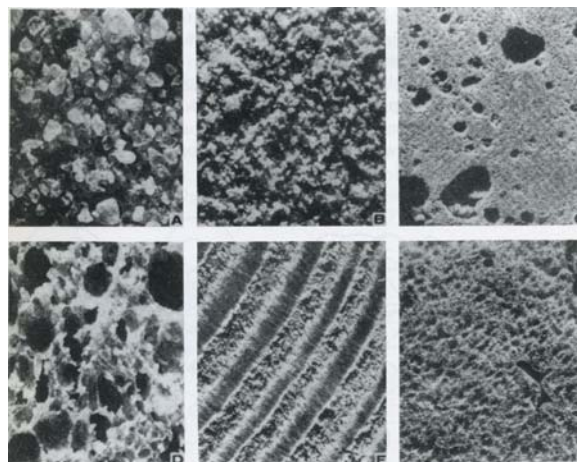


Figure 1.1: Examples of porous media (10 x magnified): (A) beach sand, (B) sandstone; (C) limestone; (D) rye bread; (E) wood; (F) human lung, (Dullien, 1992 [6]).

The pore structure can be characterized by some parameters of the porous medium, such as pore size distribution (*PSD*), coordination number Z , and porosity ψ . Due to the complexity of pore structure, it is interesting to study a correlation between pore structure and transport parameters on the transport phenomena inside the porous medium. Vu et al. (2006 [36]) described a correlation of transport parameters with pore size distribution.

The *PSD* is a major factor to influence transport phenomena in the porous medium because the mechanism of transport of fluid in the liquid and vapour phases, such as capillary forces, evaporation, vapour diffusion and viscous forces depend on the pore size (throat radii). The *PSD* of porous media can be known by a measurement, such as helium adsorption, mercury porosimetry and nitrogen sorption. Armatas and Pomonis (2004 [2]) used a N_2 adsorption - desorption to measure pore size distribution of silica (SiO_2). Then, the pore size distribution was converted to the pore network model by a dual-site bond model (DSBM). The pore size distribution from experiment and network model was compared (see Figure 1.2). The experiment and simulation have almost the same pore radii. The simulation at the small radii has smaller normalized pore volume than the experiment, because the simulation is not able to reliably cover this lower nanoporous region.

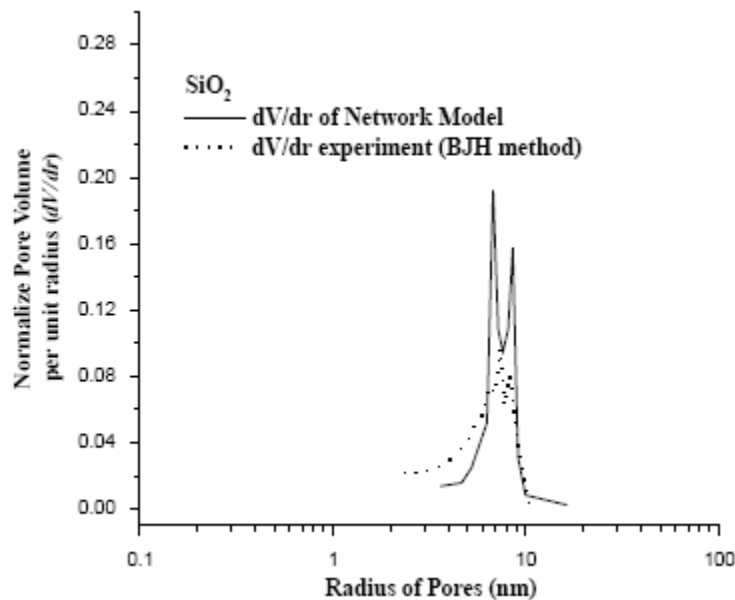


Figure 1.2: Pore size distribution of silica (SiO_2) obtained by network model and experiment (Armatas and Pomonis, 2004 [2]).

The *PSD* in the modelling can be generated by distribution methods in statistics, such as normal volume distribution, log normal distribution, uniform distribution etc. Vu et al. (2006 [36]) described a correlation between *PSD*, free water saturation (S_{fw}) and maximum pore radius by bundle of capillaries. They used a normal volume distribution as *PSD*:

$$\frac{dV}{dr} = \frac{1}{\sqrt{2\pi}\sigma_0} e^{-\frac{1}{2}\left(\frac{r-r_0}{\sigma_0}\right)^2} \quad (1.1)$$

where r_0 is mean throat radius and σ_0 standard deviation.

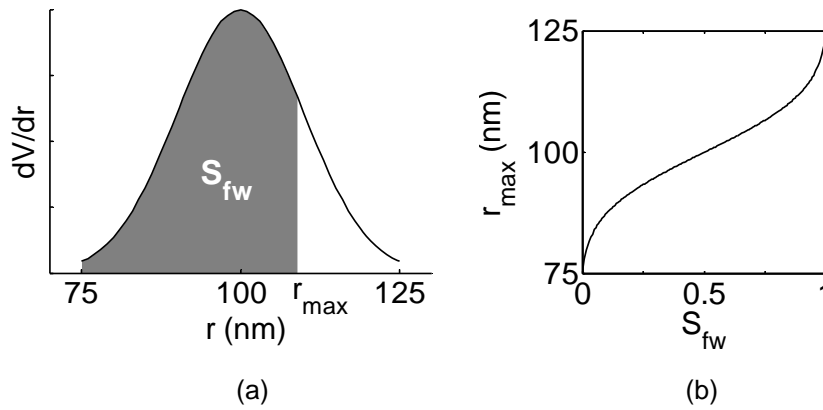


Figure 1.3: Relation between (a) r_{\max} and PSD ; (b) S_{fw} and r_{\max} (Vu et al., 2006 [36]).

The porous media can contain free and/or bound water depending on the type of material which can be hygroscopic or non-hygroscopic. Free water is usually located in large pores and bound water is usually located in smaller pores. Free water saturation, S_{fw} , is volume of free water in the pore space of the porous medium. Figure 1.3 shows the relation between PSD and r_{\max} , as well as between r_{\max} and S_{fw} . Integral of PSD (dV/dr) from small pore radius to maximum one is equal to the free water saturation:

$$S_{fw} = \int \frac{dV}{dr} dr \quad (1.2)$$

The maximum pore radius decreases with decrease of free water saturation as shown in Figure 1.3b. This can explain why the area under the curve of Figure 1.3a becomes smaller with a decrease of maximum pore radius.

Capillary pressure is different pressure of liquid and gas at the meniscus due to the surface tension. Capillary pressure in the porous medium is highly correlated with pore size distribution in terms of pore size. This capillary pressure is function of a maximum pore size r_{\max} and surface tension σ .

$$p_c(S_{fw}, T) = \frac{2 \cdot \sigma(T)}{r_{\max}(S_{fw})} \quad (1.3)$$

For isothermal condition ($T = \text{constant}$), the capillary pressure only depends on the maximum pore radius (r_{\max}). A smaller r_{\max} results in higher capillary pressure and a larger r_{\max} gives lower capillary pressure. Therefore, the capillary pressure can be correlated to the free water saturation, because the maximum pore radius is correlated to free water saturation as explained above. Vu et al. (2006 [36]) calculated the capillary pressure for different pore size distributions, i.e. monomodal with small pore radii and bimodal with two type of pore size (small and large pore radii).

Figure 1.4 shows the relation between capillary pressure and saturation for different pore size distributions in a bundle of capillaries. The fluid in the bundle of capillaries is air-water and the material is hygroscopic.

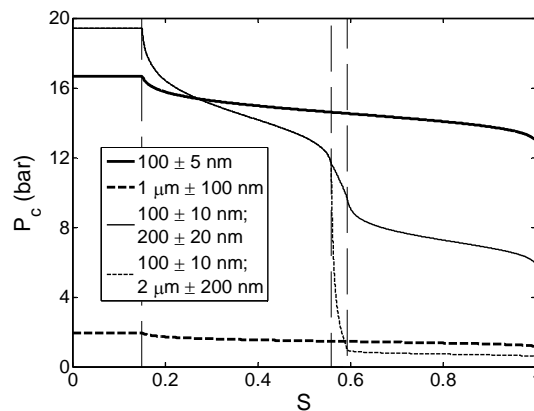


Figure 1.4: Relation between capillary pressure and saturation for four different pore size distributions (*PSD*) (Vu et al., 2006 [36]).

As shown in Figure 1.4, the capillary pressure decreases with increase of saturation, because liquid will be first removed from large pores. For monomodal *PSD*, the capillary pressure is higher for smaller pore radius (bold solid line) than for higher one (solid dashed line). For bimodal *PSD*, the capillary pressure increases dramatically around a saturation of 60 %, because it is predicted that all large pore radii are empty and removal of liquid continues in small pore radii. This means that the *PSD* is one factor influencing capillary pressure in isothermal condition.

The connectivity or coordination number Z is defined as the number of throats that are connected to a pore. The connectivity can influence transport parameters in the porous medium such as permeability and diffusivity, so that the phase distribution in the porous medium during drying is also influenced by connectivity. The porous medium has a random distribution of connectivity (see Figure 1.5). In pore network modelling, this random connectivity is converted to the same connectivity in order to understand easily transport phenomena inside the porous media. Figure 1.6 shows some two-dimensional pore networks with different connectivity.

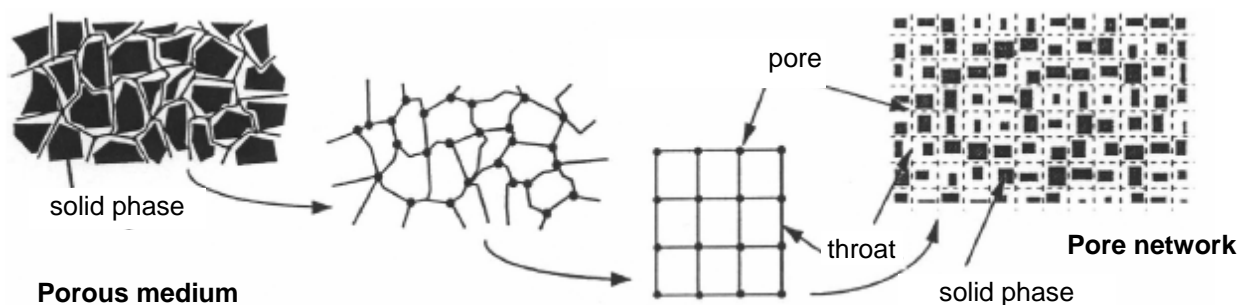


Figure 1.5: Conversion from porous medium to the pore network as a representation of porous medium (Prat, 2002 [26]).

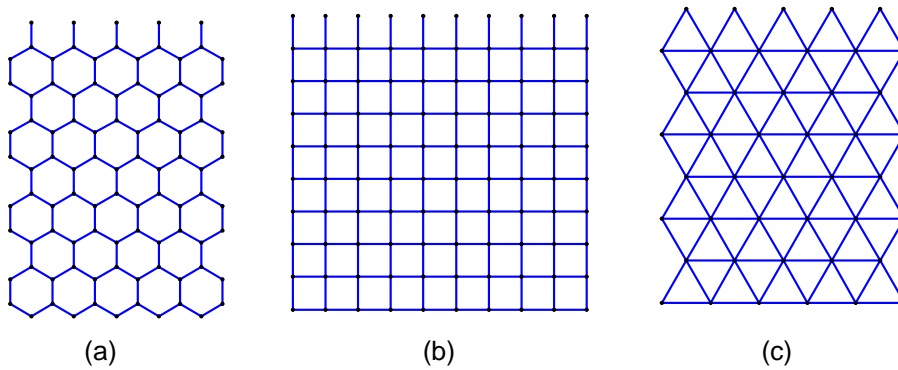


Figure 1.6: Two-dimensional networks for (a) connectivity 3 (hexagonal); (b) connectivity 4 (square); (c) connectivity 6 (hexatriangular).

The 2D and 3D pore network can be constructed by statistical physics from data structure of pore size distribution and connectivity of a real porous medium. Some of the statistical methods to construct such networks are multiple point statistics (Okabe and Blunt, 2005 [21]) and dual site bond model (DSBM) (Cordero et al. (2001) [4]). The multiple-point statistic is based on the geostatistical technique and it needs an image of 2D porous medium obtained by some imaging technique (SEM, micro-CT scanning). This image is captured to generate 3D porous medium representation. Figure 1.7 shows an image of 2D porous medium converted to a 3D pore space representation.

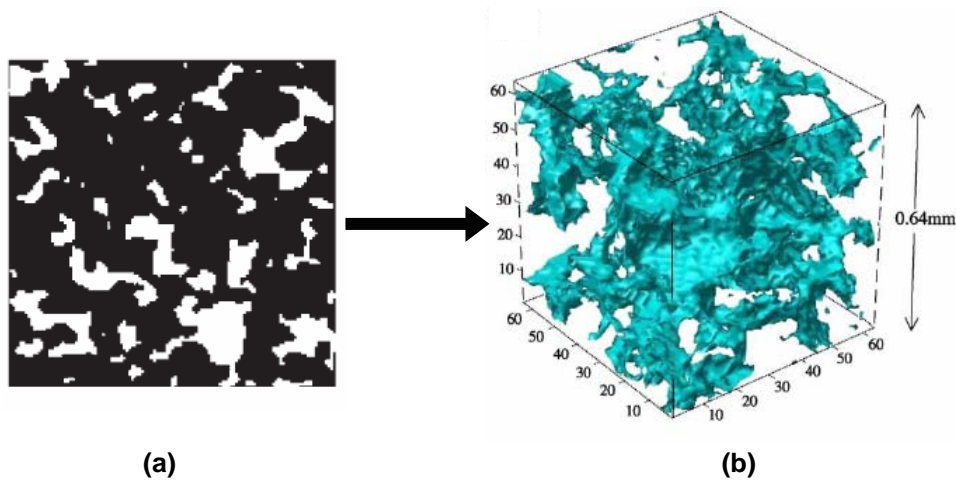


Figure 1.7: (a) 2D porous medium generated using micro-CT images and (b) 3D pore reconstructed images (Okabe and Blunt, 2005 [21]).

White colour in Figure 1.7a is void fraction (porosity) of the porous medium in 2D. Porosity, ψ , is ratio of void fraction and volume of material and, as a macroscopic parameter of pore structure, is determined by pore size distribution. Porous media having large pores with many inter-pore connections is possible to have high porosity. The porosity of the porous medium can be measured by several methods, such as optical methods, injection of mercury or gas expansion methods. In the mercury injection method, the porous medium is immersed in the mercury and the mercury goes inside the pore space. As the volume of mercury inside of porous medium is known, the porosity can be calculated.

1.3 Drying of Porous Media

Drying of porous media can be defined as removal of a volatile substance (water) from inside of the porous solid by means of evaporation. The aim of drying is to get better quality of the product and to handle the product more easily for next process. Generally, hot air with low humidity is blown over the surface of the porous solid to remove the liquid. Then, the liquid can escape from the interior of the porous media due to different concentration and partial vapour pressure between inside and outside of the porous media. Drying of porous media, which involves simultaneous mass and heat transfer, is influenced by temperature, relative humidity, and velocity of air (external factors) as well as pore space and pore size distribution (internal factors).

Drying rate is an important factor to characterise phenomena of drying at macroscale. Drying rate of convective drying process can be divided into two periods, i.e. a period of constant drying rate (*CRP*) and a period of falling drying rate (*FRP*). For isothermal case, the drying rate depends on the competition between capillary forces, friction forces and evaporation rate. The largest pore at the surface of porous medium will be invaded by the air first, because the largest pore has the lowest capillary pressure. Therefore, the liquid pressure at the meniscus of the largest pore is high so that the liquid can be pumped from meniscus of the largest pore to the other meniscus throats which have smaller pressure at the meniscus. The maximum value of capillary pressure difference between two menisci (r_1 and r_2) can be calculated as follows:

$$\Delta p_m = 2\sigma \cdot \left(\frac{1}{r_1} - \frac{1}{r_2} \right) \quad (1.4)$$

The capillary flow decreases in the presence of viscous forces during the transport of liquid. Therefore, the liquid flow rate must be calculated in presence of viscous forces as:

$$\dot{M}_{w,k} = \frac{\pi r_k^4}{8\nu_w L_{w,k}} (p_{w,i} - p_{w,j}) \quad (1.5)$$

Eq. (1.5) describes the liquid flow rate that depends on the throat radius r_k , length of throat $L_{w,k}$ and difference between two liquid pressures ($p_{w,i} - p_{w,j}$). The liquid flow rate can be decreased for longer throat $L_{w,k}$, smaller throat radius (r_k) and higher liquid viscosity ν . So, the viscous forces play an important role in liquid flow. The competition between capillary and viscous forces can be described through the capillary number, which is ratio between viscous forces and capillary forces.

During the *CRP*, evaporation is governed by diffusion through boundary layer due to the difference in vapour pressure between material surface ($p_{v,s}$) and bulk of air ($p_{v,\infty}$). Mass flux of evaporation can be calculated by:

$$\dot{m}_{v,I} \approx \beta \frac{\tilde{M}_v}{\tilde{R}T} (p_{v,s} - p_{v,\infty}) \quad (1.6)$$

where β is mass transfer coefficient, p total gas pressure, \tilde{M}_v molar mass of vapour, \tilde{R} universal gas constant and T absolute temperature. The capillary flow from the biggest menisci throat (Eq. (1.5)) must sustain the supply of enough liquid at the rate of evaporation (Eq. (1.6)) in order to produce a *CRP*. The largest menisci in the porous medium can exist at the depth of network so that the air can invade the depth of the network and create empty

pores in the depth area. The capillary flow from the depth area can still deliver liquid to the surface of the porous medium if the liquid phase is continuous up to the surface of porous medium and if the friction forces are lower than the capillary forces during liquid delivery. Nevertheless, not all surface of porous medium must be covered by wet patches, but a partially wet surface can be enough to assure the initial rate of evaporation due to lateral vapour transfer in the boundary layer. Schlünder (1988 [27]) explained why a partially wet surface can give a period of constant rate (*CRP*). He assumed spherical droplets which are evenly distributed on a dry surface. For a period of constant rate (*CRP*), the boundary layer thickness must be larger than the distance between the droplets so that lateral resistance to vapour transfer can be neglected compared to the vertical resistance through the boundary layer. A partially wetted surface can lead to a period of constant rate (*CRP*) or a period of falling rate (*FRP*) depending on wet surface fraction and boundary layer thickness. The wet fraction at the porous medium surface is determined by the ratio of cross sectional area of total wet patches and total area. Higher fraction of wet surface and thicker boundary layer will produce higher drying rates (*CRP*). Smaller fraction of wet surface and thinner boundary layer will decrease drying rate (*FRP*).

The end of the constant period is at the critical moisture content (X_{cr}) as shown in Figure 1.8. The critical moisture content depends on the drying rate of the first period, the dimensions of the product (thickness) and temperature. The critical moisture content increases when the drying rate at the first period increases because the liquid at the surface dries rapidly. The thinner porous medium also gives higher X_{cr} because capillary pumping delivers the liquid from shorter distance so that the liquid can be evaporated faster. Higher temperature gives higher vapour pressure so that the first drying rate is also at higher level.

A period of falling rate (*FRP*) starts when evaporation rate is greater than the capillary flow. The capillary flow can be at low level when the largest of meniscus throats in the porous medium is too small (high friction forces) influencing low capillary forces. Therefore, capillary pumping from biggest throat can not be enough to deliver liquid for evaporation rate. In that case, the liquid at the surface of porous medium is evaporated so that evaporation front in porous medium has a distance to the surface of porous medium. Therefore, the drying rate decreases due to the presence of this distance (additional resistance).

Initially, the porous media can contain free and/or bound water depending on the type of material. Free water is usually located in large pores and it can be removed easily by capillary flow and evaporation from solid surface, while bound water is defined as the residual moisture in the porous media at equilibrium condition and is located in smaller pores. The bound water is fixed on solid phase by several forces. It can be removed by applying the conditions of very low humidity or high temperature, but the solid material might be damaged during this treatment. Therefore, the sorption equilibrium condition must be known in order to avoid damaging of materials by applying extreme conditions. Concerning bound water, porous media can be classified into two types, i.e. hygroscopic and non hygroscopic. Hygroscopic porous media can adsorb more water vapour from the air depending on the thermodynamic condition of the ambient humid air, and these porous media still contain some water as bound water at the end of drying, while all water in non-hygroscopic porous media can be evaporated.

Recently, the importance of bound water has been proven again by Lu et al. (2005 [16]) who investigated drying of porous media with and without bound water. Their model included capillary transport of free water, diffusion of bound water, convective and diffusive transport of vapour in air for the non-isothermal condition. The results were compared with the experiments of convective drying of porous media (quartz particles). Simulations with bound water described more accurately the experimental results for moisture content, temperature and total drying time than the model without bound water. Therefore, the modelling of bound water in porous media is important in order to describe the real drying process, but the

network model of this work will not include sorbed water and will be only applied to non-hygroscopic material.

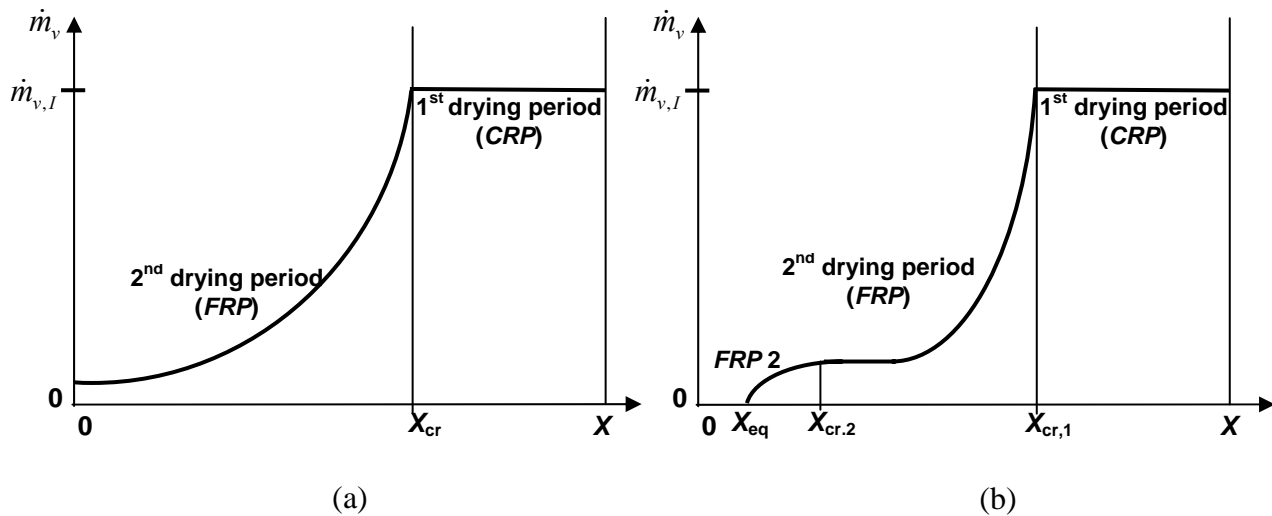


Figure 1.8: Drying curve for (a) non-hygroscopic and (b) hygroscopic porous media.

Figure 1.8 shows drying curves for different types of material (drying rate \dot{m}_v over moisture content X). Both drying curves have a constant drying rate (CRP) and a falling drying rate (FRP). During the falling drying rate (FRP), the drying rate is lower due to additional resistance in the vapour phase of porous medium. Drying of a hygroscopic material has two critical points for decreasing drying rate (see Figure 1.8b). The first period of a falling drying rate (FRP) is caused by low capillary flow to supply liquid to the material surface so that the surface of porous medium becomes dry and vapour transfer experiences an additional resistance in the porous medium, while the second decrease in drying rate (FRP 2) starts when all free water is evaporated. The end of the second decreasing drying rate is at equilibrium moisture content X_{eq} and the drying rate is at zero value.

1.4 Continuum Versus Discrete Approach

The drying phenomena can be investigated both by experiments and modelling. By experiments, the drying transport parameters can be obtained as macroscopic properties. However, the physical effects of drying are on the microscopic level and modelling can be applied to predict this physical effect. Modelling of drying of a porous medium can be simulated by two approaches, i.e. continuum and discrete approach. The continuum approach is the traditional one. The most advanced model was developed by Whitaker (1998 [42]) and it describes multiphase transport of mass, momentum and heat by setting the equations at the microscopic level and deriving macroscopic conservation equations using the volume averaging technique. The partially saturated porous medium is treated as a fictitious continuum, and drying is described in terms of homogenized fields for moisture content, temperature and gas pressure (see Figure 1.9a). The model can be developed at the macroscopic scale by assuming “length scale separation” of pore size, averaging volume and typical length for variation of macroscopic quantities. Laurindo and Prat (1998 [13], 1998 [14]) explained that the length scale separation is not always fulfilled so that the validity of the continuum approach may be questioned. Some drying parameters, such as absolute and relative permeability (K and k), effective diffusivity (D_{eff}) and effective thermal conductivity (λ_{eff}) are needed to solve mass, momentum and heat transfer equations. All effective

parameters depend on the geometry of pore space and saturation. Due to the complex structure of porous media at the pore scale, the continuum approach has difficulties to predict these effective transport parameters of drying and they must be determined by experiment. Due to the mentioned deficiencies of the continuum approach, the discrete approach offers an alternative to describe multiphase transport phenomena at the pore scale. In the discrete approach, the pore space is represented by a network of pores (Figure 1.9b). The fractal concept and statistical physics methods such as percolation and renormalization can be implemented in this approach, e.g. Laurindo and Prat (1998 [13]). Statistical physics can also be applied to develop a representative network in order to be close to a real porous medium. Until now, the discrete approach can only investigate qualitatively transport phenomena in the porous medium due to computational limitations and because of missing experimental data about exact pore structure. In the future, continuum approach and discrete approaches might be combined to investigate real porous media. However, an equivalence of the two approaches must first be investigated. The discrete approach can then be used to calculate effective transport parameters for a representative pore network. The continuum approach uses these drying parameters to describe transport phenomena of a porous medium at the macroscopic length scale.

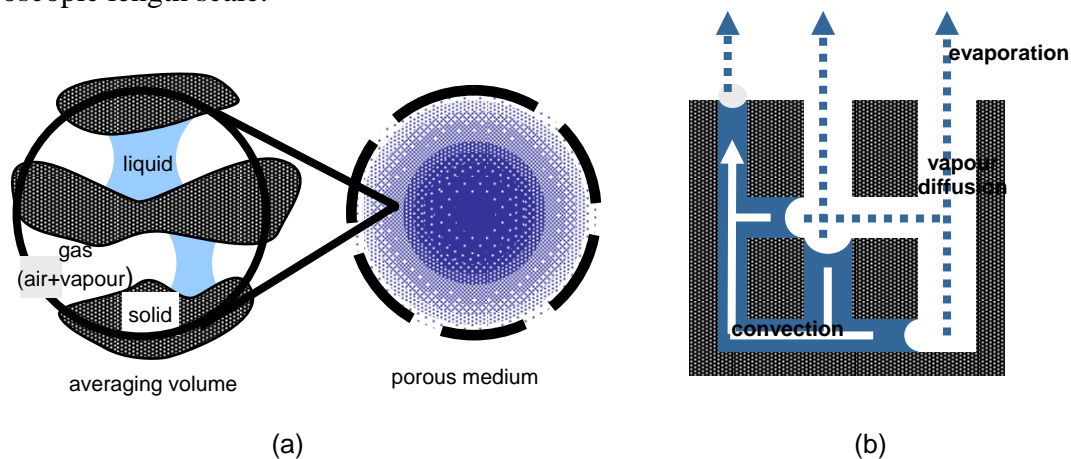


Figure 1.9: (a) Continuum and (b) discrete approach of modelling drying of porous media.

1.5 Isothermal Drying of Pore Networks

Pore network modelling has been applied in a wide area to study fluid flow at pore scale. Fatt (1956 [7]) was the first to develop a model based on an interconnected network of capillary tubes as representative of a porous medium. Each capillary tube was linked to other tubes (by a connection). The tubes and connections were given a diameter and length from which corresponding relative permeability in the drainage could be obtained. Due to the existing limits of computation, network model had difficulties to simulate detailed transport phenomena of porous media after Fatt. In the recent years, network models became popular again to describe fluid transport in porous media due to increased capabilities of computation and statistical physics (percolation theory (Stauffer and Aharony, 1992 [33])).

Nowicki et al. (1992 [20]) calculated transport parameters by a network model in the isothermal condition. The transport drying parameters are relative permeability of liquid and effective diffusivity of vapour that depend on liquid saturation and distribution of saturation. Then, two research groups (Prat et al. and Yiotis et al.) developed network models for the drying process which they used to investigate some aspects and phenomena of drying of porous media. Recently, Segura and Toledo proposed a network model similar to Prat's model.

Many aspects of drying have already been investigated using 2D pore networks by the mentioned research groups. All models are under isothermal conditions and for a single component of liquid. Only Huinink et al. (2002 [9]), Plourde and Prat (2003 [22]) investigated the influence of thermal gradients in the network; Freitas and Prat (2000 [8]) modelled drying of a binary liquid. Drying simulations for a 3D network model have already been presented by Le Bray and Prat (1999 [15]) and Yiotis et al. (2006 [41]). Comparison between drainage and drying by pore network modelling (Prat, 1995 [24]), the influence of gravity (Prat, 1993 [23], Laurindo and Prat, 1996 [12], Laurindo and Prat, 1998 [13], Laurindo and Prat, 1998 [14]), the shape of throat cross sections (Segura and Toledo, 2005 [29]), liquid films (Laurindo and Prat, 1998 [13], Laurindo and Prat, 1998 [14], Yiotis et al., 2003 [38], Yiotis et al., 2004 [39], Yiotis et al., 2005 [40]), and shrinkage on drying behaviour (Segura and Toledo, 2005 [30]) have also been investigated. Nowicki et al. (1992 [20]) and Segura et al. (2005 [28], 2005 [29], 2005 [30]) computed effective transport drying parameters as a function of saturation. Yiotis et al. (2001 [37]) has investigated the influence of viscous effects in gas and liquid phase. In order to validate the simulation, experiments with micro models have also been carried out by Segura and Toledo (2005 [28]), Laurindo and Prat (1998 [14]), and Tsimpanogiannis et al. (1999 [34]).

The methods and results from several researchers in modelling of drying by pore network will be presented in following section. First, the method and results of Nowicki et al. with biconical throats will be described, while the results of Prat will be presented to show the influence of some other aspects on the drying kinetics. Then, the work of Yiotis et al. describing the influence of viscous effect in liquid and gas will be shown. Finally, influence of some aspects on the drying transport parameters studied by Segura and Toledo will be also presented.

1.5.1 Pore Network Model by Nowicki et al.

The geometry of the pore network of Nowicki's work was defined as biconical throats (see Figure 1.10) that have converging-diverging character (Nowicki et al., 1992 [20]). These biconical throats seem to be a good representation of the real pore geometry in a porous medium. The converging-diverging character results in a changing curvature of the meniscus as a function of its position in the throat. The biconical throats serve as containers and conductors of liquid and the pore may have volume.

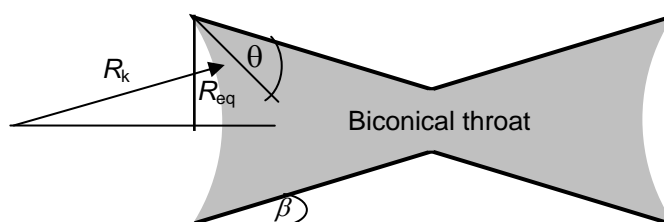


Fig. 1.10: Typical spherical pore body with its associated biconical pore throats.

The meniscus can move continuously along the throat, it is not “jumping” from one end of the throat to the other. Capillary pressure at the meniscus of biconical throats p_c depends on the radius of curvature R_k as

$$R_k = R_{eq} |\cos(\theta + \beta)|, \quad (1.7)$$

$$p_c = \frac{2\sigma}{R_k}, \quad (1.8)$$

where R_{eq} is radius of meniscus, θ contact angle, β angle of the cone and σ is surface tension of liquid (water). Due to the constriction of the pore throats, capillary pressure increases when meniscus moves from the edge to middle of the throat. Capillary pressure decreases when meniscus moves from middle of the throat the next pore centre.

Figure 1.11 shows the phenomena of the Haines jump for a simple geometry: Four throats of different radius are connected to each other. The water evaporates from the top of throats 2 and 3. First, the vapour will invade the throat number 3 because this throat has lower threshold capillary pressure (Figure 1.11a). The movement of meniscus in the throat 3 is stopped when liquid pressure at the meniscus in this throat is the same as the liquid pressure at the meniscus of throat 2, and then the liquid is stable (Figure 1.11b). After that, the throat number 2 will be invaded by vapour until equilibrium position. At the cone area of the throat number 2 with large radius (lowest threshold capillary pressure), the liquid at the cone of throat 2 will go down very fast (Figure 1.11c). This is known as a *Haines Jump*. The process will finish when the liquid pressures at the menisci in throats 4 and 3 are equal (Figure 1.11d).

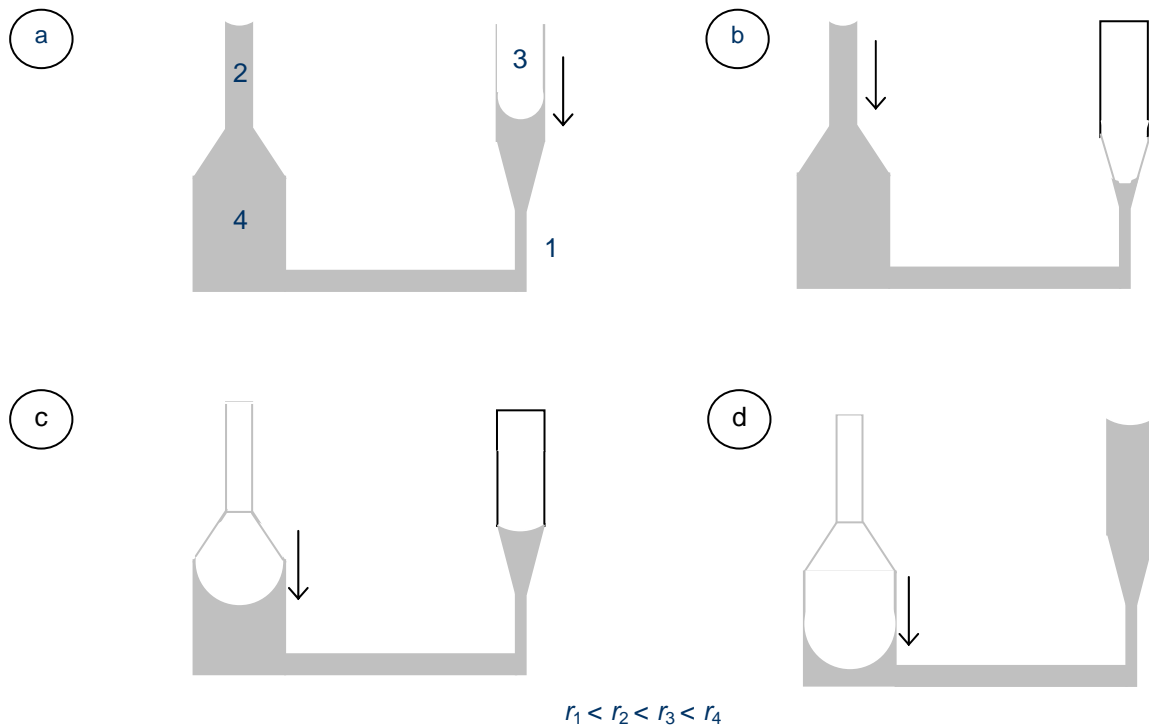


Figure 1.11: Illustration of Haines jump for conical throats.

The position and hence radii of curvature of the menisci, the liquid pressure at each meniscus and in each liquid-filled pore and the partial pressure of vapour in each gas filled pore can be solved by liquid and vapour mass balance in each pore. Boundary conditions of the vapour

mass balances are partial vapour pressure at the outside of the network, $p_{v\infty}$, and equilibrium vapour pressure, p_v^* , at the menisci. In this model, reduction of the equilibrium vapour pressure due to high curvature of menisci is calculated by the Kelvin equation:

$$p_{v,R_k} = p_v^* \exp\left(-\frac{\tilde{M}_v}{\tilde{R}T} \frac{2\sigma}{R_k \rho_w}\right) \quad (1.9)$$

Vapour can escape at the top surface of the network and periodic boundary conditions are imposed on the sides in this network model (see Figure 1.12). The network model ignores viscous effects in the gas phase because the investigated drying rates are slow. Viscosity in the liquid is included in the model, but model of viscous forces in the liquid phase was not described. The positions of menisci within the pore space are essential to know the distribution and overall amount of liquid in the porous medium. The authors did not show the saturation profile of liquid in the porous medium, but the authors show the correlation between liquid saturation and drying transport parameters.

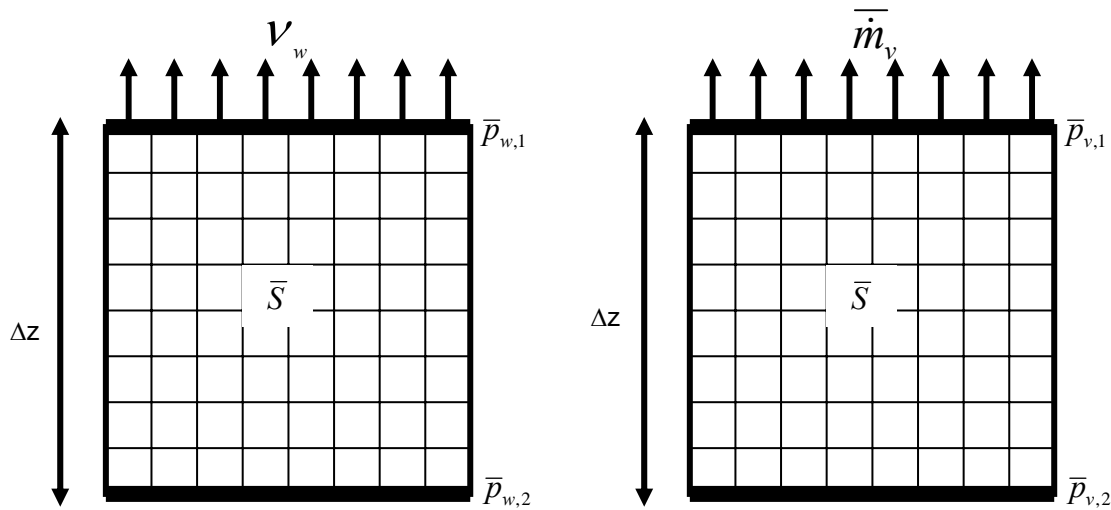


Figure 1.12: Representative network for calculating relative permeability (k_w) and effective diffusivity (D_{eff}) by pore network modelling.

Nowicki et al. used this pore network model to compute effective transport parameters relevant in drying of porous media, such as relative permeability, capillary pressure, and effective diffusivity as a function of saturation. All parameters were computed simultaneously. Figure 1.12 shows a part of network with average saturation \bar{S} in order to calculate relative permeability and effective diffusivity. According to Darcy's law, the relative permeability is:

$$k_w = \frac{\eta_w}{K} v_w \frac{\Delta z}{\bar{p}_{w,2} - \bar{p}_{w,1}} \quad (1.10)$$

where v_w is average liquid velocity at the top of the network, η_w liquid viscosity, and $\frac{\Delta z}{\bar{p}_{w,2} - \bar{p}_{w,1}}$ is the inverse of the average liquid pressure gradient over the depth Δz .

The effective diffusivity for vapour is calculated by Fick's first law:

$$D_{eff} = -\bar{m}_v \frac{\tilde{R}T}{\tilde{M}_v} \frac{\Delta z}{\bar{p}_{v,2} - \bar{p}_{v,1}} \quad (1.11)$$

where \bar{m}_v is average vapour mass flux at the top of network, and $\frac{\Delta z}{\bar{p}_{v,2} - \bar{p}_{v,1}}$ is the inverse of

average vapour pressure gradient over the depth Δz .

The size of network in this simulation is 30 pores (width) by 30 pores (depth). Nowicki et al. did not observe the data of saturation, vapour pressure, capillary pressure and liquid pressure for the whole network, but they only chose a part of the network (left-upper) as sampling. Two samples were chosen, i.e. 10 width pores x 10 depth pores and 10 width pores x 2 depth pores. The drying transport parameters were observed with variant depth of 5, 15 and 25 pores from the top of network surface. In order to investigate influence of drying rate, the initial drying rate was chosen as 1 and 100 kg/ (m²h).

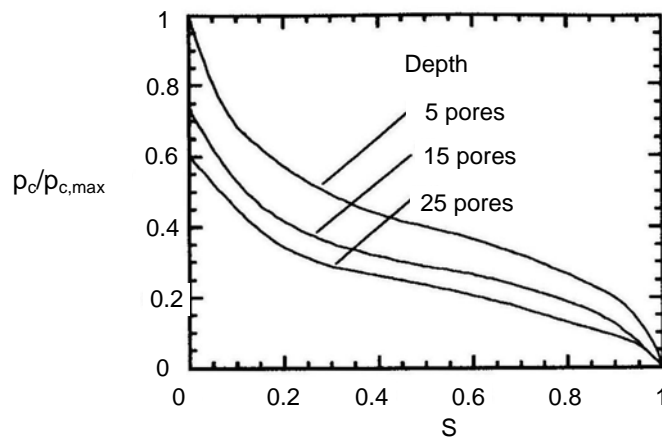


Figure 1.13: Capillary pressure and liquid saturation at different positions from the top surface for sampling volume (10 x 2) at 100 kg / (m²h) (Nowicki et al., 1992 [20]).

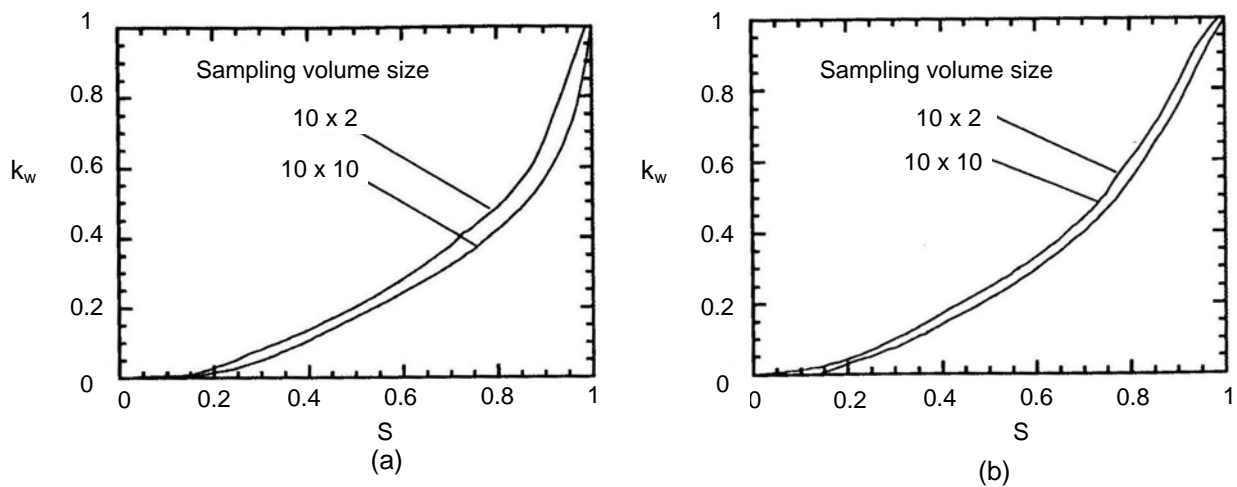


Figure 1.14: Relative permeability and liquid saturation for different sampling volumes at (a) 100 kg / (m²h) and (b) 1 kg / (m²h) initial drying rate (Nowicki et al, 1992 [20]).

Figure 1.13 shows curves for the relation between normalized capillary pressure and liquid saturation that is plotted for a depth of the sampling volume of 5, 15 and 25 pores from the top of network surface. A relation between relative permeability and liquid saturation can be seen in Figure 1.14. The relative permeability decreases rapidly with decrease of liquid saturation, and it can be seen that not only structure and saturation determine the effective parameter, but also drying condition (rate).

Figure 1.15 shows curves for the relation between normalized diffusivity and liquid saturation, where the normalized diffusivity is effective diffusivity D_{eff} divided by the vapour diffusion coefficient δ and porosity ψ . We can see again different curves for different drying rates, indicating that this effective parameter does not depend only on saturation S , but also on drying history (initial drying rate). Nevertheless, Nowicki et al. did not show the phase distribution and drying curve to describe more clearly the influence of drying rate.

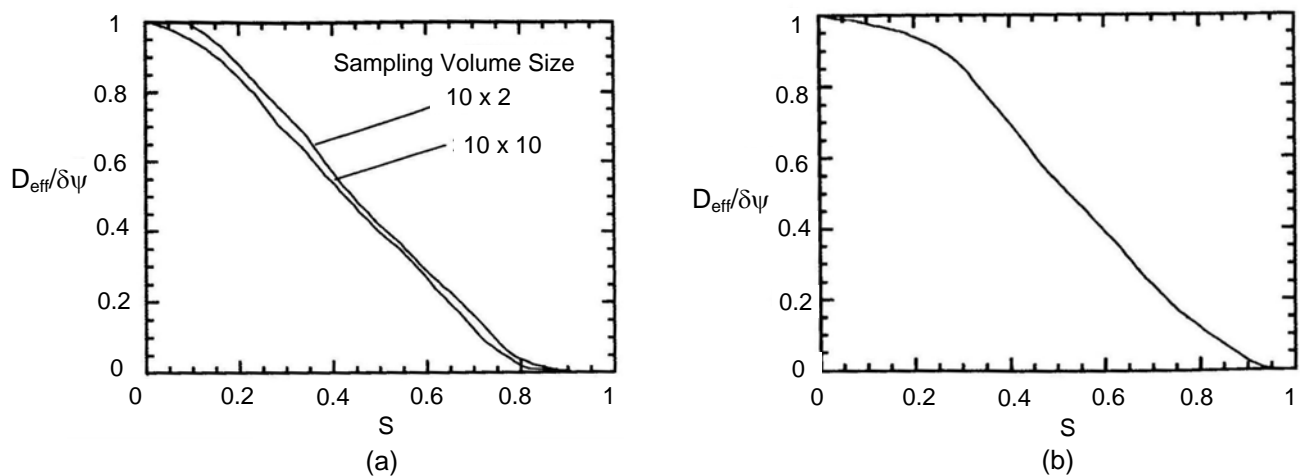


Figure 1.15: Effective diffusivity and liquid saturation for different sampling volumes at (a) 100 kg/(m²h) and (b) 1 kg/(m²h) initial drying rate (Nowicki et al., 1992 [20]).

1.5.2 Pore Network Model by Prat et al.

Prat and co-workers have been doing their research on pore-networks since 1993 (Prat, 1993 [23]). Their network consists of throats with rectangular cross section and the pores are grid points without volume. Only the throat can contain liquid and there are essentially only two positions of the meniscus, i.e. the throat is either empty or full of liquid. The discrete positions naturally give the time discretization for the drying network. The geometry of pores and throats for a two-dimensional regular square network can be seen in Figure 1.16. The width of each throat is chosen randomly according to a stochastic distribution. The geometry depends on three parameters: the distribution law, the distance between two nodes (a), and the space distribution coefficient (b) between the pore and throat, where ba represents the length of a throat. Prat et al. have developed their network size and geometry from 2D with the network size 50 x 50 pores (Prat, 1993 [23]) until 400 x 400 pores (Prat and Bouleux, 1999 [25]) and 3D with the network size 51 x 51 x 51 pores (Le Bray and Prat, 1999 [15]).

The drying algorithm of Prat et al. is a modification of invasion percolation (*IP*), i.e. displacement of a wetting fluid by a non-wetting fluid in the throats. The invasion percolation method was often applied in oil recovery, but the process in this field is only determined by capillary flow in porous media. Therefore, the invasion percolation must be modified due to additional processes in drying, i.e. evaporation at gas-liquid interfaces and vapour diffusion in

the gaseous phase. However, drying and drainage are similar processes at the beginning because the movement of menisci in the throats of both process is caused by invasion of non-wetting fluid (gas in drying) (Laurindo and Prat, 1998 [13], 1998 [14]).

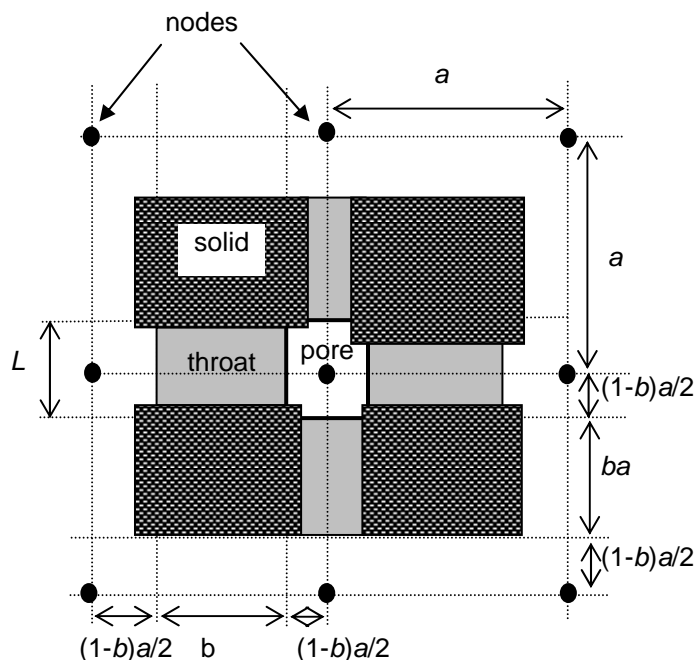


Figure 1.16: Definition and geometrical parameters of Prat's network (1993 [23]).

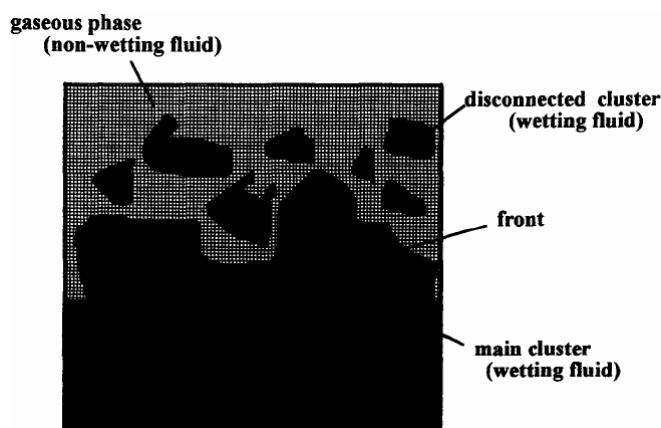


Figure 1.17: Schematic picture of the phase distribution within the network in terms of main cluster, disconnected cluster and front (Prat, 1995 [24]).

The network drying model has the following important assumptions. It is assumed that capillary forces always dominate over friction forces (neglecting viscous effect) so that only the largest throat empties first. The reduction of equilibrium vapour pressure due to influence of curvature is neglected (Kelvin effect) because the pores and throats are large. Film flows along the walls of the throats are neglected. The porous medium is assumed to be non-hygroscopic. The liquid in the network is usually single component, but also a binary liquid has been simulated (Freitas and Prat, 2000 [8]). Most of network simulations are under

isothermal conditions. More recent work investigates the influence of thermal gradients (Huinink et al., 2002 [9], Plourde and Prat, 2003 [22]).

Initially, all throats in the network are filled by liquid and connected in one cluster, evaporation takes place only at the top of the network. Then, the liquid will be separated into several clusters due to the random throat radii (see Figure 1.17).

Prat et al. did also a drying experiment with geometry similar to that of the network model in order to compare phase distribution and drying rate between experiment and simulation. In order to control external conditions in the micromodel drying experiment of a pore network, a diffusive layer was put at the top of network (see Figure 1.18) (Laurindo and Prat, 1998 [14]). Normally, the network model in the simulation must be the same as the micromodel in the experiment, so that the results of experiment and simulation can be compared. The diffusive layer contained only gas (vapour) where the vapour comes from the network. The distance between grid points is assumed to be the same as with in the network. The finite volume technique is applied in the diffusive layer in order to compute vapour pressure fields. The finite volume at the interface between network and diffusive layer has different exchange areas due to presence of solid. Vapour pressure at the outer boundary of the diffusive layer as boundary condition is assumed to be zero ($p_{v\infty} = 0$). The vapour transfer in diffusive layer is determined by vapour pressure difference between two grid points.

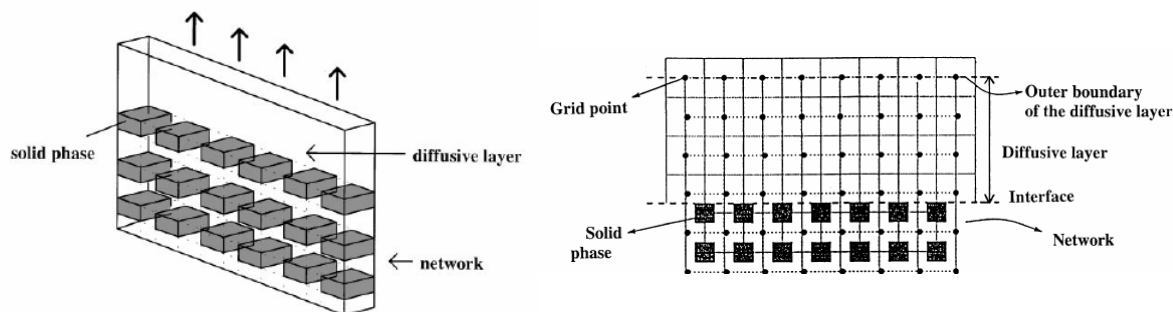


Figure 1.18: Diffusive boundary layer in experiment and simulation (Laurindo and Prat, 1998 [14]).

Comparison between Drainage and Drying

Prat (1995 [24]) has compared drainage and drying with a 2D network model. Both processes were conditioned at low capillary number because drying is generally a slow process. Initially, the network of both processes is filled by wetting fluid. In case of drainage, non-wetting fluid is injected to the network from the top and displaces the wetting fluid, which escapes through the bottom edge of the network (see Figure 1.19). In order to compare drainage and drying process, the simulation is stopped when the bottom edge is reached by non-wetting fluid (breakthrough point), because the drainage phase distribution will not change afterwards. Figure 1.19 shows simulated phase distributions in drainage and drying for an identical network of 100 x 100 nodes.

The front for the drainage as interface between liquid and gas inside the network is similar to the drying front (see Figure 1.19) because wetting fluid in throats will be replaced by the non-wetting fluid in the same procedure (invasion percolation) for both processes. The largest meniscus throat will be first invaded by the air because this throat has lowest capillary pressure. This similarity of front for both processes is only until the breakthrough point. During both processes, disconnected clusters are formed from the main cluster. In case of drainage, the non-wetting fluid can not remove these disconnected clusters because the gas

pressure remains equal after the breakthrough point, so that the disconnected clusters stay trapped, but the drying process can continue to remove these disconnected clusters by evaporation. Therefore, the number of clusters and cluster size in the network can increase and decrease due to internal evaporation.

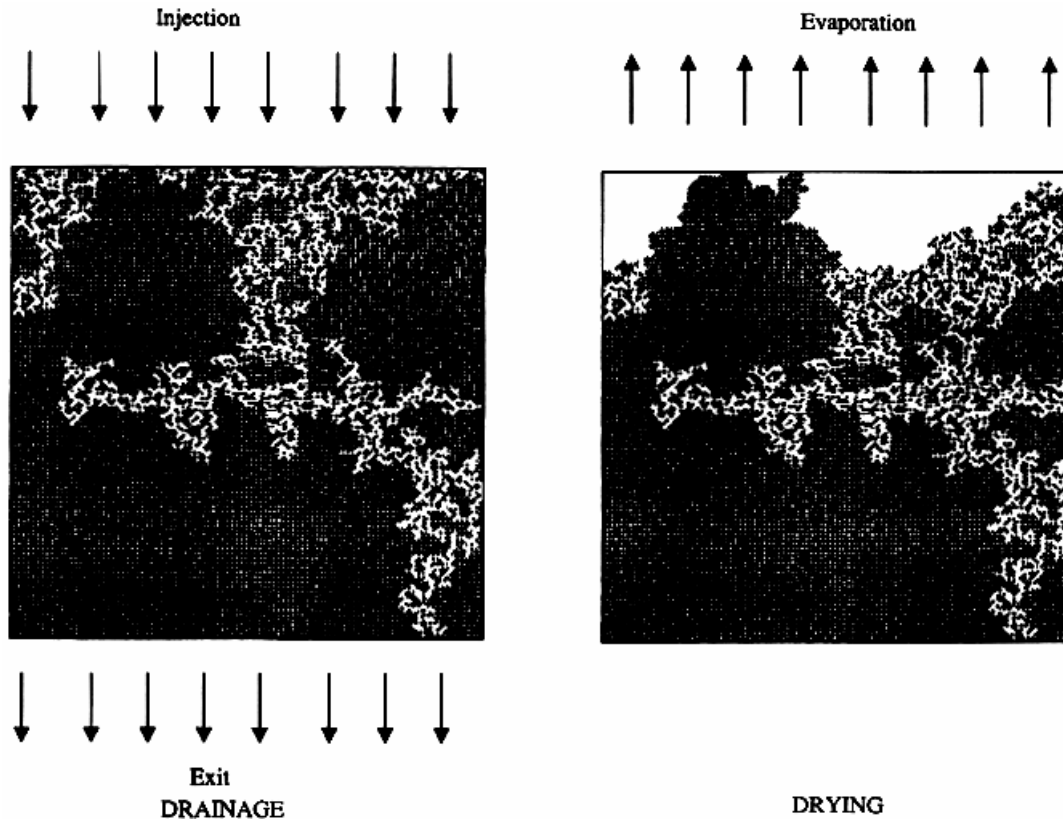


Figure 1.19: Phase distribution in drainage and drying with invasion percolation algorithm in 100 x 100 networks. Liquid phase is black and vapour is white (Prat, 1995 [24]).

Drying Experiment with Micro Model

Drying experiments of porous medium with random packing of silica spheres were conducted by Shaw (1987 [31]) in order to investigate the stability of the displacement front in drying where the non-wetting fluid moves in opposite direction as liquid vapour. Air with low viscosity displaces the water (liquid) with high viscosity. Due to the high viscosity ratio, conventional immiscible displacement produces unstable displacement fronts. In the drying experiment, stable displacement can be produced due to evaporation at the liquid-gas interface. Laurindo et al. (1996 [12], 1998 [13], 1998 [14]) investigated some aspects of drying by pore network experiments. The 2D micromodel of these experiments was created by a moulding technique. The size of network is 140 x 140 containing about 39000 ducts with seven classes of width (from 0.1 to 0.6 mm) that are distributed randomly and the fluid in this experiment is hexane (used because this fluid is easy to evaporate). The micromodel has two regions i.e. diffusive layer and network, as mentioned above.

Laurindo and Prat investigated the influence of gravity on drying kinetics by this experiment in terms of Bond number:

$$B = \frac{\Delta\rho g L_k^2}{\sigma} \quad (1.12)$$

which is the ratio of the gravity force to the capillary force ($\Delta\rho$: difference of density between liquid and gas, g : gravity vector, L_k : length of throat).

Three different conditions of gravity were studied in terms of the Bond number are includes negligible gravity force ($B = 0$), gravity force to stabilize the invasion process ($B > 0$) and gravity force to destabilize the invasion process ($B < 0$). The position of the micro model for these three different conditions can be seen in Figure 1.20. The results from these experiments were compared to the network model simulation.

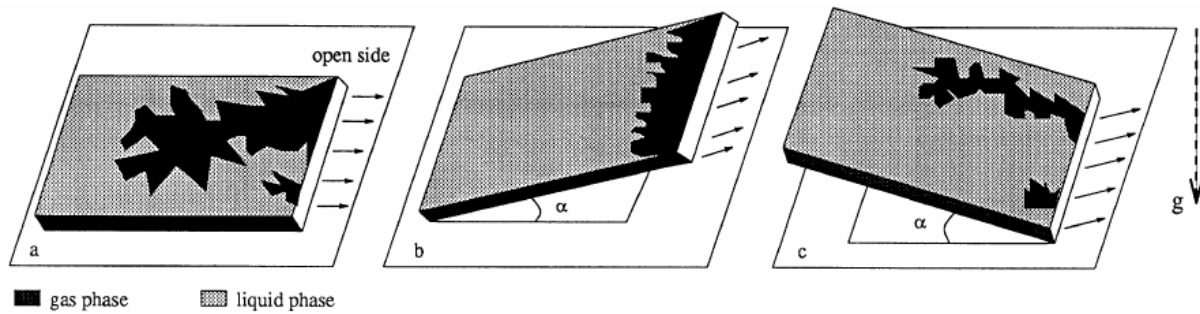


Figure 1.20: Three different conditions of gravity forces (a) horizontal case ($B = 0$) (b) stabilizing case ($B > 0$) and (c) destabilizing case ($B < 0$), (Laurindo and Prat, 1998 [14]).

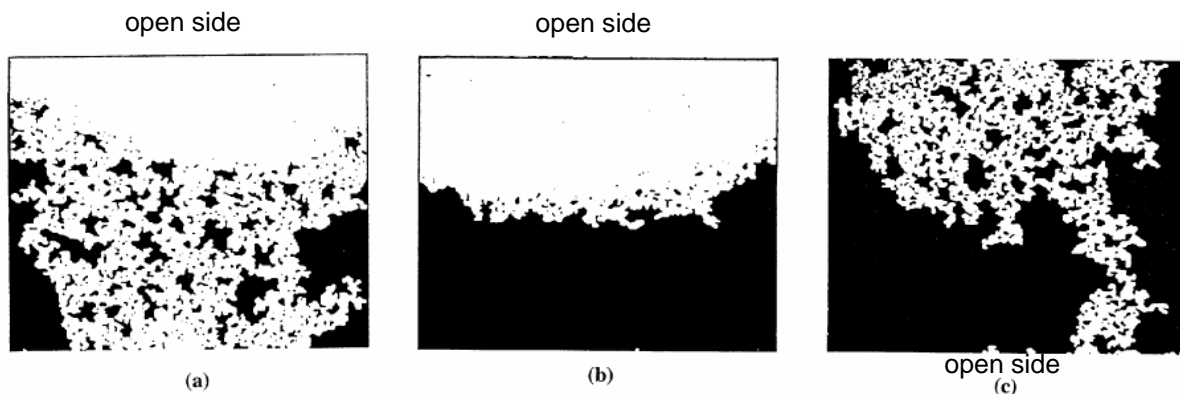


Figure 1.21: Phase distribution of experiment for different orientations of gravity force (a) $B = 0$, (b) $B > 0$ and (c) $B < 0$. Vapour phase is white and liquid phase is black (Laurindo and Prat, 1996 [12] and 1998 [14]).

Figure 1.21 shows phase distributions of experiment for the different gravity force conditions. For the destabilizing case ($B < 0$), part of the network surface is still wet because the air invaded the depth of the micromodel until the top edge (see Figure 1.21c). The drying rate is still at high level and produces first drying period due to the evaporation being only controlled by the diffusive layer. For case $B = 0$ the air invades the depth of micro-model until bottom edge, but all network surface is already dry (Figure 1.21a). The drying rate in this case is lower than in case $B < 0$ due to additional vapour resistance in the micro-model. For case $B > 0$, the phase distribution forms a receding front and the drying rate is very small due to competition between capillary forces and gravity forces. Figure 1.22 shows drying rate for these three cases of influence of gravity, including comparison between experiment and simulations.

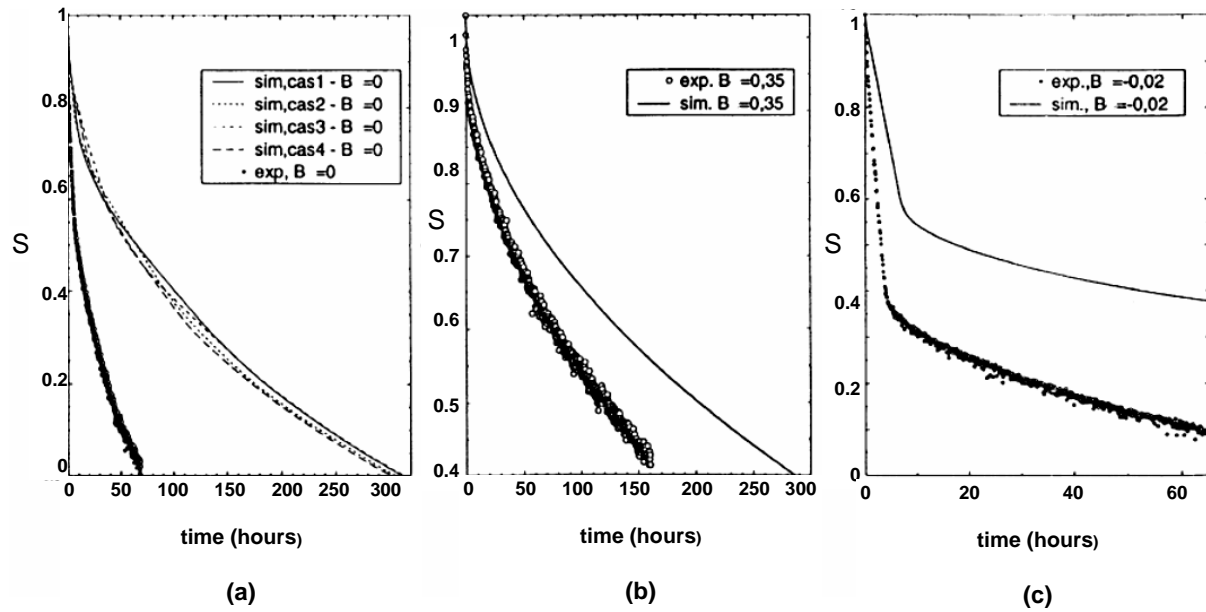


Figure 1.22: Drying curves of simulation and experiment for different orientation of gravity force (a) $B = 0$, (b) $B > 0$ and (c) $B < 0$ (Laurindo and Prat, 1998 [14]).

The comparison between experiment and simulation reveals a good qualitative agreement for all three conditions, but the drying kinetics in experiments is up to six times faster than in simulations. According to Prat, film flow in the throats is a possible reason for the difference between simulation and experiment. Figure 1.23 shows possible place of film flow in the throats. This will be discussed in the following section.

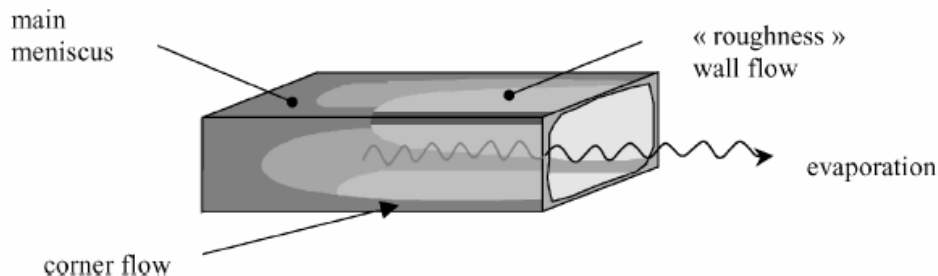


Figure 1.23: Liquid film in the corner or in surface roughness of a throat (Prat, 2002 [26]).

Film Flows

Film flow in throats is made responsible for the high experimental drying rates in comparison to simulation results (Laurindo and Prat, 1998 [14]). The film flow can exist in the roughness or in the corner. Figure 1.24 illustrates how a film region can explain the differences in simulation and experiment. In the simulation, evaporation front is located at the outer boundary of the main cluster. Due to the film region, the evaporation front in the experiment is closer to the network surface so that the drying rate in the experiment is much higher than in the simulation.

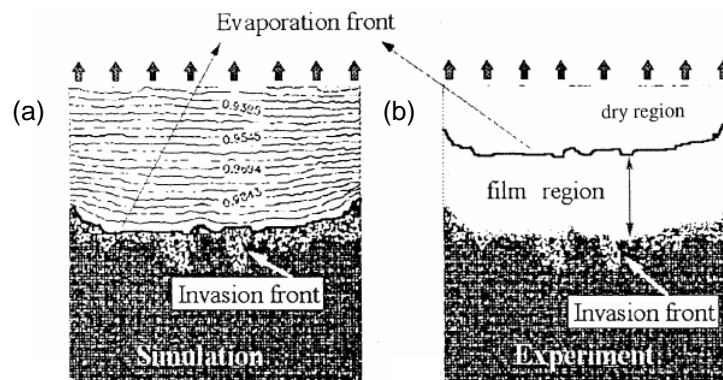


Figure 1.24: Evaporation front for (a) simulation and (b) experiment (Laurindo and Prat, 1998 [14]).

In order to prove the presence of film flow in the network, Laurindo and Prat (1998 [14]) studied qualitatively film flow by network experiments under negligible gravity ($B = 0$). Initially, the micromodel is fully saturated by liquid. Evaporation takes place at the right side. Then, liquid (hexane) was injected into micromodel at the opposite position in respect to the vapour escape side. The phase distribution in the micromodel was observed at the steady state condition. When evaporation rate is equal to the liquid flow of injection, the drying process is at the steady state. In the steady state condition, the liquid-gas interface is formed by main cluster and by trapped clusters that should be stable.

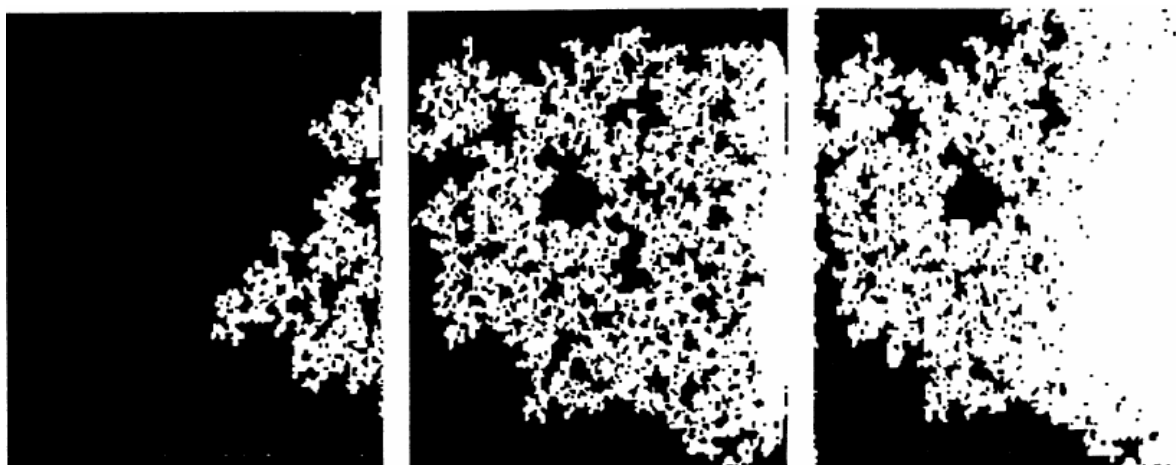


Figure 1.25: Phase distribution in three different steady state conditions. Vapour phase is white and liquid phase is black (Laurindo and Prat, 1998 [14]).

The trapped clusters exist for different steady state conditions, as shown in Figure 1.25. Film flow is considered as the reason for the existence of trapped clusters. Therefore, Prat et al. carried out another experiment by injecting dye into the micromodel. In this experiment, the dye reached even the trapped clusters. Laurindo and Prat (1998 [14]) also investigated the influence of surface roughness of the model wall as representative of throat wall. Two types of wall surface were investigated by using smooth and rough beads for the drying experiments with a packed bed. The drying curves of both cases can be seen in Figure 1.26. The drying time for rough beads is shorter than for smooth beads, because liquid can flow along the surface of rough beads through small capillary channels. However, the difference in drying time between smooth and rough beads is too small to explain the observed difference between experiment and simulation. Therefore, Prat considered corner flow in the micromodel as the major factor.

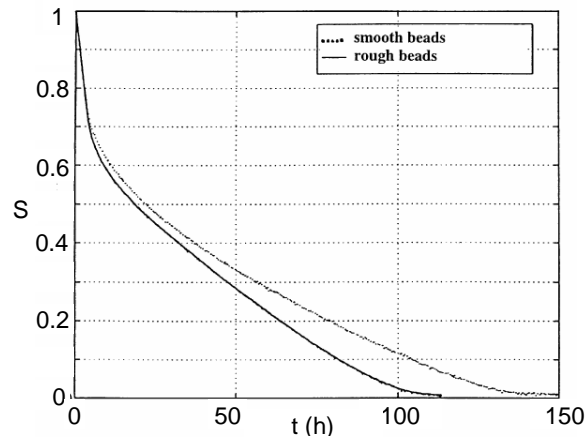


Figure 1.26: Drying curves for comparison between smooth and rough beads (Laurindo and Prat, 1998 [14]).

3D Pore Network

Le Bray and Prat (1999 [15]) investigated drying of a porous medium in 3D with a simple cubic network as shown in Figure 1.27. Vapour escapes from the top of the $51 \times 51 \times 51$ network and the other sides are impermeable boundaries. Only one realization was presented due to limitation of computation time. Geometry and assumptions of 3D network model are the same as for the 2D network model of Prat's work. Gravity effects are not taken into account in this model ($B = 0$). The result of this network simulation can only give a qualitative description of phenomena during the drying process. The 2D network model could not produce a constant drying rate period (*CRP*) so that the 3D network was used to investigate the *CRP*.

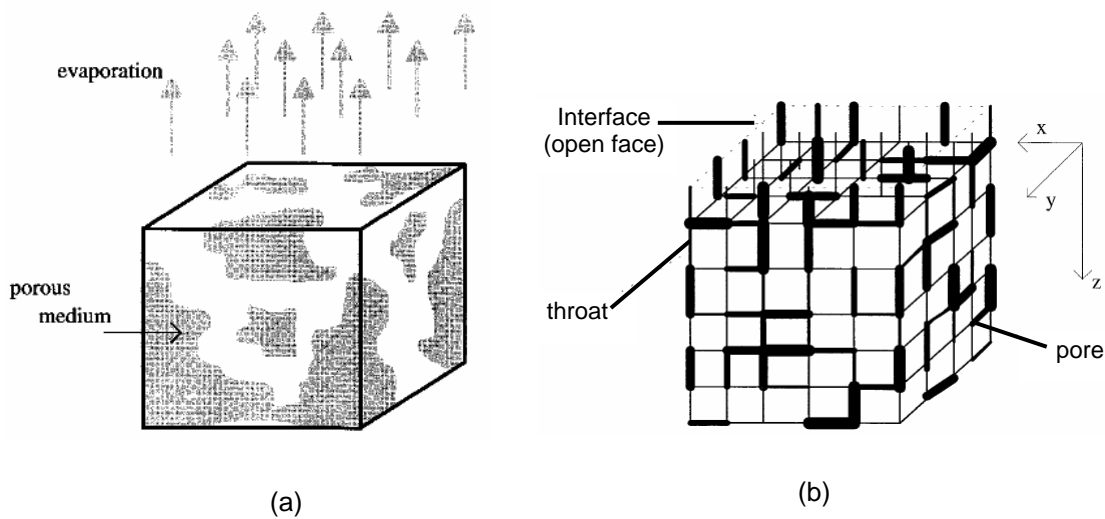


Figure 1.27: (a) Cubic porous medium and (b) model for 3D network studied (Le Bray and Prat, 1999 [15]).

Le Bray and Prat observed two events during the drying, which give an explication of the phenomena in the 3D case. These are breakthrough (*BT*) and main cluster disconnection (*MCD*). The *BT* point describes that the non-wetting fluid (gas) reaches the bottom of 3D network so that the saturation at the bottom is less than unity. *MCD* occurs when all wetting fluid (liquid) at the top of network has been evaporated so that the surface saturation of network is zero. These points can be presented by evolution of the moisture profiles along z axis of 3D network, evolution of the number of clusters and drying rate as shown in the Figure 1.28.

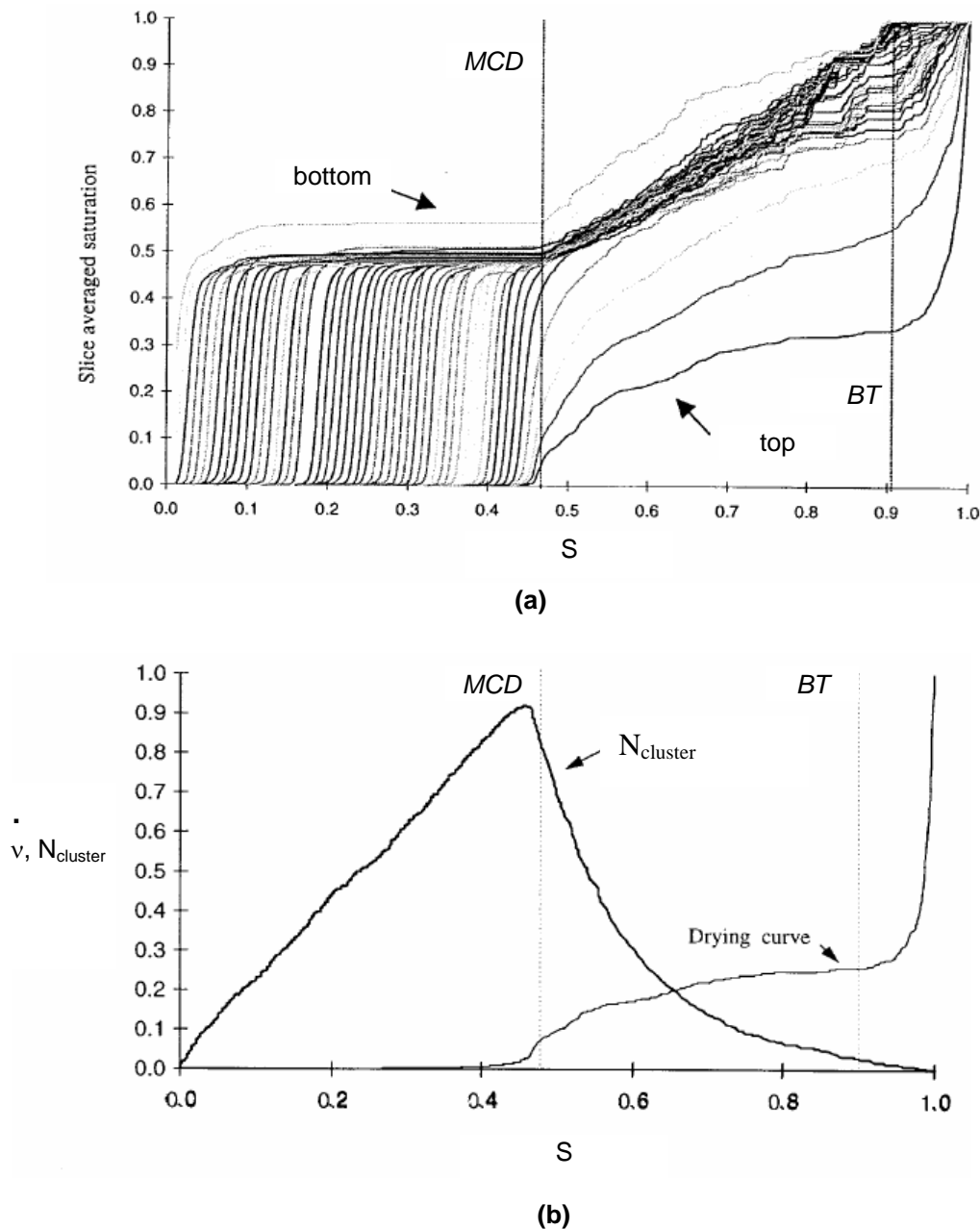


Figure 1.28: (a) Evolution of slice average saturation as a function of network saturation (each curve corresponds to a slice) (b) evolution of number of clusters and drying rate as a function of the network saturation (Le Bray and Prat, 1999 [15]).

With the help of *BT* and *MCD*, three periods can be distinguished in the drying process (see Figure 1.28). In the first period, saturation of the first slice decreases rapidly because air invades firstly this area, while other slices stay at relatively constant saturation. Therefore, drying rate decreases rapidly as shown in Figure 1.28b. The number of clusters is relatively constant because the air invades only the top of network. Then, the air invades in the depth of network until the bottom slice is reached by the air at the *BT* point.

In the second period, most of the slices in the network have uniform saturation because the air can invade all slices in network due to gas channels until the bottom of the network (*BT* point). The number of clusters increases rapidly due to the creation of new disconnected clusters. The air invades the liquid in the depth of network and capillary pumping transfers this liquid to the throats close to the surface. Accordingly, saturation of the first slice as well as drying rate is relatively constant.

During the third period after *MCD* point, the network has two regions i.e. a dry region and an unsaturated region (disconnected cluster). The disconnected clusters will dry gradually from the top to the bottom as a receding front. The remaining liquid evaporates at low drying rates. Due to more flow paths in the 3D network, trapping of clusters plays a minor role.

Viscous Effect

Drying of porous media in the isothermal condition is influenced by three forces, i.e. capillary, gravity and viscous forces. Competition between capillary and gravity forces has been presented by Laurindo and Prat (1998 [14]) by simulation at different Bond numbers (*B*). In order to study comprehensively the three forces in the drying process, Prat et al. expressed the competition between those forces by characteristic lengths (*L*), which are related to dimensionless numbers (Prat and Bouleux, 1999 [25]).

The characteristic width of the gravity front L_g can be computed from Bond number and throat length L_k as:

$$\frac{L_g}{L_k} \approx B^{-1} \quad (1.13)$$

The length describing the typical width of the viscous front L_{cap} can be obtained from the Capillary number

$$Ca = \frac{(\eta_w \dot{M}_v L_k)}{(\rho_w \pi r_0^2 \sigma \sigma_0)} \quad (1.14)$$

$$\frac{L_{cap}}{L_k} \approx Ca^{-1} \quad (1.15)$$

where η_w dynamic liquid viscosity, \dot{M}_v vapour mass flow rate, ρ_w density of water, r_0 mean throat radius, σ interface tension of water and σ_0 standard deviation of throat radius. These lengths of gravity and viscous front have to be compared to the length of the network L_{tot} . By variation of the lengths of gravity front L_g and viscous front L_{cap} , the dominating force can be mapped in a drying phase diagram (see Figure 1.29). The phase distribution with capillary fingering indicates that capillary forces dominate over gravity or viscous forces as invasion percolation (*IP*). At this condition, the length of gravity and viscous front is greater than network size L_{tot} . The receding front forms if gravity and viscous forces are larger than capillary forces. Then, L_g and L_{cap} are smaller than L_{tot} and the area is in the invasion percolation stabilizing gradient (*IPSG*). If $L_g < 0$ the area is in the invasion percolation destabilizing gradient (*IPDG*).

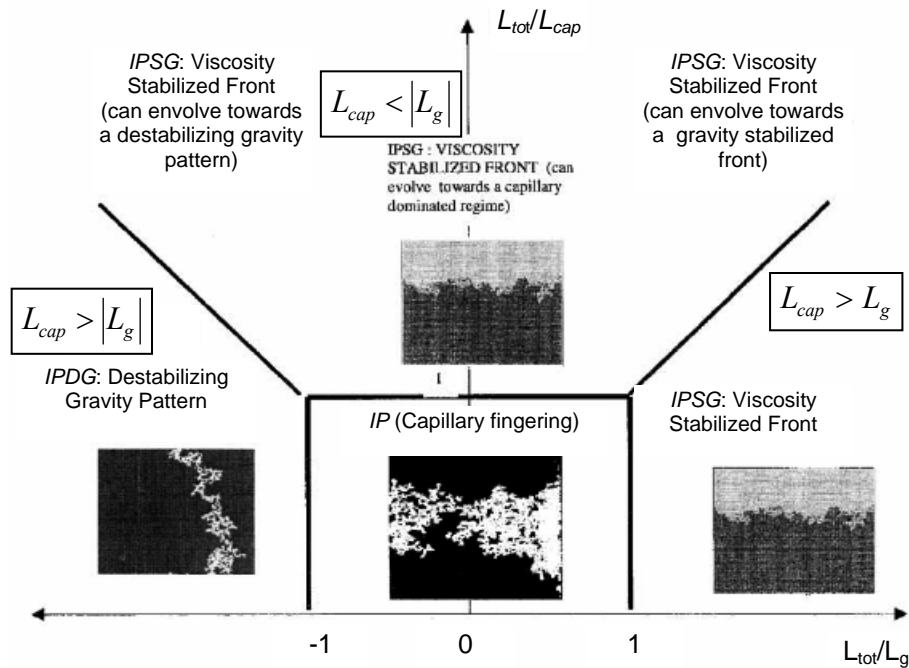


Figure 1.29: Drying phase diagram in isothermal condition (Plourde and Prat, 2003 [22]).

Thermal Gradients

In the real convective drying process, moisture in the porous media can be removed due to temperature and vapour pressure gradients inside and outside of porous media. Nevertheless, most simulations of drying by pore networks assume isothermal conditions due to low drying rate. In order to approach the real process, Huinink et al. (2002 [9]), Plourde and Prat (2003 [22]) studied the influence of a temperature gradient in the network on drying behaviour. The temperature gradient influences several parameters in the drying calculation, such as liquid viscosity η_w , surface tension σ , saturation vapour pressure p_v^* and binary diffusion coefficient δ_{va} .

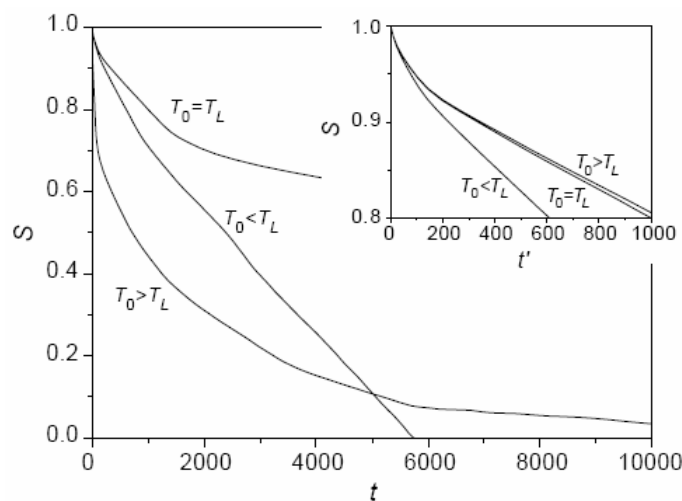


Figure 1.30: Drying curve of network simulation with thermal gradient for three cases ($T_0 = T_L$, $T_0 < T_L$ and $T_0 > T_L$) (Huinink et al., 2002 [9]).

Huinink et al. only focused on the temperature dependency of saturation vapour pressure, p_v^* . They imposed linear T-gradient with temperature T_0 at the open top and T_L at the sealed bottom of network. Three different cases were observed, i.e. $T_0 > T_L$, $T_0 = T_L$ and $T_0 < T_L$. Generally, the drying process has the case $T_0 > T_L$ so that the liquid can be removed at high drying rate. The drying curves with dominating capillary force ($B = 0$) for those cases can be seen in Figure 1.30. In the case $T_0 > T_L$, the initial drying rate is high because the menisci at the network surface have high equilibrium vapour pressure. For $T_0 < T_L$ at low saturation, the drying rate is rather constant and low because the distance between evaporation front and top is relatively constant and the air invades the bottom area.

Plourde and Prat developed a thermal network model in order to study the influence of thermal gradients on drying via surface tension gradients. The heat transfer is modelled by conduction in liquid and solid phase; additionally, heat sinks (due to evaporation) influence the resulting T-field. Plourde and Prat investigated the influence of thermal gradient and pore size distribution on drying behaviour (phase distributions) where the capillary pressure is influenced by temperature and radius (see Eq. (1.3)).

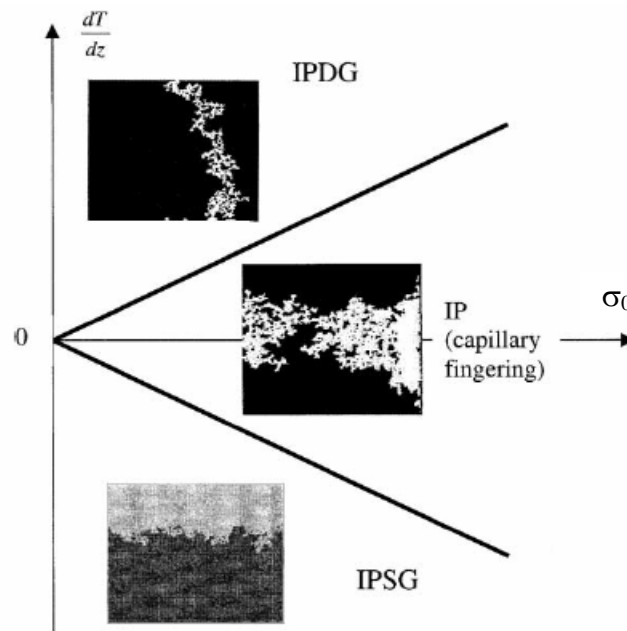


Figure 1.31: Drying phase diagram as function of thermal gradient and radius distribution (Plourde and Prat, 2003 [22]).

Figure 1.31 shows a drying diagram for the influence of thermal gradient $\frac{dT}{dz}$ and width of pore size distribution σ_0 . For a broad distribution (large σ_0), the thermal gradient does not influence drying behaviour because capillary pumping is dominated by radius distribution. In the case of a narrow pore size distribution (small σ_0), the thermal gradient plays a role in the drying kinetics. The drying process is similar to invasion percolation in a stabilizing gradient (*IPSG*) pattern when temperature at the top is higher than at the bottom of the network. The drying process is similar to invasion percolation in a destabilizing gradient (*IPDG*) pattern when temperature at the top is lower than at the bottom of the network.

1.5.3 Pore Network Model by Yiotis et al.

Yiotis et al. (2001 [37]) studied viscous effects in liquid and gas phases for drying of porous media by pore network modelling. In order to get a strong effect of viscous forces, a fracture was put on the top of the network (see Figure 1.32a). The fracture in the network model is a representative for a fracture in a porous medium but the length and width of the fracture are set to be of the same value as for network throats. The viscous forces in the gas phase can be observed for large differences in gas pressure. Therefore, gas with high flow rates was injected to create high pressure drop between inlet and outlet of the fracture.

The network model is 2D with spherical pores, connected by cylindrical throats. In their model, the pores serve as containers for gas and liquid; the capillary pumping does not happen in the pore but only via the throats (without volume) which serve as conductors and as capillary barriers. Evaporation takes place at the top of network and the vapour is swept by gas injection into the fracture area. Other sides of the pore network are impermeable to flow and mass transfer.

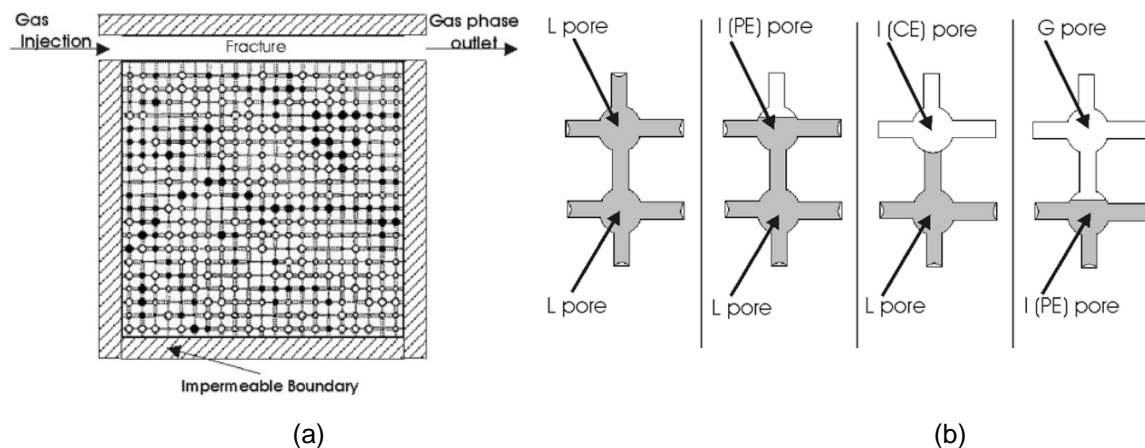


Figure 1.32: (a) Pore network model as representation of a porous medium and (b) types of pores in Yiotis model (2001 [37]).

In this method, the pores can be divided into three types according to their filling state: fully occupied by liquid (L pore), fully occupied by gas (G pore) and those at the gas liquid interface (I) (see Figure 1.32b). The pore is considered as L pore if all neighbouring throats are full with liquid. If all neighbouring throats are empty, the pore is considered as G pore. Interface gas-liquid pores as shown by experiment in Figure 1.33 can be distinguished into two different types: (i) completely empty (CE), where menisci are stationary at the pore throats, (ii) partially empty (PE), where menisci are receding in the pore. If an L pore is invaded continuously by the gas, it becomes of type I, PE.

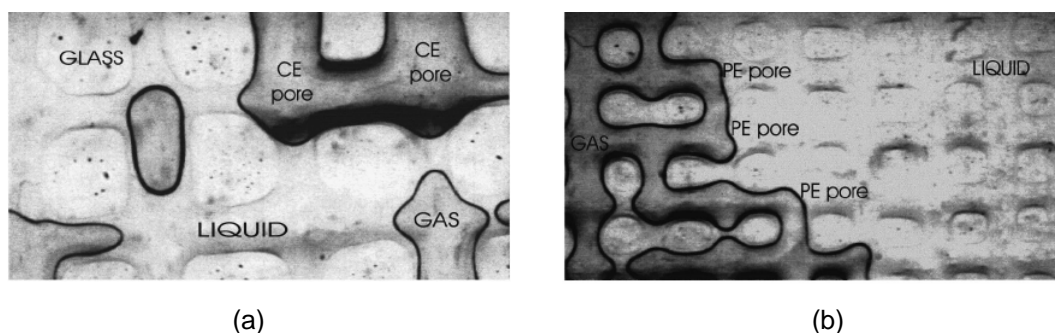


Figure 1.33: Experimental visualization of two different types of pores during drying (a) CE pores and (b) PE pores (Tsimpanogiannis et al., 1999 [34]).

Viscous Effect

Yiotis et al. (2001 [37]) studied viscous effects in liquid and gas phase. Some dimensionless numbers (Pe and Ca) were varied to work out different influences of viscous forces. Figures 1.34 and 1.35 show phase distributions for the two limiting cases in 50×50 networks. In case of high gas flow rate (Figure 1.34), the gas at the inlet fracture will push the liquid from the network surface close to the fracture inlet. Then, liquid will move to the area which is close to fracture outlet (low gas pressure area). This is like a piston displacement driven by gas flow rate, so that the liquid still forms a more or less main cluster (MC) and has a “stabilized front” in the area $IPSG$.



Figure 1.34: Phase distributions at high gas flow rate for saturation $S = 80 \%$, 60% , 40% and 20% (Yiotis, et al., 2001 [37]).

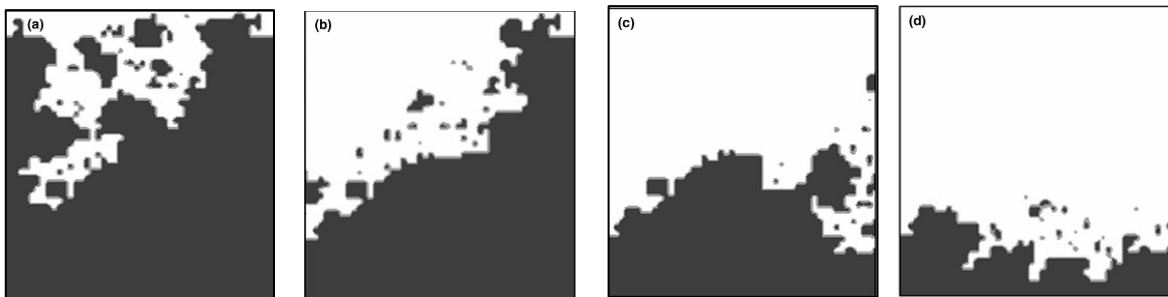


Figure 1.35: Phase distributions at low gas flow rate for saturation $S = 80 \%$, 60% , 40% and 20% (Yiotis, et al., 2001 [37]).

In case of low gas flow rate (1000 times less than above), drying is controlled by capillary forces and vapour diffusion in the network. Therefore, this condition results in capillary fingering of many disconnected clusters (DC), shown in Figure 1.35, as for invasion percolation (see drying phase diagram in Figure 1.29).

Film Flow

According to Laurindo and Prat (1998, [14]), there is a discrepancy in drying times obtained by experiment and simulation. Laurindo and Prat suggested film flow along walls and corners of throats as a reason. They have proven by experiment the presence of film flow in the micromodel and studied quantitatively the influence of surface roughness on the drying rate. In order to study these phenomena theoretically, Yiotis et al. (2003 [38], 2004 [39], 2005 [40]) formulated a model for 2D networks, which accounts for film flow.

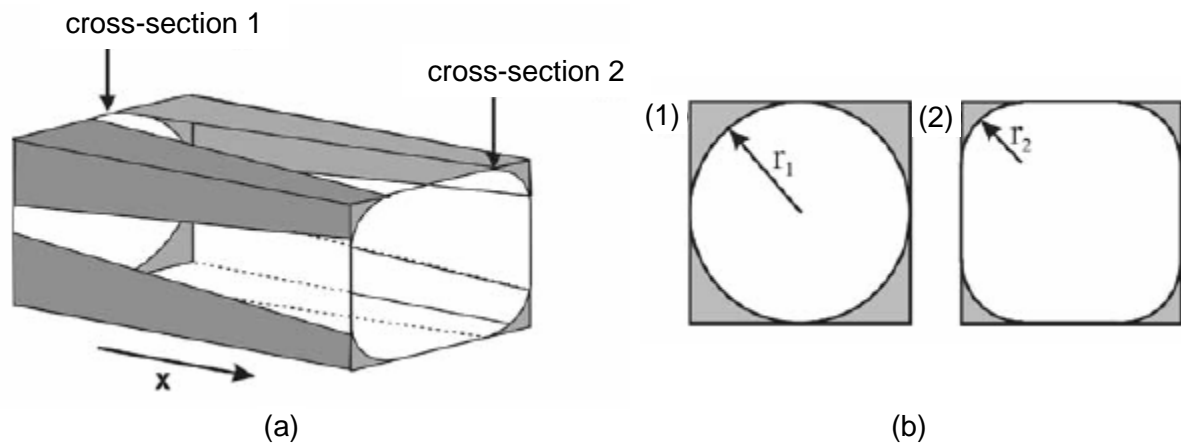


Figure 1.36: (a) Liquid film along the corners of a capillary with square cross section (b) evolution of the film radius (Yiotis et al., 2005 [40]).

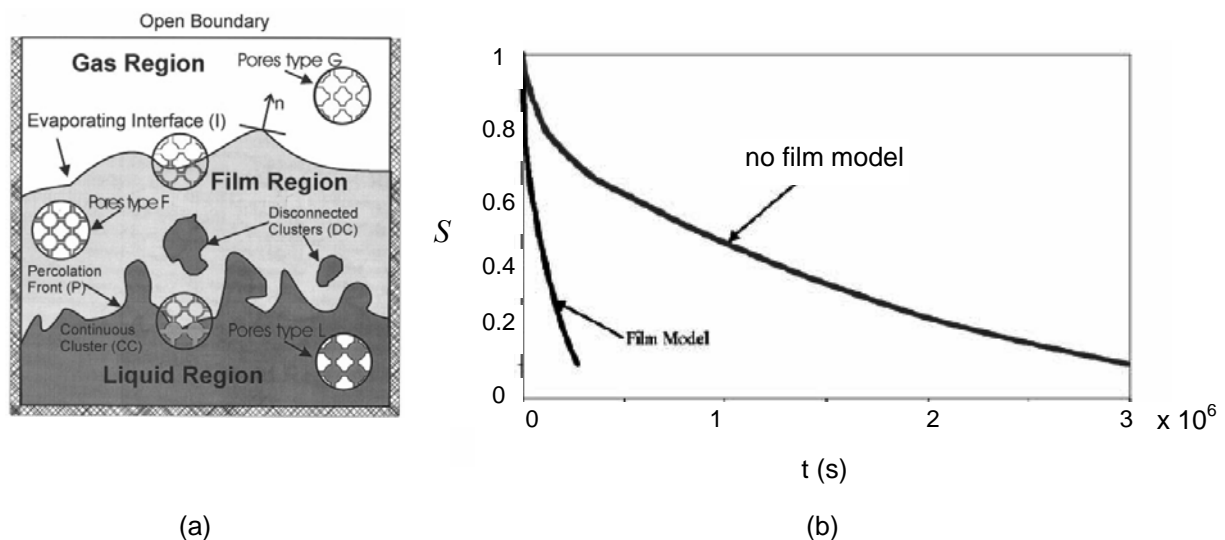


Figure 1.37: (a) Phase distribution with presence of film region and (b) drying curves for comparison of network drying models with and without film flow (Yiotis et al., 2005 [40]).

A liquid film along the corners of the throats in the situation of evaporation will develop differences in radius of curvature (see Figure 1.36), so that the liquid can be transported to the top of the network by capillary flow through the film. Yiotis et al. defined type-F pores in their model (see Figure 1.37a), which contain gas, but also a liquid film. For F pores, liquid viscous effect is included in the film and the process is similar as for the bulk of liquid phase and capillary flow. The result of this model was compared to the model without liquid film flow, showing that the drying kinetics with liquid film is faster than without liquid film and getting for long time a constant drying rate (*CRP*) due to the presence of capillarity in the film (see Figure 1.37b).

Simulation of 3D Network

In order to investigate the influence of the diffusive layer on the drying behaviour, Yiotis et al. (2006 [41]) studied 3D pore networks by varying boundary layer thickness. Figure 1.38a shows a normalized drying curve without boundary layer ($n_{bl} = 0$), where this curve refers to Le Bray and Prat (1999 [15]). The drying curve can be categorized into four drying periods, i.e. initial drying period, constant rate periods (*CRP*), falling rate period (*FRP*) and receding front period (*RFP*), as shown in Figure 1.38a. The *CRP* in that figure is not really constant drying rate at the beginning, so that that network model still fails to produce *CRP*.

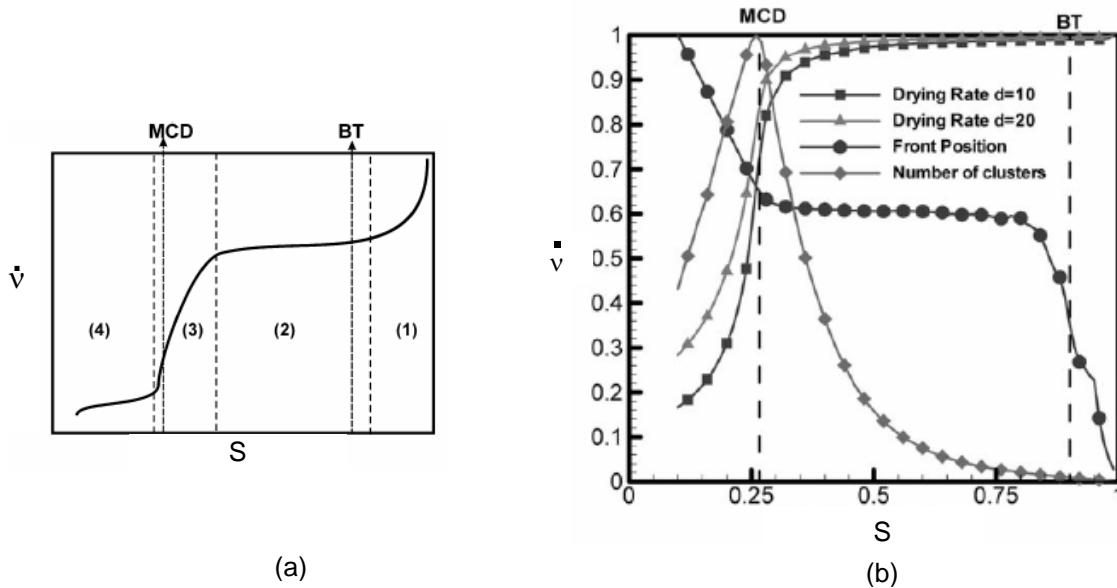


Figure 1.38: (a) Four periods of the drying curve and (b) drying kinetics for negligible gravity and variation of the number of nodes in diffusive layer ($n_{bl} = 10, 20$) (Yiotis et al., 2006 [41]).

Drying of a $80 \times 80 \times 80$ network in Yiotis model was simulated for different conditions of gravity force and diffusive boundary layer thickness. Figure 1.38b shows normalized drying rate for different diffusive layer thickness ($n_{bl} = 10$ and 20), evaporation front position and number of clusters. The normalized drying rate is higher and the *CRP* longer for a thicker boundary layer, because lateral vapour diffusion is more intensive in a thicker diffusive layer. Therefore, the diffusive layer thickness is important to produce a true *CRP*. The *CRP* of Yiotis et al. is at the initial drying rate, while *CRP* of Le Bray and Prat is at lower than initial drying rate (see Figure 1.38).

1.5.4 Pore network model by Segura et al.

Segura and Toledo are the latest researchers to investigate drying of porous media by pore network modelling since 2005 (Segura and Toledo, 2005 [28]). Their network model is based on the work of Prat. They investigated transport parameters in drying with network modelling, i.e. liquid permeability and vapour diffusivity. The methods to obtain effective transport parameters of Nowicki et al. (1992 [20]) and Segura and Toledo (2005 [28], 2005 [29], 2005 [30]) are rather different. Nowicki et al. took saturation and flow rate and difference of average pressures at the top and the bottom as explained in section 1.5.1., while Segura et al. calculated the drying parameters from network conductances for phase distribution as obtained during drying. However, in their drying model liquid viscosity is neglected, so that there is some inconsistency. Relative liquid permeability is calculated by using Darcy's law and effective vapour diffusivity by Fick's first law as by Nowicki – see Isothermal Drying of Pore Networks

Eqs.(1.10) and (1.11) – only that Segura and Toledo applied uniform liquid or vapour pressures on each side of the network (independent of those occurring during drying).

During the drying process, the porous medium can undergo structural changes or damages, such as shrinkage, fractures or cracks. These damages can be caused by stress or temperature, and may decrease the quality of the product. Segura and Toledo (2005 [30]) studied the influence of shrinkage on drying kinetics and effective transport parameters, i.e. permeability and diffusivity. 2D network with size 100 x 100 and 3D network with size 15 x 30 x 15 were simulated for the condition with and without shrinkage. The shrinkage in this case is caused by very high capillary pressure difference between two meniscus throats, so that throat radius and porosity ψ are reduced. Figure 1.39 shows curves for the influence of shrinkage on the drying rates for 2D and 3D network. The drying rate is slower for case with shrinkage than without shrinkage, because the size reduction will reduce the permeability. Then, it is difficult to deliver the liquid to the surface of the network and the throats there dry rapidly.

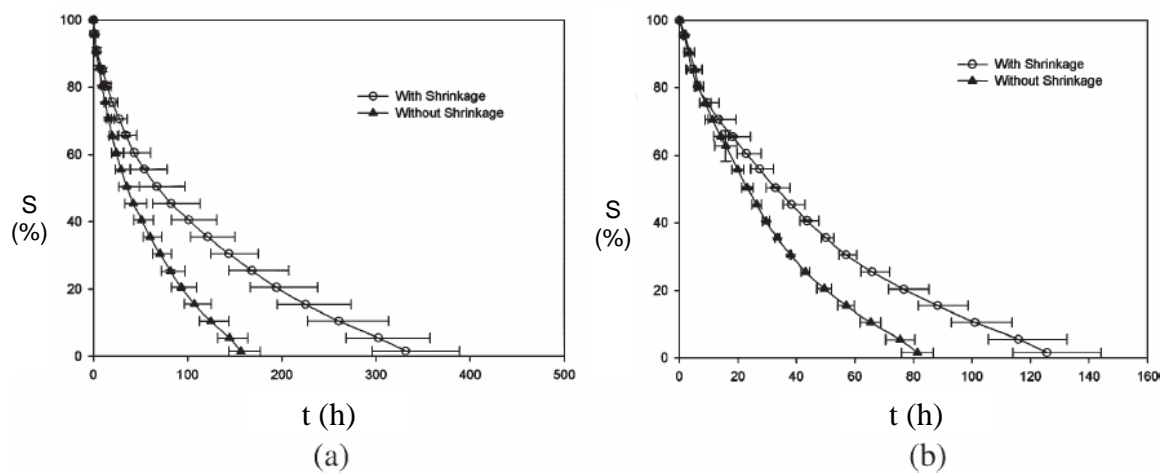


Figure 1.39: Influence of shrinkage on the drying rates for (a) 2D network (b) 3D network, (Segura and Toledo, 2005 [30]).

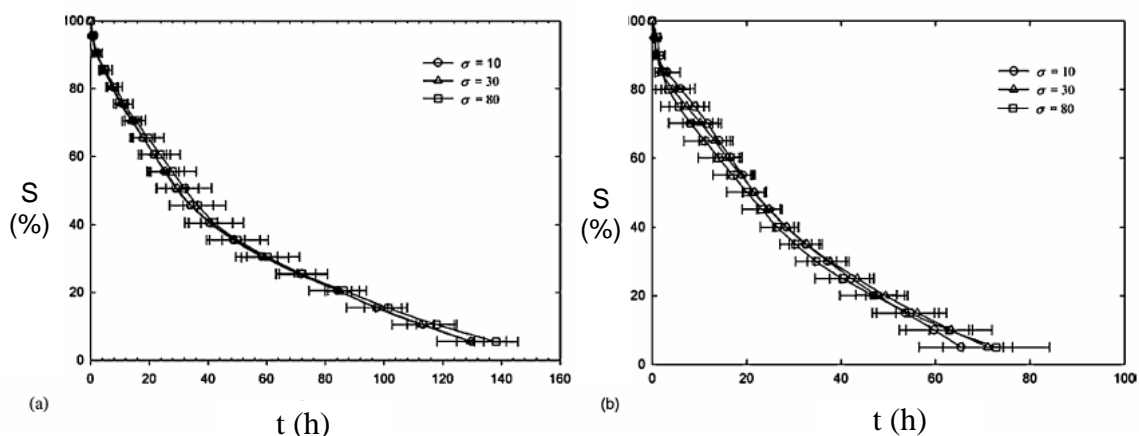


Figure 1.40: Influence of pore size distribution on the drying rates for (a) 2D network (b) 3D network (Segura and Toledo, 2005 [29]).

Segura and Toledo also studied the influence of pore size distribution by varying the standard deviation of throat radii in the log normal distribution (Segura and Toledo, 2005 [29]). The variations of standard deviation (σ_θ) are 10, 30, 80 μm . Figure 1.40 shows the influence of pore size distribution (standard deviation) on the drying curve. The standard deviation has almost no influence on the drying curve because they did not include liquid viscous effect. If liquid viscosity, gravity or temperature gradient are modelled (see Prat's work), the capillary forces will compete with other forces so that the drying rate will be influenced by pore size distribution (Metzger and Tsotsas, 2005 [18]).

CHAPTER 2

DESCRIPTION OF ISOTHERMAL PORE NETWORK DRYING MODEL

2.1 Overview

In this chapter, the pore network model for drying under isothermal conditions is presented. The model is constructed by two sub-models: the data structures for geometry and the drying algorithm, as shown in Figure 2.1. The connection of both sub-models is that the data structures for geometry give information about connections between throats and pores to the drying algorithm. The data structures for geometry describe the pore network representing the porous solid and the boundary layer. Several input parameters are needed to generate these data structures, such as network size and pore connectivity.

The drying algorithm is an algorithm to identify and calculate several drying parameters, so that the drying behaviour can be observed. It comprises updating of phase distribution in the network, labelling of liquid clusters and drying kinetics. Local saturation as phase distribution is saturation of single pores and throats, namely liquid and gas pores as well as full, partially filled and empty throats. This saturation must be stored and updated at every time step because it defines the phase of pore or throat to be liquid or vapour. The saturation of throats and pores and data structure for geometry give information about the liquid cluster. The labelling of liquid clusters is necessary to know the topology of the liquid for identification of the throats that are connected for capillary flow. Drying kinetics are obtained from the evaporation rate data by solving mass balances in liquid and vapour so that the saturation of throat and pore can be updated.

Drying of porous media involves many transport phenomena at the pore scale, such as the motion of menisci in the throats, viscous flow in liquid and capillarity. The drying kinetics is described by rules of calculation so that the phenomena of drying at the pore scale can be modelled. The rules of calculation are how to calculate the evaporation rate of meniscus throats, how to deal with trapped clusters, how to define the menisci as moving in viscous effect calculation, how to compute the time step to update the throat and pore saturation. These rules must be formulated in such an algorithm to get a complete model of drying. Finally, the complete model will be implemented in a computer program (MATLAB) and applied to different structures of porous media.

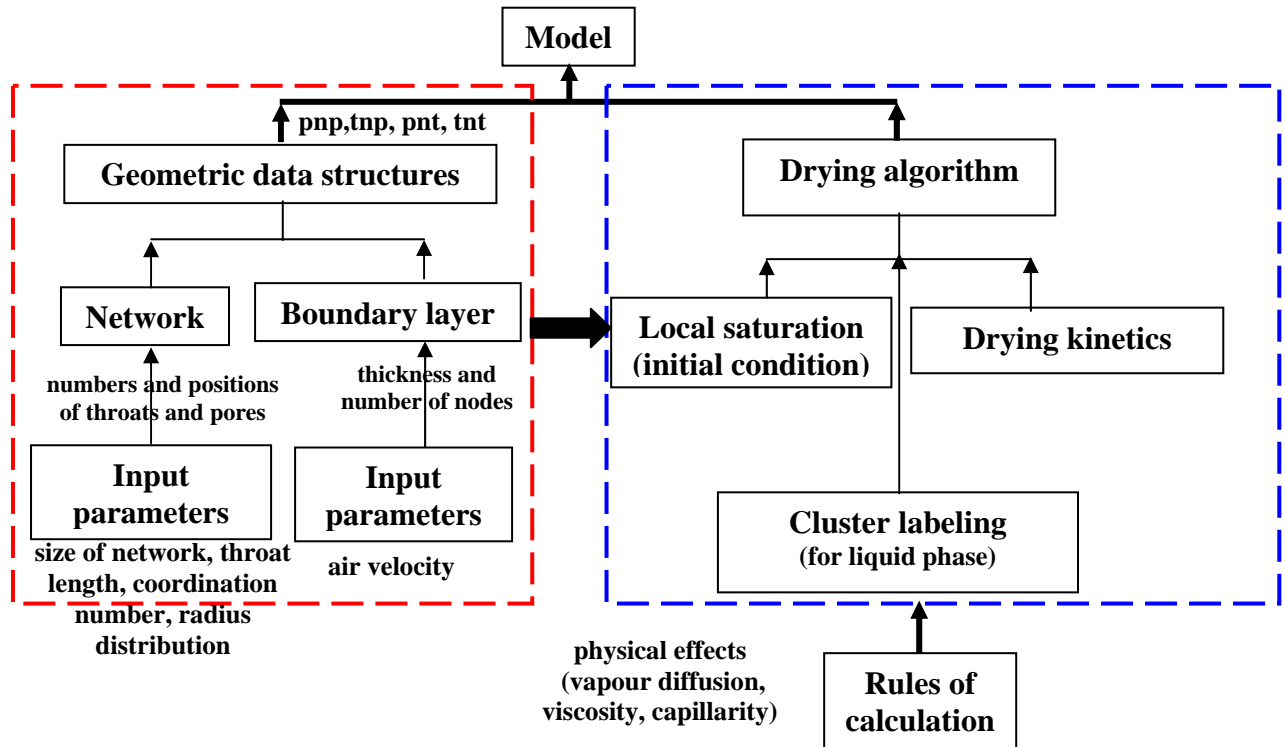


Figure 2.1: Scheme of the model for isothermal drying of a pore network.

2.2 Data Structures of Geometry

Two-dimensional networks with different coordination numbers and three-dimensional cubic networks will be considered for simulating in the drying of porous media. Square networks with four connections per pore were mostly used. This network is a regular one with periodic geometry and constant throat length. The square network consists of throats as conductors that connect pores. The shape of throat is cylindrical with length of throat L and radius r . The pore is only a node without liquid inside as shown in Figure 2.2. If distance between pore nodes and throat length are set to be equal, an overlap between throats exists at the pore, but is not corrected in this model (see Figure 2.2a). The network model becomes easier if arrangement of geometric data structures is in a certain format applicable to any structure of porous media (to irregular networks as well).

The data structures of geometry contain pore and throat numbers, pore positions, neighbouring relationships between throats or pores in the network and boundary layer. Each pore and throat must be numbered because these numbers are used as identity of throat and pore in this modelling. Then, the pore must be arranged in order to know the pore positions. Throat positions will follow from the pore positions because a throat is a connector of two pores. The neighbouring pores and throats can be identified from the data of pore and throat positions. Data structure of neighbouring pores and throats is “pnp”, “pnt”, “tnp” or “tnt”. “pnp” contains for every *pore* information about its *neighbouring pores* and “pnt” about its *neighbouring throats*. “tnp” contains for every *throat* information about *neighbouring pores* and “tnt” about its *neighbouring throats*. These data structures will be applied to the network and boundary layer. The pore and throat numbers are the input parameters of “pnp”, “pnt”, “tnp” and “tnt”. As mentioned in the literature review, lateral transfer in the boundary layer is important to produce first drying period (refer to section 1.5.3, 3D network). Input parameter for boundary layer is a thickness of the boundary layer. Knowing this, the number of nodes in vertical direction and the distance between nodes can be defined.

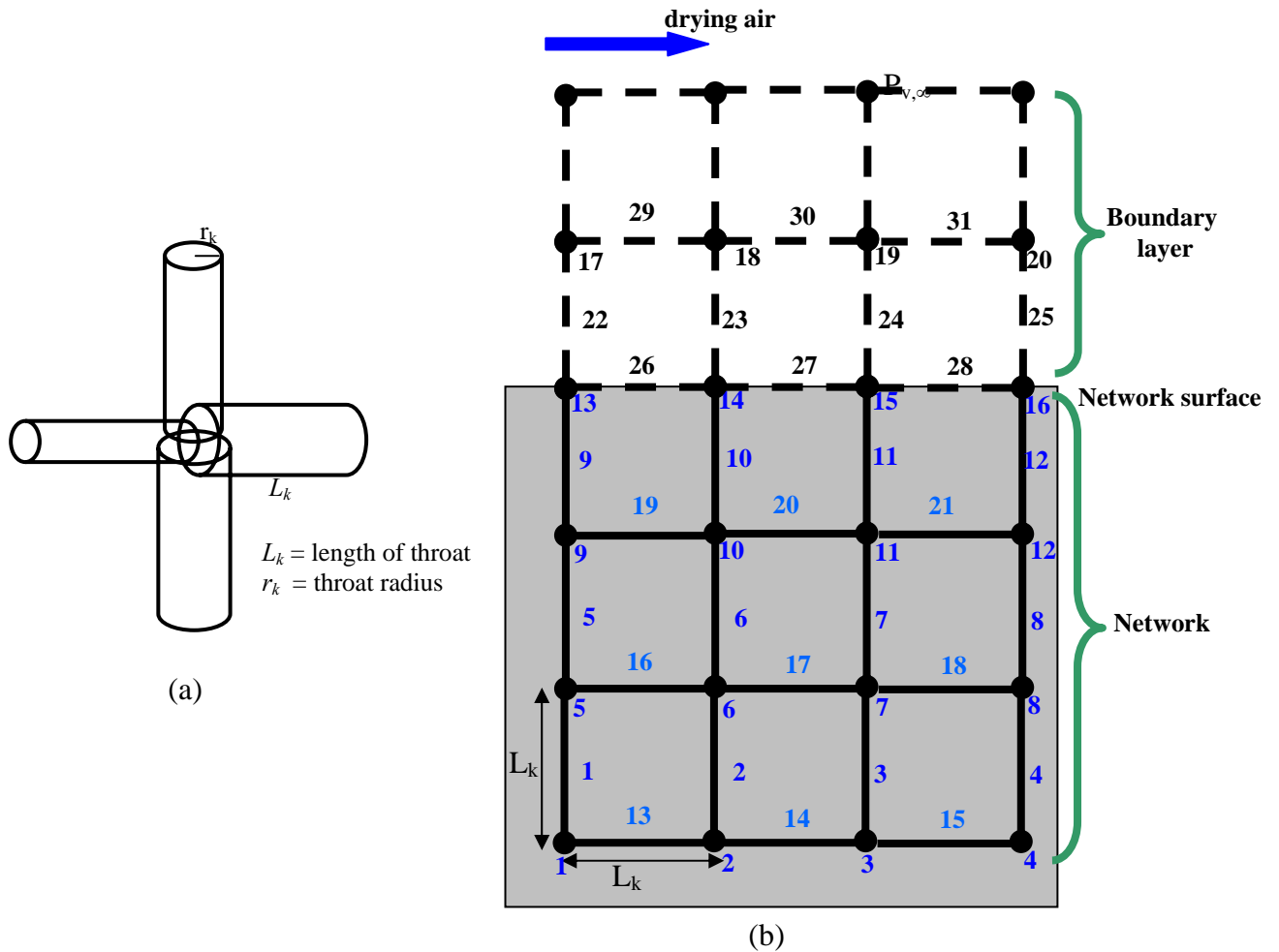


Figure 2.2: (a) geometry of throats and (b) 2D square network with pore and throat numbers.

Construction of a 2D square network

The construction of a 2D square network is started from calculating total throat and pore numbers, arranging the pore positions, and numbering pores and throats. Total number of pores and throats can be calculated from number of nodes in y and x directions. The pore positions are defined from distance between two pores (L) in x and y directions; then, each pore is connected to other pores by throats in order to get square network. The 2D square network can be constructed in this way, and numbers can be given to the pores and throats, as shown in Figure 2.2b.

The pore and throat numbers start from the bottom left corner and continue till the right end of the network. After completing one row, the pore number will go to next row in the direction from the bottom to the top of network and continue to the nodes in boundary layer. The nodes at the top of boundary layer will be attributed (as boundary condition) the same vapour pressure $p_{v,\infty}$, so that there will be no horizontal transfer and no numbering of pores and definition of throats is necessary there (see Figure 2.2b).

The throat numbering starts with vertical throats and continues with the horizontal ones (from left to right, and bottom to top). In this way, all network throats are numbered first; then all boundary layer throats, so that there is a clear separation for easy investigation of network properties (such as saturation). The complete numbering of pores and throats in the network and boundary layer can be seen in Figure 2.2b.

2.2.1 Data Structures of Geometry in 2D Square Network

The 2D square network has coordination number 4, which means that every pore is connected to maximally four pores or throats. The best way to describe the proposed data structures is through an illustrative example as shown in Figure 2.2b. In a square network, the throats have two neighbouring pores and six neighbouring throats. In the following, the data structures for pores and throats will be described.

“*pnp*” and “*pnt*” data structure

The “*pnp*” and “*pnt*” data structures can be derived by scanning neighbouring pores or throats for every pore. The “*pnp*” data structure stores all neighbouring pores that are connected to the pore. This data structure is needed to compute mass balances in liquid and vapour by use of the pressure differences between the pore and its neighbour pores (see Figure 2.3). The size of matrix array of “*pnp*” is the total number of pores in the network by maximum coordination number. A pore that has four neighbouring pores can fill all columns of matrix array, but for the pores at the border or in the corner, having less neighbouring pores, zeros are assigned to the remaining column entries.

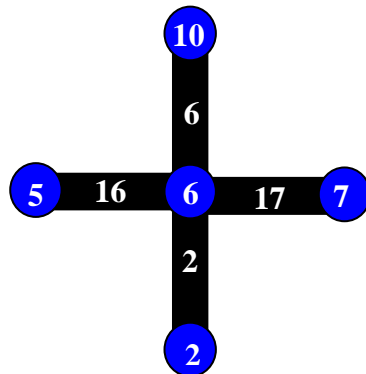


Figure 2.3: Throat and pore neighbours of a pore in a square network.

In order to solve the mass balance, the identity number of the pores neighbouring throats must be known, because many relevant properties are stored under this number such as saturation, flow conductivity and cross section area of throat. The pores have maximally four neighbouring throats, so that the matrix array of this data structure is similar to the “*pnp*” data structure, total number of pores times number of maximal connectivity. Examples of “*pnp*” and “*pnt*” entries for 6th pore, as shown in Figure 2.3, are given as:

$$\begin{array}{c}
 \begin{matrix} \vdots \\ \vdots \\ \vdots \end{matrix} \\
 \begin{matrix} 10 & 5 & 2 & 7 \end{matrix} \\
 \begin{matrix} \vdots \\ \vdots \\ \vdots \end{matrix}
 \end{array}
 \left[\begin{array}{c} \\ \\ \\ \end{array} \right]
 \begin{array}{l} \\ \leftarrow 6^{\text{th}} \\ \\ \text{row} \end{array}
 \end{array}
 \qquad
 \begin{array}{c}
 \begin{matrix} \vdots \\ \vdots \\ \vdots \end{matrix} \\
 \begin{matrix} 6 & 16 & 2 & 17 \end{matrix} \\
 \begin{matrix} \vdots \\ \vdots \\ \vdots \end{matrix}
 \end{array}
 \left[\begin{array}{c} \\ \\ \\ \end{array} \right]
 \begin{array}{l} \\ \leftarrow 6^{\text{th}} \\ \\ \text{row} \end{array}
 \end{array}$$

“*tnp*” and “*tnt*” data structure

The data structures that correlate to the throats are “*tnp*” and “*tnt*”. The “*tnp*” data structure is used to identify neighbouring pores of a throat. All throats in square network have two neighbouring pores that can be up and down or left and right of throat as shown in Figure 2.4. This data structure will be useful for checking the state change of neighbouring pores from liquid to gas when a meniscus throat is emptied by evaporation. Then, the neighbouring throats of that new gas pore will possibly contain one (more) meniscus. These throats can be directly identified from “*tnt*” data structure. Examples of “*tnp*” and “*tnt*” data structures from Figure 2.4 can be given as:

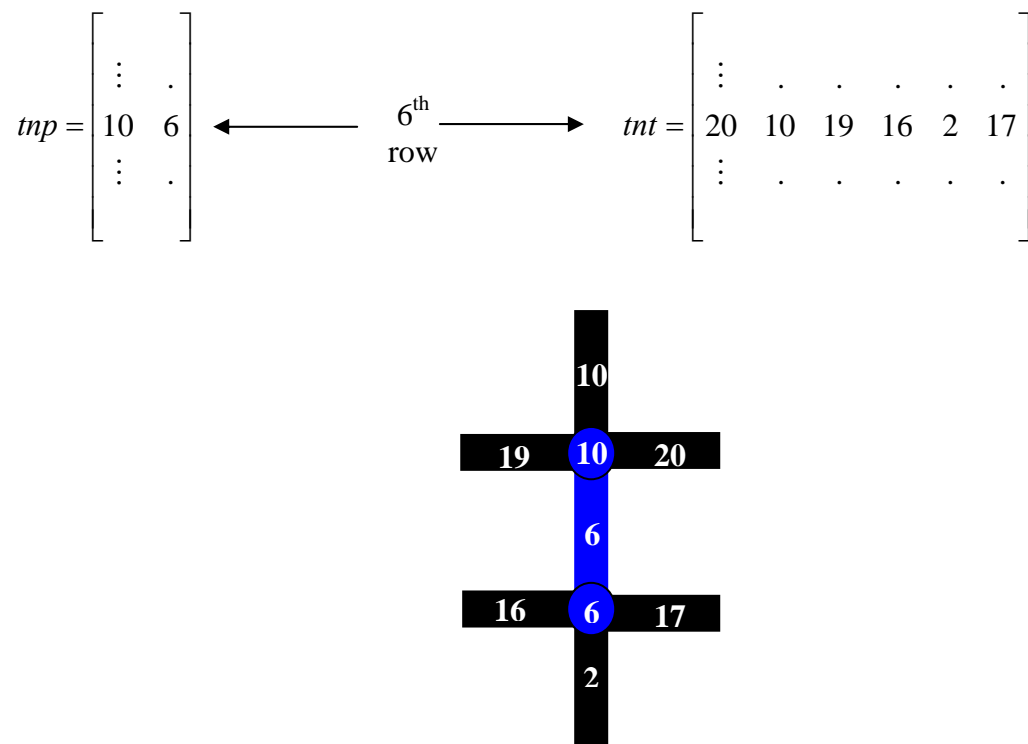


Figure 2.4: Throats and pore neighbours of a throat in a square network.

In order to belong to the same liquid cluster, two throats must be connected by a liquid pore. The “*tnp*” and “*tnt*” can provide these data, but the “*tnp*” data structure has two neighbouring pores and gives different matrix size (see above). The “*tnp*” data structure can be extended to the same matrix size as the “*tnt*” data structure to tell by what pore the neighbouring throats are linked. Following the above example, this can be illustrated as:

$$tnp = \begin{bmatrix} \vdots & \cdot & \cdot & \cdot & \cdot & \cdot \\ 10 & 10 & 10 & 6 & 6 & 6 \\ \vdots & \cdot & \cdot & \cdot & \cdot & \cdot \end{bmatrix} \xleftarrow[6^{\text{th}} \text{ row}]{\longrightarrow} tnt = \begin{bmatrix} \vdots & \cdot & \cdot & \cdot & \cdot & \cdot \\ 20 & 10 & 19 & 16 & 2 & 17 \\ \vdots & \cdot & \cdot & \cdot & \cdot & \cdot \end{bmatrix}$$

2.2.2 Data Structure of Geometry in Boundary Layer

The boundary layer of the model is a diffusive gas layer between the top surface of the network and the bulk of air (see Figure 2.5). The average mass transfer coefficient of the boundary layer can be computed by Prandtl's relationship assuming that the network surface is a plate, the flow is laminar, and the boundary layer is fully developed. It holds:

$$Sh = 0.664 Re^{1/2} Sc^{1/3} \quad (2.1)$$

with Reynolds number $Re = uL_{tot}/\nu$, Schmidt number $Sc = \nu/\delta$ and Sherwood number $Sh = \beta L_{tot}/\delta$, where u is bulk fluid velocity, L_{tot} total length of the plate and ν kinematic fluid viscosity. Boundary layer thickness can then be calculated by:

$$\varepsilon = \frac{\delta}{\beta} \quad (2.2)$$

The boundary layer allows for lateral diffusion and defines the region into which the network needs to be extended by gas nodes. The vertical distance L' is adjusted so that the last row of nodes is on the edge of the boundary layer. These nodes are at bulk vapour pressure and will provide the boundary condition for the network drying model. The lateral transfer between two nodes in boundary layer is assumed as diffusive transfer between two finite cubic volumes by using length of the throats as depth of the network (L), as shown in Figure 2.5 (b).

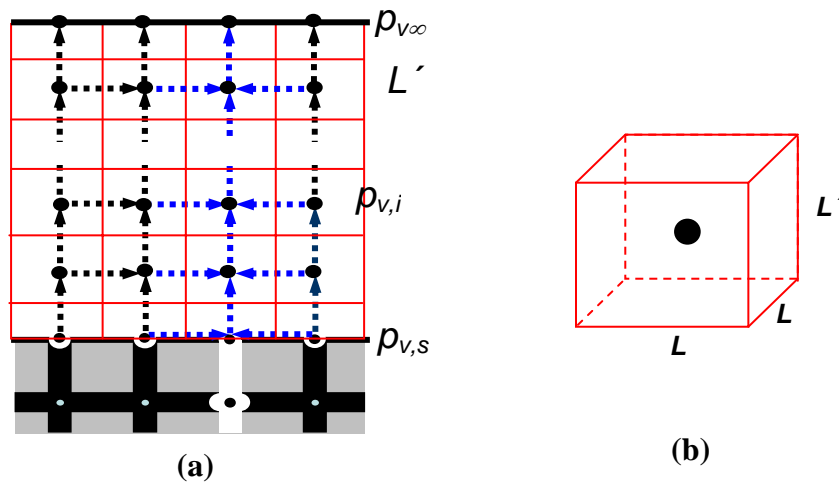


Figure 2.5: (a) Vapour transfer in the boundary layer and (b) node with associated finite volume.

In the latter case, it is necessary to define the cross section area of transfer between two finite volumes in the boundary layer. The cross section area of diffusive vapour transfer in the boundary layer of a 2D square network, as shown in Figure 2.6, can be distinguished into three types as follows:

- the cross section area for transfer between two nodes at the network surface is $0.5 \times L' \times L$ (these nodes belong to both network and boundary layer),
- the cross section area for horizontal transfer between two boundary layer nodes is $L' \times L$ and
- the cross section area for vertical transfer between two nodes is L^2 .

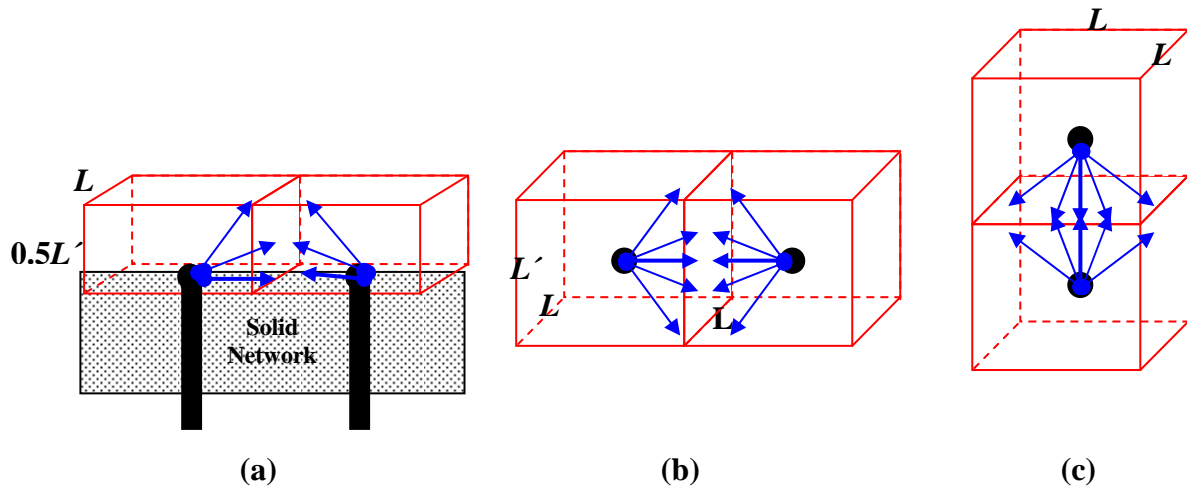


Figure 2.6: Different cases of exchange area for diffusive vapour transfer in boundary layer.

The data structures such as node location, node and connection number, “pnp”, “pnt”, “tnp” and “tnp” are also applied to the boundary layer. However, at the network surface they are differently generated because the nodes belong both to the network and boundary layer. If the nodes in boundary layer have lateral transfer as vapour diffusion, then the pores at the surface of the network have the same number of neighbouring pores as in the network. They are connected to two pores at the surface, one pore in network and one node in the boundary layer as shown in Figure 2.5.

If the vapour transfer in boundary layer is directly from the pores at network surface to the bulk of air, the pores at the network surface have two connections, one connection to bulk of air and one throat to the network (see Figure 2.7). Nevertheless, both the node in the bulk of air and the connection to it have no number because it is not needed for the drying algorithm, so that the boundary condition can be directly described. This model version corresponds to vapour diffusion in boundary layer without any lateral transfer.

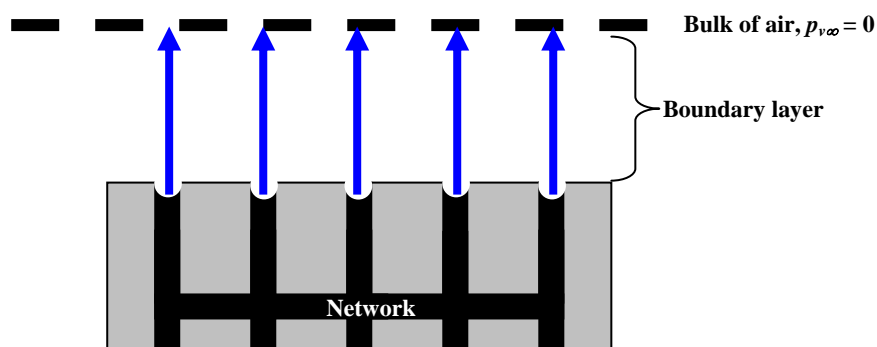


Figure 2.7: Direct connection of the network surface with the bulk of air.

2.2.3 Periodic Boundary Conditions

All research groups working on isothermal drying of pore networks had difficulties to investigate large networks as representative of porous media. Until now, the biggest size of network is 400 x 400 in 2D (Prat and Bouleux, 1999 [25]) and 80 x 80 x 80 in 3D (Yiotis et

al., 2006 [41]). The problem in modelling large networks is to find a computation tool that can solve big matrices in short time. In order to investigate large networks, the modelling in this work uses a periodic boundary condition by eliminating the border effect, so that the effective size of network is increased. Figure 2.8 shows the square network with periodic boundary condition.

In a periodic 2D square network, the throats on the right network boundary are connected to the pores on the left network boundary, allowing for lateral transfer. Due to the periodic boundary condition, the data structures at the right and left border must be rearranged, because they can now also have the maximum number of connections. The periodic boundary condition is also applied in the boundary layer.

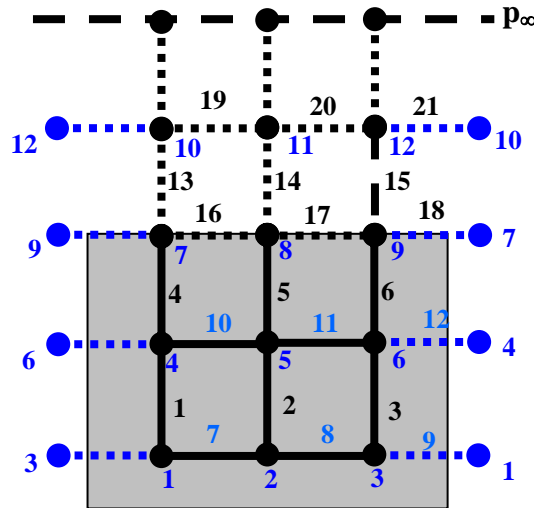


Figure 2.8: 2D square network with periodic boundary condition.

2.2.4 Algorithm to Generate Data Structures

The data structures of the model can be generated by using the correlations between them. The algorithm to generate the data structures for a 2D square network and boundary layer geometry is as follows:

1. Define pore positions in the network and boundary layer.
2. Generate the “pore neighbouring pores” matrix (“pnp”).
3. Define the throats by generating the “throat neighbouring pores” matrix (“tnp”).
4. Generate the “pore neighbouring throats” matrix (“pnt”) by combining the “tnp” and “pnp” data structures. The “tnp” data structure gives data of neighbouring pores of a throat and can help to get the entries of “pnt” using the “pnp” data structure.
5. The matrix “tnt” can be generated by combining the “pnt” and “tnp” data structures. The matrix “tnp” gives data of neighbouring pores of a throat, then one needs to look for their neighbouring throats in the “pnt” data structure.
6. The “tnp” data structure for labelling liquid cluster must have the same matrix size as the “tnt” data structure. Therefore the “tnp” data structure must be rearranged.

After that, the data structures can be applied in the drying calculation.

2.3 Drying Algorithm

Drying of porous media as complex fluid transport shall be observed at pore scale by pore network modelling. This part will describe how to construct an algorithm of pore network modelling describing the transport phenomena at the pore scale under isothermal conditions. Basics of the drying algorithm are definition of throat and pore saturation, labelling of liquid throat to know the throat members in one liquid cluster, and mass balances in liquid and vapour phase. Due to the transient character of the drying process, the time step must be defined to get the new state of throats and pores.

2.3.1 Throat and Pore Saturation

The network consists of throats that are connected by pores. The throats contain fluid and the pores are only nodes without volume. The throats as conductors between two pores (nodes) are to account for the mass fluxes that are caused by differences in state variables between two neighbouring pores. The variable that is assumed at the pore can be liquid or vapour pressure. The states of throats and pores must be defined before solving the vapour or liquid mass balances. The state of throat can be full, partially filled or empty and the states of pores are liquid and gas (filled). A gas pore can be either at equilibrium or at unknown vapour pressure. In reality, equilibrium vapour pressure prevails only at the meniscus (see Figure 2.9a), but in this model a pore is assumed to be at equilibrium vapour pressure if at least one of its neighbouring throats still has liquid in it, even if that throat is only partially filled (see Figure 2.9b). Therefore, the diffusion of vapour between menisci of partially filled throat and adjoining gas pore can happen without any resistance. This will lead to a slightly overestimated drying rate.

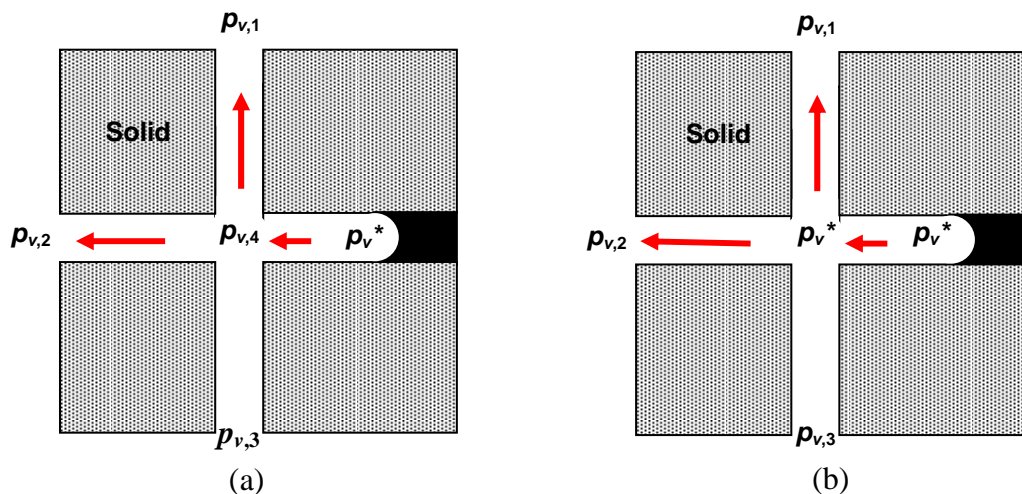


Figure 2.9: Position of equilibrium vapour pressure (a) real and (b) as assumed in this model.

Throat Saturation

Initially, the network is fully saturated by water and its full throats can be divided into two categories: full throats in the depth of network and at the surface of network. In the full throats in the depth of the network, liquid can flow by capillary pressure difference. The full throats at the surface have a vapour-liquid interface that forms a meniscus. The meniscus at this throat can move by evaporation. During drying, the full throat in the depth of the

network can have a meniscus if at least one of the neighbouring pores has already been invaded by gas and is an equilibrium gas pore as shown in Figure 2.10b. Those throats are cluster meniscus throats (*CMT*) that can be invaded by gas to be emptied. If both neighbouring pores are at equilibrium vapour pressure, the throat is a single meniscus throat (*SMT*) as shown in Figure 2.10c. This means that the liquid-filled throat is not connected to other liquid filled throats.

Due to evaporation at the network surface, the full throat will be changed to a partially filled throat that contains a vapour-air mixture and liquid water (see Figure 2.10d). The fluid transport is by capillary flow due to liquid pressure differences and by vapour diffusion due to vapour pressure differences. According to the assumption for equilibrium vapour pressure, the vapour diffusion in this throat happens without resistance. A partially filled throat can also hold two back-to-back menisci when both neighbouring pores are gas pores (see Figure 2.10e). The positions of these two menisci are assumed to be symmetric. These menisci will finally coalesce by evaporation on both sides.

If the meniscus in full or in partially filled throats moves continuously by capillary flow or evaporation, those throats will be empty at some time. The empty throats can be distinguished into three types. At first, if all neighbouring pores are at equilibrium vapour pressure, this throat is assumed to have no vapour transfer (Figure 2.10f). The second type of empty throats has one equilibrium vapour pressure in one neighbouring pore. The vapour diffusion in this throat is due to the difference in vapour pressure (Figure 2.10g). The last type of empty throat has both neighbouring pores at unknown vapour pressure and in this case vapour diffusion is due to difference of both vapour pressures (Figure 2.10h).

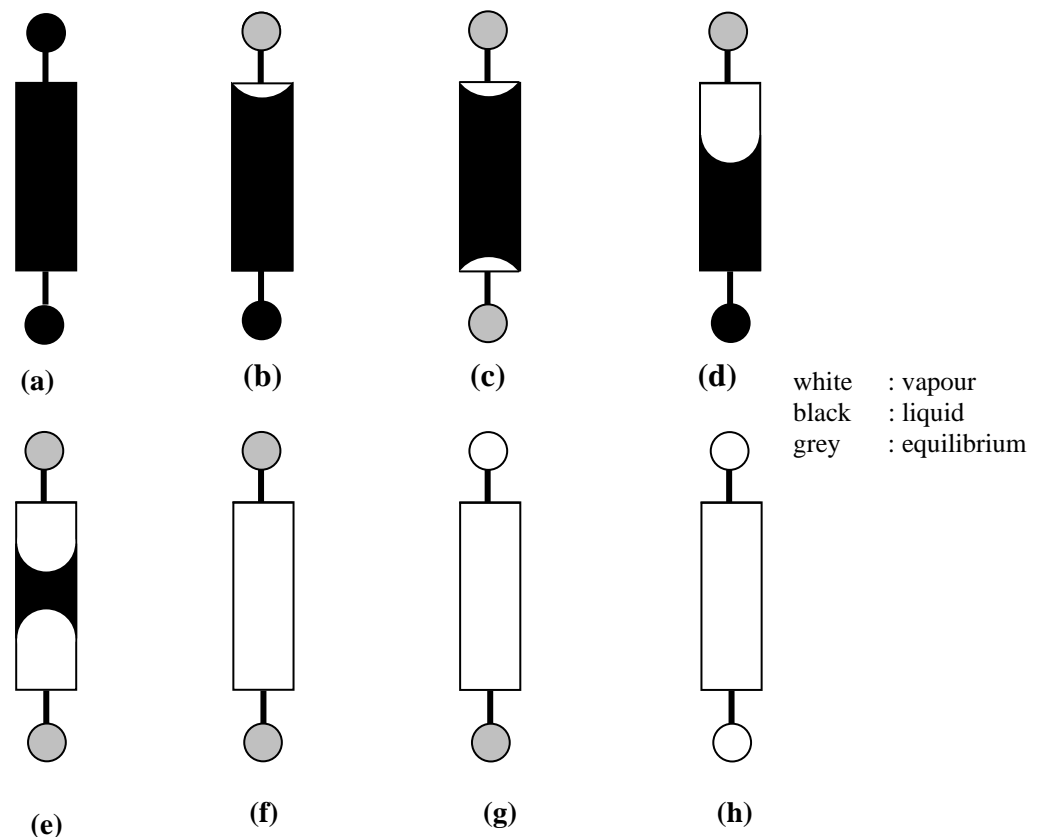


Figure 2.10: State of the throats: (a) - (c) full throat; (d) - (e) partially filled throat; (f) - (h) empty throat.

Pore Saturation

The pore as node is assumed as pressure place, although the pore does not contain fluid. The state of a pore depends on the state of its neighbouring throats. A pore is considered as liquid pore if all neighbouring throats are filled by liquid (see Figure 2.11a), even if they are only partially filled, as shown in Figure 2.11b and c. The liquid pressure in the liquid pore can be computed from liquid mass balances.

A pore is considered as gas pore if at least one of the neighbouring throats is an empty throat. Gas pores can be distinguished into two types, either they are at equilibrium or at unknown vapour pressure. The pore is assumed as equilibrium gas pore if at least one of its neighbouring throats is a (partially) filled throat (see in Figure 2.11d - g). The gas pore at equilibrium vapour pressure gives the boundary condition for vapour mass balances.

The gas pore is assumed at unknown vapour pressure if all neighbouring throats are empty throats, as shown in Figure 2.11h and i. Vapour pressure in the pore must be calculated by vapour mass balances. The transport of vapour between this pore and its neighbouring pores is by diffusion.

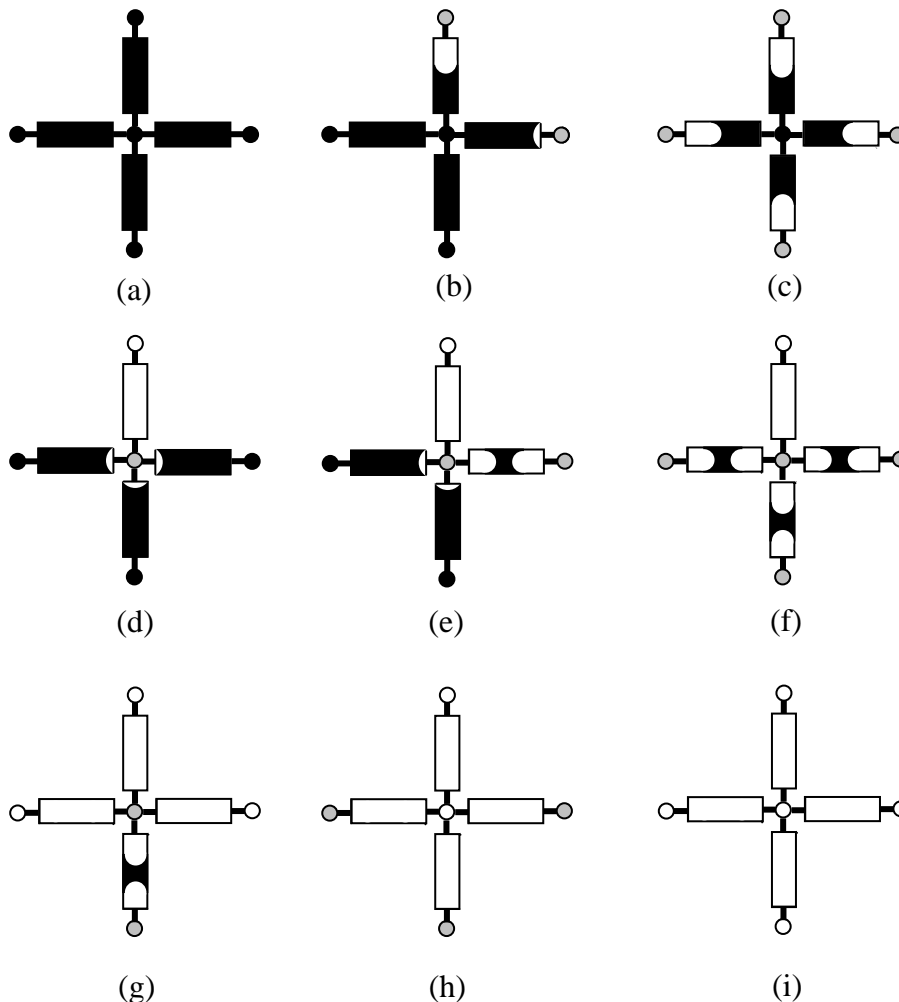


Figure 2.11: Examples of state of pores : vapour (white), liquid (black) and equilibrium (grey); state of central pore : (a) - (c) liquid pore; (d) - (g) gas pore at equilibrium vapour pressure ; (h) - (i) gas pore at unknown vapour pressure.

2.3.2 Drying Kinetics

This section is dealing with the drying kinetics, investigated at the pore scale of a network. The mass balance in liquid and vapour shall be introduced. Then, the time step of modelling is discussed. Drying as necessary process in industry is very energy consuming. Nevertheless, this model will be under isothermal condition, so that temperature at all positions in the network is homogenous at 20°C. Naturally, drying is never a truly isothermal process, since evaporation of liquid cannot occur without transfer of energy. The purpose of this modelling is, however, to understand fluid transport mechanisms at pore scale during drying. Consequently, this model only describes mass transfer caused by liquid or vapour pressure differences.

Liquid Mass Balance

The liquid flow as capillary flow in the liquid phase in the throats can be calculated from liquid pressure differences between neighbouring pores. The liquid pressure is computed by Poiseuille's law by assuming the throat to be a cylindrical tube. The sum of all liquid flows to one pore must be equal to zero. This liquid mass balance is given by:

$$\sum_j \dot{M}_{w,k} = \sum_j \frac{\pi r_k^4}{8\nu_w L_{w,k}} (p_{w,i} - p_{w,j}) = 0 \quad (2.3)$$

where i is the index for the liquid pore, j the index for its neighbouring pores ("pnp"), k is the index for the throat between pores i and j , r_k radius of throat k , ν_w kinematic viscosity of liquid water and $L_{w,k}$ liquid length of throat k ($L_{w,k} = 1$ for full throat and $0 < L_{w,k} < 1$ for partially filled throat). Equation (2.3) can be converted by definition of conductance:

$$G_{w,k} = \frac{\pi r_k^4}{8\nu_w L_{w,k}} \quad (2.4)$$

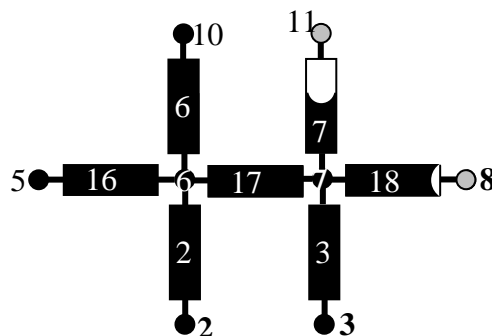


Figure 2.12: Liquid mass balance with menisci in neighbouring throats (for the numbering of pore and throat refer to Figure 2.2).

$$x = \begin{pmatrix} p_w \\ \cdot \\ \cdot \\ p_{w,6} \\ p_{w,7} \\ \cdot \\ \cdot \\ \cdot \end{pmatrix} \quad b = \begin{pmatrix} \vdots \\ 0 \\ (G_{w,7} p_{m,7} - M_{ev,18}) \\ \vdots \end{pmatrix}$$

Vapour Mass Balances

The gas pores can be divided into two types: equilibrium and unknown vapour pressure pores (refer to pore saturation). The equilibrium vapour pressure is defined as saturation pressure of water at 20°C. If the pore has unknown vapour pressure, it must be calculated by vapour mass balances according to Stefan flow equation.

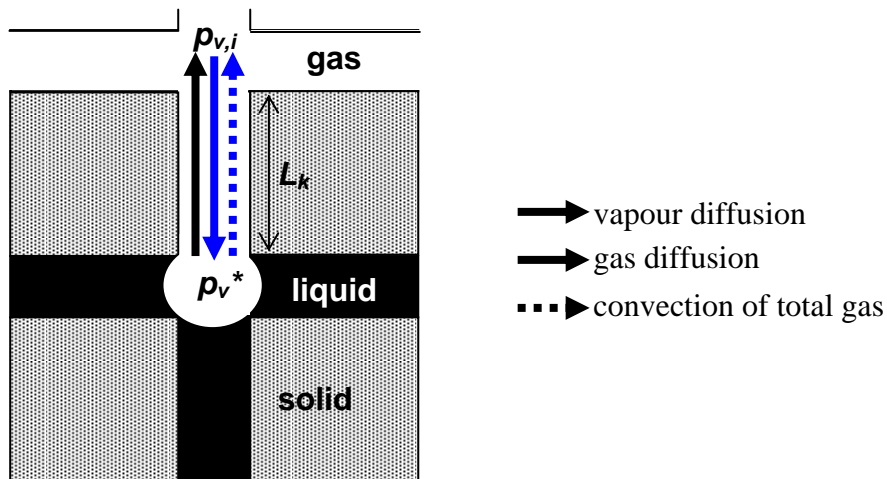


Figure 2.13: Convective Stefan flow in a gas throat.

In the following p_v^* is equilibrium vapour pressure, $p_{v,i}$ unknown vapour pressure, L_k length of throat, p total gas pressure and $\tilde{y} = \frac{p_v}{p}$ molar vapour fraction.

The Stefan effect means that the diffusion of air molecules is balanced by convective flow \dot{N}^{conv} of total gas (see in Figure 2.13) and, as a result, air molecules are immobile (meniscus is impermeable for them). Some assumptions of the Stefan effect are:

1. equimolar diffusion between vapour and air

$$\dot{N}_a^{\text{diff}} = -\dot{N}_v^{\text{diff}} \quad (2.9)$$

2. total molar flow rate of vapour

$$\dot{N}_v = \dot{N}_v^{diff} + \tilde{y}\dot{N}^{conv} \quad (2.10)$$

3. molar flow rate of air

$$\dot{N}_a = \dot{N}_a^{diff} + (1 - \tilde{y})\dot{N}^{conv} = 0 \quad (2.11)$$

By combining these equations and using Fick's law:

$$\dot{N}_v^{diff} = -nA\delta_{va}\frac{\partial\tilde{y}}{\partial z} \quad (2.12)$$

a differential equation is obtained, which can be solved by separation of variables and integration of molar fraction of vapour and length of throat so that the molar flow rate of vapour is:

$$\dot{N}_v = n_g A_k \frac{\delta_{va}}{L_k} \ln\left(\frac{1 - \tilde{y}_i}{1 - \tilde{y}^*}\right) \quad (2.13)$$

where n_g is molar density of gas.

The equation of evaporation at meniscus throats can be expressed as a function of pressure and changed into mass flow rate:

$$\dot{M}_{ev,k} = A_k \frac{\delta_{va}}{L_k} \frac{p\tilde{M}_v}{\tilde{R}T} \ln\left(\frac{p - p_{v,i}}{p - p_v^*}\right) \quad (2.14)$$

where $A_k = \pi r_k^2$ is the cross sectional area, δ_{va} the diffusion coefficient of vapour in air, \tilde{M}_v molar mass of vapour, \tilde{R} universal gas constant and T absolute temperature.

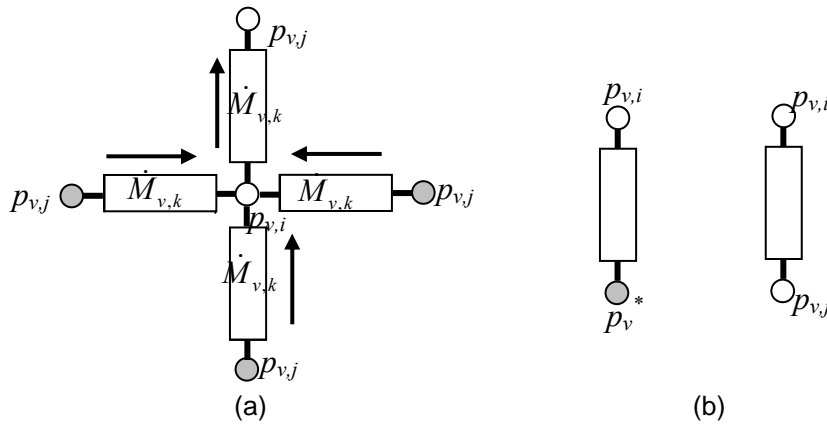


Figure 2.14: (a) Vapour mass balance with equilibrium neighbouring pores and (b) two possible conditions of vapour diffusion in the throat (grey color is for equilibrium vapour pressure and white color is for unknown vapour pressure).

Stefan effect according to Eq. (2.14) can be also applied to vapour diffusion in throats without convection because the air is practically immobile throughout the network. The drying process is assumed as quasi-steady so that the vapour mass balance does not have accumulation of vapour. The unknown vapour pressure in a gas pore can be solved by vapour mass balance (as shown in Figure 2.14a):

$$\sum_j \dot{M}_{v,k} = \sum_j A_k \frac{\delta_{va}}{L_k} \frac{p\tilde{M}_v}{\tilde{R}T} \cdot \ln\left(\frac{p - p_{v,i}}{p - p_{v,j}}\right) = 0 \quad (2.15)$$

where i is the index of a pore at unknown vapour pressure and j the indices for neighbouring pores that can be at unknown or equilibrium vapour pressure, p_v^* , k the index of the throat between pore i and j , $\dot{M}_{v,k}$ diffusive vapour mass flow rate in throat k . The sum is over all neighbouring gas nodes that are connected by an empty throat as vapour diffusion. In order to calculate vapour pressure, those equations must be converted to a linear system by switching from $p_{v,i}$ to the variable $x_{v,i} = \ln(1 - p_{v,i}/p)$:

$$\sum_j \dot{M}_{v,k} = \sum_j G_{v,k} \cdot (x_{v,i} - x_{v,j}) = 0 \quad (2.16)$$

and throat conductance $G_{v,k} = \pi r_k^2 \frac{\delta_{va}}{L_k} \frac{p\tilde{M}_v}{\tilde{R}T}$

Eq. (2.16) is converted to the linear system $Ax = b$, where A is term of conductance of neighbouring throat of unknown vapour pressure, x unknown vapour pressures as logarithmic expression and b boundary condition. Boundary condition in vapour mass balance is given by all neighbouring equilibrium vapour pores with indices j in Eq. (2.15) (see grey colour in Figure 2.14).

Vapour Diffusion

The partial vapour pressures that solve the vapour mass balance are used to calculate vapour diffusion between two pores. The vapour diffusion in empty throats is caused by different vapour pressure between the two pores (see Figure 2.14). Initially, vapour diffusion only takes place in the boundary layer because at the beginning the network is fully saturated with water. After emptying one of the throats at the network surface, vapour diffusion also occurs in the network. The diffusive vapour mass flow rate in an empty throat is:

$$\dot{M}_{v,k} = A_k \frac{\delta_{va}}{L_k} \frac{p\tilde{M}_v}{\tilde{R}T} \ln\left(\frac{p - p_{v,i}}{p - p_{v,j}}\right) \quad (2.17)$$

In the boundary layer, the vapour diffusion between two nodes is described by Eq. (2.17) with an adjusted cross sectional area A_k . The different cross section areas in the boundary layer are given in Figure 2.6.

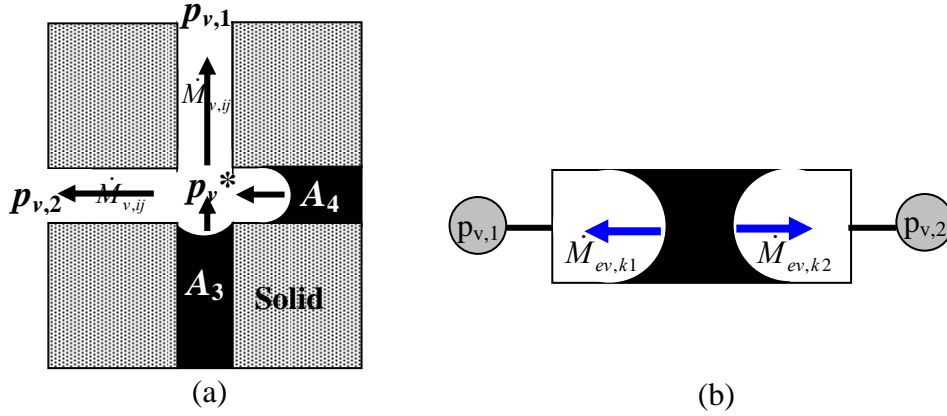


Figure 2.15: (a) Vapour diffusion in the empty throat and evaporation at the menisci
(b) evaporation in the single throat.

If one pore has several menisci in its neighbouring throats, the evaporation rates are according to their cross section area, A_k . In the vapour mass balance as shown in Figure 2.15a, total evaporation, produced from meniscus throats 3 and 4, is equal to the total vapour diffusion flow at the empty throats 1 and 2. The evaporation rate from meniscus neighbour throat k of pore i can be computed from:

$$\dot{M}_{ev,k} = \frac{A_k}{A_{tot,i}} \sum_k \dot{M}_{v,k} \quad (2.18)$$

where A_k is cross section area of the meniscus throat k , $A_{tot,i} = \sum_k A_k$ total cross section area of menisci throat at the pore i , $\sum_k \dot{M}_{v,k}$ total vapour flow away from menisci through the neighbouring gas throats.

A single throat has two neighbouring gas pores and may hold two menisci back-to-back that come together. The menisci are assumed to meet in the middle of the throat as the throat dries out. In such a single throat, as shown in Figure 2.15b, evaporation may take place at both menisci and then vapour moves to the neighbouring pores 1 and 2. The formula to calculate total evaporation rate for the single throat is:

$$\dot{M}_{ev,k} = \dot{M}_{ev,k1} + \dot{M}_{ev,k2} \quad (2.19)$$

Vapour produced by evaporation at the menisci throat will be transferred through the empty throats in network and boundary layer by vapour diffusion. Total vapour flow to the bulk of air is total evaporation rate of drying (see Figure 2.16). Due to the quasi steady condition, that evaporation rate is equal with total evaporation rate from all meniscus throats in the network. The total evaporation rate of every time step is calculated by summing up all vapour diffusion rates to the bulk of air:

$$\dot{M}_{ev,t} = \sum_i \dot{M}_{v,k} \quad (2.20)$$

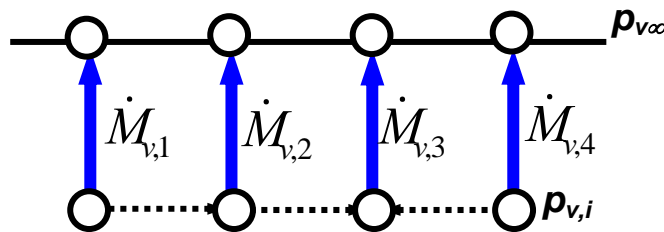


Figure 2.16: Total evaporation rate of network or drying rate.

2.3.3 Time Step for Negligible Viscosity

In case of negligible viscosity, only the menisci in the largest throats of the clusters move and other menisci are stationary, because the liquid flow from the largest throat gives high capillary flow, which is assumed enough to distribute the liquid to all meniscus throats with their local evaporation rates as shown in Figure 2.17.

The total evaporation rate in one cluster is the sum of all evaporation rates at the meniscus throats in this cluster. Now, it is assumed that only one throat is emptied during every time step and that this is the largest meniscus throat in each cluster. The time needed to empty the largest throat in one cluster, Δt_p , can be calculated by following formula:

$$\Delta t_p = \frac{V_{k,p}}{\dot{M}_{ev,p}} \quad (2.21)$$

where $V_{k,p}$ is liquid volume of largest throat of cluster p at that time and $\dot{M}_{ev,p}$ total evaporation rate of cluster p . Due to evaporation rate in single throats, that throats can also empty preferentially. The time to empty a single throat, Δt_k , is:

$$\Delta t_k = \frac{V_k}{\dot{M}_{ev,k}} \quad (2.22)$$

The time step of drying in case of negligible viscosity is chosen as the minimum value of all times ($\Delta t_p, \Delta t_k$). This time step is applied to update the saturation of pores and throats to get new conditions such as liquid flow conductivities, new candidate throats for emptying and boundary conditions for liquid and vapour mass balances.

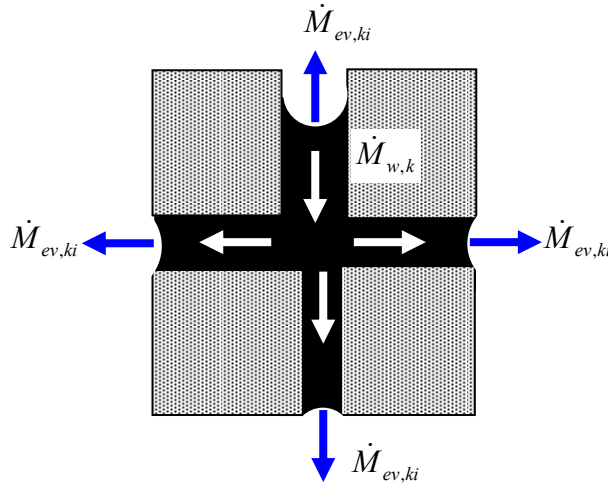


Figure 2.17: Evaporation and liquid flow in one cluster.

2.3.4 Liquid Cluster Labelling

Initially, the network is fully saturated with liquid. This condition is considered as one cluster of liquid phase. Due to random emptying of throat and pore, pore connections will be cut off and new clusters will be created. Naturally, capillary flow can only occur between pores

which are part of the same liquid cluster so that cluster labelling is an essential step of the drying model. The liquid filled throats are labelled according to their cluster affiliation using the Hoshen-Kopelman (HK) algorithm. The HK-algorithm in this model is based on the variant of Al-Futaisi and Patzek (2003, [1]).

Hoshen-Kopelman Algorithm

The HK-algorithm needs the geometric data structures and the saturation of pores and throats to label the liquid throats in the network. Those data structures are throat and pore numbers and the neighbouring relationships between throats and pores. The HK-algorithm in the present network model labels only the throats because only they contain liquid water. Firstly, the throat saturation must be defined and empty throats as well as single throats (SMT) are not labelled. The partially filled and full throats that are connected to liquid pores will be given a label.

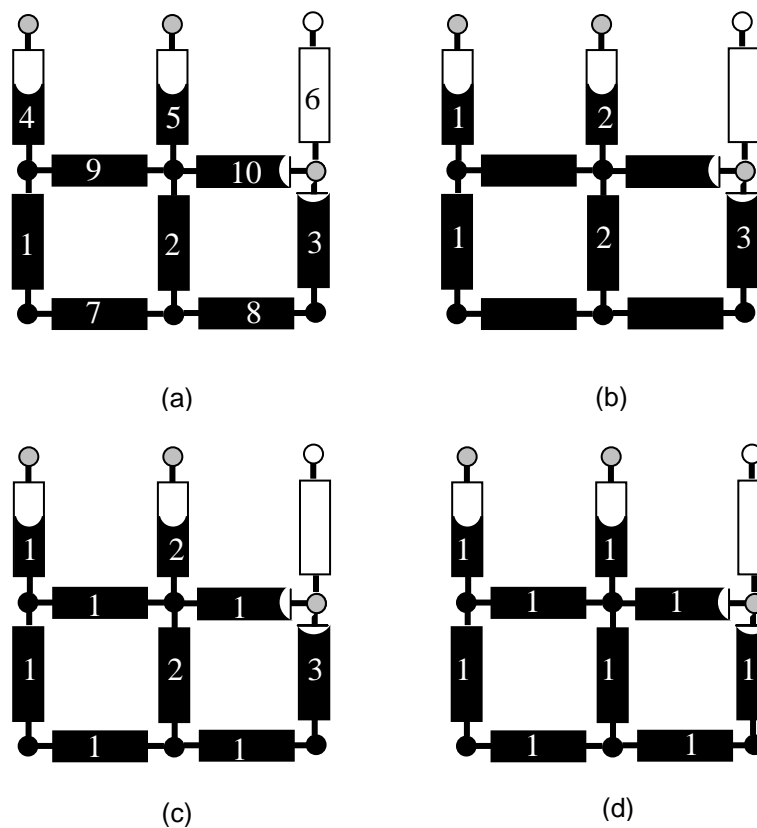


Figure 2.18: Order of throat labelling (a) throat numbers, (b) throat labels after scanning all vertical throats, (c) throat labels after scanning all throats and (d) throat label after label correction ("tl").

At the beginning, all liquid throats (partially filled and full) are scanned and then the neighbours (throat and pore) of every throat are checked. If the throat and a neighbour throat are connected by a liquid pore, they are members of the same cluster. The throats are scanned starting from vertical throat direction and continuing with horizontal throat direction. The labels of throats are stored to the matrix "tl" and data of the cluster numbers are stored in the matrix "tlp". During the scanning of the throats, the cluster number of throat in matrix "tl" does not change. The cluster number of throat in matrix "tl" refers to the matrix "tlp". Only matrix "tlp", containing data of cluster number, will be changed during labelling. Figure 2.18 shows a simple network for labelling the throats. The label of throat can be defined in two ways, which will be outlined in the following, starting with the simpler one:

1. If, for the current throat, none of the neighbouring throats is labelled, then give a new cluster label to this throat. The throat label is saved in the matrix array of throat labels (“tl”) and the cluster number in the matrix array “tlp”. After scanning all vertical throats in a simple network (see Figure 2.18), the “tl” and “tlp” data are $tl = [1\ 2\ 3\ 1\ 2\ 0\ 0\ 0\ 0\ 0]$ and $tlp = [1\ 2\ 3]$ (see Figure 2.18b). Throat numbers 1, 2 and 3 are examples of throat starting a new cluster.
2. If an already labelled neighbour exists, then set the throat label equal to the minimum throat label of the neighbouring throats. The throat number 7 has two labels (1, 2) of neighbouring throats so that the label number of throat 7 is 1 as minimum of neighbouring throat labels. After scanning all throats in a simple network, the data $tl = [1\ 2\ 3\ 1\ 2\ 1\ 1\ 1\ 1\ 0]$ and $tlp = [1\ 1\ 1]$ are obtained (see Figure 2.18c).
3. After all of the occupied throats have been labelled with a cluster number, these labels (“tl”) must be corrected by use “tlp”.

In a large network, updating of the cluster labels is more complicated due to many connections, i.e. a throat connects with its neighbouring throats and the neighbouring throats connect to their own neighbouring throats. In order to get the true minimum value of cluster number, updating of cluster number must be repeated until the cluster number is surely the minimum value. Figure 2.19a shows an example of a partially saturated 2D square network with throat numbers that will be labelled. Al-Futaisi and Patzek (2003, [1]) described their algorithm to update the cluster label (“tlp”) in the following way:

1. After completing the scan of all vertical throats, the array of cluster labels is

$$tlp = [1\ 2\ 3\ 4\ 5]$$

2. The horizontal throats start to be scanned. After the neighbouring horizontal throat has been labelled, the horizontal throats should be labelled again to the minimum value of cluster label (“tlp”) of its neighbouring throats (see in Figure 2.19b). These horizontal throats are connections of vertical throats so that the cluster number (“tlp”) should be also updated to the minimum value of cluster number of its neighbouring throats. For example:
 - when throat 53 is labelled, then label “3” changes to label “2” and label “4” changes to label “2” ($tlp = [1\ 2\ 2\ 2\ 5]$),
 - when throat 56 is labelled, then label “5” changes to label “1” ($tlp = [1\ 2\ 2\ 2\ 1]$),
 - when throat 57 is labelled, then label “3” changes to label “1” ($tlp = [1\ 2\ 1\ 2\ 1]$).

At the end of scanning, number of clusters (“tlp”) is 2 as shown in Figure 2.19b. This labelling of liquid clusters gives the wrong number of clusters. The wrong step by Al-Futaisi and Patzek algorithm is in changing the label when one throat is scanned and there exists a labelled neighbour. When throat 53 is labelled, the updating is only done to its neighbouring throats, although these throats are still connected to further neighbouring throats which have other minimum cluster number, which means that Al-Futaisi and Patzek did not perform a real update. Therefore, the cluster number (“tlp”) is not the true minimum value of cluster label.

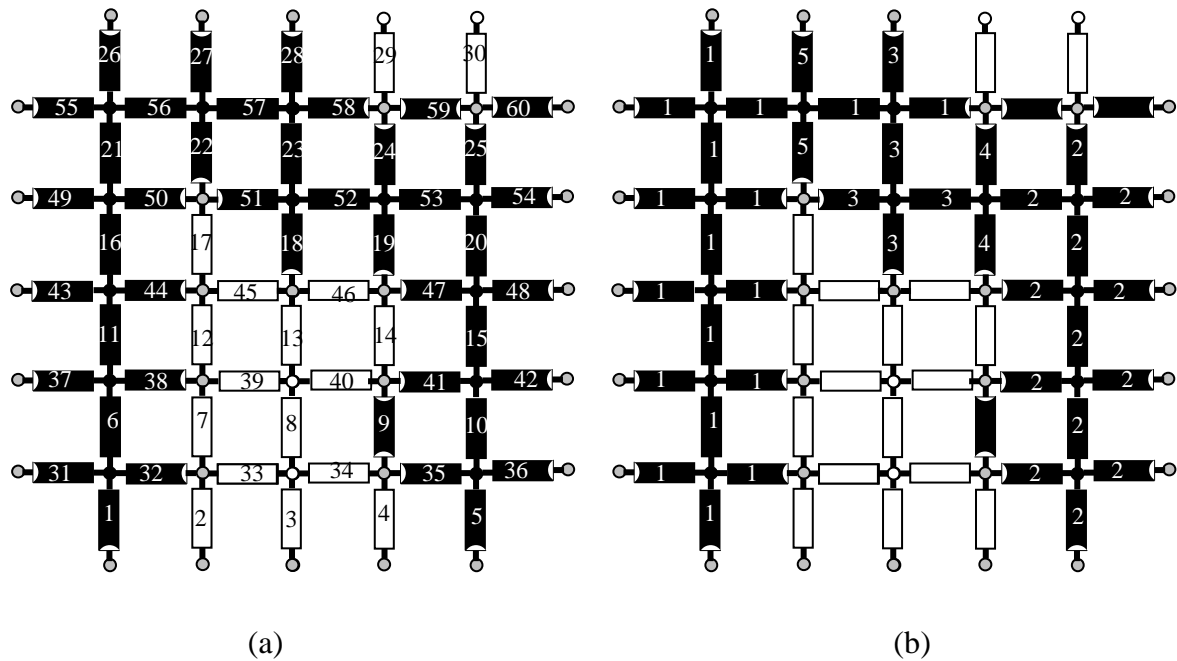


Figure 2.19: Liquid labeling of 2D square network (a) throat number
(b) throat labels before correction.

To avoid the error of the algorithm by Al-Futaisi and Patzek, a modification is done by repeating the change of throat labels until the true minimum throat number is obtained (Metzger et al., 2006 [19]), as follows:

- when throat 53 is labelled, label “3” changes to label “2” and label “4” to label “2”. Check previous label number of label “3” and “4”, those are still original (3 and 4, $tlp = [1\ 2\ 2\ 2\ 5]$),
- when throat 56 is labelled, then label “5” changes to label “1” ($tlp = [1\ 2\ 2\ 2\ 1]$), previous label “5” is still original,
- when throat 57 is labelled, label “3” changes to label “1” ($tlp = [1\ 2\ 1\ 2\ 1]$), previous label “3” has already been corrected to “2”, so label “2” changes to label “1”. Now, it is:

$$tlp = [1\ 1\ 1\ 2\ 1].$$

At the end, the data of “ tlp ” is used to relabel the throat label (“ tl ”) so that all liquid throats are correctly identified as members of one cluster.

During drying, liquid throats will empty by evaporation, so that the throats must be labelled according to the new condition. Not all liquid throats should be scanned, only members of the cluster in which a throat emptied. In a square network, when one throat of a cluster is emptied, maximally three new clusters can be created. Figure 2.20a shows a partially saturated square network with throat labels (white throats being empty, black throats filled with liquid). After emptying the throat 18, the cluster of this throat splits up into two clusters (see in Figure 2.20b). Then, all throat members of the cluster in which the throat emptied must be scanned. The throat members of the cluster in which a throat emptied will be renumbered, starting from old total cluster number (2). Finally, the total cluster number is 3 as shown in Figure 2.20b.

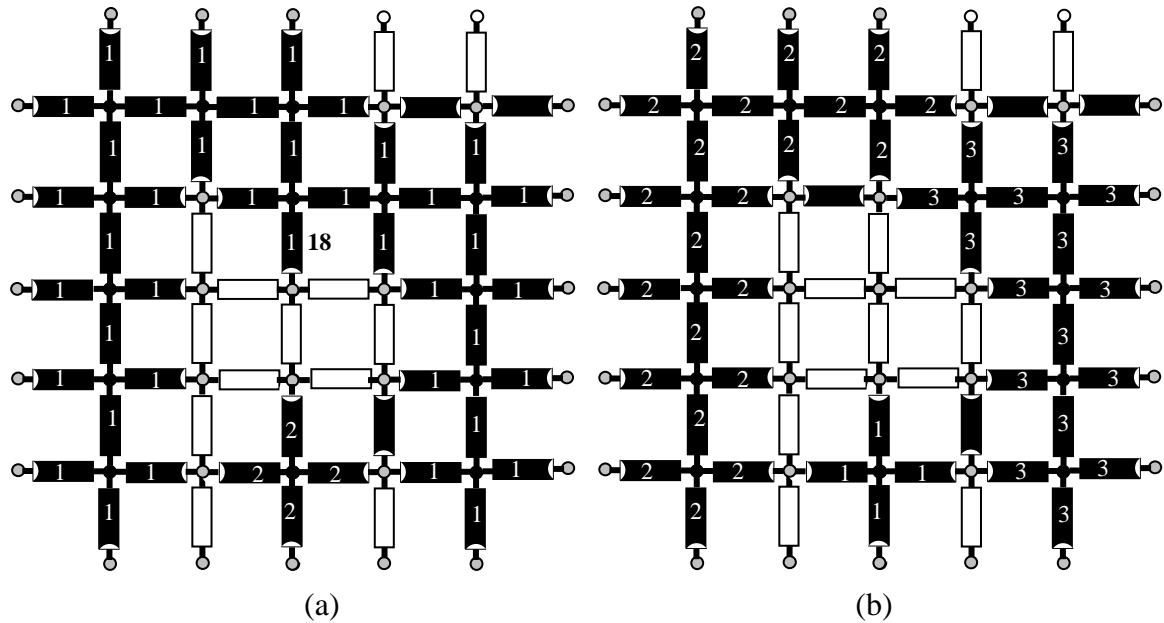


Figure 2.20: 2D square network with throat labels (a) before and (b) after emptying one throat (18).

Each cluster has meniscus throats where liquid can be evaporated. These menisci can be stationary if liquid is supplied from moving meniscus throats. But, there are also trapped clusters, in which liquid at menisci can not be evaporated because all their neighbouring pores are at equilibrium vapour pressure, as shown in Figure 2.21. Therefore, liquid can not flow, so that the liquid pressure for such a trapped cluster is not calculated in the linear system of liquid mass balances.

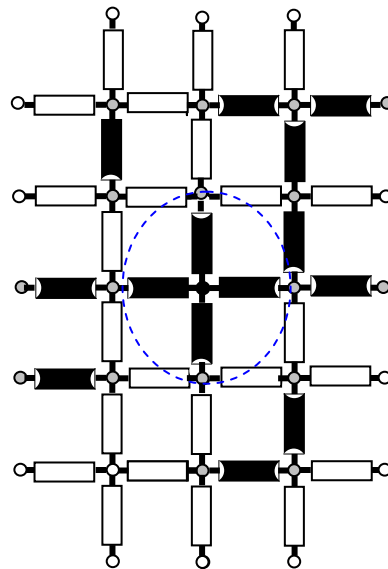


Figure 2.21: Trapped cluster in 2D square network.

2.3.5 Viscous Effect in Liquid Phase

In case of negligible viscosity, the liquid flow from the largest meniscus throat is assumed to be enough to keep the other menisci stationary. Large throat radii (in micro meter) were applied in case of negligible viscosity in order to be sure that capillary forces always

dominate over friction forces. In this section, viscous effects are included in the liquid phase, but not in the gas phase, assuming constant total gas pressure. In order to investigate viscous effect in liquid phase, smaller throat radii (nano meter), r_k , are used because smaller throats have higher pressure drop defined by following equation:

$$\Delta p_{f,k} = 8\nu_w \frac{\dot{M}_{ev,k} L_{w,k}}{\pi r_k^4} \quad (2.23)$$

where ν_w is kinematic viscosity of water, $\dot{M}_{ev,k}$ evaporation rate at the meniscus, $L_{w,k}$ liquid length of throat. Due to the high friction, the capillary flow from the biggest throat in the cluster is not always enough to distribute the liquid to other meniscus throats. All menisci cluster throats (*MCT*) must be defined as stationary or moving menisci by comparing evaporation rate and liquid flow rate of that throat, because each type has a different boundary condition. The boundary condition of stationary *MCT* is the evaporation rate at the menisci ($\dot{M}_{ev,k}$) while pressure at the menisci ($p_{m,k}$) is the boundary condition of moving menisci.

The classification of throats is based on comparison of liquid flow rate $\dot{M}_{w,k}$ and evaporation rate $\dot{M}_{ev,k}$. Types of menisci cluster throats (*MCT*) in 2D square network are:

- **Full throat with stationary meniscus** if liquid flow is provided by capillary pressure difference at least at the rate at which water evaporates. The meniscus will remain at the end position, and the boundary condition of stationary meniscus is given by the evaporation rate at the meniscus (see Figure 2.22a).
- **Full or partially filled throat with moving emptying meniscus** if liquid flow by capillary pressure difference is lower than evaporation rate or the direction of liquid flow is opposite to evaporation rate. The meniscus will move to empty the throat, and the boundary condition of moving meniscus is given by pressure at the meniscus (see Figure 2.22b).
- **Partially filled throat with moving filling meniscus** if liquid flow by capillary pressure difference is higher than evaporation rate. Meniscus will move to fill the throat, and the boundary condition of moving meniscus is given by pressure at the meniscus (see Figure 2.22c).

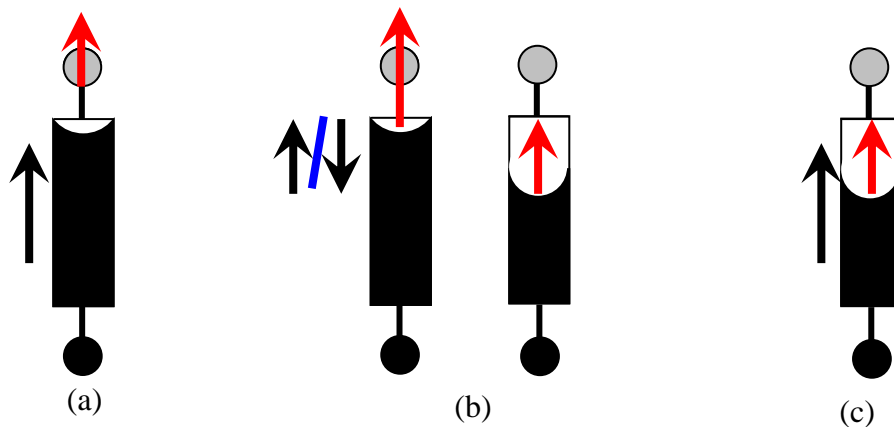


Figure 2.22: Types of menisci cluster throats (*MCT*) (a) stationary meniscus; (b) emptying moving menisci (c) filling moving menisci.

These boundary conditions must be found iteratively because the liquid flow and boundary condition of liquid flow depend on each other. Two approaches can be applied to find the correct boundary conditions and solve the liquid mass balance (Irawan et al., 2006 [11]). In the first approach, initially all full *MCT* are assumed to have moving menisci, and in the second one, all full *MCT* are assumed to have stationary menisci except of the biggest throat in every cluster. For partially filled *MCT*, both approaches are assumed to have moving menisci be emptying or filling. Subsequently, the type of throat is corrected until the same unique set of boundary conditions is found in both approaches. Figure 2.23 shows a simple cluster to find the boundary conditions by the mentioned two approaches.

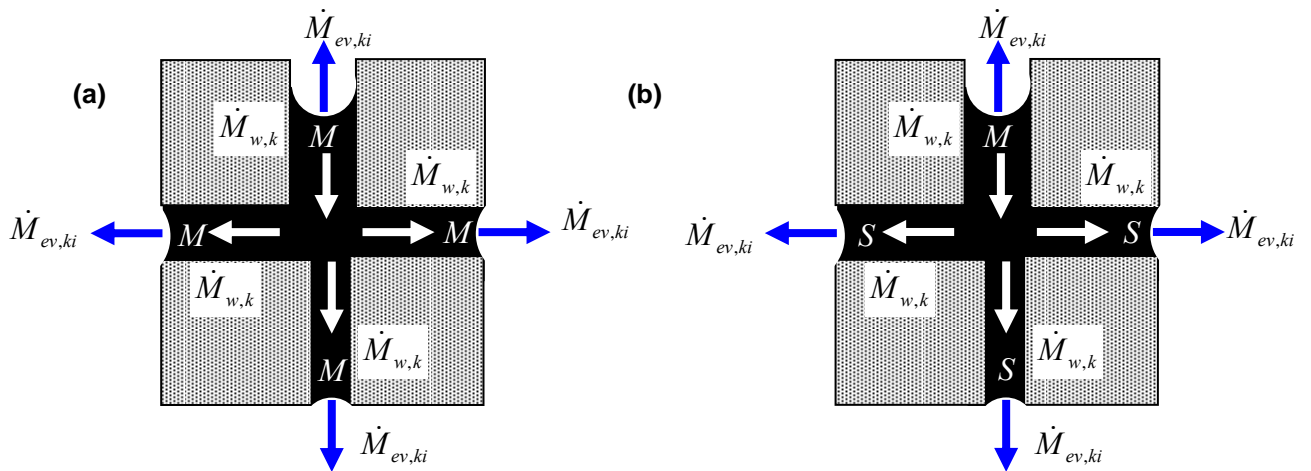


Figure 2.23: Simple cluster of 2D square network: Initial assumption of (a) first approach and (b) second approach to find boundary conditions of liquid mass balance (M = moving meniscus and S = stationary meniscus).

First approach to find boundary conditions of liquid mass balance

Initially, all meniscus throats in *MCT* are assumed as moving menisci (M) throats with pressure at the menisci as the boundary condition. The liquid flow rates $\dot{M}_{w,k}$ are obtained from liquid mass balances, and the liquid flow rate in each meniscus throat is compared with the evaporation rate at meniscus $\dot{M}_{ev,k}$. If liquid flow can pump enough liquid to the meniscus ($\dot{M}_{ev,k} < \dot{M}_{w,k}$), the boundary condition in this meniscus throat must be corrected to the evaporation rate $\dot{M}_{ev,k}$ (stationary menisci, S). In case of an M meniscus throat changing to S meniscus throat, the pressure in the liquid cluster rises. Therefore, all moving menisci with $\dot{M}_{ev,k} < \dot{M}_{w,k}$ must be changed to stationary menisci. Then, the liquid mass balances must be solved again with new boundary condition. This iteration will be stopped when no moving menisci in *MCT* need correction, which means that the correct boundary condition has been found. The algorithm of this approach can be seen in Figure 2.24.

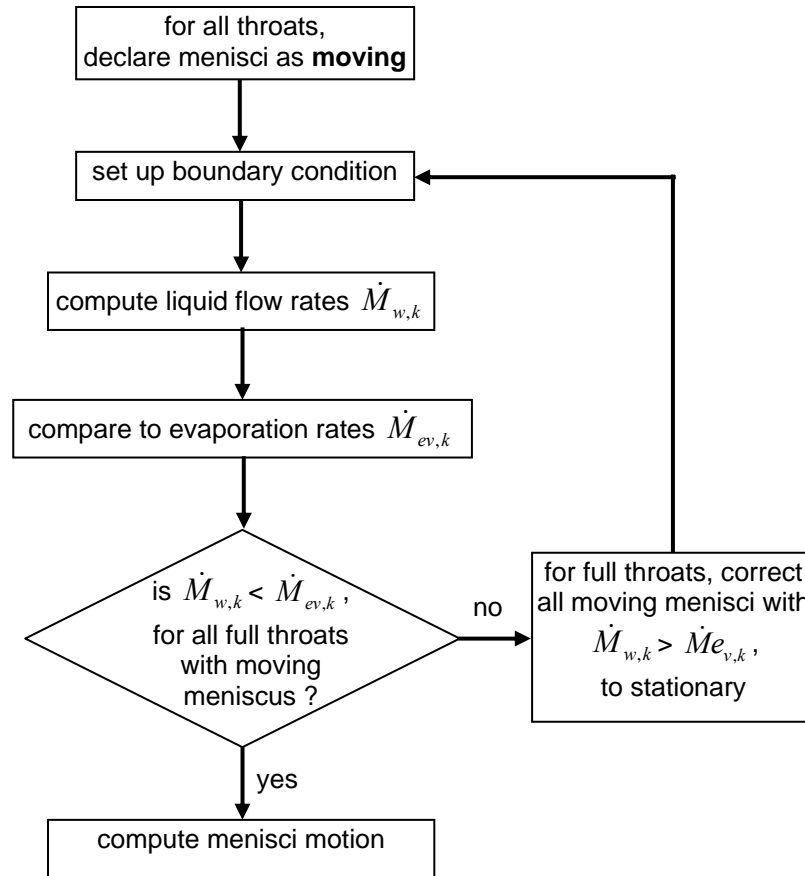


Figure 2.24: Algorithm to find boundary condition of liquid mass balances with first approach.

Second approach to find boundary condition of liquid mass balance

Initially, all full *MCT* are assumed to be stationary except of the largest throat that has the highest pressure in the cluster. From this, the liquid pressure field can be computed by liquid mass balances and then the local pressure required to provide enough liquid, p_k^{req} , can be calculated. If this pressure is compared to the pressure at the meniscus, one will find that some of the menisci can not provide enough pressure for pumping the liquid at evaporation rates $\dot{M}_{ev,k}$. Therefore, the state of full *MCT* must be corrected to avoid contradiction, so that every meniscus that is assumed to be stationary must indeed have a capillary pressure strong enough to provide the liquid at the evaporation rate.

If one stationary meniscus boundary condition is corrected to moving meniscus, then the liquid pressure field in this cluster rises. Therefore, it may not be necessary to correct all menisci which initially failed the check, but conduct a stepwise correction. The menisci having the largest discrepancy between required pressure, p_k^{req} , and lowest possible pressure (for fully developed meniscus), p_k^{pos} , will be corrected to the new moving meniscus. Then, the liquid pressure field must be computed again with new boundary condition and the check must be repeated. This iteration will be stopped if all menisci assumed as stationary pass the check. At the end, the correct boundary condition will be found. The algorithm of this approach can be seen in Figure 2.25.

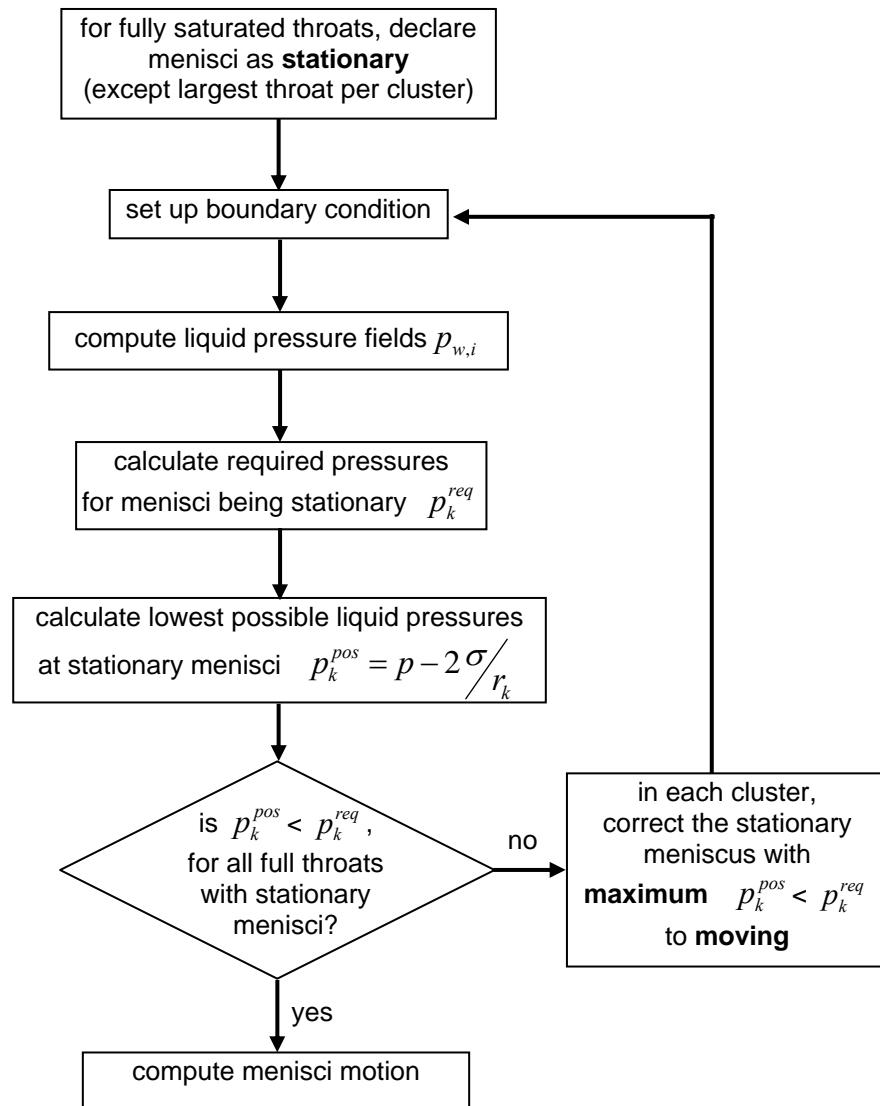


Figure 2.25: Algorithm to find boundary condition of liquid mass balances with second approach.

As both approaches give the same result of boundary condition, the first approach of defining boundary condition was chosen because this approach gives shorter computation time. The first approach is faster because not only one meniscus is corrected in each step.

2.4 Updating Liquid Volume and Calculating Network Saturation

Due to evaporation, the amount of liquid in the throats will decrease so it is necessary to update the throat saturation every time step. The time step is defined as the time that passes (with quasi-steady transport) until one throat in the network changes from i.e. partially filled or full throat to empty or partially filled. If one meniscus throat is empty, the phase distribution and the boundary condition for liquid phase have changed. As explained in the Isothermal Drying of Pore Networks

section about the of time step for negligible viscosity, the time step can be calculated by using Eqs. (2.21) and (2.22) and then choosing the smallest time from both. For model with liquid viscosity, the menisci will move to be empty or full, so that the total flow in a moving meniscus throat must be calculated as:

$$\dot{M}_{tot,k} = \dot{M}_{ev,k} + \dot{M}_{w,k} \quad (2.24)$$

where $\dot{M}_{ev,k}$ is evaporation rate of meniscus throat k at the neighbouring pore i and $\dot{M}_{w,k}$ liquid flow of throat k .

Time of moving throat can be divided into three types as following:

- time for full or partially filled throat to become empty ($\dot{M}_{tot,k} < 0$)

$$\Delta t = \left| \frac{V_k S_k}{\dot{M}_{tot,k}} \right| \quad (2.25)$$

where V_k is total volume of throat k and S_k saturation of throat k

- time for partially filled throat to become full ($\dot{M}_{tot,k} > 0$)

$$\Delta t = \frac{V_k(1-S_k)}{\dot{M}_{tot,k}} \quad (2.26)$$

- time for single throat to become empty

$$\Delta t_k = \frac{V_k S_k}{\dot{M}_{ev,k}} \quad (2.27)$$

where $\dot{M}_{ev,k}$ is total evaporation rate of single throat at both menisci.

The chosen time step is the smallest of all these time steps. Then, all saturations of moving meniscus throats and single throats are updated for that time step. The new liquid volume in the throats is known after the update, and the saturation of the network can be calculated as:

$$S = \frac{\sum_{i=1} V_k \cdot S_k}{\sum_{i=1} V_k} \quad (2.28)$$

2.5 Summary

The algorithm of this model can be summarized in the following steps:

1. Generate the data structures for network and boundary layer.
2. Calculate mass transfer coefficient and thickness of boundary layer.
3. Define initial throat and pore saturation.
4. Solve liquid and vapour mass balance equations to get liquid and vapour pressure fields.
5. Calculate total evaporation rate at the top of boundary layer.
6. Calculate vapour diffusion in the empty throats.
7. Define the type of the model, i.e. with or without liquid viscous forces.
8. For the case without liquid viscous forces, check if the capillary forces always dominate over viscous forces.
9. For the case with liquid viscous forces, investigate viscous effect and calculate liquid flow rate.
10. Compute times for emptying or filling the throats and choose the smallest time as time step.
11. Update the throat and pore saturations.
12. Label the liquid throats to know cluster number.
13. Repeat steps 4-12, until no liquid is left in the network.

The complete algorithm of this model can be seen in the flow chart of Figure 2.26. The model description has been presented with complete algorithm in the geometric data structure and drying algorithm. In the drying algorithm, the Hoshen-Kopelman algorithm of Al-Futaisi has been corrected (Metzger et al., 2006 [19]). Model with and without liquid viscous forces has been developed. These models will be used in the simulation of drying of porous media and the results will be presented in chapter 3.

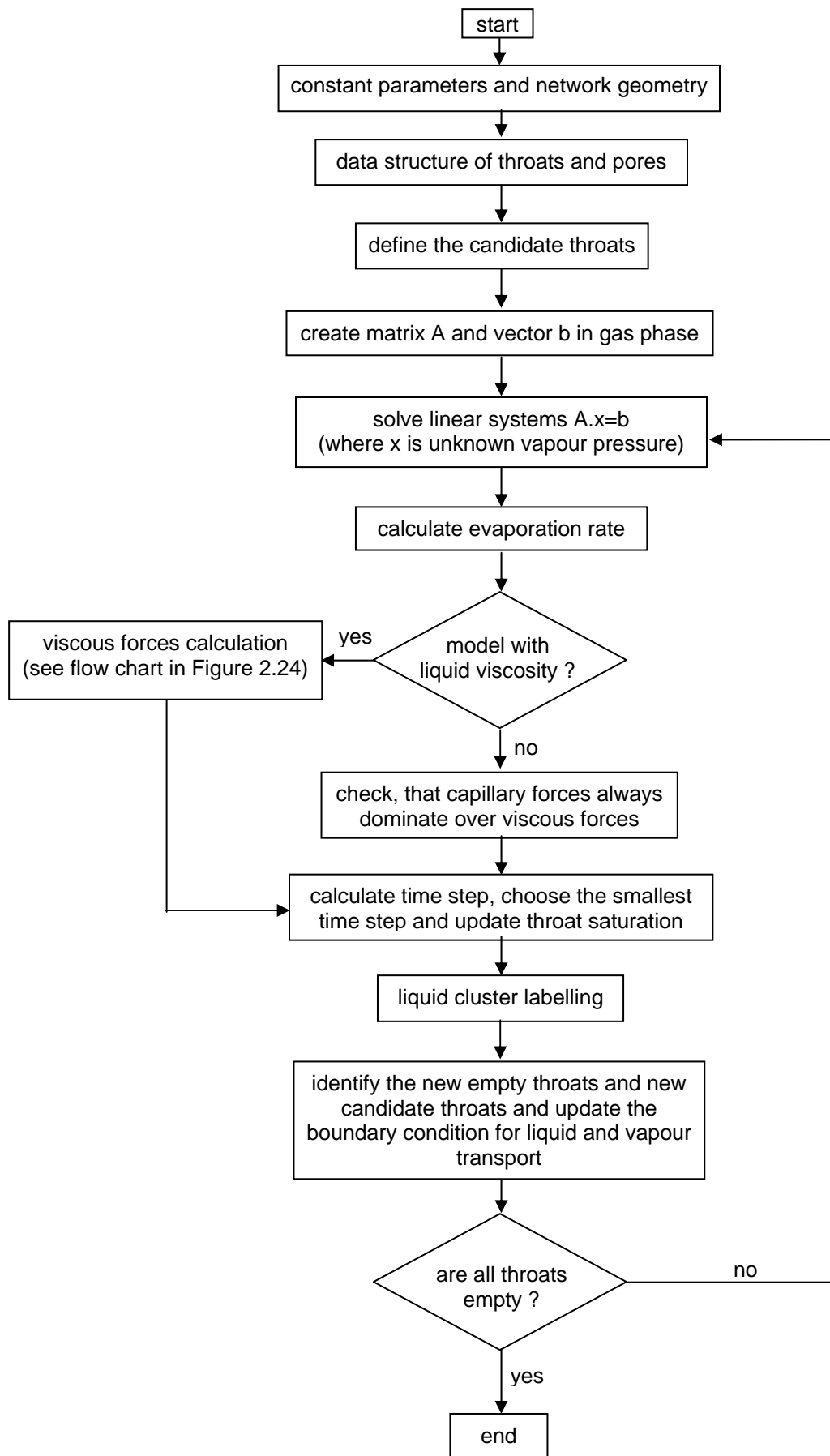


Figure 2.26: Flow chart of isothermal drying algorithm for pore networks.

CHAPTER 3

PORE NETWORK DRYING SIMULATIONS AND DISCUSSION

3.1 Overview

In this chapter, the results of drying simulations with 2D square and 3D cubic networks are presented. Drying behaviour is influenced by drying conditions and structural properties of the porous medium. In this investigation, constant values for the state of the drying air are assumed, namely atmospheric pressure ($p = 1$ bar), room temperature ($T_\infty = 20^\circ\text{C}$) and zero moisture ($p_{v\infty} = 0$). Only the velocity of drying air is varied. The main goal of these simulations is to investigate the influence of structure as major internal factor for drying of porous media. Two types of throat radii, i.e. small radii for micro pores and large radii for macro pores, are used in this simulation, both randomly generated obeying a normal number distribution. In order to investigate drying behaviour, four different network structures were simulated by different arrangement of micro and macro pores: monomodal pore size distributions of micro pores, bimodal pore size distributions with long channels of macro pores, isolated regions of micro pores and isolated regions of macro pores. Another internal factor, which might influence drying behaviour, is, the coordination number (Z), i.e. the number of throats connected to a pore. Three different cases of pore connectivity are studied in this simulation, namely hexagonal ($Z = 3$), square ($Z = 4$) and hexatriangular ($Z = 6$) arrangements. In this work, a different approach to mass transfer in the boundary layer is proposed. This approach allows describing lateral diffusive transfer by discretizing the boundary layer. It was compared with the traditional approach of an average mass transfer coefficient and with the average model for diffusive mass transfer in the boundary layer (Schlünder, 1988 [27]).

In order to investigate the influence of viscous and capillary forces, two model variants for 2D regular square network, i.e. without and with viscous forces, were simulated. For 3D cubic network, all simulations are investigated with viscous forces. In the model without viscous forces, large throat radii are applied so that the capillary forces always dominate over the viscous forces. In the model with viscous forces, viscosity and pore size distribution are varied for the different pore structures.

Drying behaviour for different structures, when viscous forces can be neglected, was investigated first. In 2D network model without viscous force, the results of the drying simulations are shown as drying curves and phase distributions for all network structures. Then, four different air velocities are applied to investigate the influence of boundary layer thickness. Higher air velocity leads to a thinner boundary layer, and lower air velocity to a thicker boundary layer. The variation of boundary layer thickness is used to study the role of lateral vapour transfer in the boundary layer. The different approaches to boundary layer modelling are compared using drying curves and the relationship between wet surface fraction and drying rate for different pore structure. Finally, results for different pore connectivities are presented and discussed.

The influence of viscosity is studied for 2D networks using smaller throat radii, because smaller throat radii induce higher viscous forces. This throat radius is chosen according to a normal distribution with mean throat radius r_0 and standard deviation σ_0 . Then, the competition between viscous and capillary forces indicated in capillary number is varied by applying different liquid viscosities and pore size distributions. A variation of liquid viscosity from zero (capillary forces dominate) to infinity (immobile water) is simulated for all network structures. For the mono-modal pore size distribution, mean throat radius r_0 and standard deviation σ_0 are varied. For bimodal pore size distribution, the size difference of micro and macro pores (Δr_0) is varied. In the frame of investigating the influence of pore size distribution, a 2D network with negligible lateral resistance in network and boundary layer, is compared with a bundle of capillaries (Irawan, et al., 2006 [11], Metzger and Tsotsas, 2005 [18]). Mean throat radius r_0 and standard deviation σ_0 of the normal distribution are varied in this comparison.

The drying behaviour results for the different structures, mentioned above, were obtained by using only *one* network of random throat radii in each case. They can not give the representative drying behaviour of each structure because each random throat radii generation results in more or less different drying behaviour. Accordingly, the drying model was used for Monte Carlo simulations with 10 networks, each randomly generated according to the same stochastic rules. Monte Carlo simulations of monomodal pore size distribution were modelled applying periodic boundary conditions. The idea of a periodic boundary condition is in representing a bigger network by connecting the left and right of network border. In this context, the influence of the network border is investigated. 10 Monte Carlo runs were performed for the drying of the different pore structures.

Additionally, for 2D square networks the influence of network depth is investigated for different network structures. In order to overcome the limitations of 2D network modelling and to investigate closer to real porous media, 3D pore networks were modelled. All simulations of 3D networks include viscous forces of liquid phase and periodic boundary conditions. Four different topologies of network structure were also simulated in 3D network. First, an investigation of lateral transfer in the boundary layer is given for 3D network to allow the comparison with the 2D results. The 3D networks were simulated with different pore size distributions, i.e. monomodal and bimodal. The monomodal pore size distribution of the 3D network is varied regarding its mean throat radius r_0 and standard deviation σ_0 . Bimodal pore size distribution is varied concerning size difference between micro and macro pores (Δr_0). The influence of viscous forces is also investigated by varying the liquid viscosity from zero (capillary forces dominate) to infinity (water is immobile). Since phase distribution is very difficult to visualize in 3D, all results of these drying simulations are given in form of drying curve and moisture profiles.

3.2 Network Geometry and Simulation Parameters

The aim of the following drying simulations is to investigate the influence of structure of porous media on their drying behaviour. Two types of throat radius are used, i.e. micro and macro pores, to create four different network topologies. The first network structure contains only micro pores, as a representative of natural porous media, with a monomodal pore size distribution (Figure 3.1a). Three other network structures are constructed by combining micro and macro pores. The second network structure is constructed by arranging the macro pores as long channels towards the network surface, but separating each long channel from the other (Figure 3.1b). This structure allows studying of efficient capillary pumping, and the arrangement of large throats at network surface gives a good wet spot distribution. In the

third network, the micro pores form isolated regions separated by the macro pores connected over long distances in both spatial directions (Figure 3.1c). This network may be seen as a simple representation of an agglomerate of micro porous particles. In the last structure, the macro pores are arranged in isolated groups surrounded by a continuous phase of micro pores (Figure 3.1d).

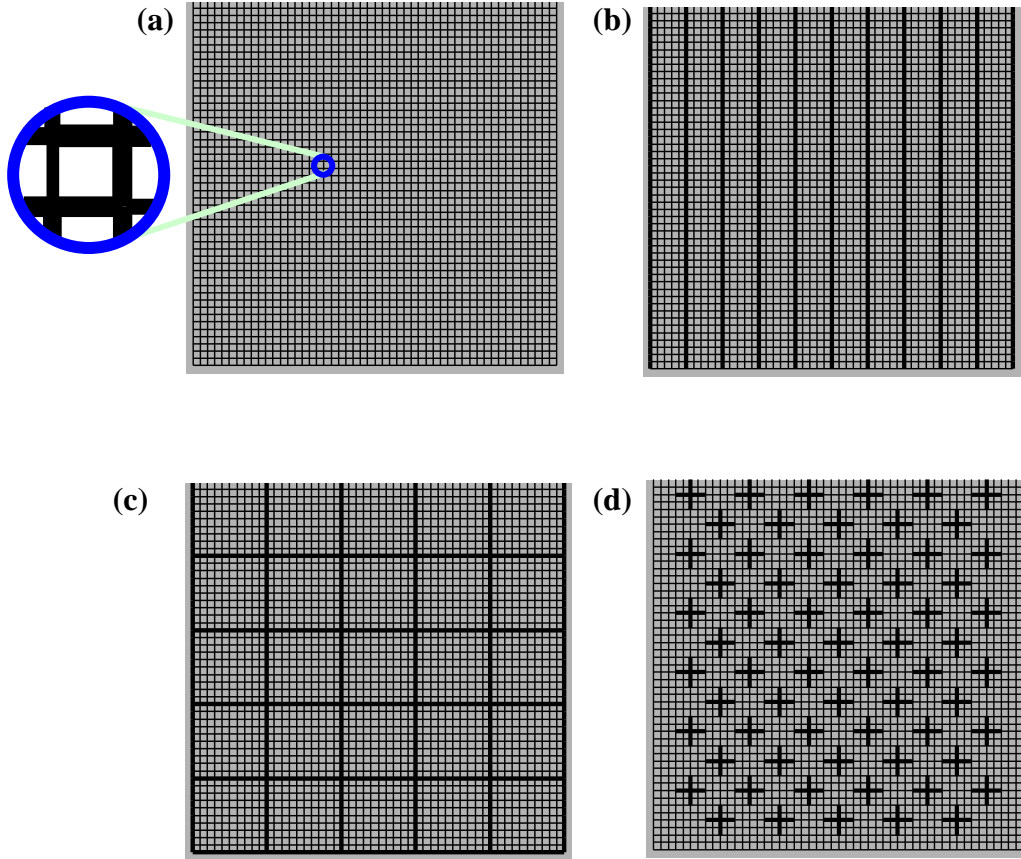


Figure 3.1: Four investigated 2D network structures (a) network 1 with monomodal pore size distribution, (b) network 2 with bimodal pore size distribution where macro pores form long channels toward network surface, (c) network 3 with bimodal pore size distribution and isolated regions of micro pores and (d) network 4 with bimodal pore size distribution where macro pores are isolated.

Throat length and radius can also influence the drying behaviour. Two cases of throat length are considered. For the model without liquid viscosity, the throat length L_k is 500 μm , while $L_k = 5 \mu\text{m}$ is used for the model with liquid viscosity. The radius for each throat is randomly chosen according to a normal distribution with mean radius r_0 and standard deviation σ_0 . This distribution can be described by the following (normalized) number density function:

$$\frac{dN}{dr} = \frac{1}{\sigma_0 \sqrt{2\pi}} e^{-\frac{(r-r_0)^2}{2\sigma_0^2}} \quad (3.1)$$

The random choice of throat radius leads to a different liquid and vapour flow conductivity in each throat. Figure 3.2 shows the distribution of throat radii and the corresponding pore volume distribution of a random realization of network 1 with mean radius $r_0 = 100$ nm and standard deviation $\sigma_0 = 10$ nm.

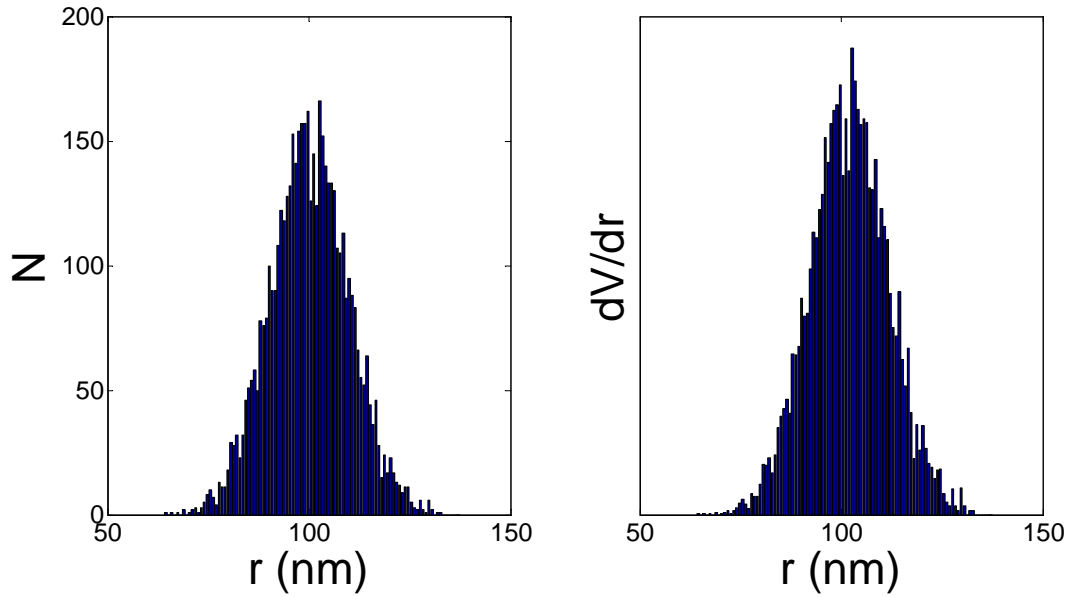


Figure 3.2: Throat radius distribution and pore volume distribution of network 1 ($r_0 = 100$ nm and $\sigma_0 = 10$ nm).

By variation of r_0 and σ_0 , the influence of pore size distribution on drying behaviour will be investigated later on. The competing effects of capillary pressure, viscous forces and vapour diffusion are influenced by the throat radius. Capillary pressure at the interface between liquid and vapour gives the boundary condition for the liquid mass balance:

$$p_m = p - \frac{2\sigma}{r_k} \quad (3.2)$$

It is obvious that bigger throat radius gives higher pressure at meniscus, while smaller throat radius gives low pressure at the meniscus. Liquid viscosity leads to a pressure drop, which is dependent on evaporation rate and throat size, and must be overcome by the difference in capillary pressure:

$$\Delta p_{f,k} = 8\eta_w \frac{\dot{M}_{v,k} L_{w,k}}{\rho_w \pi r_k^4} \quad (3.3)$$

Bigger throat radii in the range from 40 until 100 μm were used in the model without viscous forces so that capillary pumping always dominates over viscous forces. Smaller throat radii in the range from 100 until 500 nm were used in the model with viscous forces to study the influence of viscous forces.

It is already mentioned that the drying process is assumed to be isothermal at room temperature ($T_\infty = 20^\circ\text{C}$) and is simulated for atmospheric pressure ($p = 1$ bar). Some properties for setting up the liquid and vapour mass balances are given by these conditions. The values of these properties can be seen in Table 3.1. Saturation vapour pressure and vapour pressure in the bulk of air from Table 3.1 are boundary conditions for the vapour mass balances.

Table 3.1: Properties of fluid (water and vapour) at $T = 293.15$ K and $p = 1$ bar [35].

property	value
molar mass of vapour, \tilde{M}_v (kg/kmol)	18.02
dynamic viscosity of liquid, η_w (Pa.s)	0.001
density of liquid, ρ_w (kg/m ³)	998.21
equilibrium vapour pressure, p_v^* (Pa)	2339
vapour pressure in the bulk of air, $p_{v,\infty}$ (Pa)	0
surface tension between liquid and air, σ (N/m)	0.07274
diffusion coefficient (vapour in air), δ_{va} (m ² /s)	$2.5685 \cdot 10^{-5}$
universal gas constant, \tilde{R} (J/kmolK)	8314.5

As mentioned before, in the simulations air velocity was also varied to get different boundary layer thickness. The boundary layer thickness is calculated by Prandtl's relationship (refer to Eqs (2.1) and (2.2)). Then, the boundary layer is discretized into some vertical nodes to allow lateral transfer between nodes in boundary layer. For the investigated air velocities, Table 3.2 gives boundary layer thickness and number of vertical nodes in boundary layer (n_{bl}) for throat length $L_k = 500$ μm .

Table 3.2: Air flow velocities with respective mass transfer coefficient β and boundary layer thickness ε for throat length $L_k = 500$ μm and size of network 50×50 pores.

u (m/s)	Re	Sh	β (mm/s)	ε (mm)	n_{bl}
0.5	830.6	16.12	16.24	1.58	3
0.2	332.2	10.19	10.27	2.50	5
0.1	166.1	7.21	7.26	3.54	7
0.05	83.1	5.10	5.13	5.00	10

3.3 Drying of 2D Square Networks in Absence of Viscous Effects

2D square networks with large enough throat radii and drying rates slow enough to ensure the domination of capillary forces over viscous forces, so that liquid viscosity may be neglected, are presented in this section. Four different structures are investigated for four different air velocities. Different structures are taken to investigate the influence of different spatial distributions of macro pores onto drying behaviour and different air velocities lead to different boundary layer thickness. The size of network is 51×51 nodes, so that there are 2601 pore nodes and 5050 throats. The throat length is 500 μm , thus giving a total network size of 2.5×2.5 cm^2 . In order to investigate the constant drying period, three approaches to vapour diffusion through the boundary layer are presented: average mass transfer coefficient, discretized boundary layer with lateral vapour transfer and wet spot model by Schlünder.

3.3.1 Influence of Structure

Air velocity for all network structures in this section is 0.05 m/s corresponding to the thickest boundary layer (5 mm) with 10 vertical nodes (see Table 3.2). Lateral diffusion in the boundary layer is allowed in this case. Liquid is able to flow due to the capillary pumping, dominating always over friction. The pore size distribution of the first network structure (monomodal) is shown in Figure 3.1. This network structure contains only micro pores which are generated as normal random with mean throat radius 40 μm and standard deviation 5 μm , with total pore volume of network 12.9 mm^3 (see Figure 3.3a). For network with structure 4, the spatial distribution of throat radii was taken from network 1 and the mean throat radius is rescaled to 100 μm with standard deviation 5 μm for macro throats (see Figure 3.3b). Structure of network 4 is bimodal pore distribution, where macro throats are arranged in groups surrounded by micro throats which are connected continuously (refer to Figure 3.1). Pore volume distribution can be seen in Figure 3.3b. The aim of this structure is to investigate influence of isolated macro pores. The total pore volume of this network is 20.4 mm^3 and the volume fraction of large throats is 40.8 %. Each random throat radii generation results in different drying behaviour and the network in this simulation is only one representative of a class of networks with the same stochastic structural properties. The range of randomness of each network will be explained later by use of the Monte Carlo simulations (refer to section 3.4.5).

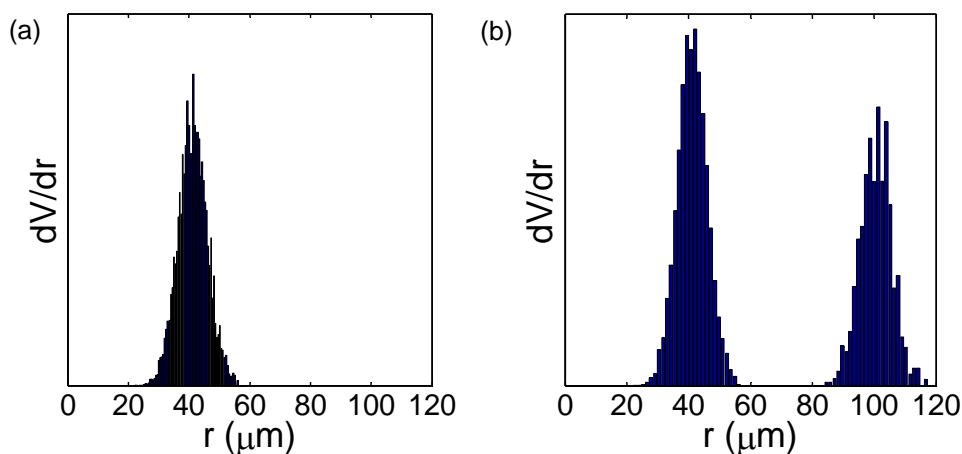


Figure 3.3: pore volume distribution for (a) network 1 and (b) network 4.

Since capillary pumping always dominates over viscous forces, the throats empty one by one. The biggest throat radius having a liquid vapour interface (meniscus) in each cluster is a candidate for emptying throat. Evaporation takes place at the top of the network and through the boundary layer. Initially, all liquid pores in the network belong to one cluster and all meniscus throats are at the network surface (refer to Figure 3.1). The biggest throat of them is emptied because it has highest liquid pressure at the meniscus.

For network structure 1, capillary pumping is not efficient enough to produce a constant drying rate at the beginning (first drying period). The throats at the network surface dry out rapidly so that the drying rate falls from the beginning as shown in Figure 3.4 (point A). The drying rate does not drop to very low values because part of network surface is still wet (see phase distribution in Figure 3.5.A). This wet surface is still connected to a large liquid cluster so that capillary pumping within this cluster can bring liquid from its biggest meniscus throat to the surface. At the same time, air penetrates into the depth of the network (see phase distribution in Figure 3.5.B).

Due to the random spatial distribution of throat radius, the probability of emptying the meniscus throats at the network surface depends on the total number of meniscus throats in the respective cluster. Bigger clusters have more meniscus throat than smaller ones. For the phase distribution in Figure 3.5C, one can see two big clusters to which the liquid throats at the network surface are connected. The throats at the network surface in the smaller cluster (cluster 2) have a higher probability to empty as explained before. It is clear that networks of this structure have many possibilities of drying behaviour due to their randomness.

During the drying process, this first network structure shows quasi constant drying periods. During such a period, gas invades only meniscus throats in the depth of the network and capillary pumping delivers liquid from those throats to the throats near or at the network surface. Therefore, the menisci at the network surface remain stationary. This structure has more than one quasi constant drying period. Point B of Figure 3.4 for network structure 1 is a part of a short period of quasi constant drying rate; a long period can be observed in point C (see phase distribution in Figure 3.5C).

After all throats at the network surface are dry, vapour diffusion suffers an additional resistance leading to a reduction in evaporation rate. The drying behaviour forms a receding front. Capillary pumping in presence of a receding front plays a role only for each cluster. Due to the randomness, this network creates many clusters as shown in Figure 3.5. Many of these clusters are small, so that capillary pumping is only over short distance and, as already mentioned, the probability that (favourable) meniscus throats oriented towards the network surface will empty is high.

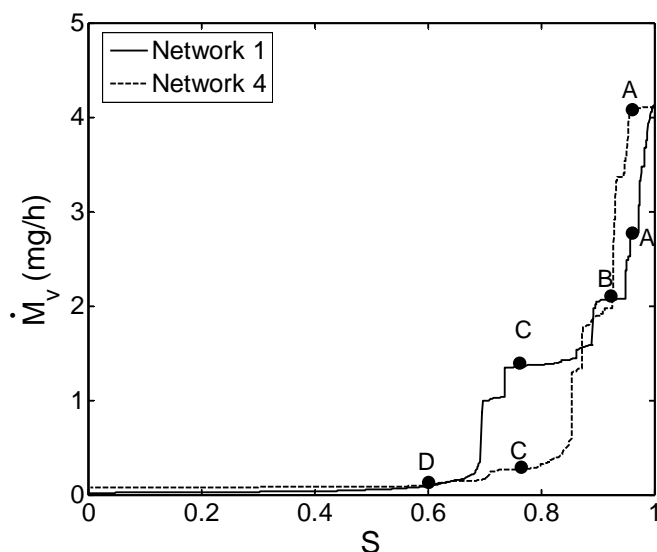


Figure 3.4: Drying curve for network structure 1 (solid line) and network structure 4 (dashed line). Lines on the drying curve refer to phase distributions in Figure 4.5.

The network structures 1 and 4 can be compared in order to know the influence of isolated regions of macro pores. Therefore, points A, B, and C in the drying curve (Figure 3.4) are at the same saturations for both network structures. The drying curve for network structure 4 (see dashed line in Figure 3.4) has a short constant drying period due to large throats at the surface. At the end of this period, the network still contains macro pores, but these macro pores are separated by micro liquid pores, so that air will only invade the micro liquid pores by a random process. Therefore, the small meniscus throats at the network surface have a high probability to become emptied throats. The drying rate falls rapidly after most of throats at the network surface are dry as seen in Figure 3.14B.

The random emptying of micro pores for network structure 4 is not continuous. If a macro pore is reached by the air, this macro pore region is first emptied completely, then, the random emptying of micro pores continues. The drying process has additional resistance in vapour phase of network after all network surface throats are empty. Then, the drying rate at this condition is at the low level (slow drying rate). At point C in the Figure 3.4, both network structures show quasi constant drying periods at different level of the drying rate. The network structure 1 is at the high drying rate because the capillary pumping from the biggest micro throats can still reach the throats at network surface.

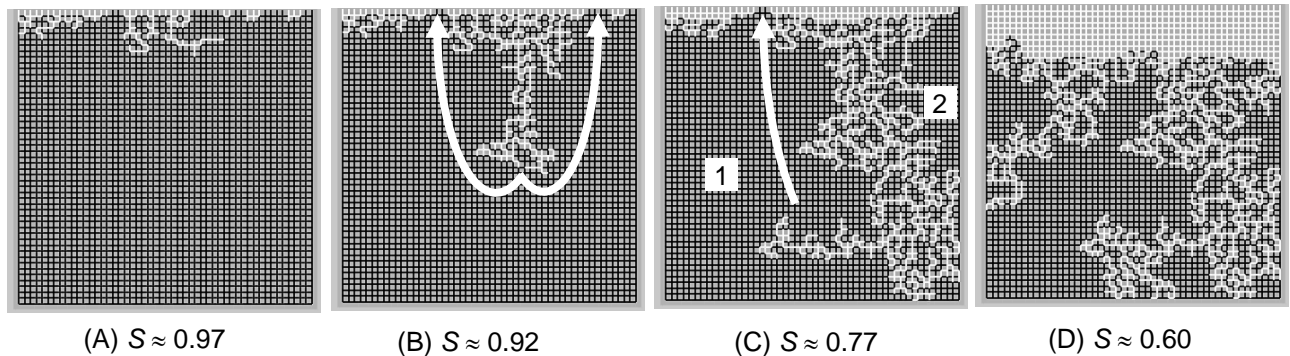


Figure 3.5: Phase distribution at different network saturation during drying for structure 1. Liquid phase is black and vapour phase is white (see Figure 3.4 for positions on drying curve).

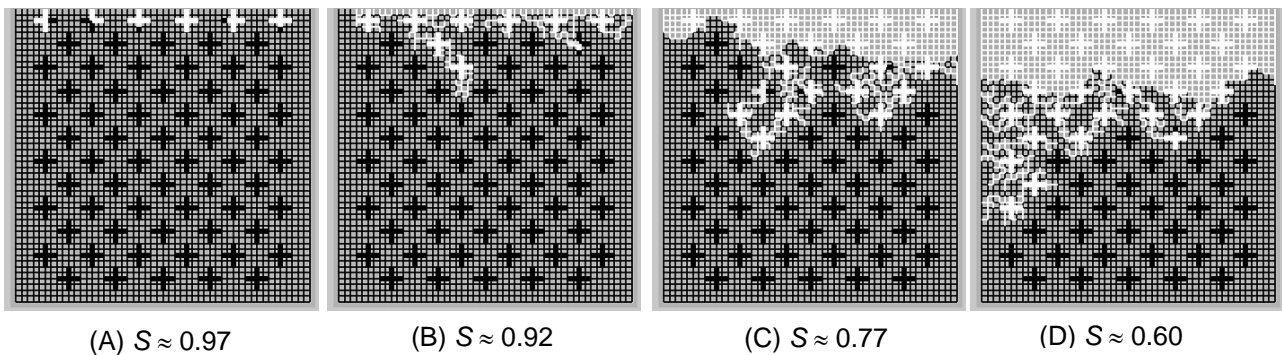


Figure 3.6: Phase distribution at different network saturation during drying for network structure 4. Liquid phase is black and vapour phase is white (see Figure 3.4 for positions on drying curve).

For network structure 2, the spatial distribution of throat radii was taken from network 1, only some throats were rescaled to large throats ($100 \pm 5 \mu\text{m}$). The large throats form long channels in the vertical direction towards the open side of the network. Each long channel is not directly connected to the others but indirectly via the small throats between them (see Figure 3.7). The total pore volume of this network is 20.2 mm^3 , and the volume fraction of large throats is 42.9 %. Throat length and size of network are the same as for network 1.

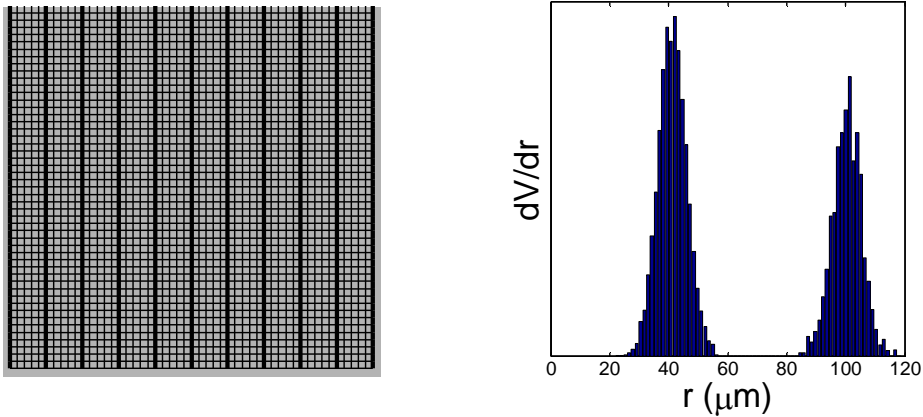


Figure 3.7: Network 2 with vertical macro channels and its bimodal pore size distribution.

In contrast to network structure 1, this network structure has efficient capillary pumping due to the presence of two more or less continuous phases, the macro channels and the small throats. This capillary pumping will transport liquid from the menisci in the macro throats to the smaller throats. If capillary pumping can provide liquid to the wet throats at the network surface, these throats can be kept wet (stationary) and these wet throats can assure a long first drying period (see drying curve in Figure 3.8). When large throats at the network surface are empty, the drying rate does not decrease significantly because this structure has a good distribution of wet spots at the network surface (see phase distribution in Figure 3.9A). Due to lateral vapour transfer in the boundary layer, the dry spots of large throats are still at elevated vapour pressure and the high level of drying rate can be maintained (first drying period). When the liquid throats are separated into two clusters, all small throats at the network surface are still wet because capillary pumping can still provide liquid to the surface from large throats of each cluster (see cluster 1 and 2 of phase distribution in Figure 3.9B). The creation of a second cluster in Figure 3.9B is only because in 2D the two phases (micro and macro throats) are not really continuous. When a liquid cluster has no more large throats, throat emptying is continued by the largest of the small throats. The wet throats at the network surface (responsible for a prevailing first drying period) can persist with a probability that decreases with decreasing cluster size (see above).

After all macro throats in cluster 2 are dry, the next empty throats are not at the network surface (see phase distribution in Figure 3.9C). Therefore, small throats at the network surface in cluster 2 are still wet and the drying rate is at high level (see drying curve in Figure 3.8 point C). At some time, the gas will invade wet small throats at the network surface. When part of wet throats at network surface are dry (see phase distribution 3.9D), the drying rate will decrease, as shows the drying curve in Figure 3.8.

When all throats at the network surface are dry (see phase distribution in Figure 3.9E), this condition leads to an additional vapour transfer resistance from the receding evaporation front to the network surface. Due to this increasing resistance, the drying rate decreases dramatically (see point E in Figure 3.8) and capillary pumping only plays an insignificant role inside each cluster. The drying process is dominated by vapour transfer until all liquid throats are dry. The efficiency of capillary pumping can also be seen from the evolution of the number of clusters (Figure 3.8). Initially, all liquid throats are part of one cluster until point B. During this period, capillary pumping plays a very important role in supplying liquid to the throats at the network surface. With increasing cluster number, capillary pumping becomes irrelevant. The combination of sustained capillary pumping and a good spatial distribution of wet spots at the network surface let the network structure 2 to dry favourably.

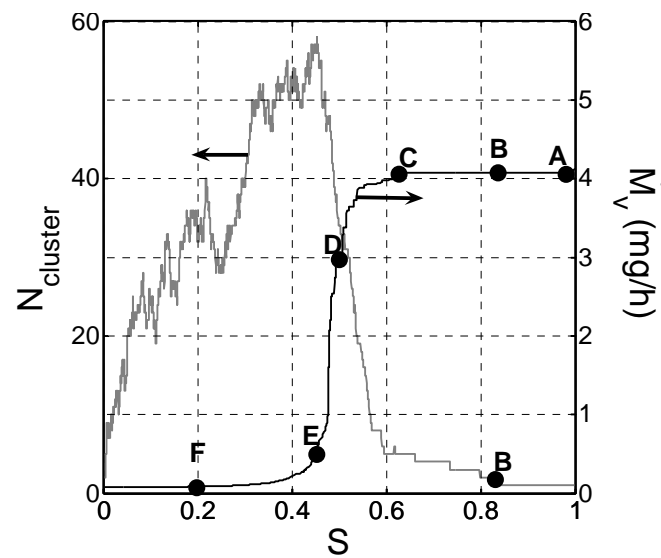


Figure 3.8: Number of clusters (left y-axis) and drying curve (right y-axis) of network 2. Points in the drying curve refer to the phase distributions in Figure 3.9.

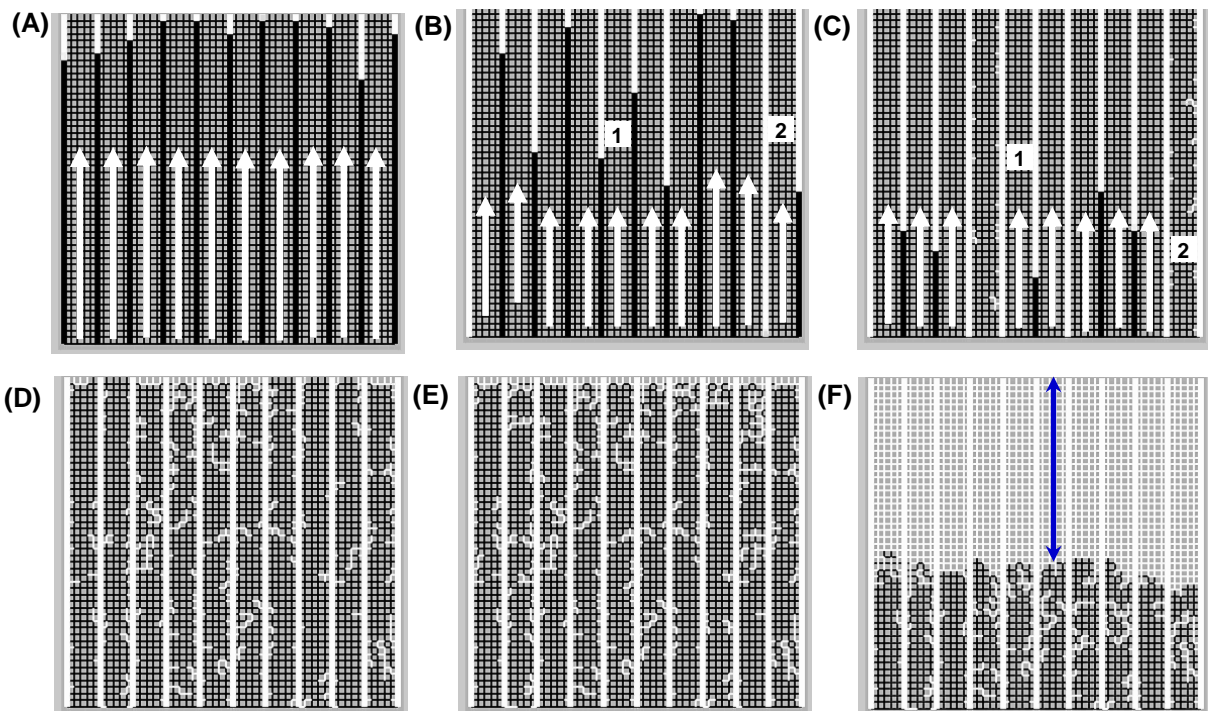


Figure 3.9: Phase distributions at different network saturation during drying for network structure 2 (see Figure 3.8 for position on drying curve).

The structure of network 3 has bimodal pore size distribution where micro throats are in isolated regions surrounded by macro channels which are interconnected, as shown in Figure 3.10. This structure can be interpreted as a 2D representation of an agglomerate of microporous particles. The total pore volume of this network is 20.2 mm^3 and the volume fraction of large throats is 42.5 %.

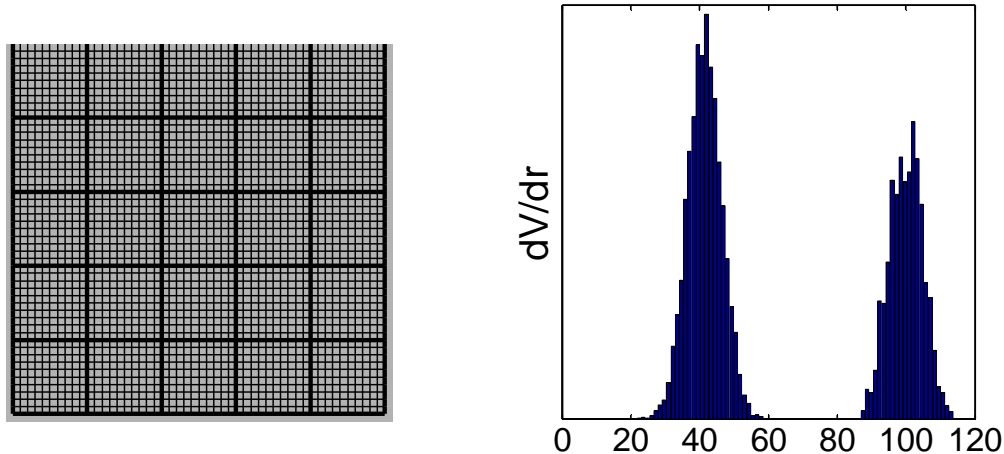


Figure 3.10: Network 3 with vertical and horizontal macro channels separating micropores into isolated regions and the corresponding bimodal pore size distribution.

Again, the radii of the macro throats were obtained by rescaling some of the throats of network 1; the micro throats were taken directly from network 1. Capillary pumping from large throats of network structure 3 can only provide a short constant drying period. This period will be ended when all macro throats around isolated micro throats near the network surface are empty and create new liquid cluster so that the capillary pumping from other large throats can not deliver liquid to this new liquid cluster (cluster 2 in Figure 3.12A). Then, the meniscus throats at the network surface of this cluster are at high probability to be empty throats so that the drying rate falls to a lower level.

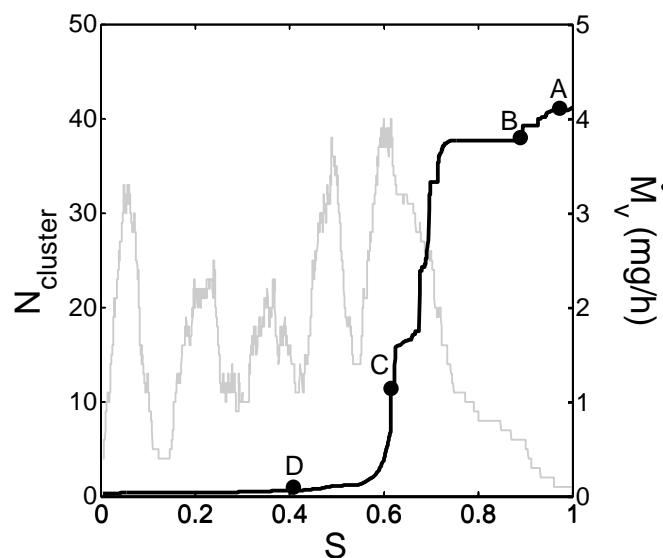


Figure 3.11: Number of clusters (left y-axis) and drying curve (right y-axis) of network 3. Points on the drying curve refer to phase distributions in Figure 3.12.

Due to the randomness of large throats, air invades large throats in the depth of network and delivers the liquid to the network surface (see Figure 3.12B). Therefore, the drying curve of this structure shows a quasi constant drying period of long duration and high drying rate. During this period, most of the emptying throats are large throats (more volume) so that the period is longer than for network structure 1. Most of throats at the network surface are connected to the emptying large throats so that the drying rate in this period is at a relatively high level.

Figure 3.11 also shows the evolution of clusters for this network. The number of clusters does not increase dramatically at the beginning of drying because air invades large throats and creates only a few isolated regions of micro throats as new clusters. Only those regions closest to the network surface have evaporation and will split up into further clusters which then gradually evaporate. Therefore, the number of clusters can increase when the liquid throats in isolated micro throats is separated again into very small clusters. Then, the number of clusters decreases when these small clusters disappear by evaporation. Other isolated regions of micro throats that are far from the surface are trapped clusters (see Figure 3.12C). These trapped clusters have no influence on the change of cluster number.

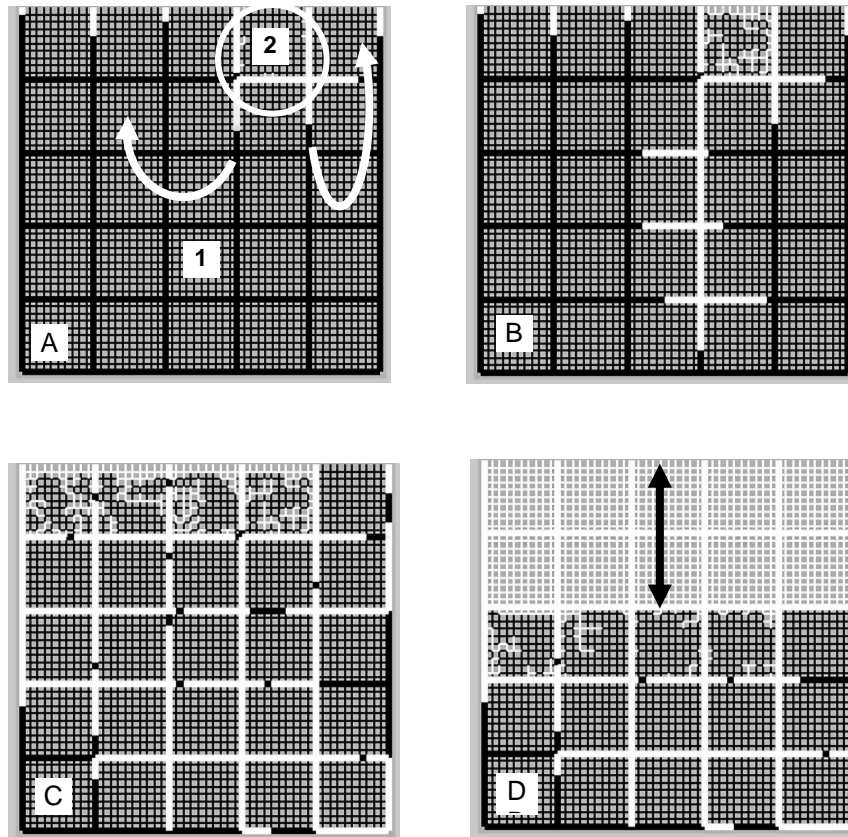


Figure 3.12: Phase distributions at different network saturation during drying for network structure 3 (see Figure 3.11 for position on drying curve).

Conclusion on Influence of Network Structure (in Absence of Viscous Effect)

Various phenomena during the drying of four network structures have been presented. The investigated networks are only examples of each network structure type. Therefore, some of these phenomena are influenced by randomness of throat radius and are only valid for the whole structural class in a qualitative manner. In the section discussing Monte Carlo simulations, the influence of this randomness of each network structure will be presented. In the present section, just one random realization has been used to describe the influence of network structure and different topology.

Conclusions about favourable network structure, i.e. having a long first drying period, can be obtained from these simulations: the network structure should have continuous “phase” of large and small throats; it should also have a good spatial distribution of small throats at network surface. Network structure 2 is favourable for drying because this structure can fulfil

all the requirements for producing a long first drying period. The emptying of large throats is continuous into the depth of the network and this emptying does not directly cut off capillary flow to the network surface. Network structure 3 is not that favourable because the small throats do not form a continuous phase (but isolated regions) and capillary flow to these isolated regions can easily be cut off by emptying large throats. Network structure 4 is also not favourable because the large throats do not form a continuous phase (isolated region). None of the requirements can be fulfilled by network structure 1 due to complete randomness. The spatial correlation of wet spots at the network surface plays an important role in producing the first drying period. Therefore, network structure 2 with a good distribution of wet spots at the network surface is a favourable structure for drying. The drying curves for all four network structures can be seen in Figure 3.13.

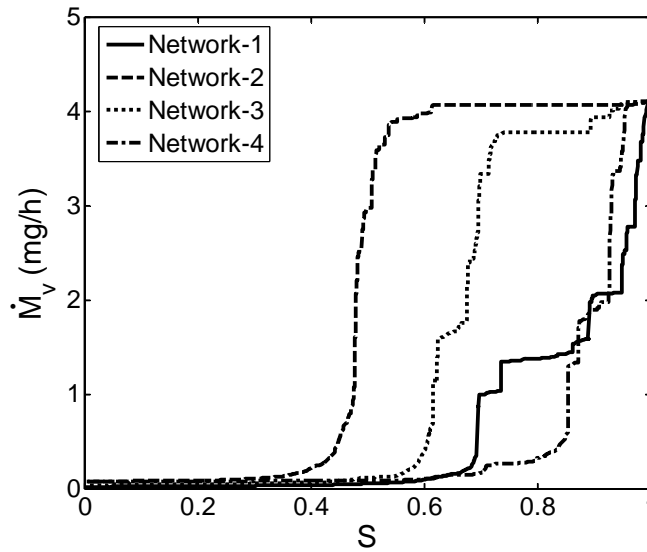


Figure 3.13: Drying curves for all four different 2D network structures of square geometry (in absence of viscous effect).

3.3.2 Influence of Lateral Transfer in Boundary Layer

Evaporation in the present simulations takes place by the surface meniscus throats and vapour will diffuse through the boundary layer due to vapour pressure differences between nodes at the network surface and towards the bulk of air. Up to now, most research groups applying pore network modelling to isothermal drying of porous media failed to reproduce a first drying period, i.e. a constant drying rate at the beginning. They used the traditional approach with an average mass transfer coefficient β (see Figure 3.14a), where vapour is transferred directly from the nodes at network surface to the bulk of air without further exchange. Vapour diffusion through the boundary layer in terms of local evaporation rate can, then, be calculated by:

$$\dot{M}_{vs,i} = A_{bl} \beta \frac{p \tilde{M}_v}{\tilde{R} T} \ln \left(\frac{p - p_{v,\infty}}{p - p_{vs,i}} \right) \quad (3.4)$$

where A_{bl} is cross section area attributed to the nodes in the boundary layer, $p_{v,\infty}$ vapour pressure in the bulk of air, $p_{vs,i}$ vapour pressure of node i at the network surface. The traditional approach fails to reproduce the first drying period because dry nodes at the network surface have low vapour pressure, which directly results in low drying rates.

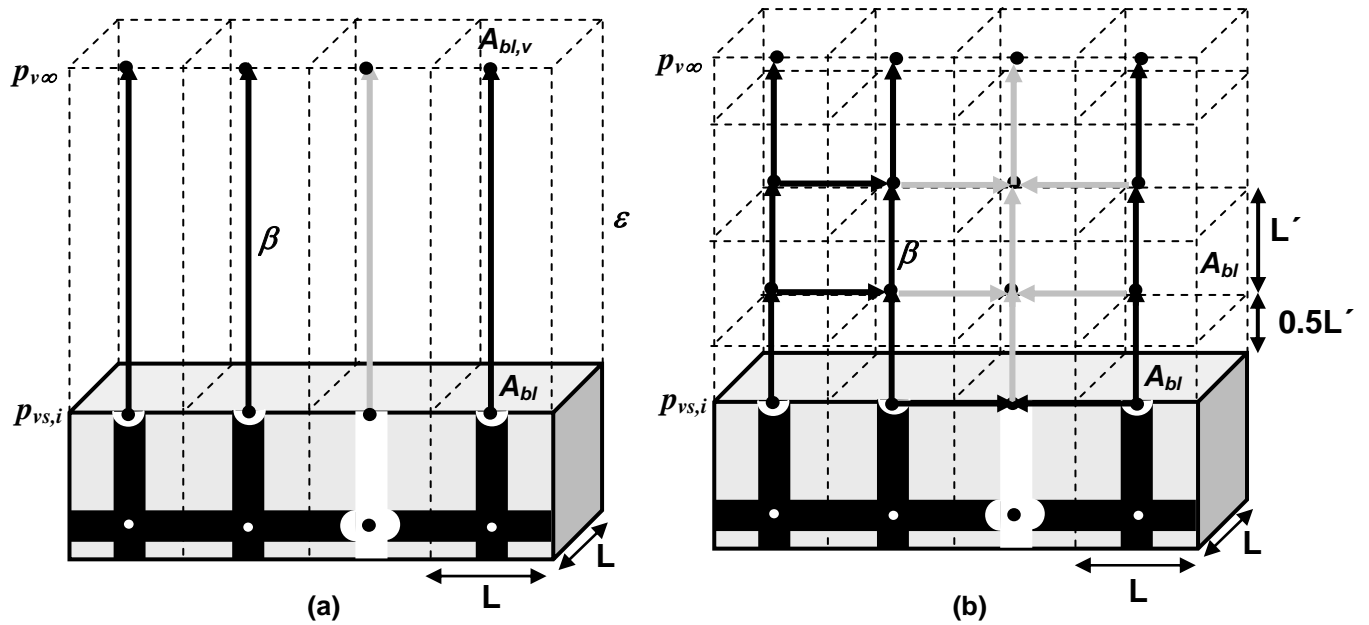


Figure 3.14: Vapour transfer in the boundary layer for (a) traditional and (b) extended network model.

In order to reproduce the first drying period, here is proposed another approach by discretizing the diffusive boundary layer and allowing for lateral transfer (see Figure 3.14b) so that dry nodes at network surface still can have high vapour pressure (Irawan et al., 2005 [10]). This approach is adapted from the work of Laurindo and Prat (1998 [14]). They introduced a diffusive layer between network surface and bulk of air in order to describe experimental drying rates by network modelling. A finite volume method, as explained in section 2.2.2, was applied in order to couple the discrete network to the continuous gas phase. In the present section, the mentioned two approaches are compared for the previously introduced four different network structures and at four air velocities in the range from 0.05 to 0.5 m/s. Different air velocity leads to different boundary layer thickness ε , which is calculated by Prandtl's relationship (Eq. (2.1)). The distance between two nodes in horizontal direction is the same as the throat length, and the distance between two nodes in vertical direction is adjusted to also be approximately the same. The highest air velocity ($u = 0.5$ m/s) leads to the thinnest boundary layer, which contains 3 nodes in vertical direction. For the lowest air velocity ($u = 0.05$ m/s) the thickest boundary layer, which contains 10 nodes in vertical direction, is obtained.

Figure 3.15 shows drying curves of both approaches for the different network structures and air velocities. Inclusion of lateral mass transfer in the boundary layer results in higher drying rates for all network structures and all air velocities. In fact, each wet surface throat has more effective cross section area to transfer vapour to the bulk of air. In other words, dry nodes at the network surface still have an elevated vapour pressure because neighbouring wet nodes can transfer vapour to them, so that they can also contribute to the evaporation rate. This is different for the case without any lateral transfer in the boundary layer, because vapour is then transferred only directly from the network surface to the bulk of air at the local evaporation rate. Therefore, dry nodes at network surface have low vapour pressure and do not significantly contribute to the evaporation rate. As a consequence, the drying rate is reduced as soon as the first surface throat dries out, so that this approach fails to reproduce the first drying rate (see especially network 2).

Table 3.3: Influence of air flow velocities on initial drying rate $\dot{M}_{v,l}$

u (m/s)	ε (mm)	n_{bl}	$\dot{M}_{v,l}$ (mg/h)
0.5	1.58	3	13.05
0.2	2.50	5	8.25
0.1	3.54	7	5.83
0.05	5.00	10	4.13

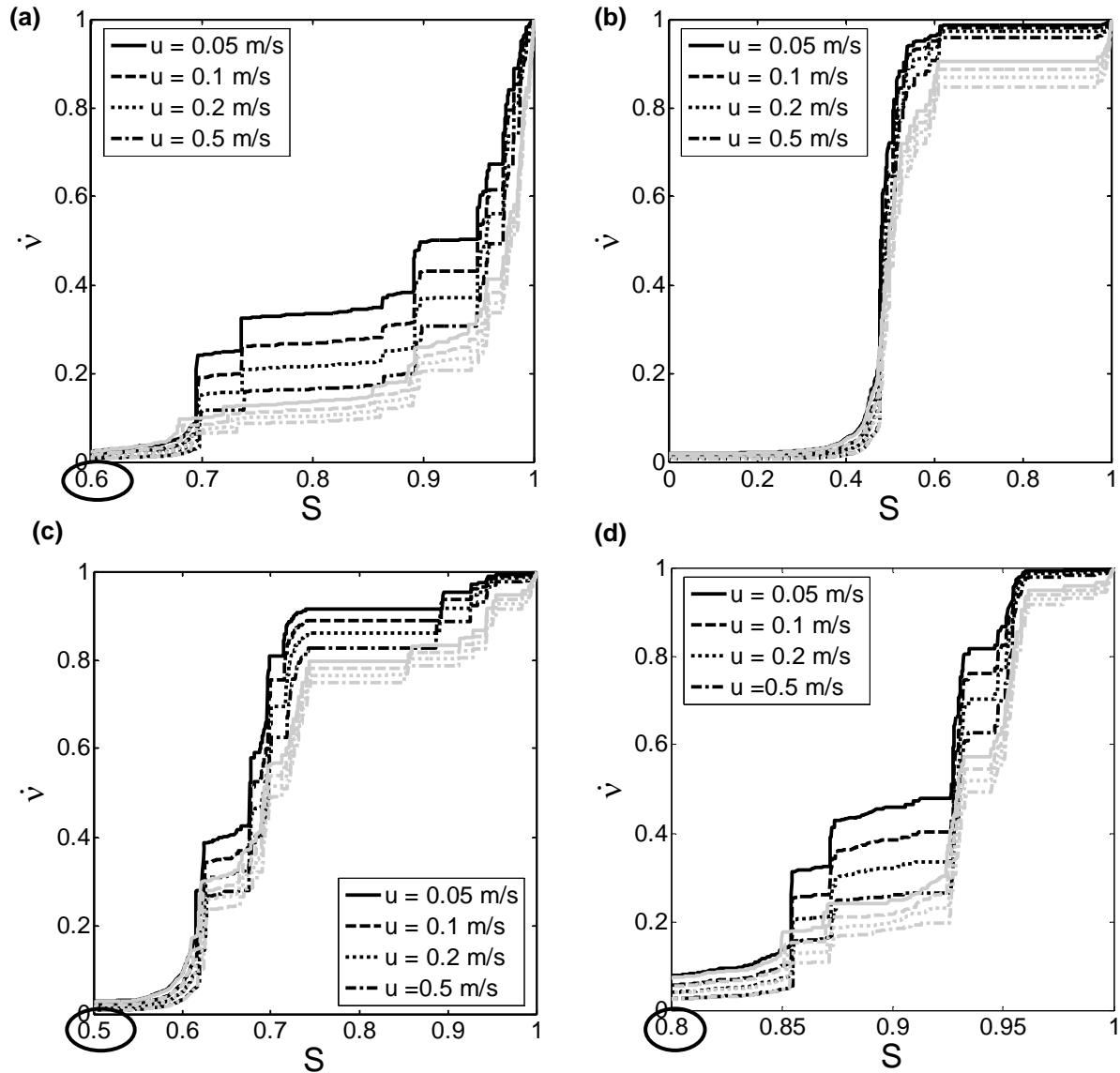


Figure 3.15: Influence of lateral vapour transfer in the boundary layer for the four different networks (a) network 1, (b) network 2, (c) network 3 and (d) network 4 at different air velocity. (Black curves are computed with a diffusive boundary layer and grey curves with a mass transfer coefficient).

The drying curve is smoothed at lower air velocity for all network structures as seen in Figure 3.15 because this condition has a thicker boundary layer or more vertical nodes in the boundary layer, which leads to more efficient lateral exchange (see Table 3.2). The drying

rate increases with increasing mass transfer coefficient for all network structures (see Table 3.3). The duration of the first drying period does not depend on boundary layer thickness and lateral exchange in the boundary layer for any network structure. It depends more on the pore structure itself, which is determined by the topological coherence of micro-macro phase in network and the spatial distribution of wet spots at the network surface. As explained in the previous discussion about the influence of network structure, network structure 2 can produce a long first drying period.

3.3.3 Influence of Wet Surface Fraction

Sometimes drying rate during the drying of porous media stays at the high initial value until saturations close to zero. This is surprising, because drying in the falling rate period would rather be expected when the moisture content is low. Schlünder (1988 [27]) tried to find out the reason of constant drying rate down to low moisture content. He found that a partially wetted surface may give the same drying rate as a totally wet surface. He assumed spherical droplets of diameter r and that the vapour from this droplet is evenly distributed on a dry surface with the distance between the droplets being d . Therefore, radius of the wet patches is small compared to the thickness of the boundary layer in order to give high lateral transfer in the boundary layer. Vapour diffusion from the droplet surface at p_v^* through the boundary layer to the bulk of air at $p_{v\infty}$ is approximated by diffusion in series as depicted in Figure 3.16b: first, from a hemisphere of radius r to one of radius $d/2$ (area 1), then from the large hemisphere through the boundary layer via a square chimney of cross section d^2 (area 2).

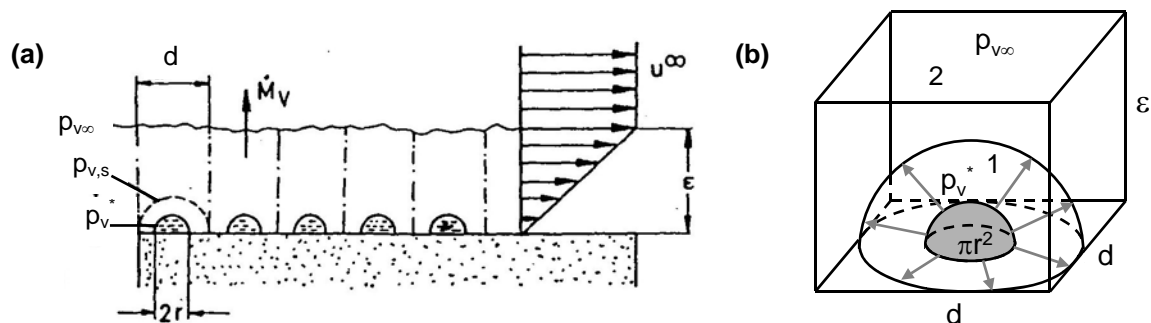


Figure 3.16: Geometry for evaporation from wet patches in Schlünder's model (Schlünder, 1988 [27])

Drying rate of each area can be calculated from the following equations:

$$\text{For hemisphere shell (area 1): } \dot{M}_{v,1} = \frac{\pi}{\frac{1}{2r} - \frac{1}{d}} \frac{\delta_{va}}{\tilde{R}_v T} (p_v^* - p_{vs}) \quad (3.5)$$

$$\text{For square chimney (area 2): } \dot{M}_{v,2} = \frac{d^2}{\varepsilon} \frac{\delta_{va}}{\tilde{R}_v T} (p_{vs} - p_{v\infty}) \quad (3.6)$$

where p_{vs} can be regarded as an average vapour pressure of the surface. The two drying rates must be equal ($\dot{M}_{v,1} = \dot{M}_{v,2}$) so that the dimensionless drying rate can be given as:

$$\dot{v} = \frac{\dot{M}_{ev}}{\dot{M}_{ev,I}} = \frac{p_{vs} - p_{v\infty}}{p_v^* - p_{v\infty}} = \frac{1}{1 + \Phi} \quad \text{with} \quad \Phi = \frac{2r}{\pi \varepsilon} \sqrt{\frac{\pi}{4\varphi}} \left(\sqrt{\frac{\pi}{4\varphi}} - 1 \right) \quad (3.7)$$

where $\dot{M}_{ev,I}$ is the drying rate for a completely wet surface, $\varphi = \pi r^2/d^2$ denotes the wet surface fraction, Φ is a reduction factor depending on the ratio of wet spot radius r and thickness of boundary layer ε as well as on wet surface fraction.

A high value of the reduction factor means that the vapour pressure at the surface is close to the vapour pressure in the bulk of air, and a low value means that the vapour pressure at the surface is close to equilibrium vapour pressure. At the limit of wet surface fraction going to zero drying rate can still be non zero because evaporation can be from the depth of the network where the menisci still exist.

We adapted Schlünder's work to the 2D network model (Irawan et al., 2005 [10]). For a square network, the vapour diffusion is considered first from small droplet as half-cylinder of radius $L/2$ to the one of radius $d/2$. It then continues via rectangular chimney of cross section area $L \times d$ and thickness of boundary layer ε to the bulk of air (see Figure 3.17).

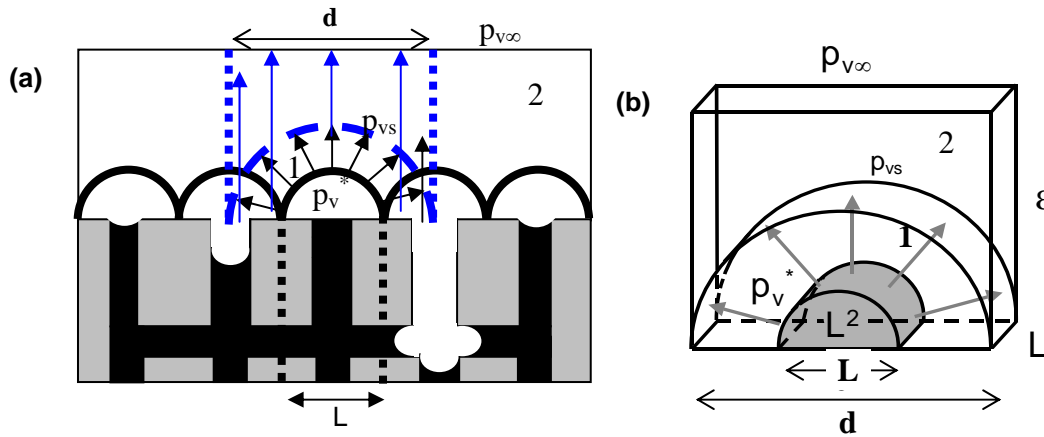


Figure 3.17: Geometry of evaporation from wet patches in adapted Schlünder's model (a) view from front and (b) in 3D view.

Vapour diffusion rates for both areas can be calculated from the following equations:

For cylindrical shell (area 1):
$$\dot{M}_{v,1} = \frac{\pi L}{\ln(d/L)} \frac{\delta_{va}}{\tilde{R}_v T} (p_v^* - p_{v,s}) \quad (3.8)$$

For square chimney (area 2):
$$\dot{M}_{v,2} = \frac{d \times L}{\varepsilon} \frac{\delta_{va}}{\tilde{R}_v T} (p_{v,s} - p_{v\infty}) \quad (3.9)$$

where L is length of the throats and d average distance between the droplets (wet surface throats). The two rates must be the same, so that the dimensionless drying rate can be defined as

$$\dot{v} = \frac{\dot{M}_v}{\dot{M}_{v,I}} = \frac{1}{1 + \Phi} \quad \text{with} \quad \Phi = \frac{1}{\pi} \frac{L}{\varepsilon} \frac{1}{\varphi} \ln\left(\frac{1}{\varphi}\right) \quad (3.10)$$

where $\varphi = L/d$ is the wet surface fraction. The reduction factor Φ is a function of wet surface fraction φ , and ratio between length of throat L and boundary layer thickness ε . Drying rates as function of wet surface fraction are investigated for four different network structures and four air velocities. Wet surface fraction φ has values in the range from 0 to 1. For $\varphi = 1$, all surface throats are (partially) saturated; For $\varphi = 0$, all surface throats are dry. Since different air velocities give different boundary layer thickness, they also change the reduction factor Φ .

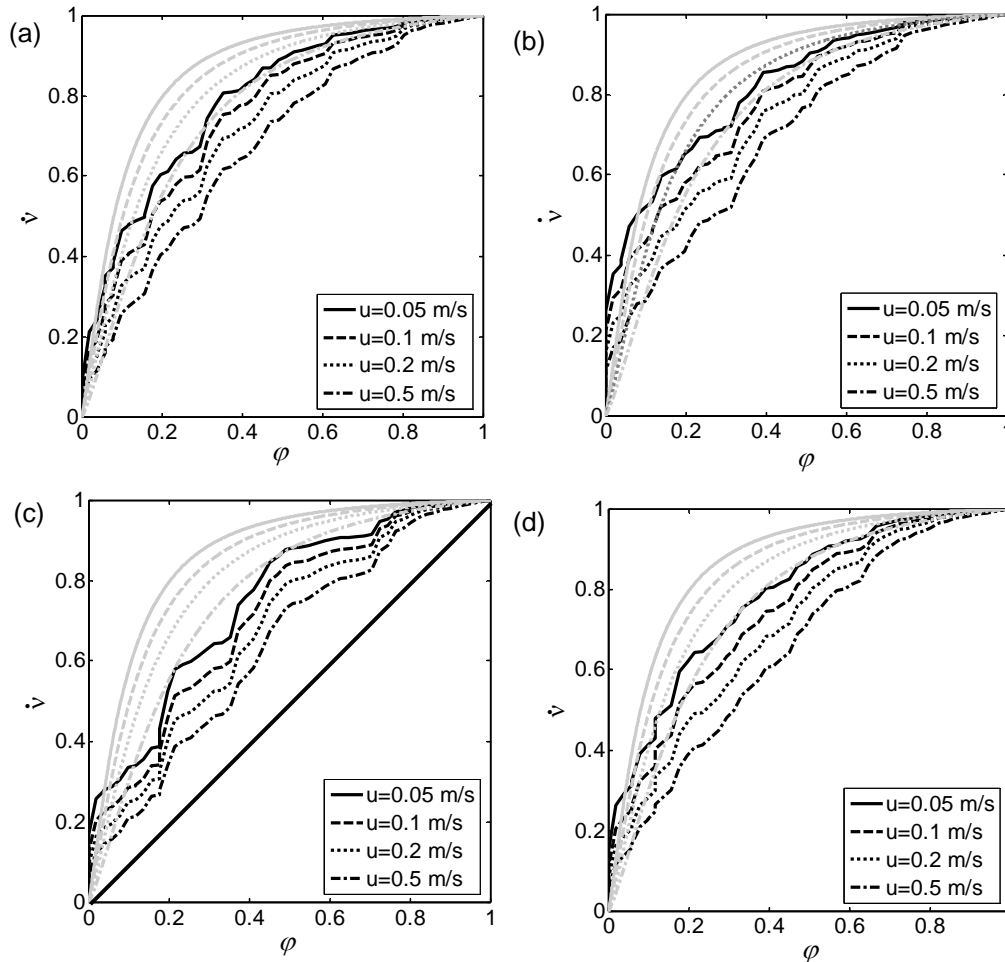


Figure 3.18: Dimensionless drying rate as function of wet surface fraction φ , for lateral transfer in boundary layer of network modelling (black curves) and Schlünder's model (grey curves). (a) Network 1, (b) Network 2, (c) Network 3 and (d) Network 4.

Figure 3.18 shows curves for a comparison between diffusive boundary layer and Schlünder's model as dimensionless drying rates versus wet surface fraction for different network structures and air velocities. These curves are not drying curves because they do not show the dependence between wet surface fraction (φ) and saturation (S), which is, again, different for the different networks. The drying rates of Schlünder's model are always higher than those for diffusive boundary layer at high wet fraction, because the wet spots in Schlünder's model are *evenly* distributed on the surface, whereas for the network drying simulations the distribution of wet surface throats can be highly correlated as for network 3. Lower air velocity that results to a thicker boundary layer can rather maintain a drying rate around the initial value, so that a lower air velocity leads to higher reduced drying rates for all network structures in both approaches (see Figure 3.18).

The first network structure has rather high reduced drying rate as shown in Figure 3.18a, because randomness of throat radius causes a good spatial distribution of wet patches on the network surface. In the second network, the position of macro and micro throats causes an almost ideal distribution of wet patches, which can also keep the reduced drying rate high. When all surface nodes of the network are dry, this network still has high drying rate because these nodes can still be at high vapour pressure due to lower vapour transfer resistance in macro channels (see Figure 3.18b). Network structure 3 has a bad wet spot distribution (see Figure 3.18c) due to isolated regions of micro throats at the surface. Lateral transfer to maintain the initial drying rate would have to be over longer distances because whole surface regions dry out in a correlated manner instead of independent single throats. The correlation between dimensionless drying rate and wet surface fraction for network structure 3 is close to the lower limit (straight line in Figure 3.18c). Network structure 4 has a better wet patches distribution (see Figure 3.18d) due to the randomness of throat radius, although this network structure has isolated macro throats.

3.3.4 Influence of Connectivity

In real porous media, nodes (pores) have a random number of throat connections to neighbouring pores. The number of connections (connectivity) determines the distribution of liquid and vapour from one throat to other throats. As explained before in the description of the model, evaporation from meniscus throats to empty throats is based on the ratio of cross section area at the connecting pore (refer to Eq. (2.18)). Therefore, the fluid that flows through a network with high connectivity will be distributed to more flow paths. Determination of equilibrium vapour pressure as boundary condition in vapour mass balance is the same for all coordination numbers. The pore is considered to be at equilibrium vapour pressure if at least one of the neighbouring throats contains liquid (also for partially filled throats).

Three different coordination numbers ($Z = 3, 4$ and 6) of 2D regular network model were simulated in monomodal and bimodal pore size distributions. The same throat volume fraction (= porosity) is set (in one unit cell) for all cases of connectivity. Therefore, a network structure with different connectivity has a different throat length. The length of square network ($Z = 4$) is used as a reference to determine throat length of other connectivities. Table 3.3 shows different parameters at three coordination numbers. In order to neglect the influence of boundary layer thickness, boundary layer thickness is set to 5 mm and number of nodes in vertical position is 10 for all coordination numbers.

Table 3.4: Parameters of network modelling for different coordination number Z .

	$Z = 3$	$Z = 4$	$Z = 6$
Throat length (μm)	$500/\sqrt{3}$	500	$500\sqrt{3}$
Size of network	101 x 58	50 x 50	59 x 17
Number of pores	5908	2500	1003
Number of throats	9829	5000	2855
Horizontal distance between two nodes in boundary layer L_x (μm)	500	500	$500\sqrt{3}$
Vertical distance between two nodes in boundary layer L_y (μm)	500	500	500

Monomodal Pore Size Distribution

The throat radii for a monomodal pore size distribution were generated as random normal with the same stochastic law for all cases of connectivity. Mean of throat radius is $40\ \mu\text{m}$, and standard deviation $2\ \mu\text{m}$. 100 Monte Carlo runs of 2D network drying model with negligible liquid viscosity were simulated in order to get a distribution of drying curves. Figure 3.19 shows the range of drying curves for 100 Monte Carlo simulations at every different coordination number. These curves show levels of cumulative distribution of drying rate: minimal, 25 %, 50 %, 75 % and maximal drying rate. The curves can be created by discretizing the saturation ($S = 0 \dots 1$) to compute a cumulative distribution of drying rate for each class of that saturation.

Due to the same value of cross section area for exchange in boundary layer ($500 \times 500\ \mu\text{m}^2$), the drying rates of connectivity 3 and 4 are more or less similar. The normalized drying rates for connectivity 6 are higher because the cross section area in the boundary layer is larger than for a connectivity of 3 or 4. Longer throat length for connectivity 6 may also contribute to the longer duration of the constant drying rate period as shown in Figure 3.19c.

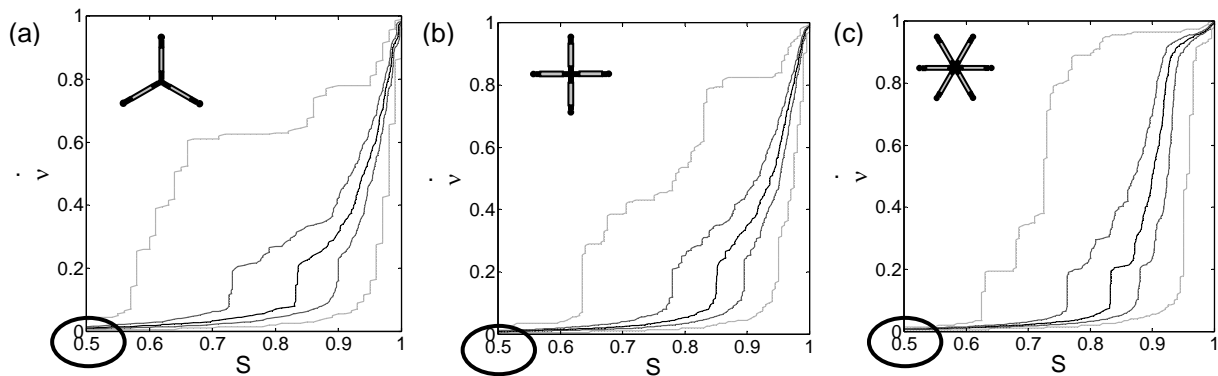


Figure 3.19: Range of drying curves for network structure with monomodal pore size distribution and different coordination number (Z) for 100 Monte Carlo runs (a) $Z = 3$; (b) $Z = 4$; (c) $Z = 6$ (minimal, 25 %, 50 %, 75 % and maximal cumulative drying rate).

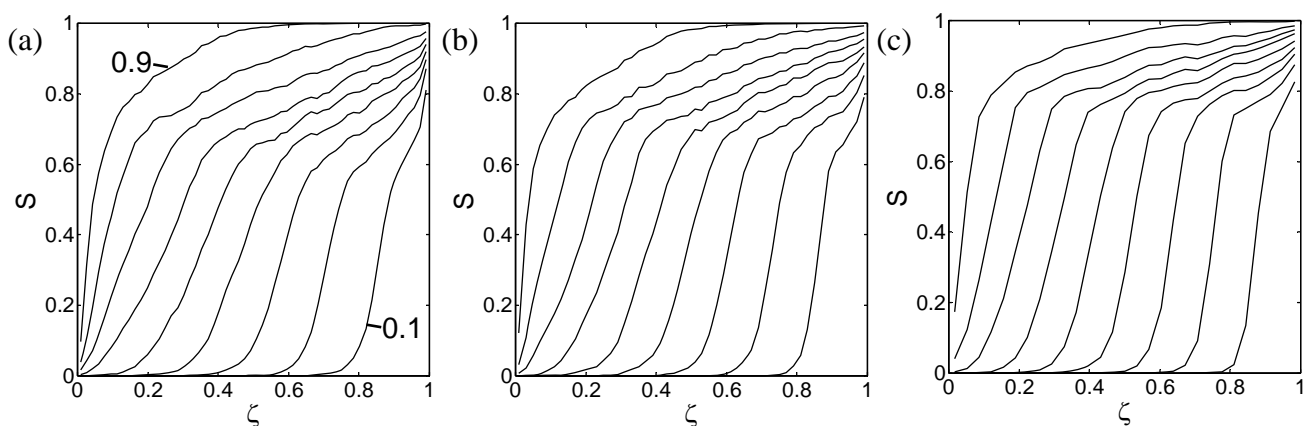


Figure 3.20: Saturation profiles for networks with coordination number (a) $Z = 3$; (b) $Z = 4$ and (c) $Z = 6$ as the averages from 100 Monte Carlo runs; (parameter is the network saturation, in steps of 10 %).

Figure 3.20 shows evolution of saturation profiles versus the dimensionless depth ζ as the abscissa. This figure can give a description of liquid distribution during constant drying period, falling drying rate period and receding front period for all coordination numbers. Surface throats of network structures with a connectivity of 3 or 4 dry rapidly (at an average saturation of about 90 %), probably because of less flow paths and shorter throat length. Longer throat length and more flow paths for coordination number 6 can deliver more liquid to the network surface. The equilibrium vapour pressure as boundary condition of vapour mass balance at the network surface can also stay for longer due to higher throat length at connectivity 6. Therefore, the network structure with a connectivity of 6 has more wet surface throats around a saturation of 90 % than the structure with other coordination numbers, as shown in Figure 3.20. Saturation profiles of connectivity 6 are steeper, because capillary pumping is not effective when one neighbouring throat of a node is empty.

Bimodal pore size distribution

In order to investigate the influence of connectivity for 2D networks with bimodal pore size distribution, network structure 2 was simulated for coordination numbers of 3 and 6 as shown in Figure 3.21. The network structure forms long channels of macro throats towards the network surface with the same tortuosity. The throat radii of macro throats are $100 \pm 5 \mu\text{m}$ (generated as normal random). The micro throats have the same size as previously, namely $40 \pm 2 \mu\text{m}$. There are four such long channels of macro throats for both coordination numbers with volume fraction 28.1 %.

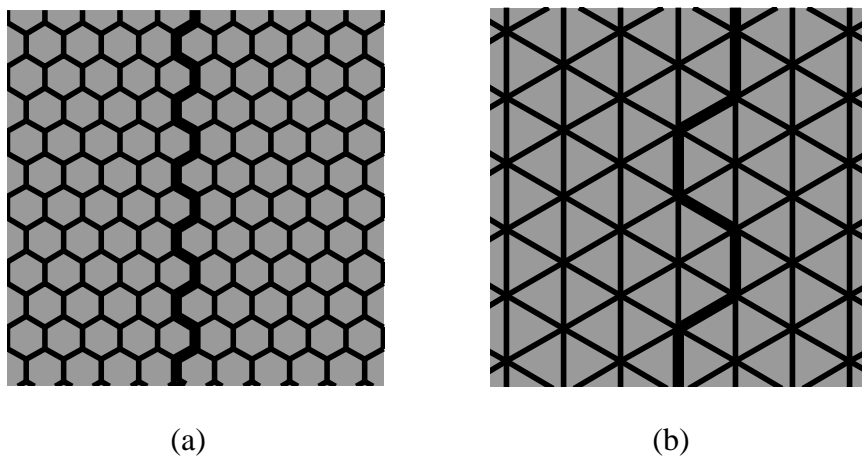


Figure 3.21: Network structures with bimodal pore size distributions and coordination numbers (a) $Z = 3$ and (b) $Z = 6$.

These network structures with bimodal pore size distribution can produce a first drying period (see Figure 3.22), where duration of this period is strongly influenced by the volume fraction of macro throats for both coordination numbers. The long channels of macro throats can give continuous capillary pumping to the throats at network surface until they are empty. Figure 3.23 shows average saturation profiles for both coordination numbers. The saturation profiles during the first drying period have a small gradient because the air invades only long channels of macro throats.

During the period of falling drying rate, the drying rate for coordination number 6 drops dramatically (Figure 3.22) and gives steeper moisture profile (see Figure 3.23). With a

coordination number of 6, the capillary flow is cut-off when one throat is empty. For a coordination number of 3, the drying rate drops slower and the saturation profiles are rather flatter, because of more full throats at the network surface and a higher possibility of capillary pumping to still deliver liquid to the network surface (see Table 3.4).

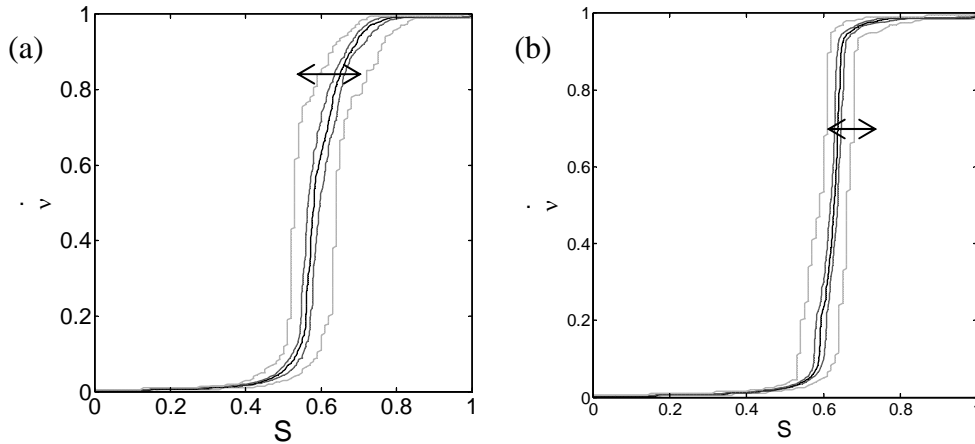


Figure 3.22: Range of drying curves for network structure with bimodal pore size distribution of coordination number (a) $Z = 3$ and (b) $Z = 6$ for 100 Monte Carlo runs (minimal, 25 %, 50 %, 75 % and maximal cumulative drying rate).

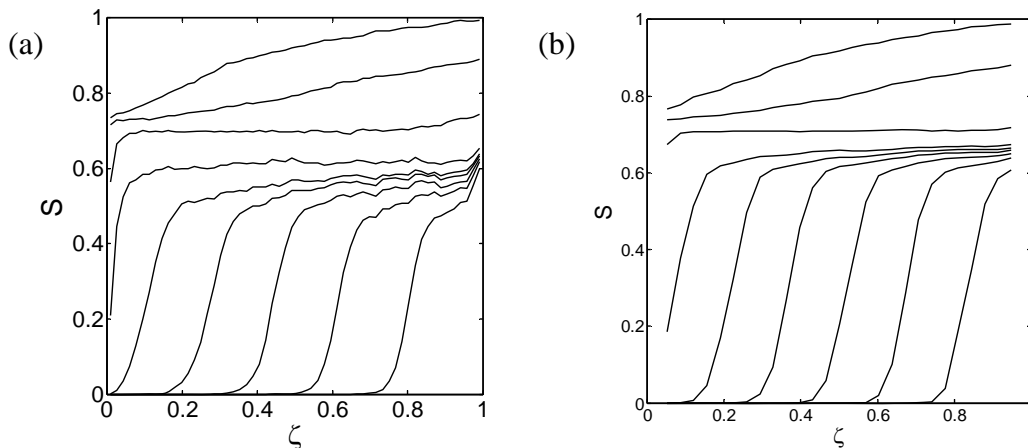


Figure 3.23: Saturation profiles for networks with coordination number (a) $Z = 3$ and (b) $Z = 6$ as the averages from 100 Monte Carlo runs with bimodal pore size distribution (parameter is the network saturation, in steps of 10 %).

3.4 Drying of 2D Square Networks with Liquid Viscosity

Drying of 2D square networks with negligible viscous force was presented in the last section. In those simulations, capillary forces were assumed always dominant over viscous forces. Therefore, the variation of mean throat radius r_0 and standard deviation σ_0 plays almost no role. In order to further investigate the influence of pore size distribution on the behaviour of isothermal drying porous media, we have introduced the liquid viscous effect in the modelling. The liquid mass flow rate through a cylindrical throat in the presence of viscosity is:

$$\dot{M}_{w,k} = \frac{\pi r_k^4}{8\nu_w L_{w,k}} (p_{w,i} - p_{w,j}) \quad (3.11)$$

where r_k is throat radius, $L_{w,k}$ length of liquid throat, ν_w kinematic viscosity of liquid and $p_{w,i}$ liquid pressure at neighbouring pore i .

Since $\dot{M}_{w,k} \sim r_k^4$, smaller throat radii are used in the following simulations in order to get lower maximal flow rates and therefore a higher influence of friction. The throat radius is around 100 nm for micro throats and 250 nm for macro throats. In that range of throat radius, a reduction of equilibrium vapour pressure due to Kelvin effect can still be neglected. Similarly, the Knudsen effect may still be neglected. The competition of viscous forces and capillary forces can be described by the dimensionless Capillary number (see Eq.(1.14)):

$$Ca = \frac{\text{viscous forces}}{\text{capillary forces}} \quad (3.12)$$

High capillary number means that viscous forces are dominant, and low capillary number means that capillary forces are dominant. As in the previous simulations, four different network structures were investigated, taking the lowest air velocity ($u = 0.05$ m/s). As mentioned before, a thick boundary layer leads to effective lateral transfer. The size of network is 51×51 nodes and the throat length is $5 \mu\text{m}$ so that total network size is $0.025 \times 0.025 \text{ mm}^2$ and there are 100 vertical nodes in boundary layer.

At first, the boundary condition for vapour diffusion is investigated in the light of partially empty and refilling throats. Later on, periodic boundary conditions are applied to the networks by connecting left and right border. The influence of such a periodic boundary condition is investigated by simulating drying for 10 different network realizations with the same spatial radius distribution as the non periodic ones. Next, the influence of different network structure will be also investigated in order to know the effectiveness of capillary pumping in different topology of network structures in presence of liquid friction. Then, the influence of viscosity is investigated to find out the ranges of dominant capillary or viscous forces for each network structure. The range of viscosity is from absolutely dominant capillary forces (negligible viscosity) to absolutely dominant viscous forces (immobile water condition). Viscous and capillary forces are also influenced by throat radius. The influence of pore size distribution is investigated by variation of mean and standard deviation of the monomodal network structure 1, and by variation of the difference between the mean radii of micro and macro throats for bimodal pore size distribution of network structure 2. In another simulation, vertical and horizontal throats are arranged to create a 2D network similar to a bundle of capillaries. Mean and standard deviation of throat radius are varied and the results are compared with those of a bundle of capillaries model (Irawan et al., 2006 [11]).

In order to investigate the influence of randomness of throat radius, 10 different random generations of throat radius of each network structure are simulated. From these, the range of drying curves for each network structure can be predicted. Additionally, the influence of network depth for structure 2 (very efficient capillary pumping) and structure 1 (rather inefficient capillary pumping) was investigated.

3.4.1 Position of Boundary Condition (Equilibrium Vapour Pressure)

In order to solve the vapour mass balances, this model needs boundary conditions. One of these boundary conditions is equilibrium vapour pressure at the liquid-gas interface in the network. The position of this boundary condition must be defined, i.e. at the pore or in throat due to state of throats (partially filled throats). In reality, the pore can be considered at equilibrium vapour pressure if at least one neighbouring throat is full, i.e. if a meniscus is directly located at the pore. If only partially filled throats are neighbours to the pore, these throats have vapour diffusion from meniscus to the pore position. Consequently, vapour pressure at the pore is lower than equilibrium vapour pressure. But in the drying model with viscosity, this definition of equilibrium vapour pressure can lead to oscillating drying rates because the meniscus of the throat can move to be filled or emptied due to the competition between viscous and capillary forces. Figure 3.24 shows this phenomenon.

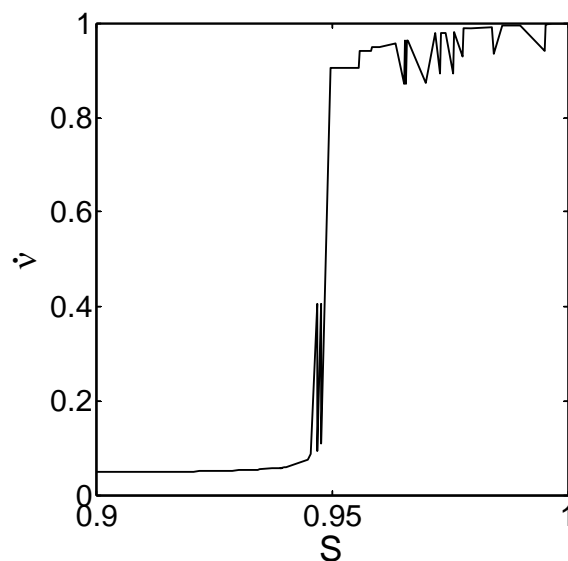


Figure 3.24: Drying rate curve as calculated with true position of boundary condition of equilibrium vapour pressure.

An oscillating drying rate, as in Figure 3.24, can be explained as shown in Figure 3.25. The description of the phenomenon is:

- Figure 3.25a shows the phase distribution of water of one cluster in the network with three full meniscus throats ($r_2 > r_3 > r_1$) at network surface. This condition has high drying rate. All meniscus throats are candidate moving menisci to be emptied or filled. Due to high drying rate, the biggest throat radius (r_2) will be emptied first but also the meniscus in throat 3 will move resulting in a partially filled throat (see Figure 3.25b). Note, that quasi steady flow is assumed during one time step (complete filling or emptying of a throat).
- After emptying the biggest throat as seen in Figure 3.25b, three new meniscus throats are created ($r_5 > r_4 > r_6$). Then, partially filled throat 3 has a resistance in vapour phase. Due to this resistance, local evaporation rate is decreased. Now, the network has five menisci ($r_5 > r_3 > r_4 > r_6 > r_1$) with very small deviation of throat radius. Due to decreasing drying rate, capillary pumping from the biggest meniscus throat 5 can completely fill meniscus throat 3.
- When partially filled throat 3 changes to full throat, as shown in Figure 3.25c, drying rate is increased again.

To omit such oscillations in the drying curve, pores which have a partially filled throat as neighbour are assumed to be at equilibrium vapour pressure (p_v^*). By this, vapour transfer from meniscus to pore node is assumed to be without resistance, and drying rate will be systematically overestimated by a small amount.

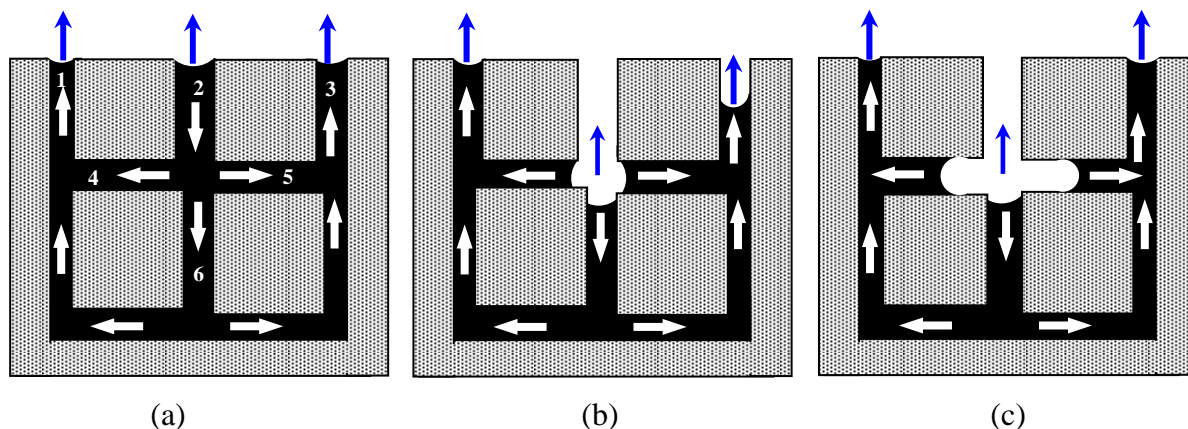


Figure 3.25: An illustration of the phenomenon of oscillating drying rate when boundary condition of equilibrium vapour pressure is taken at the menisci: (a) high drying rate (b) low drying rate and (c) high drying rate.

3.4.2 Influence of Periodic Boundary Conditions

Due to limitations of computation time to simulate big networks as better representatives of the porous medium, left and right network borders were removed and both sides of the network were connected. In this way, capillary pumping might be more efficient in transporting liquid to the surface throats due to more available connections. In order to investigate the influence of such a periodic boundary condition on drying kinetics, we simulated network structure 1 with 10 different radius realizations with and without periodic boundary condition. Network structure 1 is chosen as most sensitive to this change because of random capillary fingering.

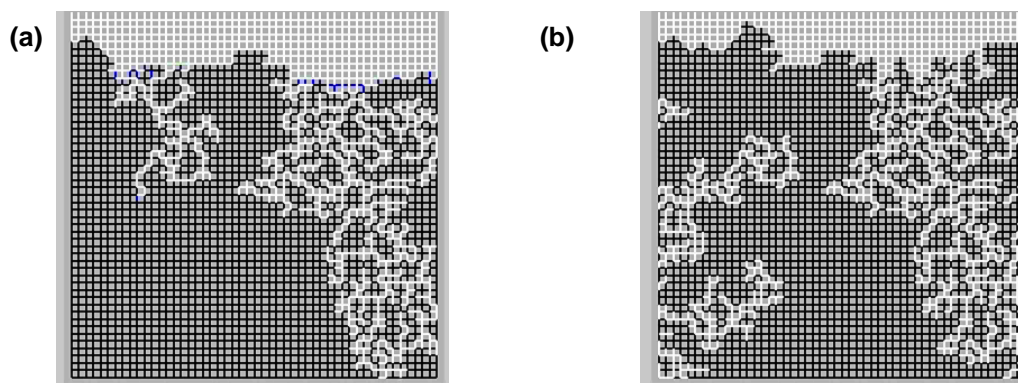


Figure 3.26: Phase distribution in network structure 1 at $S \approx 70\%$ (a) without periodic boundary condition and (b) with periodic boundary condition.

Figure 3.26 shows phase distributions for the same network saturation comparing non-periodic and periodic conditions. In Figure 3.26b, gas can invade the left network border due to periodic boundary condition so that near surface throats may stay filled and the additional resistance to vapour diffusion at the top of the network is lower. The big cluster in periodic boundary condition has more menisci than the nonperiodic so that the probability of emptying throats at the network surface is lower than for the nonperiodic boundary condition. Figure 3.27 shows the drying curve of 10 random structures with non periodic and periodic boundary condition. In that figure, the drying curve for periodic boundary condition is less influenced by the random variation because the air can invade more menisci in the depth of the network (see left side in Figure 3.26b). Therefore, the evaporation front for periodic boundary conditions is closer to the network surface than for non periodic boundary condition. This condition will give higher drying rate due to shorter additional vapour resistance.

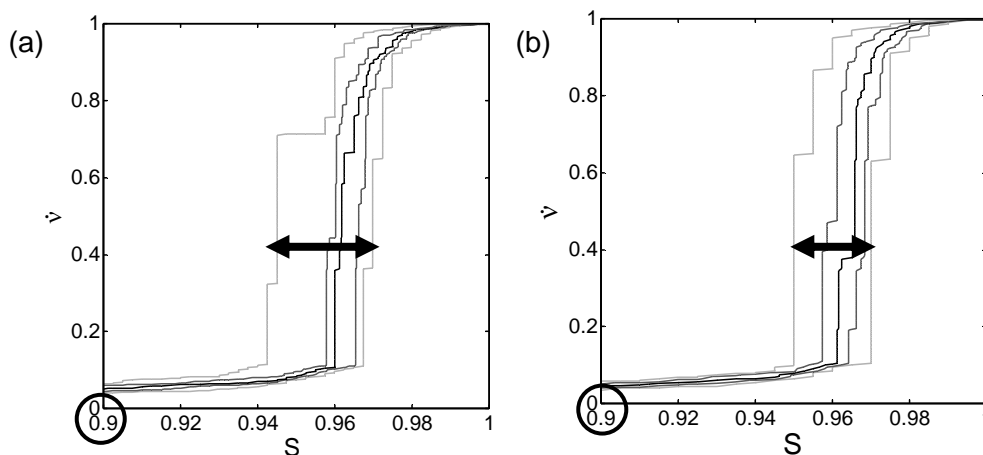


Figure 3.27: Range of drying curves for drying simulations with 10 different realizations of structure 1 using (a) non periodic and (b) periodic boundary conditions.

3.4.3 Influence of Structure

When liquid viscosity was negligible, only the biggest throat in a cluster has emptied; now, moving meniscus throats are defined by comparing evaporation rate and liquid flow. The throats can be filled or emptied depending on both rates as discussed in section 2.3.5. Figure 3.28 shows normalized drying curves for the different network structures. Network structure 1 has a small difference of capillary pressure between meniscus throats because this structure has only micro throat radius ($r_0 = 100$ nm) with small standard deviation ($\sigma_0 = 10$ nm). Due to this, capillary pumping from the biggest throat of micro throats plays a role only for a short time. When evaporation rate is higher than capillary pumping to the surface, throats dry out rapidly and there is no first drying period. Quasi constant periods at high rates seem to have disappeared because the capillary pumping is not efficient in transporting the liquid to the throats close to the network surface.

Network structure 2 has a bimodal pore size distribution and macro throats are arranged to form long channels. Macro throats will empty first and capillary pumping from these throats will be enough to supply liquid to other meniscus throats at the local evaporation rate, due to big differences in capillary pressure between macro (250 nm) and micro throats (100 nm). Therefore, standard deviation in macro and micro throats (10 nm) does not influence the capillary pumping as long as a liquid cluster still has macro throats. This structure has a long first drying period.

For network structure 3, capillary pumping from macro throats can transport liquid to surface throats, but this capillary pumping cannot prevail for long because the emptying of horizontal macro throats cuts off capillary pumping to the region of micro throats. Then, capillary pumping in this isolated cluster is provided by the biggest micro throat radius. For network structure 4, capillary pumping from macro throats plays a role for only short time, until all macro throats which are close to the network surface are empty.

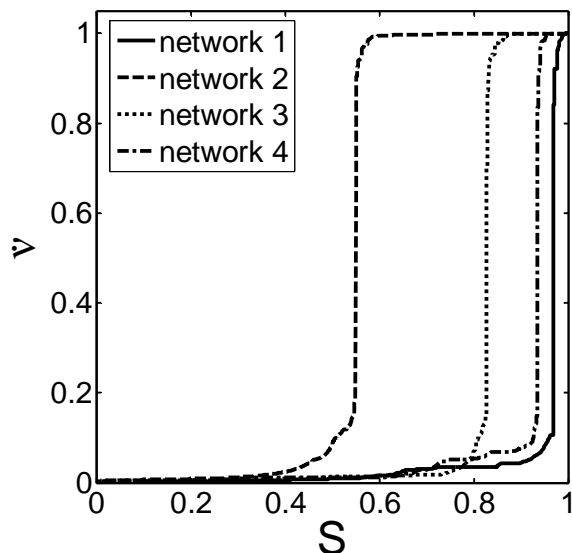


Figure 3.28: Drying curves for different network structure including viscous forces.

3.4.4 Influence of Liquid Viscosity

Liquid viscosity (η) is the major parameter to adjust and investigate the influence of viscous forces. In this simulation, liquid viscosity is varied over a wide range between two limits. The investigated cases are no viscous forces (negligible liquid viscosity), low liquid viscosity, liquid water viscosity at 20°C, high liquid viscosity and no capillary pumping (immobile water). Capillary pumping from the biggest throat of each cluster is always dominant over viscous forces in case of negligible liquid viscosity. In case of immobile water, capillary pumping is not enough to supply liquid to any other meniscus throat. We have simulated those cases in different network structures with a periodic boundary condition.

Figure 3.29 shows normalized drying curves for the four network structures to observe the influence of liquid viscosity. In the negligible viscosity condition (dominant capillary pumping) only network structure 1 can not reproduce a first drying period, but several quasi constant drying periods, as shown in Figure 3.29a. These quasi constant periods can prove that capillary pumping still plays a role at some level. For bimodal pore size distribution, capillary pumping from the biggest throats is effective to transport liquid to the surface throats so that these network structures can reproduce a short first drying period. Then, the network was simulated at low value of liquid viscosity ($\eta = 0.0001$ Pa s). For this liquid viscosity, capillary pumping still dominates over viscous forces although its role slightly decreases, especially for network structures 1 and 4, as shown in Figure 3.29a and d. This is caused by friction forces when capillary pumping is lower than evaporation rate.

All network structures in case of dominant viscous forces (immobile water) have low drying rate because capillary pumping can not transport liquid to the surface throats. Therefore, this condition has a sharply receding front from the beginning of drying. When liquid viscosity is

at a high, but finite value ($\eta = 0.01$ Pa s), only network structure 1 with monomodal pore size distribution produces low drying rates from the very beginning, like in case of a receding front, because of small capillary pressure differences. Other network structures with bimodal pore size distribution can produce a first drying period due to capillary pumping from macro throats, but capillary pumping can supply liquid to the surface throat over only a short period. Even the surface of network structure 2 with macro throats of around 40 % volume fraction dries out quickly with high friction forces at that liquid viscosity. At normal water viscosity ($\eta = 0.001$ Pa s), capillary pumping assures a long first drying period until a saturation of 60 % as compared to the case of high liquid viscosity ($\eta = 0.01$ Pa s), where the first drying period only lasts until a saturation of 80 %, see Figure 3.29b. When capillary pumping is again enough to supply the necessary evaporation rate of cluster meniscus throats, then this structure has a constant drying rate but at a low level (quasi constant drying period).

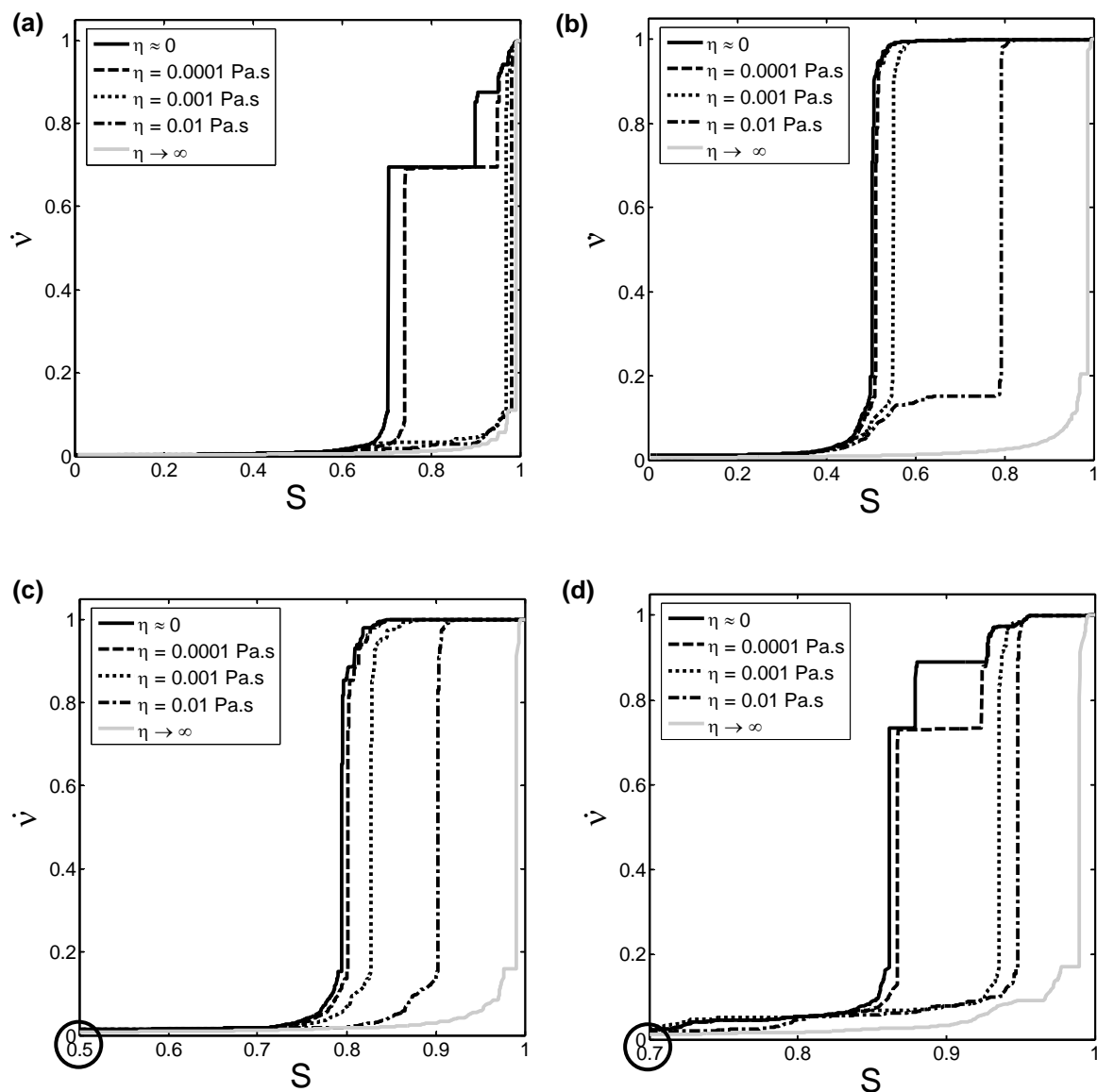


Figure 3.29: Drying curves including viscous forces at different liquid viscosities for different network structures: (a) network 1, (b) network 2, (c) network 3 and (d) network 4.

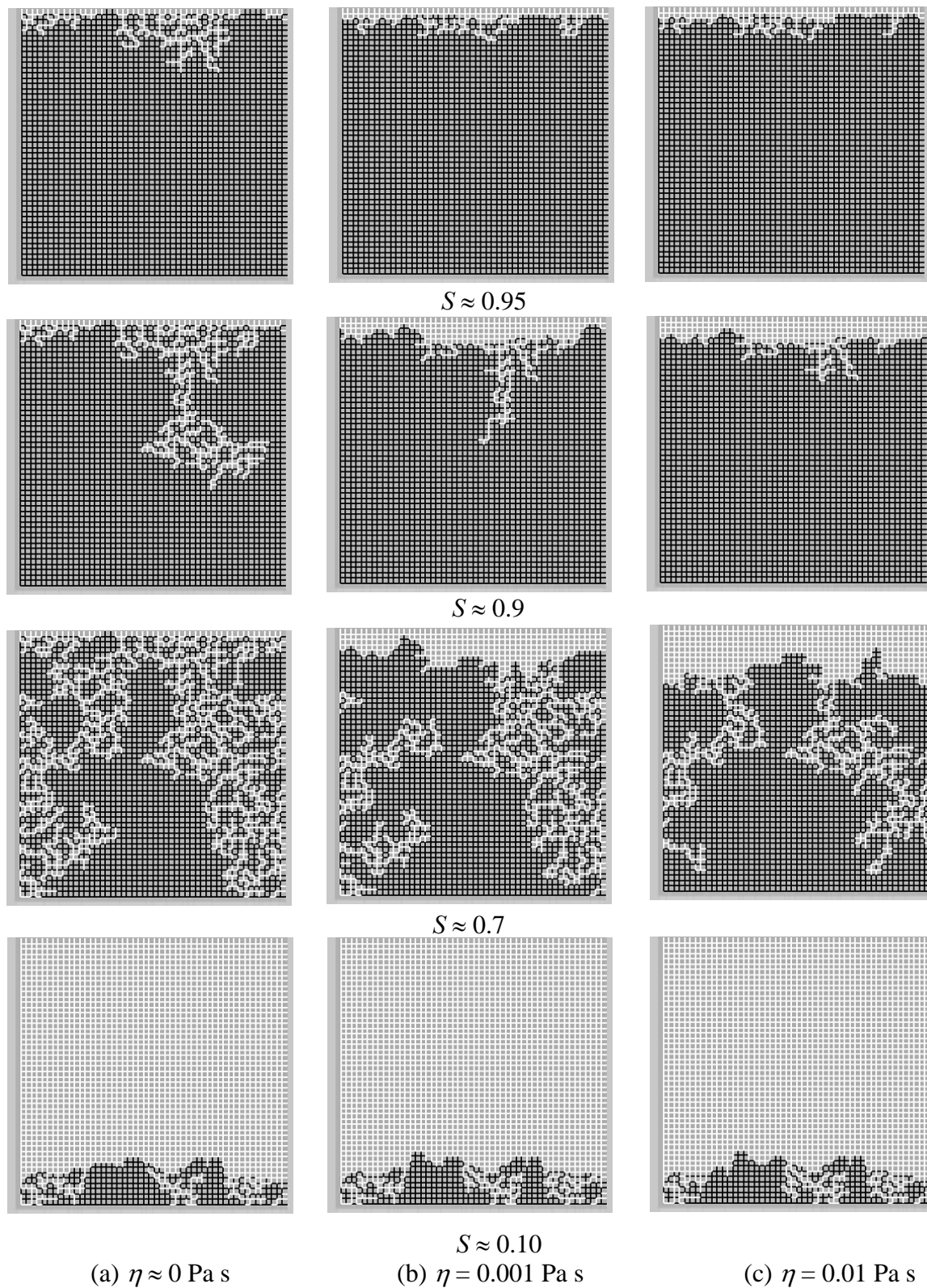


Figure 3.30: Phase distributions for network 1 with periodic boundary conditions at different network saturations and different liquid viscosities (a) no viscous forces (b) water viscosity at 20°C and (c) high viscosity. The liquid phase is black and the gas phase is white.

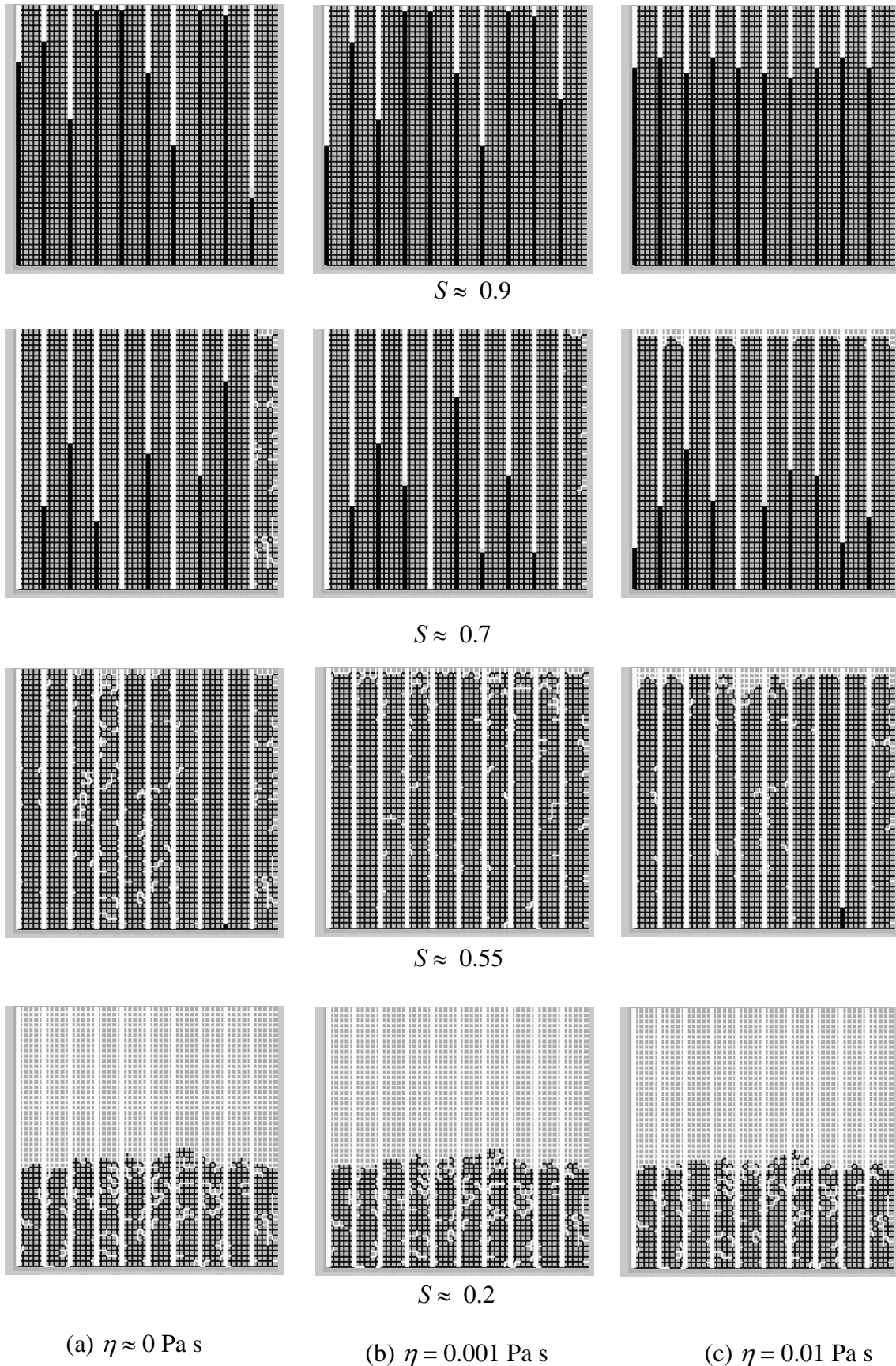


Figure 3.31: Phase distributions for network 2 with periodic boundary conditions at different network saturations and different liquid viscosities (a) no viscous forces (b) water viscosity at 20°C and (c) high viscosity. The liquid phase is black and the gas phase is white.

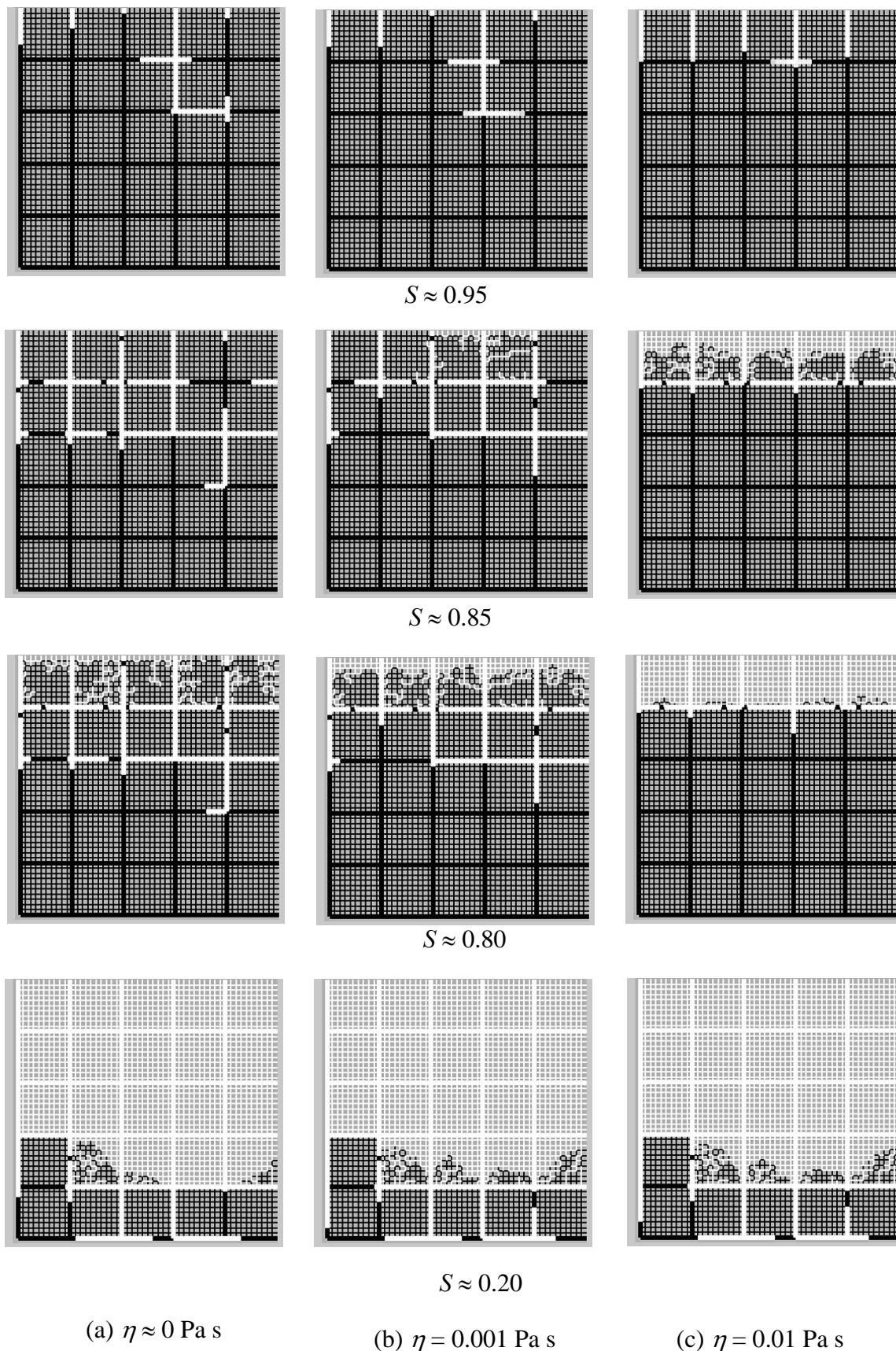


Figure 3.32: Phase distributions for network 3 with periodic boundary conditions at different network saturations and different liquid viscosities (a) no viscous forces (b) water viscosity at 20°C and (c) high viscosity. The liquid phase is black and the gas phase is white.

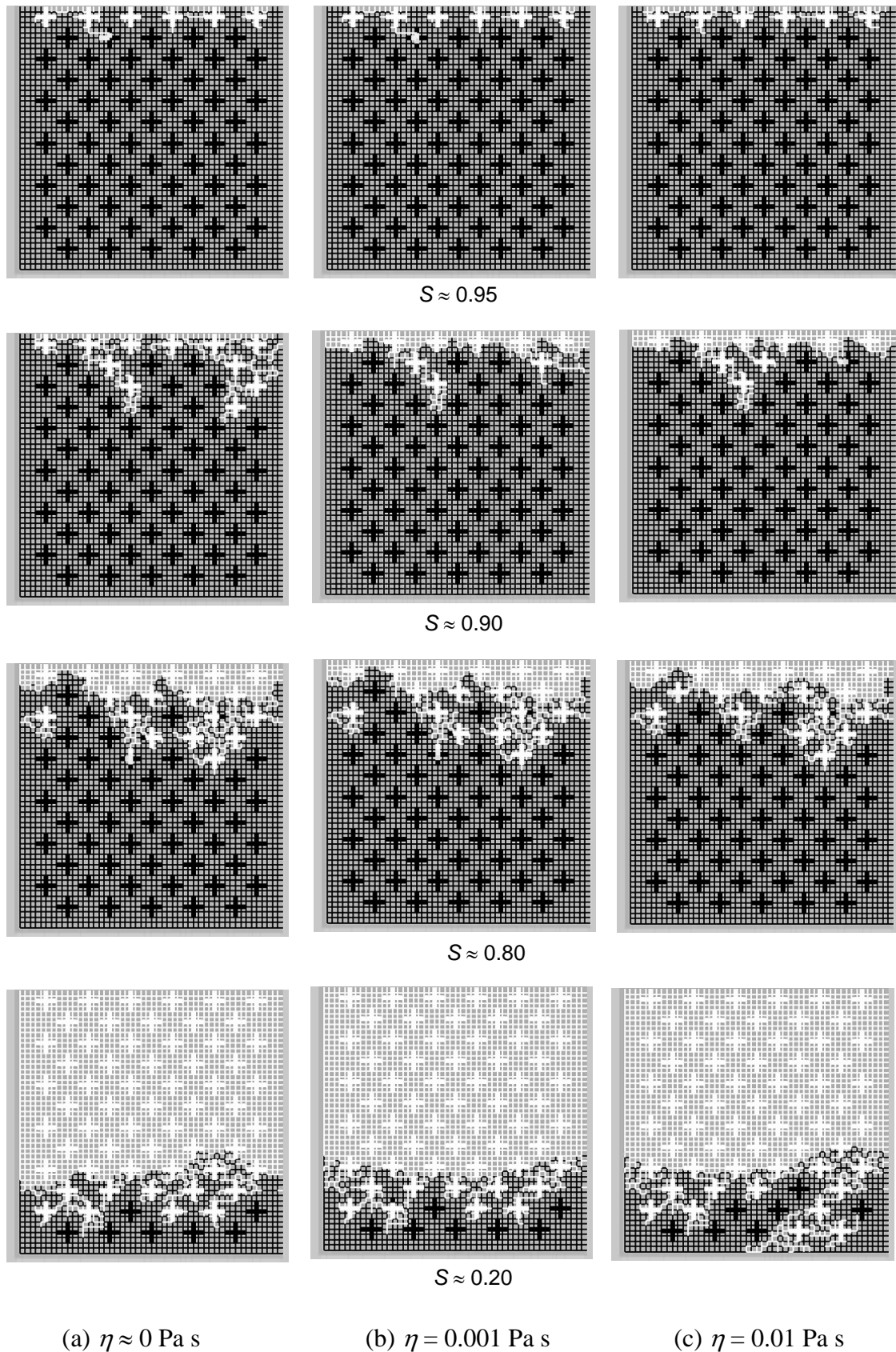


Figure 3.33: Phase distributions for network 4 with periodic boundary conditions at different network saturations and different liquid viscosities (a) no viscous forces (b) water viscosity at 20°C and (c) high viscosity. The liquid phase is black and the gas phase is white.

Figures 3.30 to 3.33 show liquid phase distributions for four network structures with different network saturation and different liquid viscosity. Liquid viscosity conditions are negligible liquid viscosity, liquid viscosity at 0.001 Pa s and liquid viscosity at 0.01 Pa s (high viscosity). These phase distributions can give a better understanding of the relevant phenomena for each structure. In the phase distribution of network structure 1 (Figure 3.30), capillary pumping still dominates over viscous forces at saturation 95 % for negligible liquid viscosity. This capillary pumping can supply liquid to the network surface, so that the drying rate is still at high level. For the two other liquid viscosity conditions, all surface throats have dried out at that network saturation, so that capillary pumping can not supply liquid to the surface. The appearance of quasi constant drying rate in the drying curve can also be explained by phase distribution at saturation 90 % (start) and 70 % (end). For this range of saturations, capillary pumping is from meniscus throats in the depth of the network to a small number of wet surface throats (see phase distribution in Figure 3.30 at saturation 70% and 90 %). The dried region widens up when the drying rate drops to low values, because at high viscous forces the capillary flow is not enough to supply sufficient liquid and sustain the evaporation rate. This condition can be seen in the phase distribution for high liquid viscosity and saturation around 70% (see Figure 3.30c).

For network structure with bimodal pore size distribution, the appearance of a first drying period in the drying curve (see Figure 3.29) is caused by capillary pumping from macro throats to the network surface (see phase distributions in Figures 3.31 to 3.33). At high liquid viscosity, the first drying period is shorter because the surface throats dry rapidly. Capillary pumping from moving menisci can still supply liquid to some meniscus throats close to the network surface, where it evaporates.

3.4.5 Influence of Pore Size Distributions

During drying, liquid flow in the network is driven by capillary pressure difference between meniscus throats. In the presence of liquid viscosity, the maximum flow rates depend on the size of throats and on their size difference which lead to differences in capillary pressure. A variation of throat size will also have a certain influence on vapour diffusion rates in the gas phase. Therefore, a variation of both mean and standard deviation of the radius distribution is of interest, if the role of friction is to be studied. Network structure 1 (monomodal) and 2 (bimodal) will be studied in this sense for the true value of water viscosity. This simulation took the same spatial radius distribution (normal random) and rescaled it with specific mean throat radius and standard deviation.

Monomodal pore size distribution

Figure 3.34 shows the drying curves for monomodal pore size distribution of network structure 1 with different mean throat radii and standard deviations. Standard deviation of throat radius is varied in the range from 1 nm to 25 nm with mean of throat radius at 100 nm. From Figure 3.34a, one can see that a broad range of throat radii ($\sigma_\theta = 25$ nm) has a longer first drying period than other standard deviations, because broad range leads to higher capillary pressure differences.

Subsequently, the variation of mean throat radius was investigated in order to find out how this variation influences drying behaviour. Three different mean throat radii ($r_\theta = 100, 200$ and 400 nm) at standard deviation 5 nm were applied and the results are shown in Figure 3.34b. All three cases have a short first drying period due to rapid drying of surface throats. During capillary pumping, the drying process has three significant and simultaneous aspects of mass

transfer. These are evaporation at the network surface, capillary pressure difference between two meniscus throats and viscous forces in liquid phase. In this simulation, evaporation rate depends on boundary layer thickness at the beginning of drying process so that the evaporation rate does not depend on the throat radius. The two other aspects of mass transfer depend on the throat radius as follows:

- The pressure drop at the menisci, Δp_f very much depends on the throat radius:

$$\Delta p_f = \frac{8\eta_w \dot{M}_v L}{\rho_w \pi r_0^4} \sim \frac{1}{r_0^4} \quad (3.13)$$

- The capillary pressure difference, Δp_c depends less on the throat radius:

$$\Delta p_c = 2\sigma \left(\frac{1}{r_0 - \sigma_0} - \frac{1}{r_0 + \sigma_0} \right) \approx \frac{4\sigma\sigma_0}{r_0^2} \sim \frac{1}{r_0^2} \quad (3.14)$$

From those relations, the friction forces decrease more rapidly than the capillary force with increasing throat radius at the beginning of drying. Therefore, the capillary pumping is more successful in delivering liquid to the surface for evaporation. In the drying curve for the largest mean throat radius ($r_0 = 400$ nm) a quasi constant drying period appears. If throat radius is increased by a factor of 4, this means that the capillary forces increase with a factor of 16 in relation to the friction forces. As a result, quasi constant drying periods may occur.

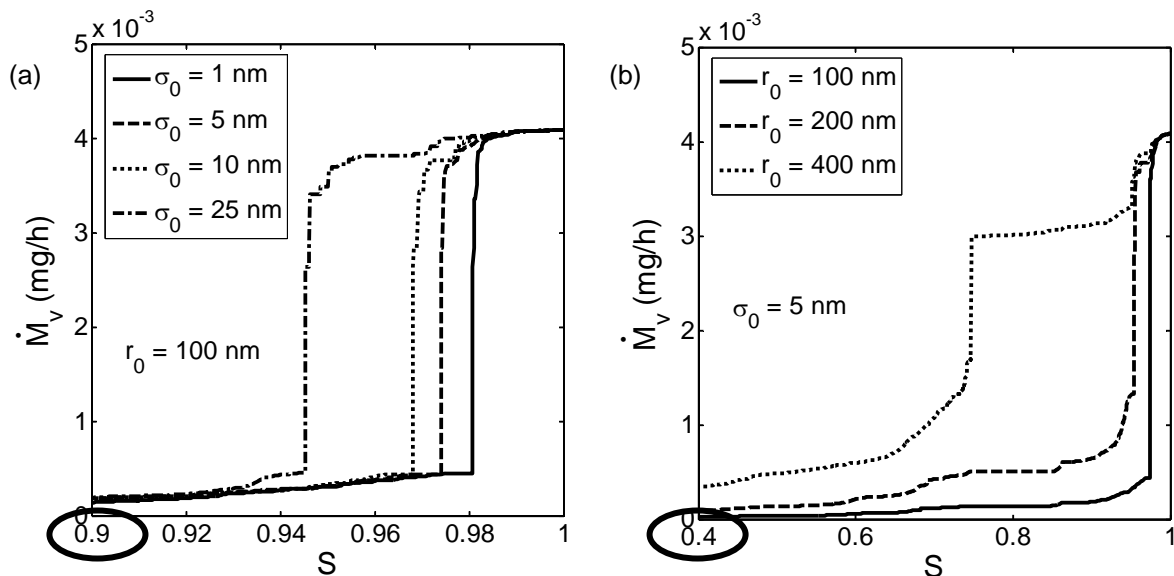


Figure 3.34: Drying curves for monomodal pore size distributions of network 1 with (a) different standard deviation σ_0 and (b) different mean throat radius r_0 .

Figure 3.35 shows liquid phase distributions at $S \approx 90$ % for different mean throat radii. It illustrates how liquid can be pumped over large distances with high evaporation rates at large mean throat radius. Note that for this example the change in r_0 from 100 nm to 200 nm leads to almost no difference in drying behaviour. Only an increase of r_0 to 400 nm enables a significant change of phase distribution.

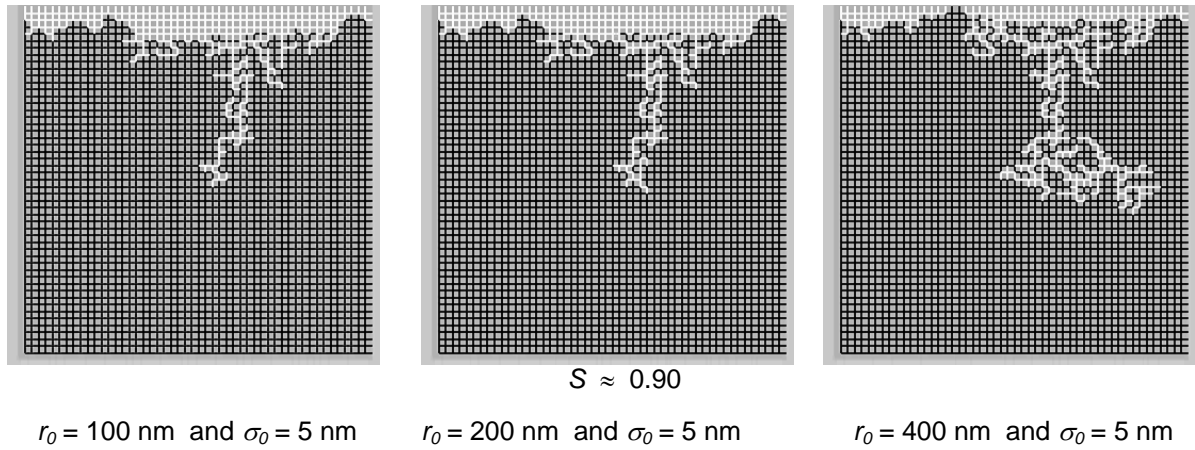


Figure 3.35: Phase distribution at $S \approx 0.90$ for monomodal pore size distribution of network 1 with different mean of throat radii.

Bimodal pore size distribution

Network structure 2 with bimodal pore size distribution will be investigated by varying the mean size of macro throats. Variation of mean macro throat radius will give different distances between means of micro and macro throat radius and also a different volume fraction of macro throats. The distance between mean of micro and macro throat radius (Δr) correlates with the capillary pressure difference. A small distance leads to small capillary pressure difference and low capillary pumping, so that surface throats empty rapidly. A large distance leads to high capillary pressure differences and more important capillary pumping. The micro throats have a radius 100 nm with a standard deviation 10 nm; the macro throats are chosen with radii of 250, 400 and 500 nm and a standard deviation of 10 % of the mean radius.

Figure 3.36 shows drying rates for simulated bimodal pore size distributions as a function of normalized saturation ($\tau = S/S_{\text{micro}}$), where S_{micro} is the initial liquid volume fraction of micro throats in the network. Network 2 has a long first drying period due to large distance between macro and micro throats radii ($\Delta r > 100 \text{ nm}$) because the friction forces do not have any effect when the liquid is transported to the micro throats. The capillary pressure difference between two macro throat radii depends on the throat radius:

$$\Delta p_c = 2\sigma \left(\frac{1}{r_{\text{macro},1}} - \frac{1}{r_{\text{macro},2}} \right) \approx \frac{4\sigma\sigma_0}{r_0^2} \sim \frac{1}{r_0^2} \quad (3.15)$$

This means that with increasing the macro throat radius, the capillary pumping between macro channels will be better, so that the liquid throats at the network surface dry out more evenly (see phase distribution in Figure 3.37). Therefore, the duration of first drying period is not influenced by the size of macro throats radius, but it is influenced by the volume of throats (saturation).

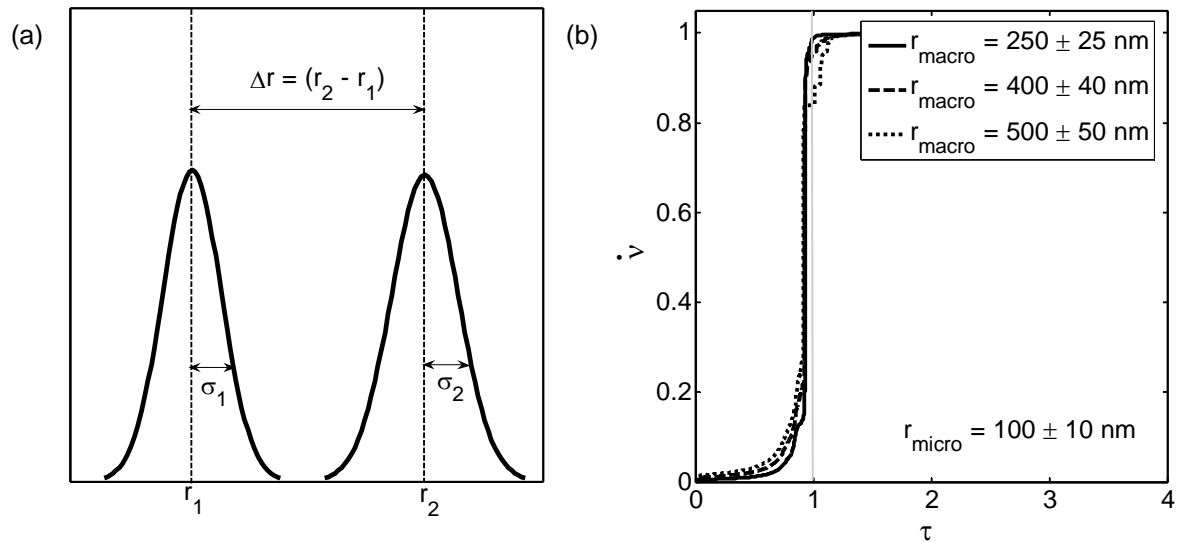


Figure 3.36: (a) Distance between mean micro and macro throat radii for bimodal pore size distributions and (b) drying curves for bimodal pore size distributions of network 2 with different distances between mean macro and micro throat radii.

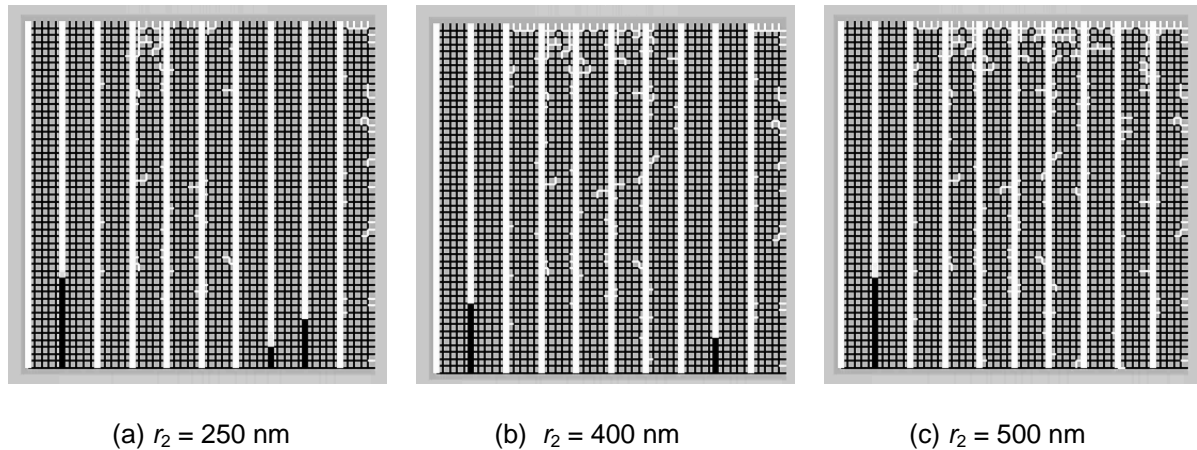


Figure 3.37: Phase distributions for bimodal pore size distribution of network 2 when $\tau = 1$ for different mean macro throat radius ($r_2 = 250, 400$ and 500 nm).

Comparison with Bundle of Capillaries

In order to better understand the influence of pore size distribution on drying behaviour, the bundle of capillaries model (Metzger and Tsotsas, 2005 [18]) can be used as a simple model for drying of porous media. The transport mechanisms are exactly the same as in the network model, viscous capillary pumping in the liquid and vapour diffusion in the gas. In this model, some cylindrical capillaries are set perpendicular to the product surface. All cylindrical capillaries are connected along their length without any resistance and divided into N_k classes of decreasing radii r_i according to a given distribution (see Figure 3.38b). Initially, all capillaries are completely filled with water, then large capillaries will empty first during drying due to capillary pumping.

This model was applied to 50 classes of cylindrical capillaries. Then radius of cylindrical capillary is generated with a normal distribution of varying mean (100, 200 and 400 nm) and standard deviation (1, 5, 10 and 25 nm). The length of capillaries is 0.1 m for all classes.

Drying conditions are the same as for the network model (absolutely dry air at 20°C and atmospheric pressure with a mass transfer coefficient of $\beta = 0.1$ m/s).

In order to compare bundle of capillaries and network models, the geometry of the network model is set up close to the bundle of capillaries. Vertical throats are arranged to form representatives of capillary tubes. Their radii are chosen according to the same normal distributions as for the bundle of capillaries model. Horizontal throats are a connection between long tubes of vertical throats to allow good lateral exchange. In order to neglect resistance between vertical channels, the horizontal throats have very small throat length; additionally, they are of small radius so that they will empty last. Therefore, capillary pumping from vertical throats can be maintained to supply liquid to the surface throats. Non-uniform geometric progression was applied for vertical throats length. Length of the vertical throat is set to decrease towards the network surface (see Figure 3.38a). Therefore, the vertical throat that is closest to the network surface has the shortest length. The length of the vertical throat at the network surface is kept short, because the last meniscus position very strongly influences the drying rate. Parameters of simulation of network model are exactly the same as in the bundle of capillaries model. Vertical throats of the network model have 50 horizontal throat connections. In contrary to the above networks, here the solid phase is not modelled ($\psi = 1$).

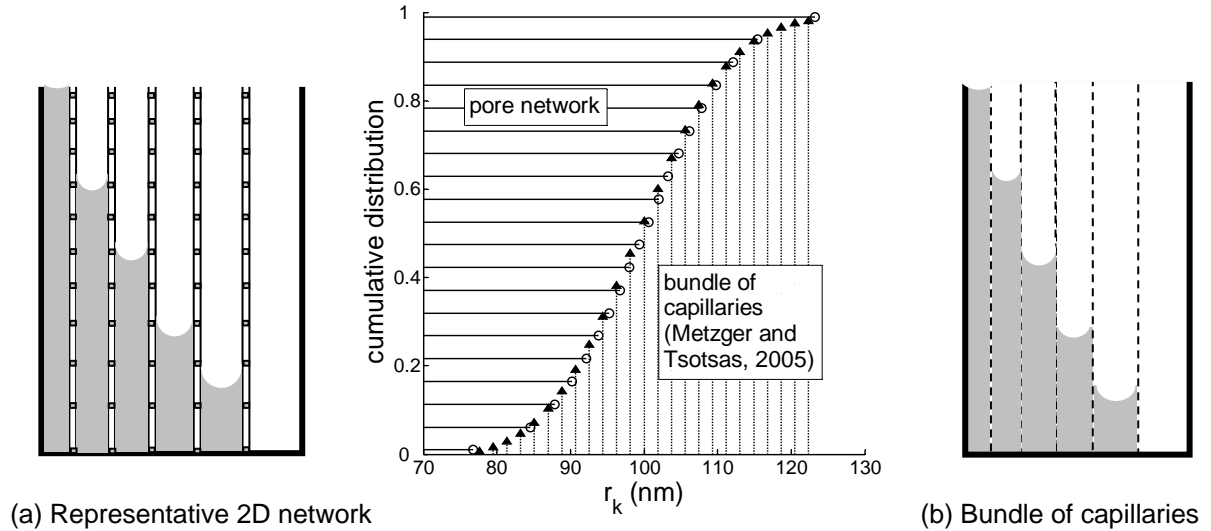


Figure 3.38: Cumulative normal distribution of radius for bundle of capillaries and network equivalent.

Figures 3.39a and 3.40 show normalized drying curves for different mean radii and standard deviations as obtained from both models. Thick lines represent the results of network model and thin dashed lines are the results of the bundle of capillaries model. It can be seen that networks with a broad pore size distribution dry with a long first drying period due to high capillary pressure difference between the capillary menisci. In the bundle of capillaries model (Metzger and Tsotsas, 2005 [18], Irawan et al., 2006 [11]), this phenomenon can be explained by the equation for the flow velocity v through a capillary of radius r_0 :

$$v = \frac{r_0^2}{8\eta_w} \frac{\Delta p_c}{L_k} \quad \text{with} \quad \Delta p_c = 2\sigma \cdot \left(\frac{1}{r_0 - \sigma_0} - \frac{1}{r_0 + \sigma_0} \right) \approx \frac{4\sigma\sigma_0}{r_0^2} \quad (3.16)$$

According to this equation, a broad pore size distribution ($\sigma_0 = 25$ nm) has a high velocity to supply liquid to other menisci.

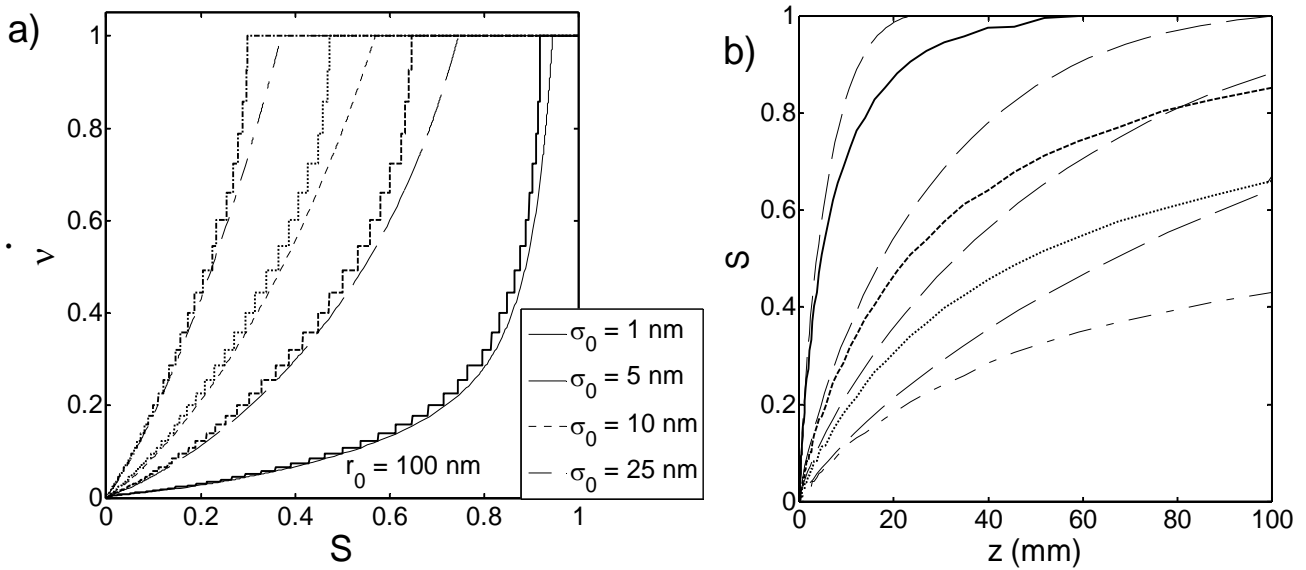


Fig. 3.39: Drying curves (a) and moisture profiles at end of first drying period (b) for a bundle of capillaries with normally distributed radius – comparison between bundle of capillary model (thin lines) and network model (thick lines).

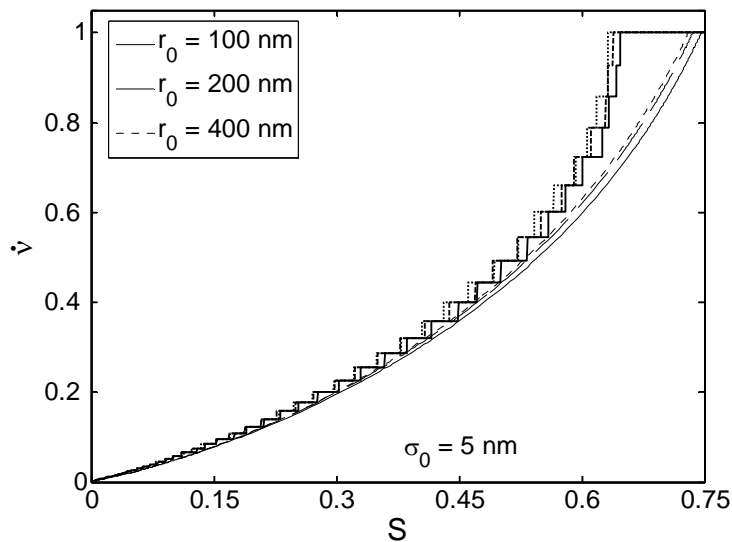


Fig. 3.40: Drying for a bundle of capillaries with normally distributed radius – comparison between capillary and network model.

The end of first drying period is reached because high drying rate can not be maintained by capillary pumping for transporting the liquid to the network surface. Then, the last meniscus with small size will move down to the horizontal throat. Figure 3.39b shows moisture profiles at the end of first drying period (critical point). From Eq. (3.16) we can also conclude that the same drying rate, i.e. the same velocity, can be achieved for different r_0 , and we can state that the drying curve is almost not influenced by the size of capillary radius (see Figure 3.40). This is because there is no difference between total cross section area of capillaries (for liquid and vapour transport in the network) and network surface (for evaporation to bulk air). Above, we obtained different results because the variation of throat radius r_0 was decoupled from network surface area (see Fig.3.34).

Both models correlate well as seen in Figures 3.39 and 3.40 because drying curves and moisture profiles of both models in variation of mean radius and standard deviation show the same trends. However, the duration of the first drying period is slightly overestimated by the network model, and the moisture profiles are flatter than for the capillary model, especially in

the depth of the network. These differences are not fully understood but may be due to different modelling of horizontal resistances and the absence of a zero flux condition (at the bottom) for the bundle of capillaries model.

Monte Carlo Simulations

In order to investigate the influence of random throat radius generation on drying behaviour, drying of 10 networks which were each randomly generated according to the same stochastic rule is simulated in this section for four network structures and non-periodic boundary condition. We have simulated only 10 random network generations due to the limitation in computation time. Figure 3.41 shows curves of normalized drying rate for those network structures. Starting with 10 drying rates, for each saturation, the cumulative distribution of dimensionless drying rate is computed. The plotted lines correspond to 25, 50, and 75 of this distribution. One individual drying curve can, however, intersect the average curves (see the example of the dashed line in Figure 3.41a). The grey lines give the range of all the drying curves.

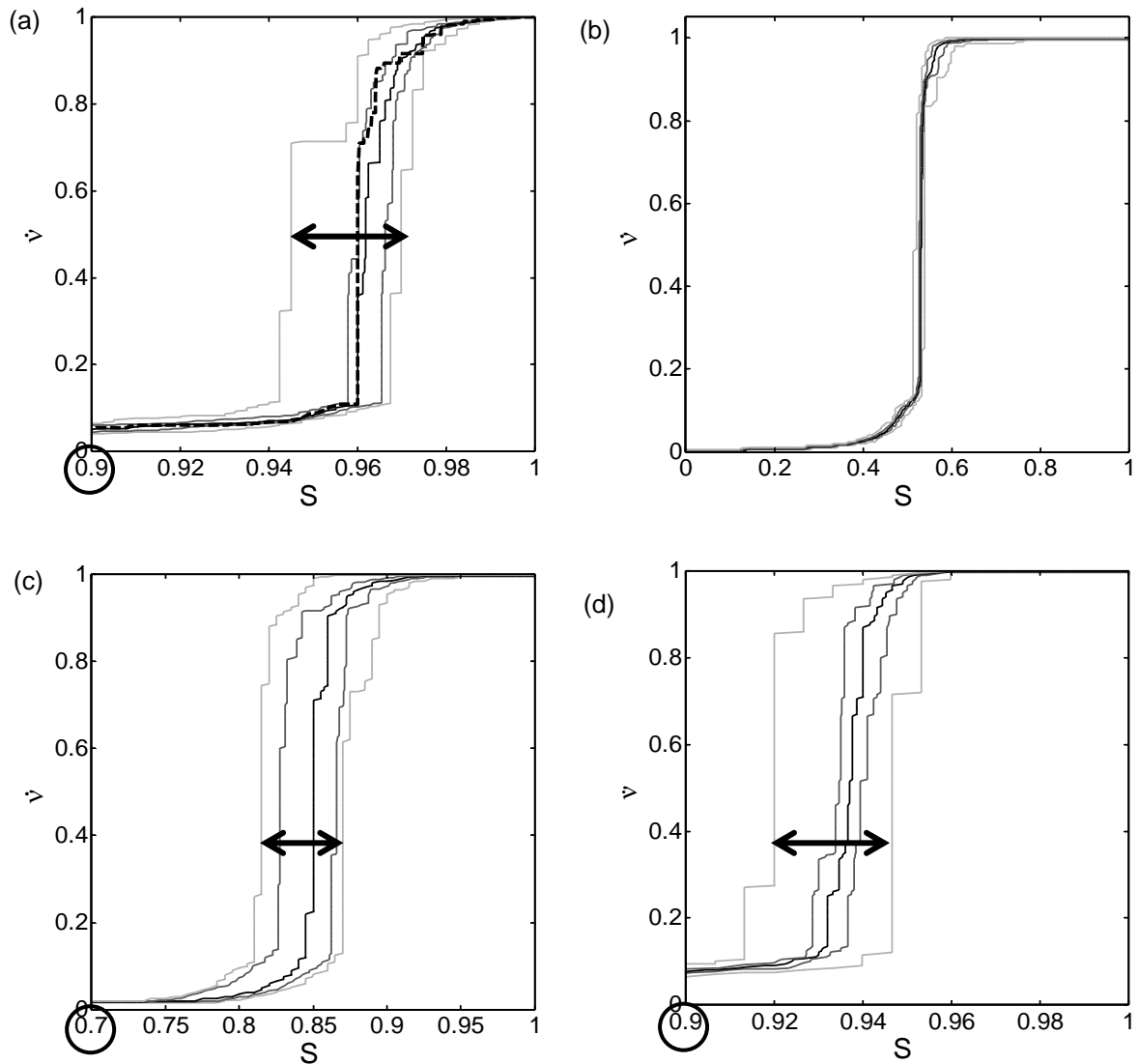


Figure 3.41: Drying curve ranges of drying simulations with 10 different network structures for (a) network 1 (b) network 2 (c) network 3 (d) network 4.

Randomness of throat radius leads to different drying kinetics of each generated network as seen in Figure 3.41. Random variation for network structure 2 only changes little the drying kinetics because the macro throats will be in the same position (long channels) and empty first. In the network structure 3, the end of the first drying period occurs by cutting off capillary pumping from macro throats to the micro throats at network surface. The cutting off of liquid flow by emptying of horizontal macro throats is a random process which depends on the realization of throat radii. Due to random cutting off of the liquid flow, the drying rate of network structure 3 has a broad variation region in the falling rate period. The quasi constant periods of this structure are usually longer than the respective periods for network structures 1 and 4 because the macro throats can still transport to the evaporation front (the liquid throats closest to the network surface) and isolated regions of micro throats play the role of “single throats” (see phase distribution in Figure 3.42). Networks 1 and 4 are highly dependent on the random generation because network 1 only consists of random micro throats. The network 4 was influenced by random generation after all macro throats, that are close to the network surface, are empty.

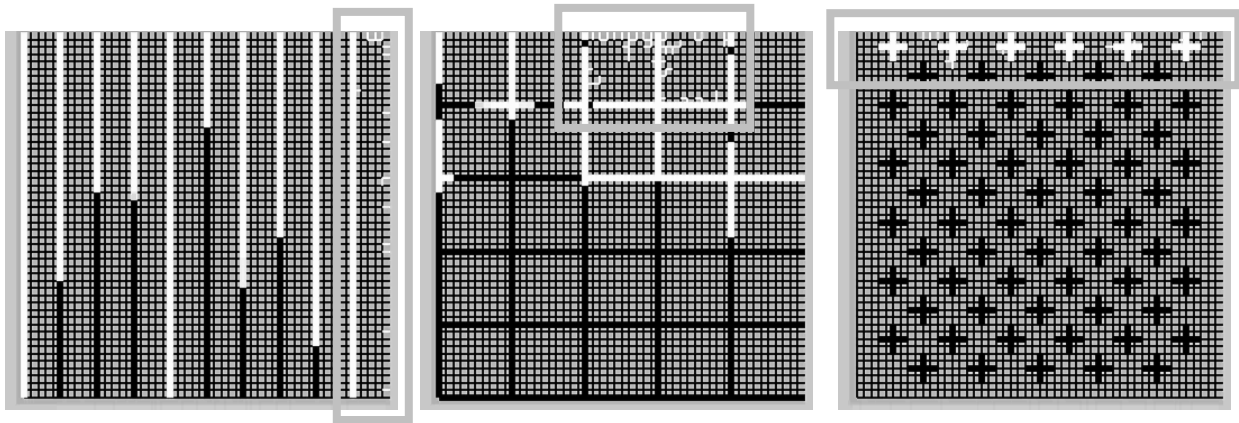


Figure 3.42: Phase distribution of bimodal pore size distribution when drying rate decreases.

Figure 3.42 shows phase distributions for network structures 2, 3 and 4 with bimodal pore size distributions at the end of the first drying period. The end of first drying period for network structure 2 is signed by the creation of new clusters where micro throats are disconnected. The same condition is valid for network structure 3: the first drying period will end when a region of micro throats is disconnected and forms a new cluster. For network 4, when all surface macro throats are empty, the first drying period will end although full macro throat radii still exist in the cluster, but the phase boundary will not easily reach them because they are isolated by micro throats. Therefore, the ending of first drying period depends for all network structures on the randomness of macro throats. Grey thick blocks in the phase distributions of Figure 3.42 show network parts with empty surface throats. Figure 3.43 shows phase distributions for two random realization of network structure 3 at a saturation of $S \approx 0.9$. The two random networks have different phase distributions due to randomness of throat radius. Part of structure surface has already dried at that saturation for one random realisation of throat size distribution, while all surface throats are still wet for the other.

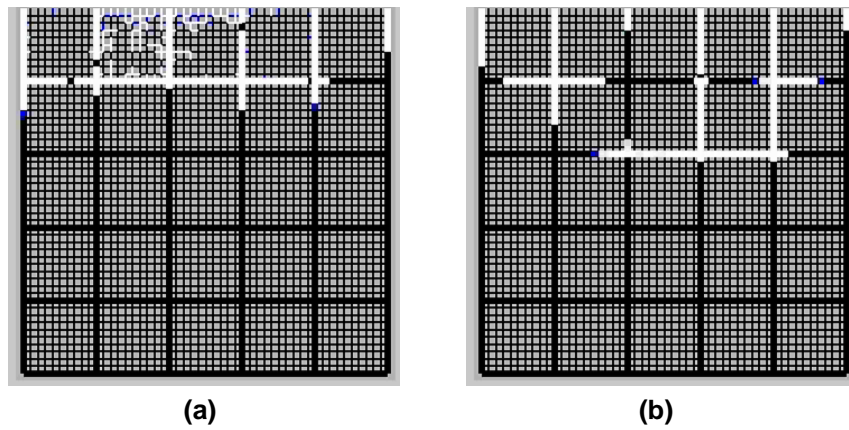


Figure 3.43: Phase distributions for two random realizations of network structure 3 at $S \approx 0.90$.

3.4.6 Influence of Network Depth

Drying was also simulated with networks of different depth ($51 \times 11 \dots 101$) for network structures 1 and 2. Network structures for this simulation can be seen in Figure 3.44. The largest network is generated first. Then, part starting at the surface are taken down to different depths. Therefore, the drying kinetics is only influenced by increasing network depth and not by random throat radius.

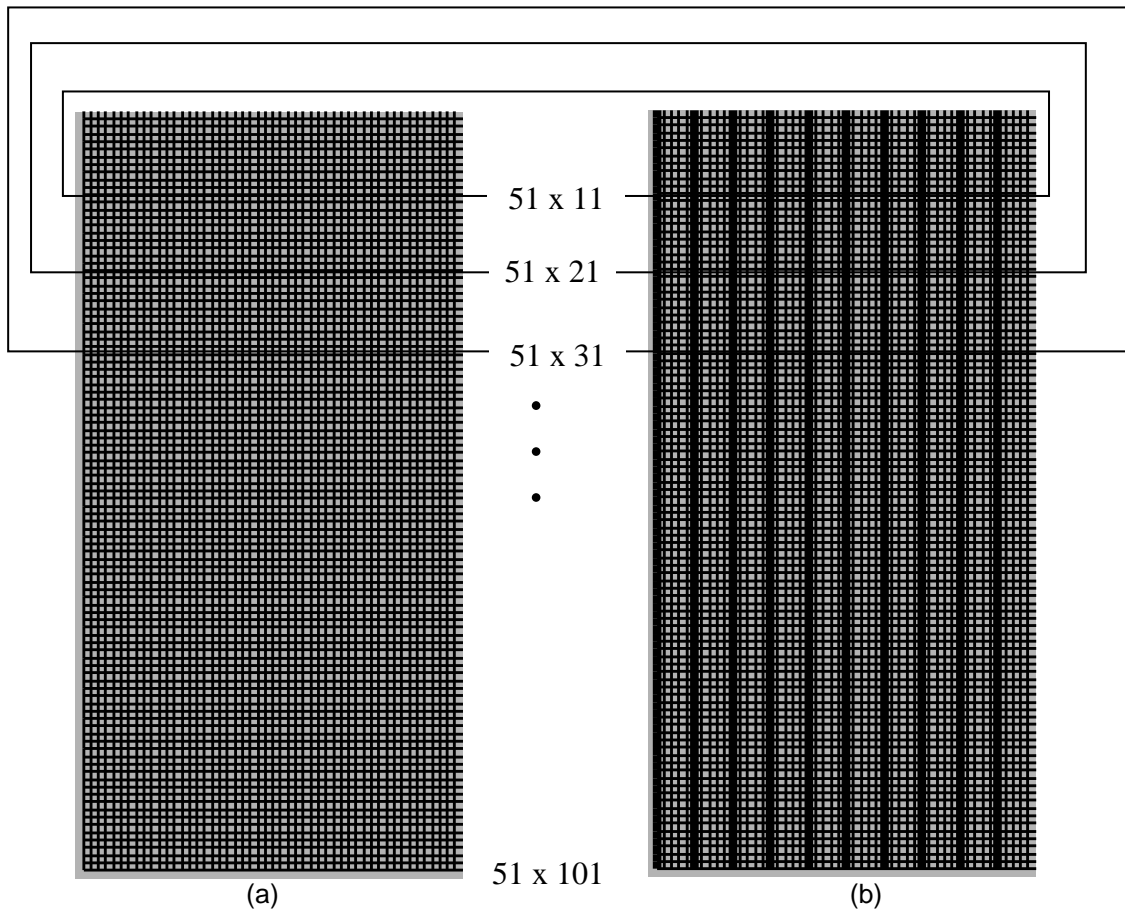


Figure 3.44: Representative networks for simulating the influence of network depth
(a) network structure 1 (b) network structure 2.

Figure 3.45 shows the drying curves for network structures 1 and 2 with different abscissa. Due to the constant number of throats at network surface, the shortest network for structure 1 gives the longest first drying period (see Figure 3.45a) because this network has the highest fraction of wet spots at network surface. The results for network structure 2 are shown in Figure 3.45b as drying rate over evaporated mass of water. The amount of water evaporated in the first period increases linearly with network depth because capillary flow during the first period is supplied from long channels of macro throats until they are empty (Metzger, et al., 2005 [17]).

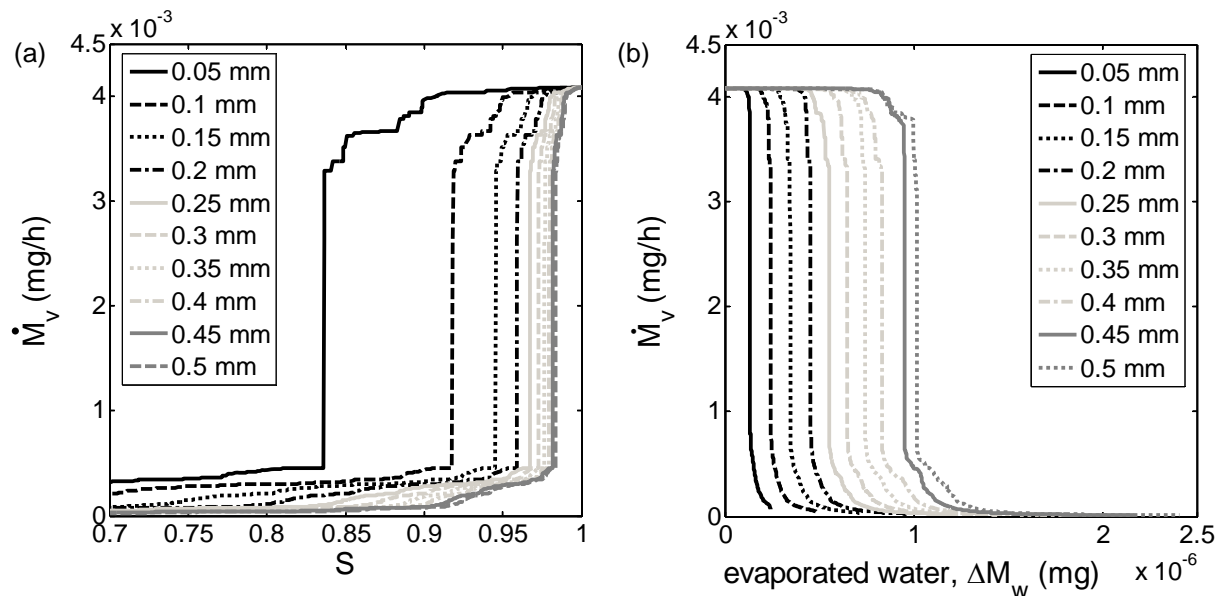


Figure 3.45: Influence of network depth on the drying curve for (a) network 1, abscissa: saturation (b) network 2, abscissa: mass of evaporated water.

3.5 Drying of 3D Cubic Networks with Viscous Effect

Drying of simple 3D cubic networks was simulated in order to come closer to the drying of real porous media, because 3D networks offer more flow paths. In these simulations, evaporation took place only at the top of network and all other sides were impervious. We used small networks ($16 \times 16 \times 16$) due to limitation of the computation time. The throat radius is generated as normal random distribution with range of mean throat radius 100 nm...400 nm and standard deviation 10 nm. Length of the throats is $5 \mu\text{m}$ for all throats in the network. Four different topologies of network structure were simulated with periodic boundary condition, and a part of each structure can be seen in Figure 3.46. Network 1 has monomodal pore size distribution with random micro throat radius ($r_0 = 100 \text{ nm}$), all other network structures have a bimodal pore size distribution with random micro and macro throat radius ($r_0 = 250 \text{ nm}$). As to the bimodal pore size distributions: network 2 has a continuous micro phase and the macro pores form long channels from the top to the bottom of the network; the micro and macro phase in the network 3 are continuous; and, the macro phase in the network 4 is dispersed (isolated).

In these simulations, lateral transfer in the boundary layer is also modelled. The mass transfer coefficient that resulted for the 2D network at the lowest air velocity has been used in order to

obtain the same boundary layer thickness ($\varepsilon = 500 \mu\text{m}$) and 100 vertical nodes. Some investigations on the 2D networks were repeated for these 3D network simulations. At first, the influence of boundary layer modelling (with and without lateral transfer) was investigated. Network structures 1 and 3 were chosen as representatives of monomodal and bimodal pore size distribution in order to study the influence of lateral transfer in the boundary layer. Then, for 3D networks the influence of different topology of network structure was investigated. We will focus on comparing of network structures 2 and 3 because both networks have a continuous phase of micro and macro throats in 3D. As in the 2D simulations, mean throat radius and standard deviation of pore size distribution were varied for the 3D networks in order to know this influence on drying kinetics. At last, the drying kinetics for the two limiting cases of negligible viscosity ($\eta \approx 0$) and immobile water ($\eta \rightarrow \infty$) will be presented.

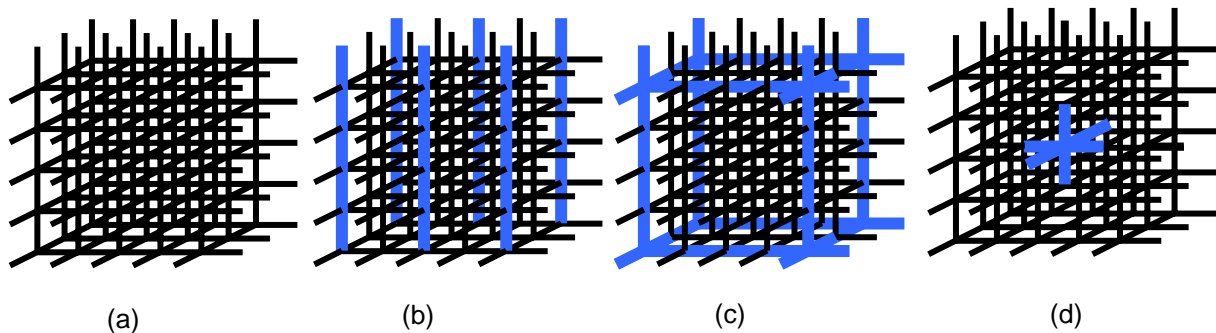


Figure 3.46: Part of geometry of 3D network model (a) network structure 1 with monomodal pore size distribution (b) network structure 2 with bimodal pore size distribution; micro phase continuous (c) network structure 3 with bimodal pore size distribution; micro and macro phase continue (d) network structure 4 with bimodal pore size distribution; macro pores dispersed.

Influence of Lateral Transfer in Boundary Layer

The results on the influence of lateral transfer in boundary layer for 2D network have shown that the approach without lateral transfer leads always to lower drying rates than the ones with lateral transfer. Again, the finite volume method is used to model the lateral vapour transfer in boundary layer with volumes being cubes of size L (throat length).

Figure 3.47 shows the drying curves for network structures 1 and 3 using two approaches to boundary layer modelling. The drying network model with lateral transfer can produce a first drying period for both network structures because of efficient vapour transfer in the boundary layer (due to a high number of vertical nodes corresponding to a large lateral exchange area). Due to more flow paths in 3D and more cross section areas at the network surface, the drying kinetics of network structure 1 in this simulation is rather different than that of the 2D network model, where a first drying period could not be observed for any boundary layer model. The duration of the first drying period with lateral transfer is longer by about 10 % of saturation than without lateral transfer, as shown in Figure 3.47a.

First drying period is longer for network structure 3 (with macro throats) than for network structure 1 (without macro throats), because when all macro throats are empty, capillary pumping in micro throats can supply liquid to the surface throats. The duration of first drying period for network structure 3 is longer by more than 10 % of saturation when accounting for lateral transfer in the boundary layer. The emptying of macro throats in this structure can create many menisci of micro throats at the depth of network. When capillary pumping of moving menisci can not supply liquid to the surface throats, the surface throats in the

approach with lateral transfer will dry rapidly because capillary pumping is lower than evaporation rate. During the second drying period, the drying rate for the approach with lateral transfer in the boundary layer is lower than for the approach without lateral transfer due to additional vapour resistance in the network.

The evolution of moisture profiles for network structure 1 in Figure 3.48 can give more detailed information about this phenomenon. Part of the surface throats is still wet at global saturation 90 % so that the capillary pumping is enough to supply liquid to the surface throat for evaporating. Then, at saturation 80 %, all surface throats are dry for approach with lateral transfer because capillary pumping is not enough to supply liquid due to high evaporation rate at the network surface. Therefore, the drying curve at that point has steeper gradient. The receding front period ($S < 0.60$) has more or less the same saturation profiles for both approaches because all liquid throats at the network surface have been evaporated and capillary pumping is not efficient anymore to supply liquid to the network surface.

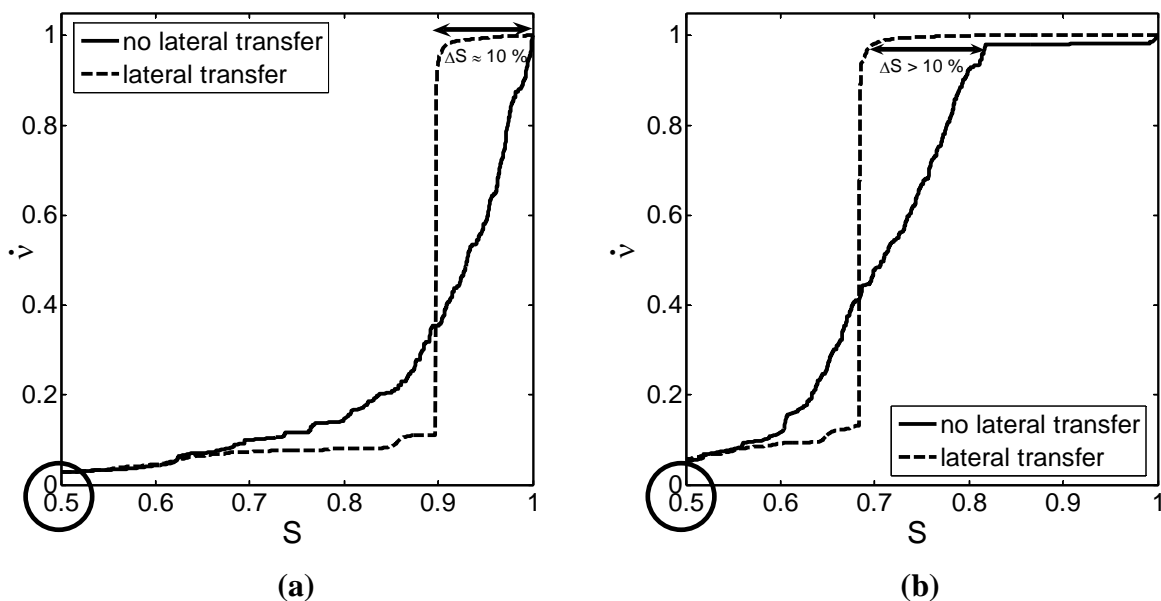


Figure 3.47: Comparison between two approaches to boundary layer modelling (without and with lateral transfer) for (a) network structure 1 (b) network structure 3.

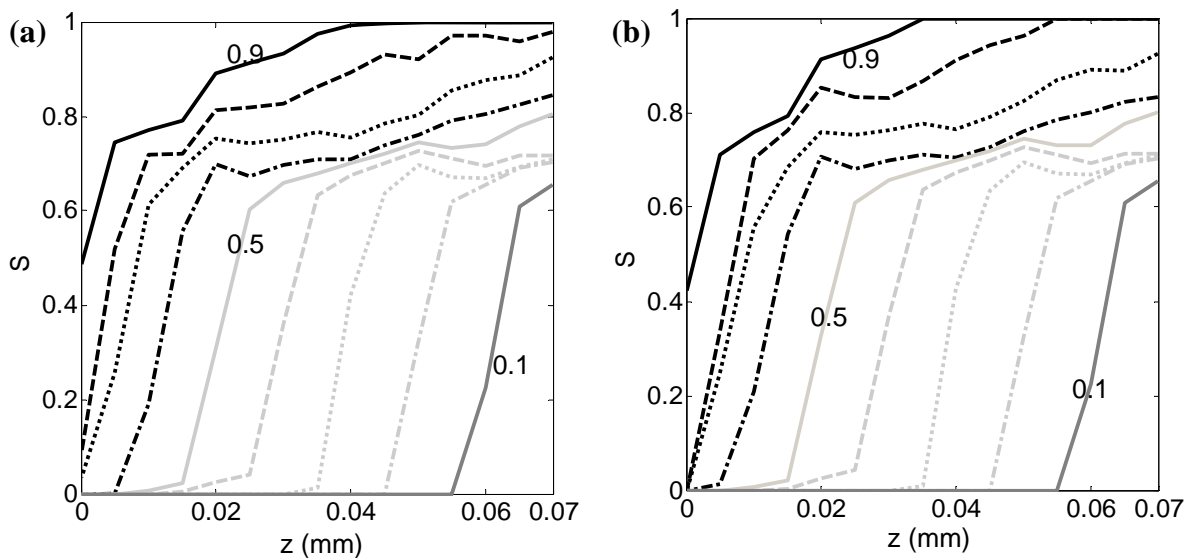


Figure 3.48: Evolution of moisture profiles for 3D network structure 1 by two approaches (a) without lateral transfer (b) with lateral transfer; lines correspond to multiples of 10% in overall saturation.

Influence of Structure

Four different 2D network structures have been presented in order to investigate the influence of different topology on drying behaviour. When transferring these network structures to 3D, network structure 3 changes its topology. In the 2D network model, the micro throats form cluster islands when the surrounding macro throats are empty and capillary pumping in the micro phase is interrupted, while all micro and macro throats in the 3D network model are connected to each other forming two continuous phases (micro and macro phases). Network structures 2 and 3 are quite comparable in 3D due the same state of micro throats. The two network structures are different only because of the state of macro throats. Macro throats in network structure 2 form long channels towards the network surface, not connected to each other, but although the macro throats are not a continuous phase, they will empty first due to the smallest capillary pressure. In the network structure 4 the macro throats are still isolated by micro throats and they are not a continuous phase.

Four different network structures were simulated in 3D network model in order to investigate the influence of network structure. For the bimodal pore size distributions, volume fraction of macro throats is around 20 %. The drying curves of 3D networks for the different network structures can be seen in Figure 3.49. In this figure, all network structures can produce a first drying period due to efficient capillary pumping and more available cross section area for vapour transfer in the boundary layer. This is also the reason why network structures 2 and 3 with bimodal pore size distribution have a long first drying period. Network structure 3 has a long first drying period in 3D because all micro throats are connected to other throats up to the network surface. Therefore, capillary pumping can supply liquid to the surface throats even if all macro throats in the network are empty. Evolution of moisture profiles of network structure 2 in Figure 3.49b corresponds to successive steps of 10 % decrease of global saturation. The flat moisture profile at saturation 80 % of that figure can be used as an indicator of emptying of all macro throats. However, the end of the first drying period is at saturation 70 % as shown in Figure 3.49a. Therefore, capillary pumping is continued by micro throats to supply liquid to the surface throats.

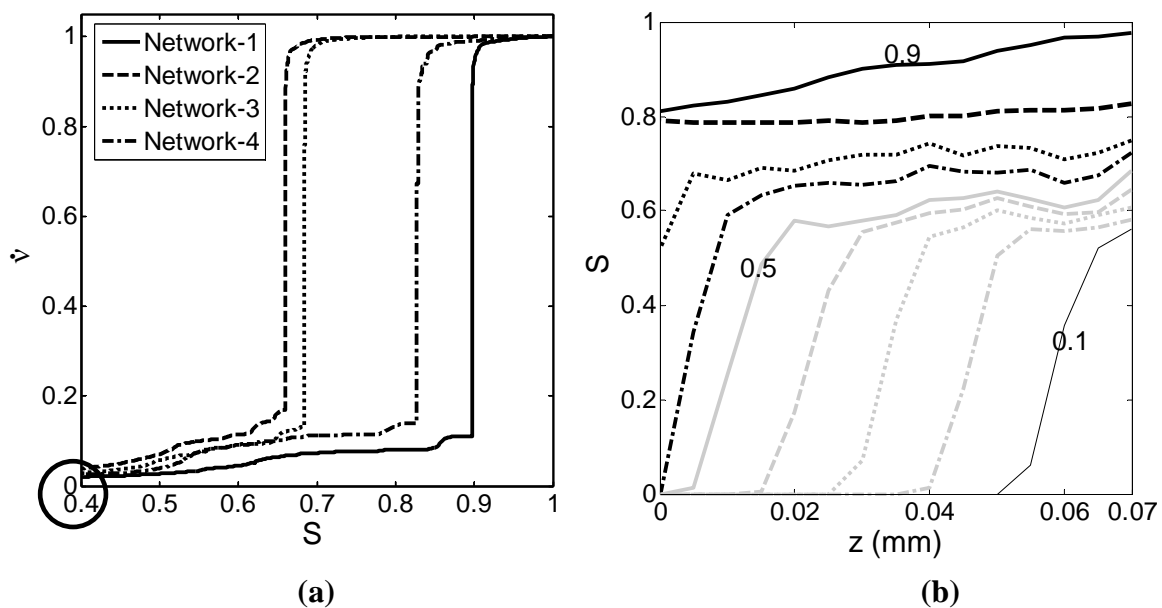


Figure 3.49: (a) Drying curves for different structure of 3D network (b) evolution of moisture profiles for 3D network structure 2.

Influence of Monomodal Pore Size Distribution

In order to investigate the influence of pore distribution on drying kinetics, variations of standard deviation and mean throat radius of monomodal pore size distribution in 3D were simulated. The bimodal pore size distribution was not varied because the macro throats always empty first. A broader distribution of throat radii (high standard deviation) has a longer first drying period due to high capillary pressure difference as seen in Figure 3.50a. This high capillary pressure difference leads to high capillary pumping. Consequently, capillary pumping of a broad distribution of throat radii can supply liquid longer to the other throats and keep wet spots at the network surface. Moisture profiles at global saturation 90 % for different standard deviations, depicted in Figure 3.51a, present the fraction of wet spots at network surface ($z = 0$ mm). This figure also shows a stepper gradient for narrow distribution due to high evaporation rate. Around 50 % of throats at the network surface are still wet for a broad pore size distribution ($\sigma_0 = 25$ nm) due to high capillary pumping.

Figure 3.51b shows drying curves for a variation of mean throat radius for monomodal pore size distribution in 3D. Large throat radii will result in good capillary pumping due to no influence of throat radius to evaporation rate at the network surface. Therefore, this pore size distribution leads to a longer first drying period. Moisture profiles for the variation of mean throat radius at global saturation 80 % are given in Figure 3.50b. We can see that for the largest mean throat radius part of the surface throats is still wet. Therefore, this can prove that capillary pumping still exists at that saturation. During the falling drying rate period the network with the largest mean throat radius ($r_0 = 400$ nm) still has higher drying rates because large cross section area increases the effective diffusivity.

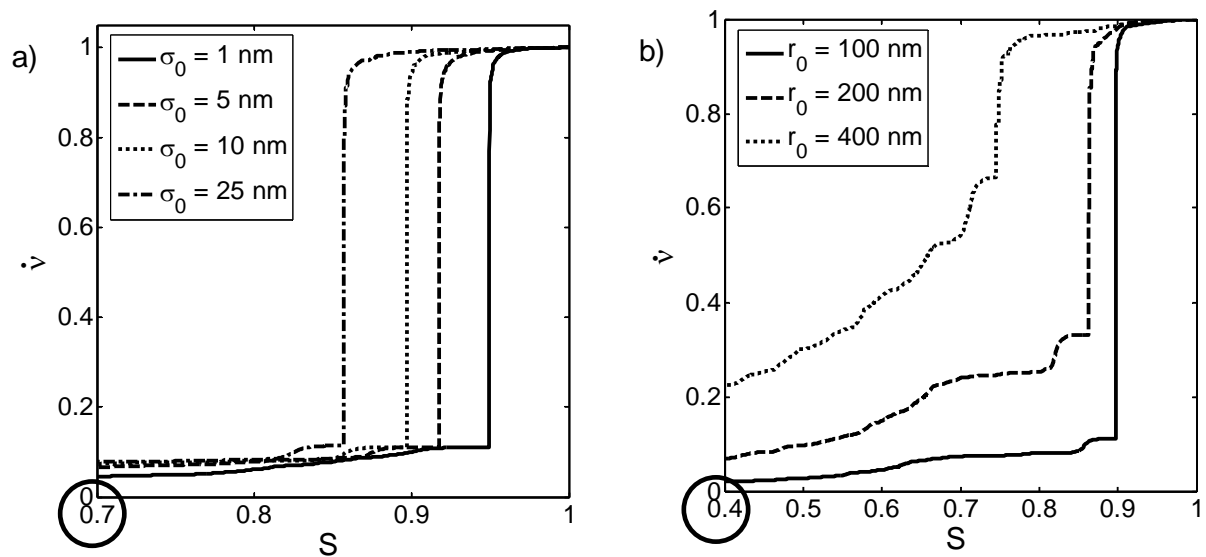


Figure 3.50: Drying curves for 3D cubic networks with monomodal pore size distribution under variation of (a) standard deviation (b) mean throat radius.

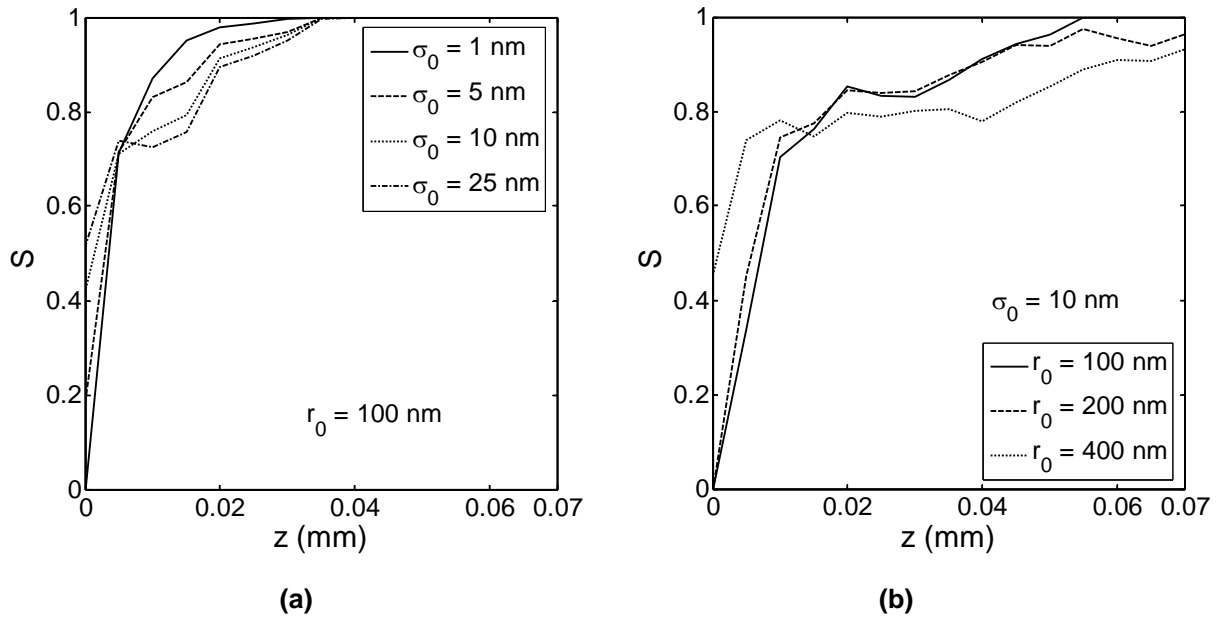


Figure 3.51: Moisture profiles for 3D network structure 1 (a) variation of standard deviation at global saturation, $S = 90\%$ (b) variation of mean throat radius at global saturation, $S = 80\%$.

Influence of Liquid Viscosity

Isothermal drying of porous media with viscous effect is not only influenced by pore size distribution but also by liquid viscosity. Two limiting cases, i.e. negligible liquid viscosity and immobile water, were simulated for 3D network structure 1 with mean throat radius 100 nm and standard deviation 10 nm. Then, the results were compared to the drying kinetics for water viscosity at 20°C (using the same pore size distribution). All cases of this simulation have lateral transfer in the boundary layer.

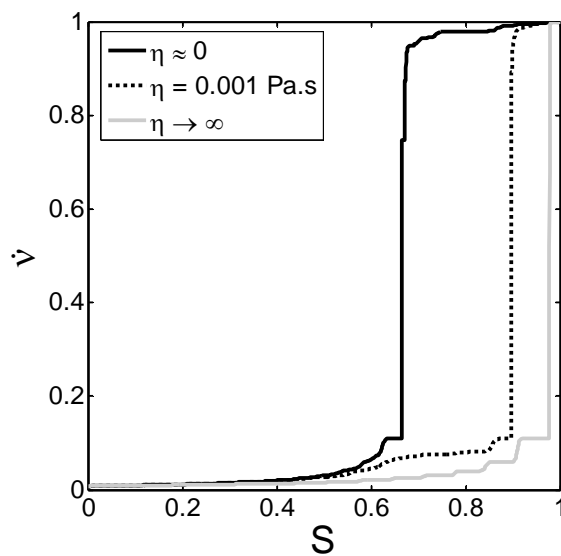


Figure 3.52: Drying curves at different liquid viscosities of network structure 1 ($r_0 = 100$ nm and $\sigma_0 = 10$ nm).

Figure 3.52 shows drying curves for the mentioned three cases. The case of negligible liquid viscosity has a longer first drying period because capillary pumping always dominates over friction forces. The moisture profiles in Figure 3.53 give an indication of liquid distribution in the network and gradient of saturation. For negligible liquid viscosity, the surface stays partially wet until a global saturation of 70 %, while for the case with water viscosity, the wet spots persist only for a short period ($S \approx 0.90 \dots 1$). Around the end of the first drying period ($S \approx 0.80$), the moisture profiles for the case with water viscosity have a steeper gradient.

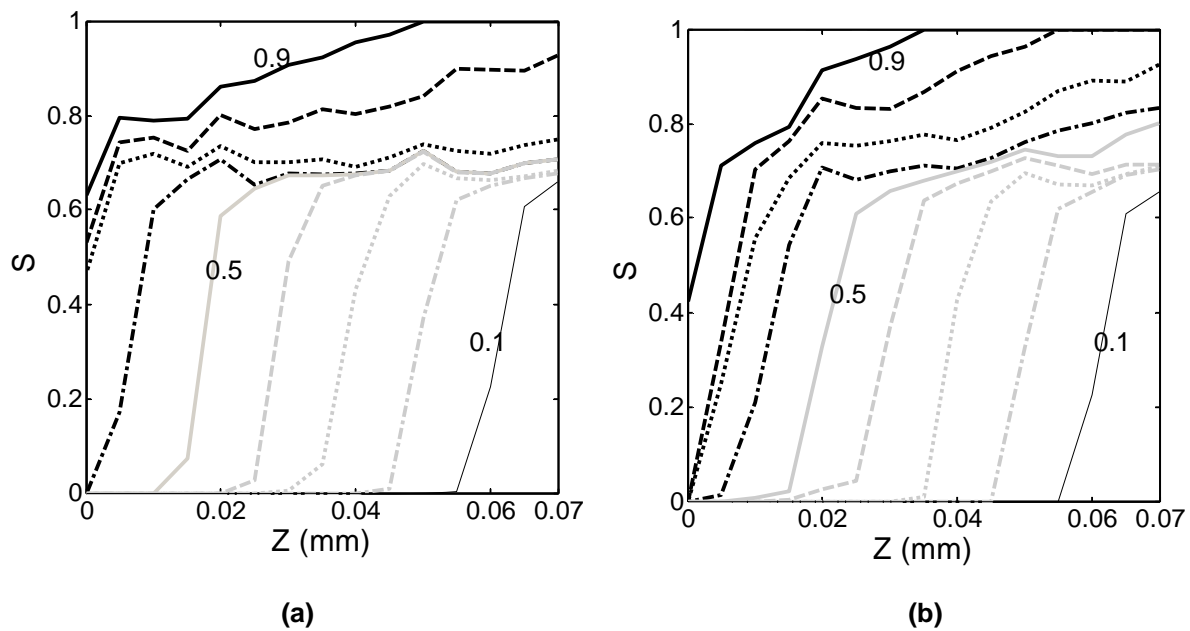


Figure 3.53: Evolution of moisture profiles for (a) negligible viscosity (b) water viscosity at 20°C.

3.6 Concluding Remarks

Drying behaviour is influenced by topology of network structure, where the first drying period can be produced by a continuous phase of micro-macro liquid throats. Lateral transfer in the boundary layer and spatial distribution of wet spots at the network surface also contribute to the first drying period. The competition between liquid viscous forces and capillary forces depends on the pore size distribution and liquid viscosity. Concerning the influence of structure, the drying kinetics for 3D network model is different than in 2D, due to more flow paths and wet spots at the network surface. The influence of other aspects, such as liquid viscosity and pore size distribution, is in 3D more or less the same as in 2D.

CONCLUSIONS AND FUTURE WORKS

Conclusions

Two- and three- dimensional network modelling of convective drying of porous media with negligible and non-negligible liquid viscosity has been presented for different network structures and pore size distributions. Concerning the influence of network structure, a favorable network structure, i.e. showing a long first drying period, should consist of continuous regions of macro and micro throats in order to deliver liquid to the network surface in a sustained manner. The small throats at the network surface must also have a good spatial distribution so that the wet spots during drying can guarantee efficient evaporation. In 2D network simulation for negligible liquid viscous forces, it could be shown that both conditions are fulfilled for a structure with long channels of large throats oriented towards the network surface.

Concerning the external conditions of convective drying, the drying curve is smoothened at lower air velocity for all network structures because this condition has a thicker boundary layer, which leads to more efficient lateral transfer. At the same time, the drying rate decreases because the resistance of mass transfer in the gas phase of the network increases. A comparison between lateral transfer approach and Schlünder's model of evenly distributed wet spots at the surface has been used to assess the wet spot distribution for different structures. It could be shown that for bimodal pore size distribution favourable and unfavourable pore size correlations exist.

The drying kinetics for a network structure with a monomodal pore size distribution was investigated by varying mean value and standard deviation of the throat radius. For the broad pore size distribution (high σ_θ), the drying process has a longer first drying period due to high capillary flow. A large throat radius (high r_θ) can maintain high drying rate as quasi constant period because in larger throats friction forces have less importance compared to capillary forces. In case of bimodal pore size distributions, the difference between mean throat radius of micro and macro throats did not influence the drying kinetics significantly.

Monte Carlo simulations have been presented in order to investigate the influence of random throat radius generation on the simulated drying behavior. The network structure with bimodal pore size distribution and large throats aligned in macro channels towards the surface was less sensitive because the imposed correlation of large throats is dominating liquid transport and drying kinetics. For other network structures (different spatial arrangement of macro throats or monomodal pore size distribution), the random generation of throat radius influenced drying behaviour significantly, especially via quasi constant drying period.

Drying of 3D networks has been simulated to investigate and to compare with the 2D results (one network structure in 3D has different topology than in 2D). 3D networks have more flow paths and more wet spots at the network surface so that a first drying period can be produced for all four network structures in 3D. The first drying period may be longer than the corresponding volume fraction of macro throats due to efficient capillary pumping to the network surface. The characteristic phenomena of 3D networks concerning influence of pore size distribution and viscous forces on drying behaviour are almost the same as for 2D networks.

Recommendations for Future Work

Drying of 2D networks has been simulated for a network size of 51×51 . The computation time is long for realization of one simulation: about 3 hours for non-negligible liquid viscosity. On the other hand, 3D networks with network size $16 \times 15 \times 15$ need around two days for one realization. Therefore, the program must be developed and made more efficient to obtain lower computational times.

Throat radius in this simulation has been generated as a normal random by a stochastic law, but the random throat radius in real porous media should not have large differences from one throat to the next. Armatas (2004 [2] and 2006 [3]) proposed a method to create a semi-random pore size distribution where the throat radius does not vary too much between neighbouring throats. On the other hand, the randomness is not only limited to throat radius, but also to positions of nodes, throat length and connectivity are also random. Therefore, the reconstruction of porous media should account for these. Two methods to reconstruct porous media are the dual site-bond model (Cordero et al., 2001 [4]) and multi point statistics (Okabe and Blunt, 2005 [21]).

Experiment in the network model can be performed by creating a micro model. The micro model can be built by lithographic or moulding techniques and the exact pore structure can be chosen. Then, the result from experiments can be compared directly with the network simulations.

Surasani et al. (2006 [32]) have started to extend the presented model to accommodate heat transfer. Therefore, some aspects of this project can soon be simulated in the non-isothermal condition. In future work, the continuum and discrete approach might be linked thus overcoming the weakness of both processes. The transport drying parameters, such as liquid permeability and vapour diffusivity may be produced by discrete approach for a representative pore network. Then, the continuum approach can use these parameters to calculate temperature and pressure in drying of porous media.

References

- [1]. **Al-Futaisi, A., Patzek, T.W.** (2003). Extension of Hoshen-Kopelman algorithm to non-lattice environments, *Physica A Journal*, 321, 665-678.
- [2]. **Armatas, G.S., Pomonis, P.J.** (2004). A Monte Carlo pore network for the simulation of porous characteristics of functionalized silica: pore size distribution, connectivity distribution and mean tortuosities, *Chemical Engineering Science*, 59, 5735 – 5749.
- [3]. **Armatas, G.S.** (2006). Determination of the effect of the pore size distribution and pore connectivity distribution on the pore tortuosity and diffusive transport in model porous network, *Chemical Engineering Science*, Article in press.
- [4]. **Cordero, S., Rojas, F., Riccardo, J.L.** (2001). Simulation of three-dimensional porous networks, *Colloid and Surfaces A Journal*, 187-188, 425-438.
- [5]. **Daian, J.F., Saliba, J.** (1991). Determining a representative random pore-network for moisture sorption and migration in cement mortar, *International Journal of Heat and Mass Transfer*, 34 (8), 2081 – 2096.
- [6]. **Dullien, F.A.L.** (1992). *Porous media: Fluid transport and pore structure*, Academic Press Inc, New York, USA.
- [7]. **Fatt, I.** (1956). The network model of porous media. *Trans AIME*, 207, 144-181.
- [8]. **Freitas, D.S., Prat, M.**(2000). Pore network simulation of evaporation of a binary liquid from a capillary porous medium, *Transport in Porous Media*, 40, 1-25.
- [9]. **Huinink, H.P., Pel, L., Michels, M.A.J, Prat, M.** (2002). Drying processes in the presence of temperature gradients – Pore scale modelling, *The European Physical Journal E*, 9, 487-498.
- [10]. **Irawan, A., Metzger, T., Tsotsas, E.** (2005). Pore Network Modelling of drying: combination with a boundary layer model to capture the first drying period, 7th World Congress of Chemical Engineering, Glasgow, Scotland.
- [11]. **Irawan, A., Metzger, T., Tsotsas, E.** (2006). Isothermal drying of pore networks: Influence of friction for different pore structures, 15th International Drying Symposium, Budapest, Hungary, 20 -23 August 2006.
- [12]. **Laurindo, J.B., Prat, M.** (1996). Numerical and experimental network study of evaporation in capillary porous media. *Phase Distributions*, *Chemical Engineering Science*, 51 (23), 5171-5185.
- [13]. **Laurindo, J.B., Prat, M.** (1998). Modelling of Drying in Capillary-Porous Media: A Discrete Approach, *Drying Technology*, 16 (9 & 10), 1769-1787.

- [14]. **Laurindo, J.B., Prat, M.** (1998). Numerical and experimental network study of evaporation in capillary porous media. *Drying rates*, *Chemical Engineering Science*, 53 (12), 2257-2269.
- [15]. **Le Bray, Y., Prat, M.** (1999). Three-dimensional pore network simulation of drying in capillary porous media, *International Journal of Heat and Mass Transfer*, 42, 4207-4224.
- [16]. **Lu, T., Jiang, P., Shen, S.** (2005). Numerical and experimental investigation of convective drying in unsaturated porous media with bound water, *Heat Mass Transfer*, 41, 1103 -1111.
- [17]. **Metzger, T., Irawan, A., Tsotsas, E.** (2005). Discrete modelling of drying kinetics of porous media, 3rd Nordic Drying Conference, Karlstad, Sweden, June 2005.
- [18]. **Metzger, T., Tsotsas, E.** (2005). Influence of pore size distribution on drying kinetics: a simple capillary model, *Drying Technology*, 23, 1797 – 1809.
- [19]. **Metzger, T., Irawan, A., Tsotsas, E.** (2006). Remarks on the paper “ Extension of Hoshen Kopelman algorithm to non-lattice environment” by A.Alfutaisi and T.W.Patzek, *Physica A* (2003) 665 – 678 , *Physica A*, 363, 665 – 678.
- [20]. **Nowicki, S.C., Davis, H.T., Scriven, L.E.** (1992). Microscopic determination of transport parameters in drying porous media, *Drying Technology Journal*, 10 (4), 925-946.
- [21]. **Okabe, H., Blunt, M.J.** (2005). Pore space reconstruction using multiple point statistics, *Journal of Petroleum Science and Engineering*, 46, 121 – 137.
- [22]. **Plourde, F., Prat, M.** (2003). Pore network simulations of drying of capillary porous media. Influence of thermal gradients, *International Journal of Heat and Mass Transfer*, 46, 1293-1307.
- [23]. **Prat, M.** (1993). Percolation model of drying under isothermal conditions in porous media, *International Journal of Multiphase Flow*, 19 (4), 691-704.
- [24]. **Prat, M.** (1995). Isothermal drying of non-hygroscopic capillary-porous material as an invasion percolation process, *International Journal of Multiphase Flow*, 21 (5), 875-892.
- [25]. **Prat, M., Bouleux, F.** (1999). Drying of capillary porous media with a stabilized front in two dimensions, *Physical Review E*, 60 (5), 5647-5656.
- [26]. **Prat, M.** (2002). Recent advances in pore-scale for drying of porous media, *Chemical Engineering Journal*, 86,153-164.
- [27]. **Schlünder, E.-U.** (1988). On the mechanism of the constant drying rate period, 6th International Drying Symposium, Versailles, France, September 1988.

- [28]. **Segura, L.A., Toledo, P.G.** (2005). Pore-level modelling of isothermal drying of pore networks. *Evaporation and viscous flow*, Latin American Applied Research, 35, 43 - 50.
- [29]. **Segura, L.A., Toledo, P.G.** (2005). Pore-level modelling of isothermal drying of pore networks. Effect of gravity and pore shape and size distributions on saturation and transport parameters, *Chemical Engineering Journal*, 111, 237 – 252.
- [30]. **Segura, L.A., Toledo, P.G.** (2005). Pore-level modelling of isothermal drying of pore networks. Accounting for evaporation, viscous flow and shrinking, *Drying Technology*, 23, 2007 – 2019.
- [31]. **Shaw, T.M.** (1987). Drying as an immiscible displacement process with fluid counter flow, *Physical Review Letters*, 59 (15), 1671-1674.
- [32]. **Surasani, V.K., Metzger, T., Tsotsas, E.** (2006). Towards a complete pore network drying model: First step to include heat transfer, 15th International Drying Symposium, Budapest, Hungary, 20 -23 August 2006.
- [33]. **Stauffer, D., Aharony, A.** (1992). *Introduction to Percolation Theory*, Taylor & Francis, London, UK.
- [34]. **Tsimpanogiannis, I.N., Yortsos, Y.C., Poulou, S., Kanellopoulos, N., Stubos, A.K.** (1999). Scaling theory of drying in porous media, *Physical Review E*, 59 (4), 4353-4365.
- [35]. **Vargaftik, N.B., Vinogradov, Y.K., Yargin, V.S.** (1996). *Handbook of Physical Properties of liquids and gases*, 3rd edition, Begell House, New York, USA.
- [36]. **Vu, T.H., Metzger, T., Tsotsas, E.** (2006). Influence of pore size distribution via effective parameters in a continuous drying model, 15th International Drying Symposium, Budapest, Hungary, 20 -23 August 2006.
- [37]. **Yiotis, A.G., Stubos, A.K., Boudouvis, A.G., Yortsos, Y.C.** (2001). Pore network model of the drying of single-component liquids in porous media, *Advances in Water Resources*, 24, 439-460.
- [38]. **Yiotis, A.G., Boudouvis, A.G., Stubos, A.K., Tsimpanogiannis, I.N., Yortsos, Y.C.** (2003). Effect of liquid films on the isothermal drying of porous media, *Physical Review E*, 68, 037303-1:4.
- [39]. **Yiotis, A.G., Boudouvis, A.G., Stubos, A.K., Tsimpanogiannis, I.N., Yortsos, Y.C.** (2004). Effect of liquid films on the drying of porous media, *AIChE Journal*, 50(11), 2721-2737.
- [40]. **Yiotis, A.G., Stubos, A.K., Boudouvis, A.G., Tsimpanogiannis, I.N., Yortsos, Y.C.** (2005). Pore network modelling of isothermal drying in porous media, *Transport Porous Media Journal*, 58, 63-86.

-
- [41]. **Yiotis, A.G., Tsimpanogiannis, I.N., Stubos, A.K., Yortsos, Y.C.** (2006). Pore-network study of the characteristic periods in the drying of porous materials, *Journal of Colloid and Interface Science*, 297, 738 -748.
- [42]. **Whitaker, S. (1998).** *Coupled Transport in Multiphase Systems: A Theory of Drying*, *Advances in Heat Transfer*, Vol. 31, Academic Press, New York,1–103.

Curriculum Vitae

Family name : Irawan
First name : Anton
Date of birth : 01.10.1975
Place of birth : Silungkang, Indonesia
Nationality : Indonesian
Gender : Male
Marital status : Married
Children : 1 son (4 years old)
Home address : Jalan Kaum No 10, Pagaden Baru, Pagaden, Subang, Indonesian
Phone: +62-260-450221; Mobile Phone: +62-81384242695
E-mail: anton11975@yahoo.com

Education:

03.2003 – 02.2006 PhD scholarship of German Research Foundation (DFG) in frame of Graduate School 828 “Micro-Macro-Interactions in Structured Media and Particle Systems” at Chair of Thermal Process Engineering (Prof. Dr.-Ing. habil. Evangelos Tsotsas), Faculty for Process and Systems Engineering, Otto-von-Guericke University Magdeburg, Germany.

09.1999 – 02.2002 M.Eng. (Chemical Engineering)
Faculty of Technology Industry,
Bandung Institute of Technology, Indonesia.
Supervisor: Dr. Yazid Bindar
Research Title:
Investigation of Inverse Flame Diffusion of Hydrogen Combustion

09.1994 – 03.1999 B.Sc. (Chemical Engineering)
Faculty of Technology Industry,
Bandung Institute of Technology, Indonesia.
Supervisor: Prof. Dr. Herri Susanto
Research Title:
Study of Hydrodynamic Gasification of Empty Palm Bench.

Work experience:

08.1999 – 02.2003 Research Assistant
Chemical Engineering Department
Bandung Institute of Technology
Bandung, Indonesia.

09.2000 – Present Lecturer
Chemical Engineering Department
General Achmad Yani University
Cimahi, Indonesia.

Lebenslauf

Name : Irawan
Vorname : Anton
Geburtsdatum : 01.10.1975
Geburtsort : Silungkang, Indonesien
Staatsangehörigkeit : indonesisch
Geschlecht : männlich
Familienstand : verheiratet
Kinder : 1 Sohn (4 Jahre alt)
Anschrift : Jalan Kaum No 10, Pagaden Baru, Pagaden, Subang, Indonesien
Phone: +62-260-450221; Mobile Phone: +62-81384242695
E-mail: anton11975@yahoo.com

Ausbildung:

- 03.2003 – 02.2006 DFG-Promotionstipendium im Graduiertenkolleg 828 “Micro-Macro-Interactions in Structured Media and Particle Systems” am Lehrstuhl für Thermische Verfahrenstechnik (Prof. Dr.-Ing. habil. Evangelos Tsotsas) an der Fakultät für Verfahrens- und Systemtechnik der Otto-von- Guericke-Universität Magdeburg.
- 09.1999 – 02.2002 Master of Engineering in Chemischer Verfahrenstechnik
Fakultät für Angewandte Technik,
Bandung Institute of Technology, Indonesien.
Betreuer: Dr. Yazid Bindar
Thema der Masterarbeit:
Investigation of Inverse Flame Diffusion of Hydrogen Combustion
- 09.1994 – 03.1999 Bachelor of Science in Chemischer Verfahrenstechnik
Fakultät für Angewandte Technik,
Bandung Institute of Technology, Indonesien.
Betreuer: Prof. Dr. Herri Susanto
Thema der Abschlussarbeit:
Study of Hydrodynamic Gasification of Empty Palm Bench.

Beschäftigungsverhältnisse:

- 08.1999 – 02.2003 Wissenschaftlicher Mitarbeiter
Abteilung für Chemische Verfahrenstechnik
Bandung Institute of Technology
Bandung, Indonesien.
- Seit 09.2000 Wissenschaftlicher Dozent
Abteilung für Chemische Verfahrenstechnik
General Achmad Yani University
Cimahi, Indonesien.